

Award Number: W81XWH-11-2-0076

TITLE: New Methods of Low-Field Magnetic Resonance Imaging for
Application to Traumatic Brain Injury

PRINCIPAL INVESTIGATOR: Matthew S. Rosen, Ph.D.

CONTRACTING ORGANIZATION: Harvard University
Cambridge MA 02138

REPORT DATE: April 2016

TYPE OF REPORT: FINAL

PREPARED FOR: U.S. Army Medical Research and Materiel Command
Fort Detrick, MD 21702-5012

DISTRIBUTION STATEMENT:

Approved for public release; distribution unlimited

The views, opinions and/or findings contained in this report are those of the author(s) and should not be construed as an official Department of the Army position, policy or decision unless so designated by other documentation.

REPORT DOCUMENTATION PAGE				Form Approved OMB No. 0704-0188	
Public reporting burden for this collection of information is estimated to average 1 hour per response, including the time for reviewing instructions, searching existing data sources, gathering and maintaining the data needed, and completing and reviewing this collection of information. Send comments regarding this burden estimate or any other aspect of this collection of information, including suggestions for reducing this burden to Department of Defense, Washington Headquarters Services, Directorate for Information Operations and Reports (0704-0188), 1215 Jefferson Davis Highway, Suite 1204, Arlington, VA 22202-4302. Respondents should be aware that notwithstanding any other provision of law, no person shall be subject to any penalty for failing to comply with a collection of information if it does not display a currently valid OMB control number. PLEASE DO NOT RETURN YOUR FORM TO THE ABOVE ADDRESS.					
1. REPORT DATE (DD-MM-YYYY) April 2016		2. REPORT TYPE Final		3. DATES COVERED (From - To) 10Jan2011 - 9Jan2016	
4. TITLE AND SUBTITLE New Methods of Low-Field Magnetic Resonance Imaging for Application to Traumatic Brain Injury				5a. CONTRACT NUMBER W81XWH-11-2-0076	
				5b. GRANT NUMBER	
				5c. PROGRAM ELEMENT NUMBER	
6. AUTHOR(S) Matthew S. Rosen, PhD email: mrosen@cfa.harvard.edu				5d. PROJECT NUMBER	
				5e. TASK NUMBER	
				5f. WORK UNIT NUMBER	
7. PERFORMING ORGANIZATION NAME(S) AND ADDRESS(ES) Harvard University Cambridge MA 02138				8. PERFORMING ORGANIZATION REPORT NUMBER	
9. SPONSORING / MONITORING AGENCY NAME(S) AND ADDRESS(ES) U.S. Army Medical Research and Materiel Command Fort Detrick, MD 21702-5012				10. SPONSOR/MONITOR'S ACRONYM(S)	
				11. SPONSOR/MONITOR'S REPORT NUMBER(S)	
12. DISTRIBUTION / AVAILABILITY STATEMENT Approved for public release; distribution unlimited.					
13. SUPPLEMENTARY NOTES					
14. ABSTRACT We have developed robust low-magnetic-field implementations of MRI (LFI) focused on brain imaging with two complimentary test scanner systems: electromagnet and permanent magnet based. We have also developed injury-sensitive MRI based on the detection of free radicals associated with injury using the Overhauser effect and subsequently imaging that modified nuclear polarization using low-field MRI (OMRI). We have optimized imaging sequences, image reconstruction, and parallel imaging based acceleration in this unique regime. Results include demonstration high-speed brain imaging in the electromagnet LFI at 6.5 mT, preliminary 3D imaging in a 100 lb scanner based on a rotating permanent magnet array, and improved free-radical OMRI both <i>in vitro</i> and <i>in vivo</i> . Application of the suite of techniques and technologies from our work could advise future development of a deployable device with a high diagnostic impact, transforming diagnosis and monitoring of secondary injury prevalent in TBI.					
15. SUBJECT TERMS Low-field brain MRI, Injury-sensitive MRI, Free radical Overhauser imaging.					
16. SECURITY CLASSIFICATION OF:			17. LIMITATION OF ABSTRACT UU	18. NUMBER OF PAGES 87	19a. NAME OF RESPONSIBLE PERSON USAMRMC
a. REPORT U	b. ABSTRACT U	c. THIS PAGE U			19b. TELEPHONE NUMBER (include area code)

Table of Contents

INTRODUCTION:	4
BODY:	4
Aim 1: Development of Low Field Imagers (LFIs)	5
<i>6.5 MILLITESLA ULTRA-LOW-FIELD ELECTROMAGNET LFI:</i>	5
<i>HALBACH ARRAY (PERMANENT MAGNET) LFI:</i>	6
Aim 2: OMRI Injury Imaging	7
KEY RESEARCH ACCOMPLISHMENTS:	11
REPORTABLE OUTCOMES:	14
CONCLUSION:	20
REFERENCES:	21
APPENDICIES:	24
<i>CONFERENCE ABSTRACTS:</i>	2
<i>MANUSCRIPTS PUBLISHED:</i>	43

INTRODUCTION:

Our applied research program has significantly advanced the development of novel methods and advanced hardware for low-magnetic-field MRI. Without major innovation, high-field MRI instruments offer limited utility for imaging TBI in widely deployable contexts. We have taken on the critical challenges that must be solved to enable deployment of a transportable human-head MRI system applicable to TBI imaging in battlefield medical facilities. We have established proof-of-principle for a suite of techniques and technologies to advise future development of a field-deployable MRI instruments with high diagnostic impact. This research effort had two specific aims:

Specific Aim 1: Develop low-field human-head MRI (LFI) suitable for high-resolution imaging, and improve the ability to attain brain images based on the intrinsic *in vivo* ^1H NMR signal.

This work includes the development of *two* robust low-field scanner hardware methodologies (electromagnet based and permanent magnet based), the development of novel high-efficiency single- and multi-channel detection systems, and work on advanced adaptive reconstruction methods including navigators and sparse sampling.

Specific Aim 2: Develop injury-sensitive MRI based on converting the electron spin of free radicals associated with injury (specifically TBI) into nuclear polarization using the Overhauser effect and subsequently imaging that modified nuclear polarization using low-field MRI (**OMRI**). The demonstration of OMRI of free radicals associated with injury will enhance image-based injury specificity and/or shortening scan acquisition times in the low-field MRI systems of **Aim 1**,

This work includes the development of a new high-speed OMRI acquisition strategy, the development of new high efficiency double resonator designs, and the demonstration of this new MRI contrast mechanism in a model system *in vivo*.

BODY:

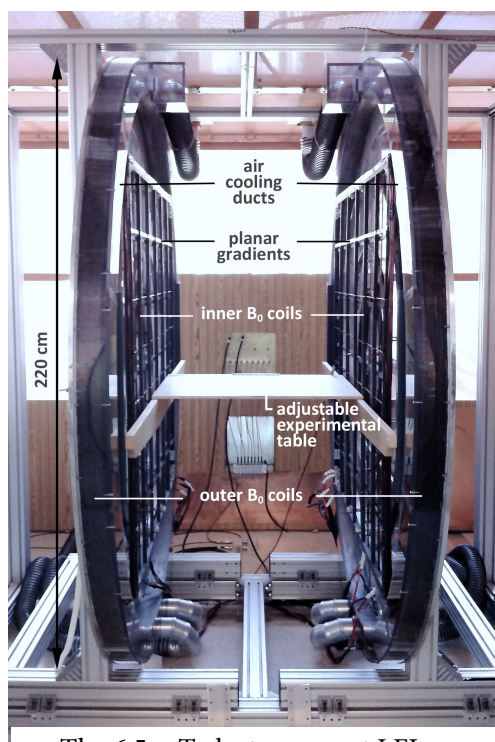
The ability to acquire high-quality images with ultra-low field MRI has improved dramatically as a result of our suite of improved hardware and image acquisition strategies in the 6.5 mT electromagnet LFI (Aim 1). We have validated image quality in multi-compartment head-shaped phantom developed for this work, including images acquired using a new single-channel receiver coil design optimized for human heads [1]. This receiver coil design demonstrates performance that exceeds the more complex multi-channel designs developed earlier in our work [2]. This system has for the first time demonstrated that high-quality MRI of human heads can be acquired at ultra-low magnetic field [3] over short acquisition times.

Additionally, our permanent magnet-based rotating Halbach LFI (Aim 1) has moved toward the acquisition of true 3D datasets in the Halbach magnet portable imaging prototype [4]. For the first time, three key ingredients – “built-in” 2D encoding using a rotating B_0 encoding field, phase encoding with a linear phase RF transmit coil, and broadband RF pulses [5] – were brought together to enable three-axis encoding in an inhomogeneous B_0 field with no gradient coils .

Our work on the detection of free radicals (Aim 2) using low-field MRI has focused on decreasing the image acquisition time in Overhauser MRI, and on improving the detection limit to low concentrations of free radicals in synthetic radical solutions. To this end, we have developed a new high speed approach to imaging free radicals with MRI [6]. We determined that significant improvements were still needed in the manner in which our OMRI detection is performed before we could attain sensitivity to superoxide, and to that end have improved our OMRI detector hardware and attained a 3-fold improvement in SNR and, critically, wide-range tunability has been attained [7].

The Annual Reports generated during the period of performance of this work contain detailed technical descriptions of the hardware and image acquisition strategies for both Aims. We summarize in this Final Report the major innovations of each Aim, and attach the relevant peer-reviewed journal publications that provide additional detail not included in the Annual Reports.

Aim 1: Development of Low Field Imagers (LFIs)



The 6.5 mT electromagnetic LFI

We have developed two approaches to MRI at low magnetic field. The first, the electromagnet LFI (shown below) is an ideal state-of-the-art test bed for all of the novel acquisition, detection methodologies, and reconstruction algorithms including navigators and sparse sampling, and additionally will provide necessary experience and data to advise optimal construction and magnetic field for any future electromagnet-based deployable systems. Currently, this state-of-the-art scanner enables high-performance spectroscopy and 8-channel imaging at 6.5 mT, and is fully equipped for Overhauser DNP experiments.

The second approach to low field MRI is a permanent magnet system build around a lightweight (45 kg) Halbach array. This Halbach array scanner is a highly specialized and potentially disruptive technology scanner that could greatly ease both the cost and burden of a field-forward instrument purpose-built for TBI imaging. This Halbach imager contrasts markedly with the electromagnet LFI in that it has a highly inhomogeneous magnetic field, but we use this inhomogeneity to our advantage as an encoding field to acquire head images without the use of an additional gradient set.

6.5 mT ultra-low-field electromagnet LFI:

High performance imaging in the 6.5 mT LFI has focused on *significantly* reducing acquisition time at low field using fast imaging techniques. Fast imaging was implemented in the LFI using 3D balanced steady-state free precession sequences (b-SSFP). To the best of our knowledge, our results represent the first time that b-SSFP has been successfully implemented in a low magnetic field scanner and represents a *tremendous* improvement for high speed MRI at low magnetic field, representing more than a **100-fold time savings** compared to traditional gradient echo imaging in this regime.

With this test-bed LFI we developed a remarkably simple, non-cryogenic approach to low-field, high-performance human brain MRI that results from a program of advanced hardware and high efficiency pulse sequence development, combining fully refocused steady-state sequences with modern k -space undersampling. Our recent human head imaging experiments with the LFI [3] have demonstrated heretofore unattainable speed and resolution: MRI images in the living human brain were acquired at 6.5 mT, a magnetic field more than 460×

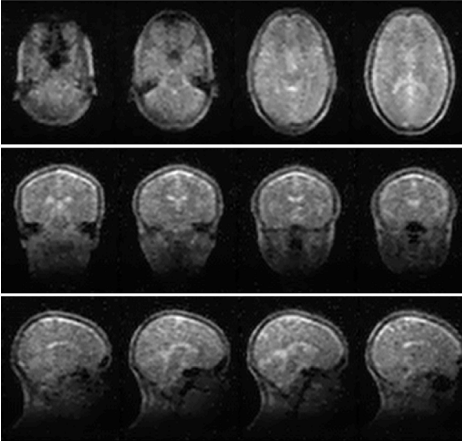


Figure 1: Brain imaging at 6.5 mT

lower than clinical 3 T MRI scanners. Shown in Figure 1 are four representative slices (in 3 orientations) acquired on our test-bed scanner with a voxel size of $2.5 \times 3.5 \times 8.5 \text{ mm}^3$. Each full 3D dataset (fifteen slices) was acquired in **6 minutes**, more than 30× faster – and with significantly higher SNR – than very recently published cryogenic SQUID-detected low field MRI [8].

This work represents by far the highest SNR per unit time in low field MRI, and our data were acquired without time-wasting pre-polarization techniques or fragile SQUID-based cryogenic detectors. This result demonstrates that high quality ^1H brain MRI at 6.5 mT is attainable over reasonable averaging times. This safe and inexpensive technology operates at fixed magnetic field at room temperature with no need for magnetic

shielding or cryogenics as in SQUID systems, and without the power burden and potential danger of magnetic field-cycled systems, which can ramp to as much as 0.1-0.2 T during operation.

See attached manuscript: “Low-Cost High-Performance MRI,” *Sci Rep*, vol. 5, p. 15177, Oct. 2015.

Halbach array (permanent magnet) LFI:

This test bed scanner is based around a lightweight array of permanent magnets in a so-called Halbach configuration Figure 2. This magnet is ideal for portable MRI in that it creates a relatively uniform field transverse to the head without the use of a cryostat or power supplies. This Halbach array scanner is a highly specialized scanner and a potentially disruptive technology that could greatly ease both the cost and burden of a field-forward instrument purpose-built for TBI imaging. This Halbach imager contrasts markedly with the electromagnetic LFI in that it has a highly inhomogeneous magnetic field, but we use this inhomogeneity to our advantage and use it to acquire head images without the use of an additional gradient set.

We have designed and built the very portable 45 kg Halbach array magnet for portable MRI, and mapped the magnetic field and drift using NMR measurements at 3.3 MHz. We then fo-

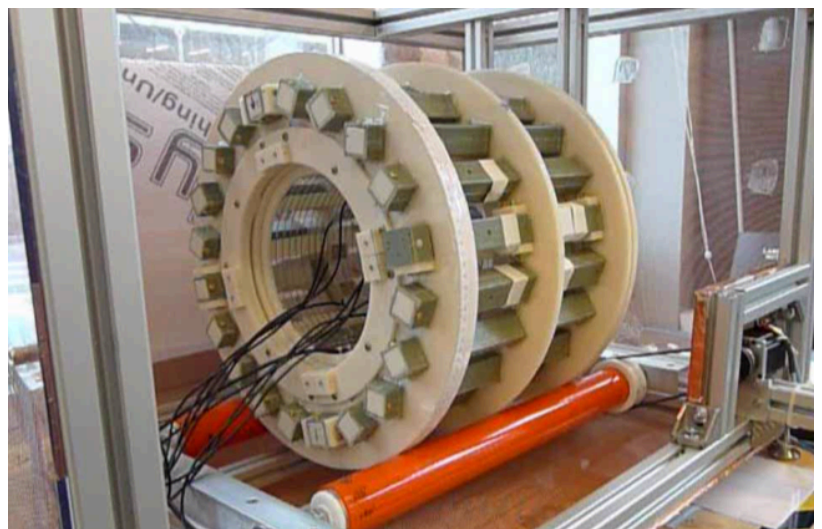


Figure 2: The Halbach magnet with RF shield, aluminum support struts, urethane-clad rollers, and stepper motor assembly.

cused on the hardware and encoding techniques needed to turn this magnet into an imager. We solved some critical challenges including the ability to acquire 2D multi-channel images. Research in 2014 (Y4) saw substantial progress toward the acquisition of true 3D datasets in the Halbach magnet portable imaging prototype [4]. For the first time, three key ingredients – “built-in” 2D encoding using a rotating B_0 encoding field, phase encoding with a linear phase RF transmit coil, and broadband RF pulses – were brought together to enable three-axis encoding in an inhomogeneous B_0 field with no gradient coils.

See attached manuscripts:

“Two-dimensional imaging in a lightweight portable MRI scanner without gradient coils,” *Magnetic Resonance in Medicine*, vol. 73, no. 2, pp. 872–883, Mar. 2014.

“Transmit Array Spatial Encoding (TRASE) using broadband WURST pulses for RF spatial encoding in inhomogeneous B_0 fields,” *Journal of Magnetic Resonance*, vol. 268, no. C, pp. 36–48, Jul. 2016.

Aim 2: OMRI Injury Imaging

Overhauser-enhanced MRI (OMRI) is an electron-proton double resonance imaging technique of much interest due to its ability to detect the concentration and distribution of free radicals. Tracking of exogenous free radicals with OMRI *in vivo* has enabled the development of oxymetry probes [9] and the imaging of redox reactions [10]. The large gyromagnetic ratio of electrons (28 GHz/T) demands that *in vivo* OMRI is performed at very low magnetic fields (~ 10 mT) in order to minimize RF heating and penetration depth issues. Operation at low magnetic field causes a drastic reduction in NMR sensitivity despite the signal enhancement that comes from the Overhauser effect, and emphasizes the need for high S/N probes. OMRI probe design is still relatively unexplored, despite its importance, and presents challenges unique to the frequencies of operation ($f_H = 276$ kHz and $f_e = 140.8$ MHz in our experiments at 6.5 mT).

A critical result from our effort is the development of a new method for 3D OMRI based on b-SSFP that provides up to 7-fold acceleration compared to the fastest OMRI sequence reported in the literature, by combining the high acquisition efficiency of b-SSFP by applying the Overhauser saturation pulses during the phase encode step, with the addition of undersampling strategies and compressed sensing (CS) techniques to increase the temporal resolution while also reducing the total number of EPR RF pulses [6].

A key challenge in implementing OMRI for TBI will be detecting the small concentrations of radical present *in vivo*. We have demonstrated that 10 μM nitroxide radical in water and 50 μM nitroxide radical in water can be detected with Overhauser spectroscopy (Figure 3) and OMRI (Figure 4), respectively. The concentration of free radical at the location of injury remains *unknown*, but estimates range from 50 nM to 50 μM [11]–[17]. Additionally, detecting free radicals *in vivo* will be more difficult than in phantoms due to extra relaxation pathways reducing the efficiency of DNP.

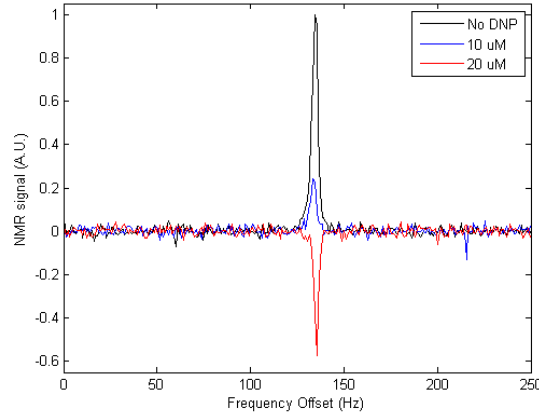


Figure 3: Measurement of the sensitivity threshold to small concentrations of nitroxide radical via Overhauser enhanced NMR spectroscopy. These spectra were acquired in the electromagnet LFI at 6.5 mT (276 kHz). The ESR frequency was 140 MHz.

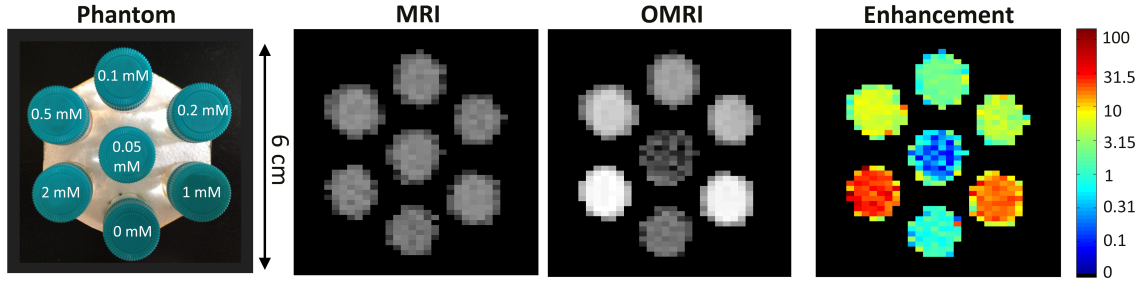


Figure 4: Photograph of phantom used to demonstrate the sensitivity of OMRI to nitroxide radical concentration. All seven vials have very similar image magnitudes in the conventional **MRI** image. The **OMRI** scan demonstrates marked image-based free radical sensitivity. The signal magnitude from the control vial remains unchanged in OMRI scan. **OMRI enhancement** image is computed from the ratio of OMRI to MRI magnitude. MRI and OMRI were both obtained at 6.5 mT. The NMR frequency is 276 kHz and the ESR frequency is 140 MHz.

In order to further improve the detection efficiency to lower concentrations of radicals, we developed a high performance OMRI probe with broad tunability, capable of imaging enhancement over a wide range of free radical electron g -factors. This OMRI probe consists of an NMR solenoid inside a modified Alderman-Grant Resonator (Figure 5), and interfaces with the 6.5 mT electromagnet LFI ($f_H = 276$ kHz). Images were acquired using our fast, high-resolution b-SSFP based OMRI methodology [6]. NMR probe design in the low-field regime is fundamentally different to that at conventional MRI fields as thermal noise due to the intrinsic resistance of the pickup coil dominates over sample noise. This leads to a compromise where S/N improvements come at the expense of imaging bandwidth $S/N \sim \sqrt{Q} \sim 1/\sqrt{BW}$. An 85 turn solenoid was wound, using low AC resistance 5/39/42 litz wire, on a 3D printed polycarbonate former. This high filling factor coil has a bandwidth of 3 kHz.

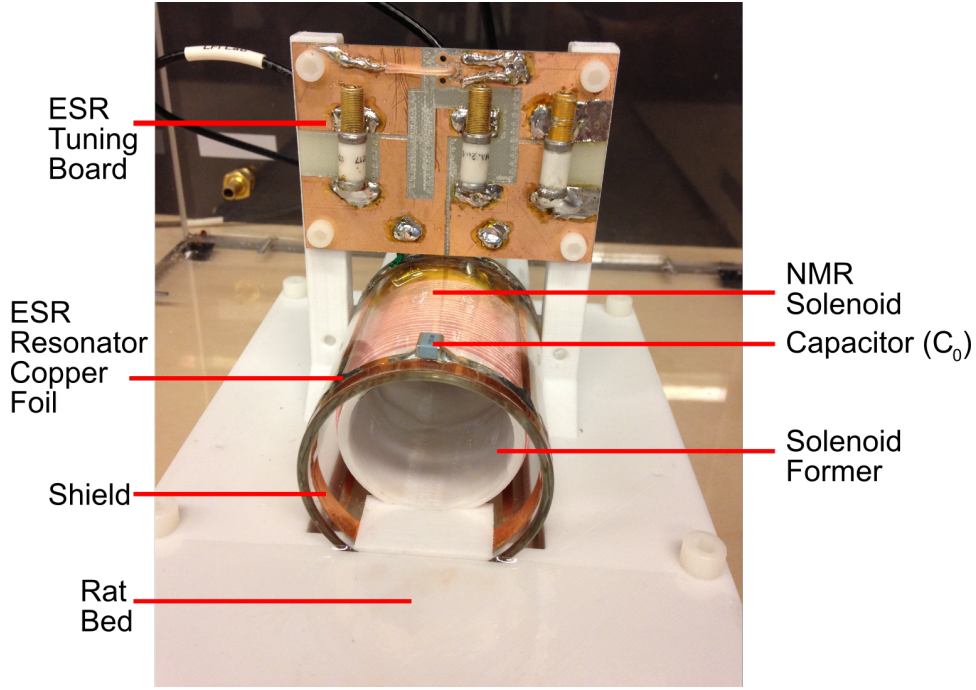


Figure 5: NMR/ESR rat head probe for operation at 6.5 mT. The ESR resonator is tuned to 140.8 MHz. The litz wire NMR solenoid coil (276 kHz) resonator board is not shown.

A modified Alderman-Grant ESR resonator was built using copper foil on Pyrex tubing. All metal placed in close proximity to the NMR solenoid strongly couples, reducing the NMR sensitivity. We therefore minimized amount of copper in the ESR resonator. Windows were removed from the panels on the sides of an Alderman-Grant resonator, a region of low current flow [18], in an attempt to reduce coupling whilst maintaining B_1 homogeneity. Shielding at the ends of the resonator prevents high electric fields at the capacitors penetrating the imaging volume, important because $P_{\text{RF-absorbed}} \sim E^2$. Slits in the shielding prevent the formation of closed loops that couple to the solenoid. Figure 6 demonstrates the high B_1 homogeneity and strong E suppression in our ESR resonator.

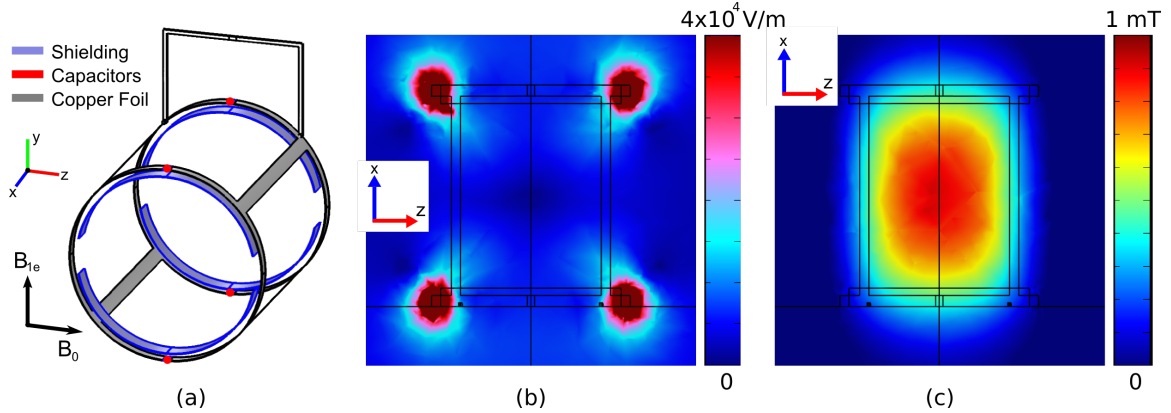


Figure 6: COMSOL Multiphysics simulations (a) Our modified Alderman-Grant Resonator. (b) Plot of $|E|$ showing that the electric field is strongly suppressed inside the resonator. (c) B_{1e} shows high homogeneity in the imaging volume – less than 10% variation across the imaging region.

TEMPOL (4-hydroxy-TEMPO) a stable radical, is detected by OMRI with high sensitivity, and because of its small size may facilitate imaging blood brain barrier leakage in cases of oxidative stress [19]. Simulations were

validated in 2 mM TEMPOL solutions using simple spectroscopic measurements as well as fast imaging strategies [6]. The ESR resonator was tuned to 141 MHz, the lowest frequency of the TEMPOL triplet state at 6.5 mT, to minimize RF heating during ESR irradiation.

In vivo performance

Previously we described the development of an OMRI probe for a rat head model utilizing an NMR solenoid and ESR surface coil. Testing of this new OMRI probe indicates that it has $3\times$ the S/N of the probe reported [19], and rectifies problems with B_{1c} homogeneity, yielding homogeneous enhancement of -6.7 in 2 mM TEMPOL when 10 W of RF power is applied. *In vivo* OMRI signal enhancement is clearly visible in the rat brain after TEMPOL injection, as shown in Figure 7. As the Overhauser-enhanced signal has a phase opposite to that of the thermal signal, the phase image in Figure 7 provides sensitive contrast in regions of low TEMPOL concentration.

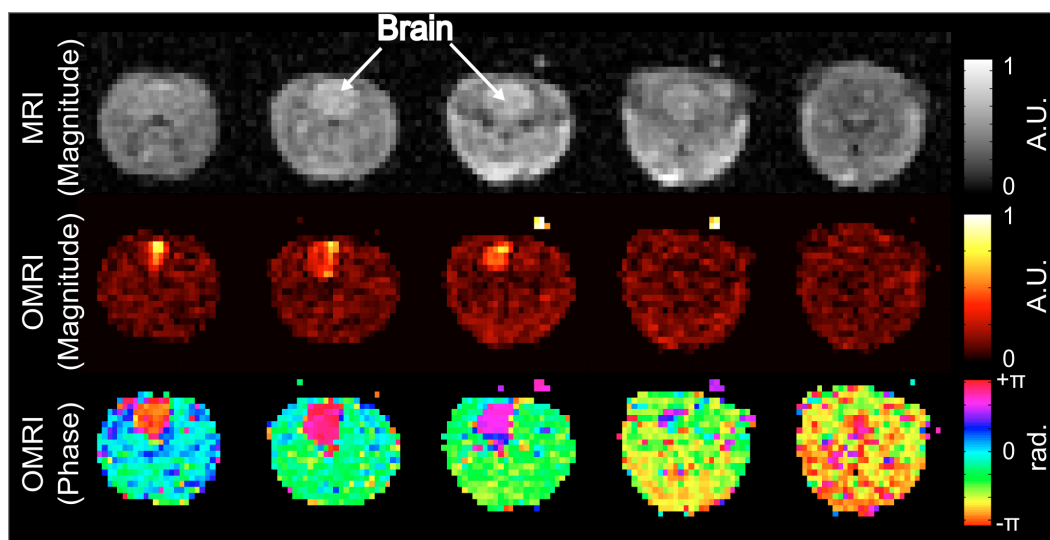


Figure 7: OMRI images acquired from a rat at 6.5 mT following injection of 1 mL of 150 mM TEMPOL. Five slices from an 11 slice data set shown. OMRI (NA=1) imaging time was **9 seconds**. Anatomical MRI (NA=30) was acquired in the OMRI scanner with ESR power disabled. All images, voxel size: $1.1 \times 1.6 \times 8 \text{ mm}^3$, Matrix: $128 \times 35 \times 11$. A fiducial containing 2 mM of TEMPOL was placed outside the animal and is seen in both MRI and OMRI images.

In summary, we have developed a high performance probe for high temporal and spatial resolution OMRI and demonstrated it *in vivo* in the brain of living rats. The S/N of this probe may be further improved, whilst maintaining imaging bandwidth, by using an active feedback circuit [20]. Higher S/N could also be realized through supercooling of the NMR solenoid or by using a free radical with a longer T_{1e} such as triphenylmethyl [9]. This probe may allow the *in vivo* detection of rapid redox changes in pathologic tissues, specifically in the context of brain trauma or stroke.

See attached manuscript, “High speed 3D overhauser-enhanced MRI using combined b-SSFP and compressed sensing,” *Magnetic Resonance in Medicine*, vol. 71, no. 2, pp. 735–745, Feb. 2014.

KEY RESEARCH ACCOMPLISHMENTS:

The key research accomplishments are listed below by program year.

Year 1:

- Reconfigured and modified the biplanar electromagnet LFI as an optimized high-performance head imager test bed capable of high-speed acquisitions at low magnetic field and demonstrated its preliminary performance.
- Achieved ^1H line widths of 5 Hz in biplanar LFI of 20 cm spherical phantom at 276 kHz
- Acquired image-based phase-sensitive static magnetic field maps on biplanar LFI
- Designed and built a very portable 45 kg Halbach array magnet for portable brain MRI that requires no power to maintain the field. The accessibility of this magnet has the potential to offer basic head trauma and hemorrhaging detection to a broad range of applications.
- Performed NMR at 3 MHz in Halbach LFI for field mapping.
- Designed, built, and tested broadband coil parallel-array preamp system.
- Designed form for 8 coil head parallel array
- Tested and integrated Tecmag Redstone nine channel Rx/two channel Tx console.
- Set up bidirectional control and processing pipeline between TNMR and MATLAB.
- Co-located OMRI system with biplanar LFI
- Built and tested OMRI RF transmit coils
- Demonstrated Overhauser-enhanced spectroscopy in solutions of TEMPO radical.
- Investigated pulsed frequency modulation RF Overhauser excitation at high field.

Year 2:

Electromagnet LFI:

- Demonstrated ^1H imaging in the reconfigured biplanar electromagnet LFI head imager test bed at 6.5 mT (276 kHz) with 2 mm in-plane resolution using 3D gradient echo imaging
- Demonstrated 25 \times faster ^1H imaging in LFI using the first low-field implementation of b-SSFP
- Demonstrated an additional 6 \times acceleration in ^1H imaging using the first implementation of compressed sensing and undersampled b-SSFP at low field
- Developed 3D printed polycarbonate phantoms for use in both ^1H MRI and OMRI experiments

Permanent magnet Halbach LFI:

- Acquired high spatial resolution NMR-based magnetic field maps of the Halbach imaging field
- Developed and simulated strategy for spatial encoding and reconstruction
- Designed, built, and tested RF transmit coils
- Designed, built, and evaluated 8-channel RF receive array and channel multiplexer
- Evaluated and simulated effect of finite RF pulse length and off-resonance RF pulses
- Acquired initial 1D and 2D projection images of test phantom

Parallel imaging in electromagnet LFI

- Designed, built, and evaluated 8-channel Rx array for 276 kHz
- Acquired and reconstructed the first 8-channel MRI image in the Johnson noise regime
- First demonstration of accelerated SENSE imaging in the Johnson noise regime.
- Developed and implemented passive multi-channel decoupling strategy suitable for low frequency

System control/Integration of Redstone console with electromagnet LFI

- Fully integrated TNMR/MATLAB pulse sequence control
- Installed digital attenuator board and spec'd/tested new low-noise RX4 receiver module
- Developed NMR spectroscopy data processing suite
- Developed multi-channel data processing user interface
- Developed image reconstruction tools for accelerated parallel imaging

Overhauser NMR and MRI in electromagnet LFI:

- Improved high-power high- Q EPR coils for OMRI imaging
- Simulated and measured NMR spin dynamics under b-SSFP combined with Overhauser DNP
- Developed new MRI sequence for free radical imaging: Overhauser-enhanced MRI using b-SSFP
- Acquired 32 slice, 1 mm in-plane resolution very high-speed OMRI free-radical images at 6.5 mT
- Calculated and measured sensitivity limit for free radicals Overhauser-enhanced spectroscopy
- Investigated free radical sensitivity in OMRI b-SSFP imaging sequences
- Established protocol to measure NO via *ex vivo* OEPS/OMRI in whole blood

Year 3:

Electromagnet LFI:

- Designed, constructed, and characterized high-efficiency single channel spiral "helmet" for human head imaging at 6.5 mT
- Constructed non-magnetic subject table suitable imaging in human subjects
- Acquired high-quality head images from human subjects with $3 \times 3 \times 10$ mm resolution in 29 minutes
- Compared brain images obtained at 6.5 mT with images obtained at 1.5 T

Permanent magnet Halbach LFI:

- Automated magnet rotation with stepper motor under pulse sequence control
- Integrated Halbach magnet and rotation assembly in a lightweight RF Faraday shield
- Developed high-performance probe array for field mapping critical for reconstruction
- Acquired single-channel 2D images of test phantoms to optimize reconstruction
- Modeled angular dependence of array coil B1 profiles critical for multichannel image reconstruction
- Acquired and reconstructed multi-channel 2D images of test phantoms and fruit

- Simulated ultimate attainable image resolution in Halbach encoding field
- Simulated TRASE array to enable 3D encoding

Parallel imaging in electromagnet LFI

- Evaluated accelerated imaging in new structured phantoms
- Designed, built, and evaluated 8-channel “helmet” Rx array for head imaging at 276 kHz
- Acquired the first 8-channel human head MRI image in the Johnson noise regime
- Evaluated optimal coil element orientation
- Evaluated several multi-channel decoupling strategies suitable at low frequency

System control and image acquisition in electromagnet LFI

- Integrated TNMR/MATLAB pulse sequence control and processing pipeline is stable
- Developed and implemented k -space mapping pulse sequences
- Implemented spiral imaging and image reconstruction
- Implemented “magnetic resonance fingerprinting” and Bloch simulation engine
- Migrated 8-channel SENSE reconstruction to a new optimized reconstruction code

Overhauser MRI in electromagnet LFI:

- Designed and simulated improved free radical detection methodology using interleaved OMRI/MRI acquisition
- Acquired the first accelerated images combining SENSE and OMRI
- Measured the decay of free radical in TEMPO bound to albumin in rodent blood
- Designed and built combined MRI/OMRI probe for rodent imaging
- Acquired 10 slice, $1.1 \times 1.6 \times 8$ mm in-plane resolution MRI and OMRI in *ex vivo* rats
- Measured temperature rise due to OMRI sequence in tissue sample

Year 4:

Electromagnet 6.5 mT LFI:

- Designed, constructed, and characterized optimized high-efficiency single channel spiral “helmet” for human head imaging at 6.5 mT
- Designed and built new multi-compartment head-shaped imaging phantom
- Acquired high-quality images from multi-compartment phantom using human head coil $2.5 \times 3.5 \times 5$ mm resolution (18 slices) in 10 minutes
- Acquired high-quality images in human head at 6.5 mT

Permanent magnet Halbach LFI:

- Simulated TRASE array to enable 3D encoding
- Designed and built TRASE array coils with switchable 180° phase shifter
- Implemented 3D encoding using simultaneous 2D rSEM and TRASE

- Implemented WURST-40 acquisition to mitigate quadratic phase from frequency-swept pulses
- Demonstrated proof-of-concept 3D imaging in the inhomogeneous 45 kilogram Halbach magnet without the use of gradient coils.

Overhauser MRI in electromagnet LFI:

- Developed and built high performance OMRI/MRI probe with wide-range OMRI tuning and low SAR, and 3-fold improved MRI SNR.
- Acquired 11 slice, $1.1 \times 1.6 \times 8$ mm in-plane resolution MRI (4.5 minutes) and OMRI (9 seconds) in rats
- Developed methodology to measure dynamic time resolved OMRI *in vivo*

REPORTABLE OUTCOMES:

1. Zimmerman CL, Wald LL, Rosen, M, Blau, J., “Design and construction of a Halbach array magnet for portable brain MRI”, presented at the *2012 International Society for Magnetic Resonance in Medicine*, May 2012, Melbourne Australia.
2. J P Stockman, C Z Cooley, M S Rosen, and L L Wald, “Flexible encoding and reconstruction strategies using a rotating inhomogeneous magnetic field for new MRI applications”, presented at the *ISMRM Data Sampling and Image Reconstruction Workshop*, 3–6 February 2013, Sedona, AZ.
3. M Sarraçanie, B D Armstrong, and M S Rosen, “High speed 3D b-SSFP at 6.5 mT”, presented at the *2013 Experimental NMR Conference*, 14–19 April 2013, Pacific Grove, CA.
4. B D Armstrong, M Sarraçanie, J Stockman, and M S Rosen, “High speed 3D Overhauser-enhanced MRI using combined b-SSFP and compressed sensing”, presented at the *2013 Experimental NMR Conference*, 14–19 April 2013, Pacific Grove, CA.
5. C D LaPierre, M Sarraçanie, L L Wald, and M S Rosen, “Parallel imaging and acceleration in the Johnson noise dominated regime”, presented at the *2013 Experimental NMR Conference*, 14–19 April 2013, Pacific Grove, CA.
6. C Z Cooley, J P Stockman, B D Armstrong, M S Rosen, and L L Wald, “A lightweight, portable MRI brain scanner based on a rotating Halbach magnet”, presented at the *2013 Experimental NMR Conference*, 14–19 April 2013, Pacific Grove, CA.
7. M Sarraçanie, B D Armstrong, and M S Rosen, “High speed 3D b-SSFP at 6.5 mT”, presented at the *2013 International Society for Magnetic Resonance in Medicine*, 20–26 April 2013, Salt Lake City, UT.
8. B D Armstrong, M Sarraçanie, J Stockman, and M S Rosen, “High speed 3D Overhauser-enhanced MRI using combined b-SSFP and compressed sensing”, presented at the *2013 International Society for Magnetic Resonance in Medicine*, 20–26 April 2013, Salt Lake City, UT.

9. C D LaPierre, M Sarraçanie, L L Wald, and M S Rosen, “Parallel imaging and acceleration in the Johnson noise dominated regime”, presented at the *2013 International Society for Magnetic Resonance in Medicine*, 20–26 April 2013, Salt Lake City, UT.
10. C Z Cooley, J P Stockman, B D Armstrong, M S Rosen, and L L Wald, “A lightweight, portable MRI brain scanner based on a rotating Halbach magnet”, presented at the *2013 International Society for Magnetic Resonance in Medicine*, 20–26 April 2013, Salt Lake City, UT.
11. J P Stockman, C Z Cooley, M S Rosen, and L L Wald, “Flexible spatial encoding strategies using rotating multipolar fields for unconventional MRI applications”, presented at the *2013 International Society for Magnetic Resonance in Medicine*, 20–26 April 2013, Salt Lake City, UT.
12. M S Rosen, invited talk, “New methods of low-field MRI for application to TBI”, given at the *Next Generation Medical Imaging Workshop*, Carnegie Mellon University, 5 Sept 2012.
13. M S Rosen, invited talk, “New methods of low-field MRI for application to TBI: first results”, given at the *Military Health System Research Symposium*, Ft Lauderdale, FL, 13-16 August 2012.
14. M S Rosen, “Molecular imaging at low magnetic field; endogenous and exogenous free radical MRI”, 28 January 2013, *MGH/Martinos Molecular Imaging Seminar*, Boston MA.
15. M Sarraçanie, BD Armstrong, and MS Rosen, “High speed 3D b-SSFP at 6.5 mT”, presented at the *2013 Experimental NMR Conference*, 14–19 April 2013, Pacific Grove, CA.
16. BD Armstrong, M Sarraçanie, J Stockman, and MS Rosen, “High speed 3D Overhauser-enhanced MRI using combined b-SSFP and compressed sensing”, presented at the *2013 Experimental NMR Conference*, 14–19 April 2013, Pacific Grove, CA.
17. CD LaPierre, M Sarraçanie, LL Wald, and MS Rosen, “Parallel imaging and acceleration in the Johnson noise dominated regime”, presented at the *2013 Experimental NMR Conference*, 14–19 April 2013, Pacific Grove, CA.
18. CZ Cooley, JP Stockman, BD Armstrong, MS Rosen, and LL Wald, “A lightweight, portable MRI brain scanner based on a rotating Halbach magnet”, presented at the *2013 Experimental NMR Conference*, 14–19 April 2013, Pacific Grove, CA.
19. M Sarraçanie, BD Armstrong, and MS Rosen, “High speed 3D b-SSFP at 6.5 mT”, presented at the *2013 International Society for Magnetic Resonance in Medicine*, 20–26 April 2013, Salt Lake City, UT.
20. BD Armstrong, M Sarraçanie, JP Stockman, and MS Rosen, “High speed 3D Overhauser-enhanced MRI using combined b-SSFP and compressed sensing”, presented at the *2013 International Society for Magnetic Resonance in Medicine*, 20–26 April 2013, Salt Lake City, UT.

21. CD LaPierre, M Sarracanie, LL Wald, and MS Rosen, "Parallel imaging and acceleration in the Johnson noise dominated regime", presented at the *2013 International Society for Magnetic Resonance in Medicine*, 20–26 April 2013, Salt Lake City, UT.
22. CZ Cooley, JP Stockman, BD Armstrong, MS Rosen, and LL Wald, "A lightweight, portable MRI brain scanner based on a rotating Halbach magnet", presented at the *2013 International Society for Magnetic Resonance in Medicine*, 20–26 April 2013, Salt Lake City, UT.
23. JP Stockman, CZ Cooley, MS Rosen, and LL Wald, "Flexible spatial encoding strategies using rotating multipolar fields for unconventional MRI applications", presented at the *2013 International Society for Magnetic Resonance in Medicine*, 20–26 April 2013, Salt Lake City, UT.
24. MS Rosen, invited seminar, "High performance low-field MRI: fact or fiction?", Southern Illinois University, Department of Chemistry and Biochemistry, Carbondale IL, 8 March 2013.
25. MS Rosen, invited talk, "Free Radical MRI", *MGH/NSF Physics of Cancer Imaging Workshop*, MGH/A.A. Martinos Center, 6 November 2013.
26. M Sarracanie, BD Armstrong, JP Stockman, and MS Rosen, "High Speed 3D Overhauser-enhanced MRI using combined b-SSFP and Compressed Sensing", published in *Magnetic Resonance in Medicine*, 2014; 71(2):735–45.
27. C LaPierre, M Sarracanie, B D Armstrong, J Polimeni, and M S Rosen, Overhauser-enhanced MRI with SENSE Acceleration in the Johnson Noise Dominated Regime, presented at the 55th Meeting of the Experimental NMR Conference, Boston, MA, March 23-28 2014.
28. M Sarracanie, B D Armstrong, and M S Rosen, High Speed MR Fingerprinting at 6.5 mT, presented at the 55th Meeting of the Experimental NMR Conference, Boston, MA, March 23-28 2014.
29. M Sarracanie, P Stanwix, and M S Rosen, A Single Channel Variable Density Spiral Coil for High Sensitivity MRI at 6.5 mT, presented at the 55th Meeting of the Experimental NMR Conference, Boston, MA, March 23-28 2014.
30. C Z Cooley, J P Stockmann, M Sarracanie, B D Armstrong, M S Rosen, and L L Wald, 2D Imaging in a Portable MRI Scanner without Gradient Coils, presented at the 55th Meeting of the Experimental NMR Conference, Boston, MA, March 23-28 2014.
31. C LaPierre, M Sarracanie, L L Wald, and M S Rosen, An Optimized 8-Channel Helmet Array for Head Imaging at 6.5 mT, presented at the 55th Meeting of the Experimental NMR Conference, Boston, MA, March 23-28 2014.
32. C Z Cooley, J P Stockmann, B D. Armstrong, M Sarracanie, M S. Rosen, and L L. Wald, Spatial resolution in rotating Spatial Encoding Magnetic field MRI (rSEM-MRI), presented at the 22nd Meeting of the International Society of Magnetic Resonance in Medicine, Milan, Italy May 10-16 2014.

33. C LaPierre, M Sarracanie, B D. Armstrong, J R Polimeni, and M S. Rosen, Overhauser-enhanced MRI with SENSE Acceleration in the Johnson Noise Dominated Regime, presented at the 22nd Meeting of the International Society of Magnetic Resonance in Medicine, Milan, Italy May 10-16 2014.
34. C LaPierre, L L Wald, and M S. Rosen, An Optimized 8-Channel Helmet Array for Head Imaging at 6.5 mT, presented at the 22nd Meeting of the International Society of Magnetic Resonance in Medicine, Milan, Italy May 10-16 2014.
35. M Sarracanie, B D. Armstrong, and M S. Rosen, High Speed MR Fingerprinting at 6.5 mT, presented at the 22nd Meeting of the International Society of Magnetic Resonance in Medicine, Milan, Italy May 10-16 2014.
36. M S Rosen, “New methods of low-field MRI for application to TBI”, Invited talk, TBI Neuroimaging Meeting, US Army Medical Research and Materiel Command and Defense Centers of Excellence for Psychological Health and Traumatic Brain Injury, Fort Detrick, 30 Jan 2014.
37. M S Rosen, invited talk, “Overhauser-enhanced MRI as a Non-invasive Probe of BBB Breakdown and Redox State in Stroke”, 55th meeting of the Experimental NMR Conference, Boston, MA, 27 Mar 2014.
38. M S Rosen, invited talk, “Overhauser-enhanced MRI as a Non-invasive Probe of BBB Breakdown and Redox State in Stroke”, 22nd Meeting of the International Society of Magnetic Resonance in Medicine, Milan, Italy, May 10-16 2014.
39. M S Rosen, invited seminar, “High-performance Low-field MRI: Brain Imaging & Free Radicals”, Psychiatry Neuroimaging Laboratory seminar, Brigham and Women’s Hospital, Boston MA, 22 June 2014
40. M S Rosen, invited talk, “Low-field MRI for Non-invasive imaging of brain function”, NSF Workshop on Noninvasive Imaging of Brain Function, Arlington, VA, 23 July 2014.
41. CZ Cooley, JP Stockman, BD Armstrong, M Sarracanie, MH Lev, MS Rosen, and LL Wald, “2D Imaging in a Lightweight Portable MRI Scanner without Gradient Coils”, published in *Magnetic Resonance in Medicine*, 2014.
42. M S Rosen, “High-performance millitesla MRI: Brain imaging and *in vivo* DNP”, Invited talk, Physics/Theory department colloquium, Los Alamos National Laboratory, Boston, MA, 4 Mar 2015.
43. M S Rosen, “Non-cryogenic millitesla brain MRI”, Invited talk, Society for Brain Mapping and Therapeutics, 12th Annual World Congress, Los Angeles, CA, 6 Mar 2015.
44. M S Rosen, “Low-Cost, High-Performance Millitesla MRI”, Invited Special Seminar, Virginia Tech Carilion Research Institute, Roanoke, VA, 13 Apr 2015.
45. M S Rosen, “MRI in the Wild”, Invited talk, ARPA-E Workshop: Novel Methods for Phytosequestration, Chicago, 23 Jul 2015.

46. M S Rosen, "How low can you go: millitesla MRI in 2015", Invited Bioimaging/Applied Physics seminar, National Institute of Standards and Technology (NIST), Boulder CO, 23 Sept 2015.
47. M Sarraçanie, C LaPierre, N Salameh, D Waddington, T Witzel, M S Rosen, Low-cost high-performance MRI, 56th presented at the 56th Meeting of the Experimental NMR Conference, Pacific Grove, CA, Apr 19-24 2015.
48. M Sarraçanie, F Herisson, N Salameh, D Waddington, C Ayata, M S Rosen, Dynamic *in vivo* free radical imaging with Overhauser-enhanced MRI, presented at the 56th Meeting of the Experimental NMR Conference, Pacific Grove, CA, Apr 19-24 2015.
49. D Waddington, M Sarraçanie, N Salameh, M S Rosen, High performance probe for *in vivo* Overhauser MRI, presented at the 56th Meeting of the Experimental NMR Conference, Pacific Grove, CA, Apr 19-24 2015.
50. M. Sarraçanie, O Cohen, M S Rosen, 3D Balanced-EPI Magnetic Resonance Fingerprinting at 6.5 mT, presented at the 56th Meeting of the Experimental NMR Conference, Pacific Grove, CA, Apr 19-24 2015.
51. C LaPierre, M Sarraçanie, D Waddington, M S Rosen, A single channel spiral volume coil for *in vivo* imaging of the whole human brain at 6.5 mT, presented at the 56th Meeting of the Experimental NMR Conference, Pacific Grove, CA, Apr 19-24 2015.
52. C Z Cooley, J P Stockmann, M Sarraçanie, M S Rosen, L L Wald. Portable MRI Scanner using Rotating Spatial Encoding Magnetic Fields: Extension to 3D Imaging using Transmit Array Spatial Encoding (TRASE), presented at the 56th Meeting of the Experimental NMR Conference, Pacific Grove, CA, Apr 19-24 2015.
53. M. Sarraçanie, O Cohen, M S Rosen, 3D Balanced-EPI Magnetic Resonance Fingerprinting at 6.5 mT, presented at the 23rd Meeting of the International Society of Magnetic Resonance in Medicine, Toronto, Canada, 30 May-5 June 2015.
54. C Z Cooley, J P Stockmann, M Sarraçanie, M S Rosen, L L Wald. 3D Imaging in a Portable MRI Scanner Using Rotating Spatial Encoding Magnetic Fields and Transmit Array Spatial Encoding (TRASE), presented at the 23rd Meeting of the International Society of Magnetic Resonance in Medicine, Toronto, Canada, 30 May-5 June 2015.
55. M Sarraçanie, F Herisson, N Salameh, D Waddington, C Ayata, M S Rosen, Dynamic *in vivo* free radical imaging with Overhauser-enhanced MRI, presented at the 23rd Meeting of the International Society of Magnetic Resonance in Medicine, Toronto, Canada, 30 May-5 June 2015.
56. D Waddington, M Sarraçanie, N Salameh, M S Rosen, High performance probe for *in vivo* Overhauser MRI, presented at the 23rd Meeting of the International Society of Magnetic Resonance in Medicine, Toronto, Canada, 30 May-5 June 2015.

57. M Sarraçanie, C LaPierre, N Salameh, D Waddington, T Witzel, M S Rosen, Low-cost high-performance MRI, presented at the 23rd Meeting of the International Society of Magnetic Resonance in Medicine, Toronto, Canada, 30 May-5 June 2015.
58. C LaPierre, M Sarraçanie, D Waddington, M S Rosen, A single channel spiral volume coil for in vivo imaging of the whole human brain at 6.5 mT, presented at the 23rd Meeting of the International Society of Magnetic Resonance in Medicine, Toronto, Canada, 30 May-5 June 2015.
59. J Stockmann, C Z Cooley, M Sarraçanie, M S Rosen, L L Wald. Transmit Array Spatial Encoding (TRASE) with Broadband WURST Pulses for Robust Spatial Encoding in Inhomogeneous B₀ Fields. presented at the 23rd Meeting of the International Society of Magnetic Resonance in Medicine, Toronto, Canada, 30 May-5 June 2015.
60. M. Sarraçanie, C. D. LaPierre, N. Salameh, D. E. J. Waddington, T. Witzel, and M. S. Rosen, “Low-Cost High-Performance MRI,” published in *Sci Rep*, vol. 5, p. 15177, Oct. 2015.
61. J. P. Stockmann, C. Z. Cooley, B. Guerin, M. S. Rosen, and L. L. Wald, “Transmit Array Spatial Encoding (TRASE) using broadband WURST pulses for RF spatial encoding in inhomogeneous B₀ fields,” published in *Journal of Magnetic Resonance*, vol. 268, no. C, pp. 36–48, Jul. 2016.
62. M S Rosen, “Millitesla MRI as a platform for brain injury triage”, invited talk, 13th SBMT meeting, Miami FL, 8 April 2016.
63. M S Rosen, “Millitesla MRI: Brain and Beyond”, invited talk at educational session on Portable MRI, 24rd Meeting of the International Society of Magnetic Resonance in Medicine, Singapore, 8-13 May 2016.
64. MGH/Partners provisional patent MGH-22726, (Mar 14, 2014). This patent describes optimized receive arrays for parallel imaging in the Johnson noise dominated regime. **LICENSED**
65. MGH/Partners provisional patent MGH-22727, (Mar 14, 2014). This patent describes Overhauser-enhanced MRI (OMRI) is used in combination with an exogenously administered free radical probe to (for example) tomographically probe blood brain barrier breakdown and tissue oxidative stress status *in vivo*.
66. MGH/Partners provisional patent MGH-22728, (Mar 14, 2014). This patent describes a new efficient method for high-speed Overhauser MRI (OMRI) where ESR irradiation is applied within the TR of a conventional MRI pulse sequence, typically during the phase-encode part of the sequence. **LICENSED**.
67. MGH/Partners provisional patent MGH-22729, (Mar 14, 2014). This patent describes the use of a variable density spiral design to provide homogeneous magnetic field and high sensitivity over broad regions of interest when used for either transmit, receive, or both.

68. MGH/Partners provisional patent MGH-22730, (Mar 14, 2014). This patent describes a new form fitting spiral coil design to provide homogeneous magnetic field and high sensitivity over three-dimensional volumes. **LICENSED**.
69. MGH/Partners provisional patent MGH-22731, (Mar 14, 2014). This patent describes a new approach to Magnetic Resonance Fingerprinting (MRF) whereby a user defined fraction (including the whole) of k -space is acquired in a sequential fashion, in two or three dimensions. **LICENSED**
70. Funding obtained (2014): NIH R21 NS087344-01 (PI Rosen), “Non-invasive Free Radical MRI in Stroke”.
71. Funding obtained (2014): NIH R01 EB018976-01 (PI Wald), “Technology for Portable MRI”.

CONCLUSION:

The reason MRI is not widely deployable is that high-strength magnetic fields (of order 1 T) are necessary with conventional MRI to obtain useful brain images. Such high field scanners involve large, heavy, fragile, expensive equipment (such as superconducting magnets) that are difficult to site in field hospitals. We contend that that low-magnetic-field implementations of MRI can be developed to allow robust, transportable imaging modalities well suited to diagnose the types of battlefield injuries prevalent in TBI and practical for operation in field hospitals. Application of the suite of techniques and technologies from our work could advise future development of a deployable device with a high diagnostic impact and could be transformative, enabling improved diagnosis and monitoring of battlefield injuries prevalent in TBI.

The electromagnet LFI provides an ideal state-of-the art test bed for all of the novel acquisition, detection methodologies, and reconstruction algorithms including navigators and sparse sampling, and additionally will provide necessary experience and data to advise optimal construction and magnetic field for any future electromagnet-based deployable systems. In its current configuration, this state-of-the-art scanner enables high-performance spectroscopy and 8-channel imaging at 6.5 mT, and is fully equipped for Overhauser DNP experiments. We have improved the ability to acquire images based on the intrinsic ^1H signal by combining new low-field hardware methodology and advanced pulse sequence and reconstruction methods, and demonstrated high-quality imaging in the human head.

Our second low field imaging test bed, the permanent magnet Halbach LFI is based around a lightweight (45 kg) and portable magnet with a built-in encoding field for MRI. It is a highly specialized and potentially disruptive scanner that could greatly ease both the cost and burden of a field-forward instrument purpose-built for TBI imaging. The 2D and preliminary 3D imaging results acquired in the highly inhomogeneous magnetic field of the Halbach scanner using simultaneous NMR measurement to track magnet drift, and multi-channel receive arrays to unwrap image aliasing, and are encouraging. A truly portable MR system based on this technology has the potential to quickly detect brain injury at the site of injury, for instance in an ambulance prior to transportation to the hospital.

We have also developed technology for a wholly new approach to brain imaging that may revolutionize the use of MRI for the assessment and treatment of secondary brain injury following TBI: direct tomographic detection

of endogenous free radicals as an early marker for TBI. This new form of contrast, “injury-sensitive MRI”, is based on the enormous signal enhancement attainable with Overhauser DNP, converting the electron spin of endogenous free radicals into nuclear polarization using the Overhauser effect and subsequently imaging that modified nuclear polarization using low-field MRI (OMRI).

The imaging experiments summarized above in the optimized electromagnet LFI are compelling: high quality ^1H brain MRI at 6.5 mT is in fact attainable over reasonable averaging times using high performance hardware and advanced MRI sequences. A critical question for this work is the understanding of the clinical balance and impact that the tradeoff between acquisition time and resolution implicit in imaging plays on the operation of a deployable scanner.

The low-field OMRI results presented above demonstrate promise for high-speed high-resolution free-radical imaging, and offers new perspectives for the measurement of free radicals in living organisms. The long-term goal of this work is an *in vivo* implementation of this technique. Free-radical sensitive low-field OMRI as a novel imaging and diagnostic MRI-based method with specificity to secondary-injury has the potential to clarify the mechanisms involved in secondary damage and the local effects of novel therapies. Time-critical imaging of free radicals can provide the unique interventional access critically needed for drug therapies and this technique would fill the clear need for an “injury imager”, suitable for non-invasive tomographic measurement (Figure 8).

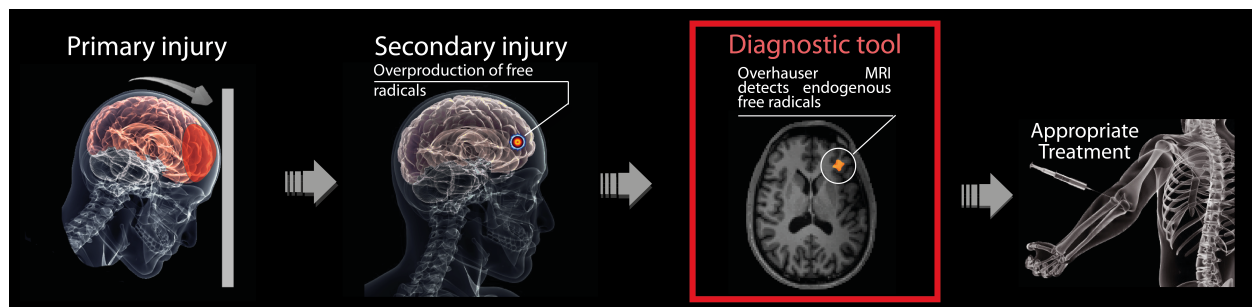


Figure 8: Schematic of the development of a new interventional imaging and treatment tool for *in vivo* detection of endogenous free radicals associated with secondary injury following TBI using low-field OMRI as developed here. This same approach can similarly open up new treatment windows into stroke and other ischemic events. MRI-based *in vivo* free radical imaging using OMRI is impossible at high-field due to the inability of the ESR pulse to penetrate into tissue, and the danger of RF heating in the microwave regime.

Successful demonstration of this system *in vivo* will provide image-based injury specificity for TBI and for the first time open a window into a critical mechanism of TBI-related disease and an unambiguous non-invasive *in vivo* marker for cerebral injury. Time-critical imaging of free radicals associated with secondary imaging can provide the unique interventional access critically needed to develop and deliver drug therapies to mitigate brain damage, reducing disability and death from secondary injury following TBI. The low-field approach would allow placement of this critical new diagnostic “injury imager” tool close to the source of injury—as well as in hospitals and clinics where rehabilitation takes place.

REFERENCES:

- [1] C. D. LaPierre, M. Saracanie, D. E. J. Waddington, and M. S. Rosen, “A single channel spiral volume coil for *in vivo* imaging of the whole human brain at 6.5 mT,” presented at the Intl Soc Mag Res Med, Toronto, 2015.

- [2] C. D. LaPierre, L. L. Wald, and M. S. Rosen, "An Optimized 8-Channel Helmet Array for Head Imaging at 6.5 mT," presented at the Proc. Intl. Soc. Mag. Reson. Med. 23 (2015), Milan, Italy, 2014, p. 1325.
- [3] M. Sarraçanie, C. D. LaPierre, N. Salameh, D. E. J. Waddington, T. Witzel, and M. S. Rosen, "Low-Cost High-Performance MRI," *Sci Rep*, vol. 5, p. 15177, Oct. 2015.
- [4] C. Z. Cooley, J. P. Stockmann, B. D. Armstrong, M. Sarraçanie, M. H. Lev, M. S. Rosen, and L. L. Wald, "Two-dimensional imaging in a lightweight portable MRI scanner without gradient coils," *Magnetic Resonance in Medicine*, vol. 73, no. 2, pp. 872–883, Mar. 2014.
- [5] J. P. Stockmann, C. Z. Cooley, B. Guerin, M. S. Rosen, and L. L. Wald, "Transmit Array Spatial Encoding (TRASE) using broadband WURST pulses for RF spatial encoding in inhomogeneous B0 fields," *Journal of Magnetic Resonance*, vol. 268, no. C, pp. 36–48, Jul. 2016.
- [6] M. Sarraçanie, B. D. Armstrong, J. Stockmann, and M. S. Rosen, "High speed 3D overhauser-enhanced MRI using combined b-SSFP and compressed sensing," *Magnetic Resonance in Medicine*, vol. 71, no. 2, pp. 735–745, Feb. 2014.
- [7] D. E. J. Waddington, M. Sarraçanie, N. Salameh, and M. S. Rosen, "High Performance Probe for in vivo Overhauser MRI," presented at the Intl Soc Mag Res Med, Toronto, 2015, p. 6710.
- [8] M. A. Espy, M. A. Espy, P. E. Magnelind, P. E. Magnelind, A. N. Matlashov, A. N. Matlashov, S. G. Newman, S. G. Newman, H. J. Sandin, H. J. Sandin, L. J. Schultz, L. J. Schultz, R. Sedillo, R. Sedillo, A. V. Urbaitis, A. V. Urbaitis, P. L. Volegov, and P. L. Volegov, "Progress Toward a Deployable SQUID-Based Ultra-Low Field MRI System for Anatomical Imaging," *Applied Superconductivity, IEEE Transactions on*, vol. 25, no. 3, pp. 1–5, Jun. 2015.
- [9] K. Golman, J. S. Petersson, J.-H. Ardenkjær-Larsen, I. Leunbach, L.-G. Wistrand, G. Ehnholm, and K. Liu, "Dynamic in vivo oxymetry using overhauser enhanced MR imaging," *Journal of Magnetic Resonance Imaging*, vol. 12, no. 6, pp. 929–938, 2000.
- [10] H. Utsumi, K. Yamada, K. Ichikawa, K. Sakai, Y. Kinoshita, S. Matsumoto, and M. Nagai, "Simultaneous molecular imaging of redox reactions monitored by Overhauser-enhanced MRI with ¹⁴N- and ¹⁵N-labeled nitroxyl radicals," *Proceedings of the National Academy of Sciences of the United States of America*, vol. 103, no. 5, p. 1463, 2006.
- [11] M. J. Ahn, E. R. Sherwood, D. S. Prough, C. Yie Lin, and D. S. DeWitt, "The effects of traumatic brain injury on cerebral blood flow and brain tissue nitric oxide levels and cytokine expression," *Journal of Neurotrauma*, vol. 21, no. 10, pp. 1431–1442, 2004.
- [12] X. Zheng, K. Liu, and Y. Yang, "Real-Time Measurement of Murine Hippocampus Hippocampus NO Levels in Response to Cerebral Ischemia/Reperfusion Reperfusion," in *Nitric oxide methods and protocols*, vol. 704, no. 6, Totowa, NJ: Humana Press, 2010, pp. 73–80.
- [13] T. Malinski, F. Bailey, Z. G. Zhang, and M. Chopp, "Nitric oxide measured by a porphyrinic microsensor in rat brain after transient middle cerebral artery occlusion," *Journal of Cerebral Blood Flow & Metabolism*, vol. 13, no. 3, pp. 355–358, 1993.
- [14] C. Iadecola, "Bright and dark sides of nitric oxide in ischemic brain injury," *Trends in neurosciences*, vol. 20, no. 3, pp. 132–139, 1997.
- [15] L. Cherian, J. C. Goodman, and C. S. Robertson, "Brain nitric oxide changes after controlled cortical impact injury in rats," *Journal of neurophysiology*, vol. 83, no. 4, pp. 2171–2178, 2000.
- [16] L. Cherian, J. C. Goodman, and C. Robertson, "Neuroprotection with Erythropoietin Administration Following Controlled Cortical Impact Injury in Rats," *Journal of Pharmacology and Experimental Therapeutics*, vol. 322, no. 2, pp. 789–794, May 2007.
- [17] P. A. Rashid, A. Whitehurst, N. Lawson, and P. M. W. Bath, "Plasma nitric oxide (nitrate/nitrite) levels in acute stroke and their relationship with severity and outcome," *Journal of Stroke and Cerebrovascular Diseases*, vol. 12, no. 2, pp. 82–87, Mar. 2003.
- [18] J. Mispelter, M. Lupu, and A. Briguët, *NMR probeheads for biophysical and biomedical experiments :*

theoretical principles & practical guidelines. London : Imperial College Press ; Hackensack, NJ : Distributed by World Scientific,, 2006.

- [19] M. S. Rosen, M. Sarraçanie, B. D. Armstrong, F. Herisson, N. Salameh, and C. Ayata, “Overhauser-enhanced MRI as a non invasive probe of BBB breakdown and redox state following ischemia/reperfusion,” presented at the Proc. Intl. Soc. Mag. Reson. Med., Milan, Italy, 2014, vol. 22, p. 6461.
- [20] E. Baudin, K. Safiullin, S. W. Morgan, and P. J. Nacher, “An active feedback scheme for low field NMR experiments,” *J. Phys.: Conf. Ser.*, vol. 294, p. 012009, Jun. 2011.

APPENDICIES:

Conference abstracts:

We attach as an **Appendix** conference abstracts from the years 2013, 2014, and 2015 that have resulted from research funded in the Rosen lab by DoD/DMRDP.

Manuscripts published:

We attach as **Appendix** the following manuscripts:

“High speed 3D overhauser-enhanced MRI using combined b-SSFP and compressed sensing,” *Magnetic Resonance in Medicine*, vol. 71, no. 2, pp. 735–745, Feb. 2014.

“Two-dimensional imaging in a lightweight portable MRI scanner without gradient coils,” *Magnetic Resonance in Medicine*, vol. 73, no. 2, pp. 872–883, Mar. 2014.

“Low-Cost High-Performance MRI,” *Sci Rep*, vol. 5, p. 15177, Oct. 2015.

“Transmit Array Spatial Encoding (TRASE) using broadband WURST pulses for RF spatial encoding in inhomogeneous B₀ fields,” *Journal of Magnetic Resonance*, vol. 268, no. C, pp. 36–48, Jul. 2016.

Low Cost High Performance MRI

Mathieu Sarraçanie^{1,2}, Cristen LaPierre^{1,2}, Najat Salameh^{1,2}, David E J Waddington^{1,3}, Thomas Witzel¹, and Matthew S Rosen^{1,2}

¹MGH/A.A. Martinos Center for Biomedical Imaging, Charlestown, MA, United States, ²Department of Physics, Harvard University, Cambridge, MA, United States,

³ARC Centre of Excellence for Engineered Quantum Systems, School of Physics, University of Sydney, Sydney, NSW, Australia

Purpose

Magnetic Resonance Imaging (MRI) is unparalleled in its ability to non-invasively visualize anatomical structure and function with high spatial and temporal resolution and a broad range of clinically relevant contrasts. Yet to overcome the low sensitivity inherent in NMR-based detection, the vast majority of clinical scanners incorporate superconducting magnets operating at 1.5, 3 tesla (T), and more exceptionally at 7T. These powerful magnets are massive, costly to purchase and maintain, and operate with very strict infrastructure demands and siting requirements that preclude operation in many environments. For brain imaging, low-field alternatives have been developed that rely on superconducting quantum interference devices (SQUID) detector arrays combined with magnetic field cycling techniques [1-4]. To date, this approach is limited by prohibitively long acquisition times (> 1 hr) and restrictions on attainable fields of view. We demonstrate here 3D brain MRI *in vivo* at 6.5mT (more than 450 times lower than clinical MRI scanners) in 6 minutes, by combining a high performance single channel Tx/Rx coil with modern undersampling techniques and b-SSFP [5].



Figure 1 : 3D printed single channel volume head coil. The coil was used for both transmit and receive at 276 kHz (6.5 mT)

Methods

To minimize B_1 inhomogeneity and maximize filling factor, a close fitting single channel inductive head coil for operation at 276 kHz was designed and 3D printed (Fig. 1). The coil features a 30-turn 3D spiral with turn-to-turn distance of 5.6 mm, thus ensuring the B_1 field produced is everywhere orthogonal to the main magnetic field B_0 . The hemispheric spiral design results in a very homogeneous magnetic field [6,7] over the volume of interest, making it suitable for both RF transmit and receive. Litz wire was selected due to its lower AC resistance compared to solid copper wire, reducing the Johnson noise of the coil while maintaining the same inductance. Previously [8], we described our use of undersampling strategies to accelerate low-field imaging. We make use of this here by randomly sampling 50% of k-space using a variable density Gaussian pattern. Once reconstructed, the images were apodized and processed using Perona and Malik anisotropic diffusion filtering [9] (ADF).

Results

Three-dimensional undersampled images acquired in 6 minutes (NA=30) are shown in Fig. 2 for each of the three spatial orientations (axial, coronal, and sagittal). We obtain $2.5 \times 3.5 \times 8.5$ mm³, $2.5 \times 3.5 \times 14.4$ mm³, and $2.5 \times 3.5 \times 11.5$ mm³ voxel resolution images in axial, sagittal and coronal orientation, respectively. Images with NA=160 acquired at 6.5 mT are compared to b-SSFP images acquired at 3T in Fig. 3.

Conclusion

At 6.5 mT, (more than 450 times lower than clinical MRI scanners) we demonstrate $2.5 \times 3.5 \times 8.5$ mm³ resolution in the living human brain in 6 minutes. We contend that robust non-field-cycled low-field implementations of MRI (< 10 mT) have the potential to make clinically relevant images and set new standards for a completely new category of affordable and robust portable devices.

References:

[1] Zotev *et al.* J. Magn. Res. 2008

194(1):115-120; [2] Espy *et al.* J. Magn. Res. 2012 228:1-15; [3] Vesonen *et al.* Magn. Reson. Med. 2012 69(6):1795-1804; [4] Inglis *et al.* PNAS 2013 110(48):19194-201; [5] Scheffler K *et al.* Eur Radiol 2003 13:2409-18; [6] Harpen J. Magn. Res. 1991 94(3):550-556; [7] Everett *et al.* J. Scientific Instruments 1966 43:470-474; [8] Sarraçanie *et al.* Magn. Reson. Med. 2013 71:735-745; [9] Perona *et al.* 1990 IEEE Trans. Pattern Anal. Mach. Intell. 12(7):629-639.

Acknowledgement: This research was supported by the Department of Defense, Defense Medical Research and Development Program, Applied Research and Advanced Technology Development Award W81XWH-11-2-0076 (DM09094).

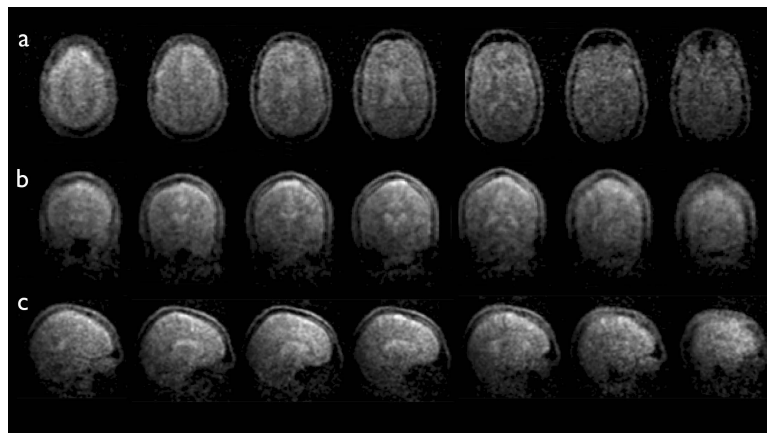


Figure 2: 3D images of the living brain (7 central slices of 15 slice dataset are shown) acquired in 6 minutes at 6.5 mT (276 kHz) in a. axial, b. coronal, and c. sagittal orientation. Acquisition matrix: $64 \times 75 \times 15$, Flip angle = 70° , BW = 9091 Hz, TR/TE = 23/11.7 ms, NA=30, voxel size: a. $(2.5 \times 3.5 \times 8.5)$ mm³, b. $(2.5 \times 3.5 \times 11.5)$ mm³, and c. $(2.5 \times 3.5 \times 14.4)$ mm³.

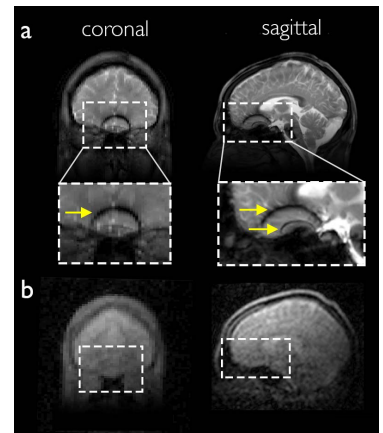


Figure 3: Comparison of b-SSFP images at a. 3T and b. 6.5 mT. Strong banding artifacts appear at high magnetic field (yellow arrows) whereas no artifact is seen in the images acquired at low field.

3D Balanced-EPI Magnetic Resonance Fingerprinting at 6.5 mT

Mathieu Sarraclanie^{1,2}, Ouri Cohen¹, and Matthew S Rosen^{1,2}

¹MGH/A.A. Martinos Center for Biomedical Imaging, Charlestown, MA, United States, ²Department of Physics, Harvard University, Cambridge, MA, United States

Purpose

In recent work [1], we demonstrated high speed MRI in the very low magnetic field regime (6.5 mT) using a balanced steady state based (b-SSFP [2]) acquisition scheme. b-SSFP provides the highest SNR per unit time [2] and image contrast depends on the ratio T_2/T_1 . At very low field, most species have T_2 relaxation times approaching T_1 , so b-SSFP images are essentially proton density (PD) weighted. In previous work [3] we have shown that 2D MR Fingerprinting [4] can be implemented at low magnetic field and provide simultaneous quantification of T_1 and T_2 as well as proton density and B_0 field maps. MRF at low magnetic field creates a rapid dynamic series of low signal to noise ratio (SNR) images where the magnitude of each voxel of each image changes at every time step. Generally, the TR and flip angle of each image in the time series is varied pseudo-randomly [5]. Here, we demonstrate MRF in 3D at 6.5 mT, using an optimized set of 15 flip angles and repetition times (FA/TR), in a Cartesian acquisition of k -space with a new hybrid b-SSFP-EPI sequence.

Methods

The low field MRI scanner was previously described [5]. The imaging sequence is a hybrid multishot b-SSFP-EPI with an echo-train of 4 echoes (Fig. 1). The sequence was set with matrix size = $64 \times 64 \times 5$, corresponding voxel size = $(2.5 \times 3.5 \times 10) \text{ mm}^3$, FOV = $(125 \times 175 \times 50) \text{ mm}^3$, number of average NA = 2. The minimum TR was 62 ms with 9091 Hz bandwidth. The total acquisition time was 25 min. A flip (FA/TR) trajectory of length $N=15$ was generated using an optimization method previously described [6]. Lack of SNR at low magnetic field required redesigning our optimization scheme with a narrow range of larger flip angles $[60-120^\circ]$ and shorter TRs $[62-400 \text{ ms}]$. The optimized FA/TR trajectory is compared to a non-optimized trajectory in Fig. 2. The imaged phantom consists in a stack of three 10 mm thick compartments of similar volume with different T_1 and T_2 properties.

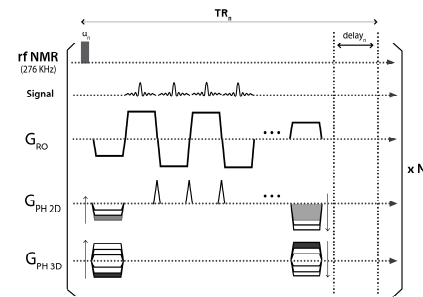


Figure 1: Pulse sequence diagram of the hybrid b-SSFP-EPI sequence used for 3D MR Fingerprinting. The FAs and TRs were set according to the optimized trajectory.

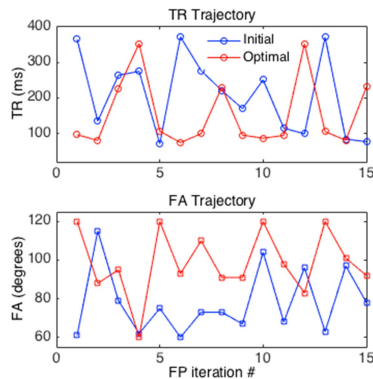


Figure 2: Comparison of our optimized trajectory with a random non-optimized trajectories for $N=15$.

parameters in 3D, and generate several image contrasts in a single acquisition (proton density, T_1 , T_2) in less than 30 minutes. This technique is of particular relevance at low magnetic field where SNR and contrast are tied to long acquisition times. The combination of 3D MRF with low field MRI scanners has great potential to provide clinically relevant contrast with portable low cost MR scanners.

References: [1] Sarraclanie M *et al.* Proc. ISMRM 2013 #5322; [2] Scheffler K *et al.* Eur Radiol 2003 13:2409-18; [3] Sarraclanie M *et al.* Proc. ISMRM 2014 #6370; [4] Ma D *et al.* Nature 2013 495:187-193; [5] Tsai LL *et al.* JMR 2008; 193:174-85; [6] Cohen *et al.* Proc ISMRM 2014 #7153

Acknowledgement: This research was supported by the Department of Defense, Defense Medical Research and Development Program, Applied Research and Advanced Technology Development Award W81XWH-11-2-0076 (DM09094).

Results

Each image generated in the reconstructed fingerprinting set (Figure 3) reveals different information. In regions with no signal (Slice 1, Slice 5), no matched value can be found. The spin density (M_0) map of Figure 3.a is equivalent to traditional b-SSFP, and only subtle differences are seen between compartments. Figure 3. b-c reveals that the compartment in slice 3 has the lowest T_1 and T_2 values, and that the compartment in slice 4 has the highest T_1 and T_2 values. Mean T_1 values are 200ms, 168ms, and 320 ms in slices 2, 3, and 4 respectively. Mean T_2 values are 180, 157, and 260 ms in slices 2, 3, and 4 respectively.

Conclusion

We have demonstrated 3D MR Fingerprinting at very low magnetic field with a hybrid b-SSFP-EPI sequence enabling fast and robust acquisition of k -space. The optimized FA/TR strategy provides good dispersion while drastically reducing the total acquisition time. We measure quantitative

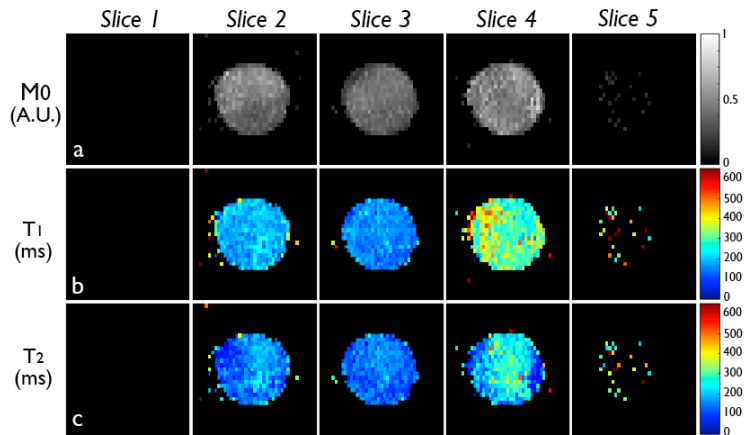


Figure 3 : MR Fingerprinting results at 6.5 mT : a. M_0 , b. T_1 , and c. T_2 in 3D, in a 3 compartment phantom. Each slice in the figure matches one of the phantom compartments.

3D Imaging in a Portable MRI Scanner using Rotating Spatial Encoding Magnetic Fields and Transmit Array Spatial Encoding (TRASE)

Clarissa Zimmerman Cooley^{1,2}, Jason P Stockmann^{1,3}, Mathieu Sarraoane^{1,3}, Matthew S Rosen^{1,3}, and Lawrence L Wald^{1,2}

¹A. A. Martinos Center for Biomedical Imaging, Dept. of Radiology, Massachusetts General Hospital, Charlestown, MA, United States, ²Harvard Medical School, Boston, MA, United States, ³Dept. of Physics, Harvard University, Cambridge, MA, United States

PURPOSE: MRI could find wider applicability if low-cost, portable systems were available for siting in unconventional locations such as ICUs, physician offices, ambulances, or rural healthcare sites. The development of a previously described portable (<100kg) MRI scanner for brain imaging¹ is advanced with the implementation of 3rd axis encoding using the TRASE technique^{2,3}.

METHODS: Our 2D axial plane imaging without gradient coils utilized a rotating, 45 kg, 77 mT inhomogeneous Halbach cylinder based magnet¹. The built-in field variation of the permanent magnet array is used as a rotating spatial encoding magnetic field (rSEM). As the magnet is rotated around the sample, generalized projections onto the non-linear SEM are acquired as a spin-echo train.

To enable imaging in the 3rd direction (along the axis of the cylindrical magnet), we use the TRASE method. TRASE is a B_1^+ encoding method that requires 2 different switchable B_1^+ phase gradients (often equal and opposite) along the encoding direction^{2,3}. The 1D TRASE sequence (Fig. 2) is a modified RARE spin-echo train in which the slope of the B_1^+ phase gradient switches for consecutive refocusing pulses (indicated by the + or -). The 2 phase gradients correspond to 2 k-space origins ($-k_1$ and k_1), and the previous k-space point is flipped across the k-space origin of the refocusing pulse to traverse k-space.

Coils: A TRASE array was designed that consists of two nested cylindrical coils (Fig. 3). Coil 1 is a short 4-turn birdcage coil (12 rungs, 18cm diam., 22cm length)⁴ that produces a B_1^+ field in Y with a cosine shape along X, $B_{1y}^+(x) = |B_{1xy}^+| \cos(2\pi k_1 x)$. Coil 2 is a 10 turn Maxwell coil (22cm diam., 18cm length) that produces a B_1^+ field in X with a sine shape along X, $B_{1x}^+(x) = \pm |B_{1xy}^+| \sin(2\pi k_1 x)$. The coils are tuned to the Larmor frequency (3.29 MHz) and decoupled with a transformer (-20 dB isolation). Figure 3b, shows the relative magnitude of B_{1x} and B_{1y} from the 2 coils measured with a pick-up loop. When the two coils are driven with equal $|B_{1xy}^+|$ magnitude and spatial frequency, k_1 , they produce the desired B_1^+ field, $B_1^+(x) = |B_{1xy}^+| e^{+i 2\pi k_1 x}$ (uniform magnitude and linear phase). A switchable 180° phase shifter is added in the Maxwell coil RF path, which applies a sign change to every other refocusing pulse. The pulses with the phase shift thus have a negative phase gradient; $B_1(x)^+ = |B_{1xy}^+| e^{-i 2\pi k_1 x}$.

Acquisition: The 2D rSEM method and TRASE are performed simultaneously for 3D imaging. The TRASE array must rotate with the magnet because the Y direction changes as the magnet rotates. For every magnet rotation, the projection onto the SEM is acquired as a TRASE-modulated 16-echo spin-echo train (each echo: readout = 196 pt, BW = 40 KHz, echo spacing = 9.7 ms). Data is acquired at 180 rotations of the magnet spaced 1° apart. Frequency-swept WURST pulses are used to achieve the same flip angle across the inhomogeneous field (BW = 25 KHz, [pw90, pw180] = [6,3] ms)⁵. The birdcage coil of the TRASE array is used as the receiver coil.

Reconstruction: **Step one** separates the echo train data along X to obtain 16 different YZ-datasets corresponding to each slice. For each of the 196 points in the readout window, the set of 16 points along the echo train populates a k-space vector (Fig. 2). The points are rearranged and FFT'ed to generate a 1D projection along X (Fig. 4). Only the k-space lines formed from the center points of the echos result in 1D projections that are not modulated by the B_0 SEM. This is repeated for the echo trains from each of the 181 magnet rotations. **Step two** reconstructs each set of 181 echoes (YZ-data) into a 2D image of the corresponding slice. The encoding matrix for each slice is calculated using 2D B_0 field maps and then iterative matrix inversion¹ is performed to separately obtain each 2D image.

RESULTS: Figure 4 shows experimental 3D imaging results using a 7.5cm thick phantom with 1.5 cm water-filled compartments spaced 3 cm apart in X. A 1D projection along X shows the water-filled compartments. Three slices are reconstructed from data at X = -3cm, 0cm, and 3cm using the corresponding 2D B_0 field maps.

DISCUSSION: The non-bijectivity of the SEMs results in image aliasing across the center. This is usually resolved using a surface coil array⁶, but as a first step, the birdcage coil of the array was used for a receiver coil and only the reduced FOV image is shown. The blurring in the image slice is due to a combination of the spatially varying resolution of the SEMs and systematic calibration errors in our model-based reconstruction.

CONCLUSION: We demonstrate proof-of-concept 3D images in an inhomogeneous 45 kg magnet without the use of the gradient coils. TRASE encoding along X is ideal because like our 2D method it uses spin-echo trains, and it prevents the need for a B_0 gradient coil and GPA, which would add weight, cost, and power requirements to the portable, low-cost system. Future work will extend this 3D imaging method using larger diameter magnets and coils with the goal of portable low-cost MRI brain imaging.

REFERENCES: (1) Cooley C, MRM 2014. (2) Sharp JC, MRM 2010. (3) Sharp JC, NMR in Biomed. 2013. (4) Borsboom H, Magn. Reson. Mater. Phys. 1997. (5) Casabianca LB, JMR 2014, (6) Hennig J, Magn. Reson. Mater. Phys. 2008.

ACKNOWLEDGMENTS: The authors thank Jonathon Sharp, Scott King, Michael Garwood, Soumyajit Mandal, and Zohaib Mahmood for their help and advice. Support by NIH R01EB018976, NIH T90DA022759/R90DA023427, DoD/USAMRAA W81XWH-11-2-0076 (DM09094)

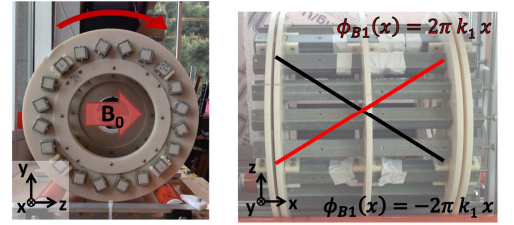


Figure 1: (a) Y-Z encoding is done with the rotating SEM method. (b) TRASE is done in the X direction using a switchable linear B_1^+ phase along X.

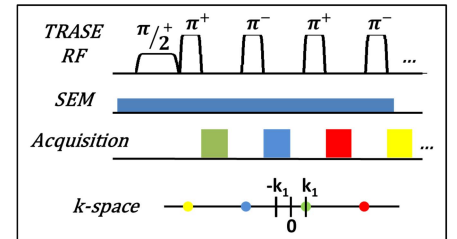


Figure 2: The TRASE sequence is repeated for every magnet rotation of the imaging sequence. The +- indicates the sign of TRASE phase slope.

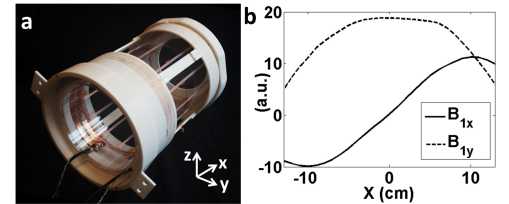


Figure 3: (a) The TRASE array is a nested birdcage and Maxwell coil. (b) The measured magnitude of B_{1x} from the Maxwell coil and B_{1y} from the birdcage coil.

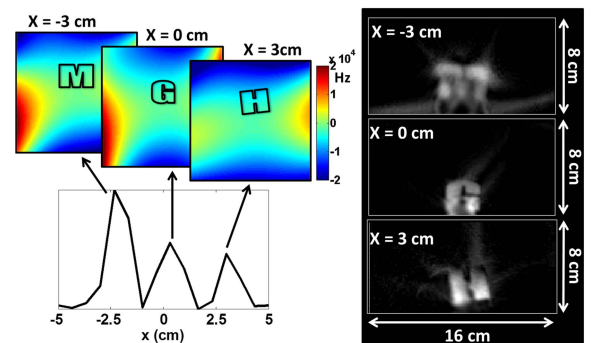


Figure 4: Image of a 3D phantom consisting of three water-filled compartments spaced 3 cm apart in X. A 1D projection along X for 1 rotation angle is shown (lower left). 3 image slices were reconstructed using the appropriate 2D field maps.

Transmit Array Spatial Encoding (TRASE) with broadband WURST pulses for robust spatial encoding in inhomogeneous B₀ fields

Jason P Stockmann^{1,2}, Clarissa Cooley^{3,4}, Mathieu Sarraoane^{1,2}, Matthew S Rosen^{1,2}, and Lawrence L Wald^{1,4}

¹A. A. Martinos Center for Biomedical Imaging, Massachusetts General Hospital, Charlestown, MA, United States, ²Department of Physics, Harvard University, Cambridge, MA, United States, ³Massachusetts General Hospital, Charlestown, MA, United States, ⁴Harvard Medical School, Boston, MA, United States

TARGET AUDIENCE: MRI engineers working with inhomogeneous B₀ fields

PURPOSE: Transmit array spatial encoding (TRASE)¹ uses RF coils with linearly-varying B₁⁺ phase to replace B₀ gradient phase encoding along one more directions. To traverse k-space, the sign of the B₁⁺ phase is flipped for alternating refocusing pulses in a spin echo train, imparting an additional Δk phase modulation to each successive echo in the train. TRASE provides an alternative for performing high resolution spatial encoding in applications where conventional B₀ gradients are not feasible. However, the TRASE point spread function degrades rapidly for refocusing pulse angles outside the range 150-195° due to accumulation of flip angle and phase errors along the echo train². For the hard pulses (as shown in TRASE results to date), the refocusing angle falls below 150° when ΔB₀ > 40% of the pulse Rabi frequency. This constrains the use of TRASE in applications where peak RF power is limited or ΔB₀ is large. We propose a method for overcoming this problem using broadband “WURST” RF pulses along with a simple deconvolution method to render the acquired echoes compatible with TRASE. **METHODS:** To demonstrate 1D TRASE in the presence of strong off-resonance, we acquire projections in an inhomogeneous Halbach array magnet (±20 KHz over FOV) originally developed as a lightweight, permanent magnet-based portable MRI prototype³ with Larmor frequency 3.285 MHz (Fig. 1). WURST-40 pulses⁴ with phase cycling⁵ are used for spin excitation and refocusing. Pulses with linear frequency sweep impart a quadratic phase across the spin bandwidth, but if the pulse sweep rate satisfies the condition $R_{exc} = \frac{1}{2}R_{ref}$ and the ΔB₀ field is constant, then the refocusing pulse removes the phase applied by the excitation pulse and all isochromats refocus at TE⁶. Further readouts in the echo train alternate between conventional echoes and “spectral” echoes⁵ that resemble the frequency distribution of spins in the ΔB₀ field. This additional RF phase modulation must be removed in order to make the spectral echoes compatible with TRASE. The spectral echo signal can be approximated as a convolution of the conventional spin echo signal with a chirp function, $\exp(i2\pi\Omega t^2)$, where Ω depends on the sweep rate. **DECONVOLUTION** is performed by either (a.) convolving the spectral echo with a scaled, conjugated version of the chirp function, or equivalently (b.) in the Fourier transform (FT) domain by dividing the FT of the echo (1D projection) by the FT of the chirp function⁷. Since the FTed chirp kernel is a pure phase term, method (b.) requires simply taking the difference between the phase of the first and second projections in the echo train (Fig. 2). This phase difference is used to correct all subsequent spectral echoes. The FT of the corrected spectral echoes yields echo magnitudes and phases that correspond closely to the conventional echoes in the train. **EXPERIMENT:** Tube phantoms are placed in the inhomogeneous B₀ field and a train of 129 echoes are acquired each with 196 readouts points, 40 KHz BW, and echo spacing 9.4ms. WURST-40 excitation and refocusing pulse durations are [τ_{exc}, τ_{ref}] = [6, 3] ms and sweep rates are [R_{exc}, R_{ref}] = [4.15, 8.3] MHz/s over a 25 KHz bandwidth. A multi-turn Maxwell coil (B_{1x}⁺) is paired with a concentric multi-turn birdcage coil⁸ (B_{1y}⁺) to generate sine and cosine-shaped B₁⁺ amplitudes, respectively, along the encoding axis, x. When both coils are driven simultaneously, the desired linear phase slope is generated: $B_{1tot}^+(x) = |B_{1xy}^+| \cos(2\pi kx) \pm i|B_{1xy}^+| \sin(2\pi kx) = |B_{1xy}^+| \exp(\pm i2\pi kx)$

The TRASE B₁⁺(x) phase is switched using an RF phase shifter to play the pattern: {90°, 180°, echo, 180°, echo, 180°, echo, 180°, echo, 180°, ...}. The first two echoes have no TRASE modulation and can therefore be used to calculate the phase difference required for the spectral echo correction. To create a 1D projection along x, the point from the center of each readout is selected to avoid modulation imparted by the ΔB₀ field (Fig. 3). The points are reordered and FT'ed to create a 1D projection of the object. **RESULTS:** Fourier domain phase subtraction faithfully restores spectral echoes so that their real and imaginary components align closely with those of conventional echoes. The TRASE-WURST acquisition successfully generates projections of phantoms with bandwidths >10 KHz in the inhomogeneous B₀ field. By contrast, recognizable projections could not be obtained using hard pulse excitations since available RF power constrained the minimum pulse duration ([75, 150] μs for [90°, 180°] pulses) and thus the bandwidth of the pulses. **CONCLUSION:** We demonstrate robust spatial encoding using WURST pulses for TRASE encoding in an inhomogeneous B₀ field. We further show a simple phase correction that allows WURST spectral echoes to be used for TRASE encoding. In future work, TRASE-WURST slice encoding will be combined with in-plane B₀ gradient encoding to generate 3D images. Potential applications include silent imaging, oil well prospecting, and portable low-field scanners. **REFERENCES:** [1] Sharp JC, NMR Bio. 2013. [2] Sharp JC, ISMRM 2010, p. 1469. [3] Cooley C, MRM 2014. [4] Kupce E, JMR 1995. [5] Casabianca LB, JMR 2014. [6] Kunz D, MRM 1987. [7] Ito S, MRM 2008. [8] Borsboom H, MAGMA 1997. **ACKNOWLEDGEMENTS:** The authors thank Jonathan Sharp, Scott King, and Soumyajit Mandal. Support from R01EB018976 and DoD/USAMRRA W81XWH-11-2-0076 (DM09094).

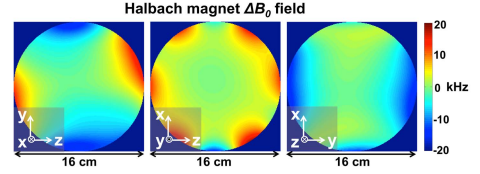


Fig. 1. Halbach magnet ΔB₀ field plotted along three planes. TRASE encoding is implemented along x direction.

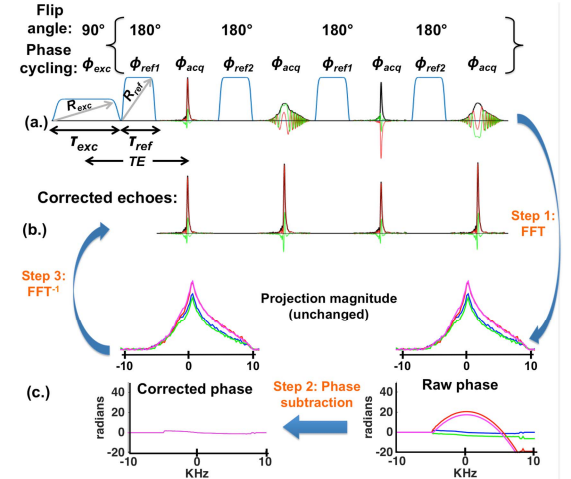


Fig. 2. WURST pulse sequence diagram with four echoes acquired on a water bottle phantom. The bracketed block is repeated as needed. Conventional echoes alternate with “spectral” echoes modulated by the quadratic phase of the frequency swept RF pulses. This effect is compensated by removing the quadratic phase from the projections corresponding to each spectral echo. After phase correction the echo real and imaginary parts overlay for all echoes in the train. Phase cycling scheme is as follows: $\phi_{exc} = [90, 270, 180, 0]^\circ$, $\phi_{ref1} = [0, 0, 90, 90]^\circ$, $\phi_{ref2} = [90, 90, 0, 0]^\circ$, $\phi_{acq} = [0, 180, 90, 270]^\circ$. The 3rd and 4th echoes in the block are multiplied by π to compensate for phase cycling.

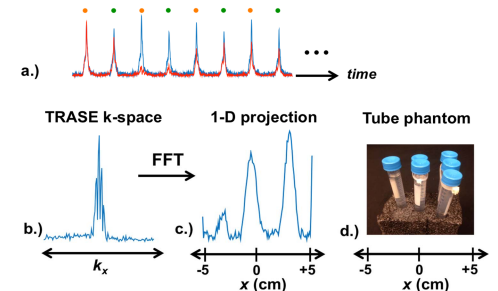


Fig. 3. The first 8 corrected echoes (a.) from a 128-echo train shown with (red) and without TRASE phase modulation. Orange and green dots at each echo time denote positive and negative k-space points, respectively, which are reordered into 1D k-space (b.). The Fourier transform yields a 128-point 1D projection (c.) of the water-filled tube phantom (d.).

A single channel spiral volume coil for in vivo imaging of the whole human brain at 6.5 mT

Cristen LaPierre^{1,2}, Mathieu Sarraclanie^{1,2}, David E J Waddington^{1,3}, and Matthew S Rosen^{1,2}

¹MGH/A.A. Martinos Center for Biomedical Imaging, Charlestown, MA, United States, ²Department of Physics, Harvard University, Cambridge, MA, United States,

³ARC Centre of Excellence for Engineered Quantum Systems, School of Physics, University of Sydney, Sydney, NSW, Australia

Purpose: MRI at low magnetic field (<10 mT) without cryogenic or hyperpolarization techniques presents unique engineering challenges. Imaging coils must maximize coverage over the volume of interest while minimizing losses in a regime unusual in contemporary MRI—where Johnson noise dominates the noise floor. Our previous work validated our scanner hardware and pulse sequences MRI at 6.5 mT. The purpose of the present work is to construct a high-performance coil for low-field imaging of the human brain *in vivo*.

Methods: Our previous coils focused on implementing array coil technology common at clinical field strengths, and we constructed an 8 channel receive-only coil for our 6.5 mT low-field imager at 276 kHz. While our results were promising^{1,2}, a lack of low noise high-impedance pre-amplifiers at our frequency regime prevented us from achieving sufficient coil decoupling, resulting in images with poor SNR. We present here a single channel coil with greatly improved SNR for these applications.



Figure 1: Form fitting helmet with 30-turn spiral design.

We designed a spiral volume coil design for combined Tx and Rx and optimized for human head imaging in the transverse B₀ field of our low field scanner. This places the receive element close to the head while still covering the entire volume uniformly. Additionally, the symmetry of a spherical spiral results in a homogeneous magnetic field over its volume, minimizing B₁ inhomogeneity^{3,4}. Losses in low field imaging are mainly due to resistive losses in the coil (the so-called Johnson noise regime). Rather than lower this resistance by cooling, we instead use of multistranded Litz wire. When compared to a solid copper wire of the same gauge, a loop made of Litz wire will have the same inductance but a fraction of the AC resistance, resulting in a lower noise floor and higher image SNR.

The optimal number of turns and appropriate wire gauge were determined through simulation. The helmet shape was designed to fit closely to an anatomically accurate human head model. The spiral path was generated in a custom MATLAB (Mathworks Inc.) script and imported into BiotSavart (Ripplon Software Inc.) for an estimate of inductance. Resistance was computed from the estimated wire length and the characteristic impedance per length of wire for that gauge. Coil Q was estimated as $\omega L/R$. Bandwidth was estimated from the Q value. We iterated through several

designs until we achieved our target $Q \sim 40$ and $BW = 6\text{kHz}$.

Results: From simulations, we built a 30-turn spiral wound with Type 1 40/38 Litz wire. Our aligned turn-to-turn spacing was 5.6 mm. The final design was 3D printed using fused deposition modeling technology with polycarbonate in a Fortus 360 mc printer (Stratasys, Eden Prairie, MN, USA), (Figure 1).

Images were acquired at 6.5 mT in a head shaped phantom using 3D b-SSFP with 50% undersampling. Resulting voxel size was $3.9 \times 3.5 \times 16.7\text{ mm}^3$ ($NA=110$) (Figure 2a). A maximum in-plane SNR of 130 was calculated. An image of a similar slice obtained with the 8-channel array coil is shown for comparison (Figure 2b, combined image using RSS, voxel size = $4.4 \times 4.2 \times 22\text{ mm}^3$, $NA = 80$, max SNR = 16.5).

19 slices of structured resolution phantom imaged with optimized spiral volume coil are shown in Figure 3. This four-quadrant phantom is filled with liquid-filled spheres of various diameters. Voxel size in this scan is $3.5 \times 2.5 \times 5\text{ mm}^3$ with $NA=40$ and maximum SNR of 24.8. Total acquisition time is 10 minutes.

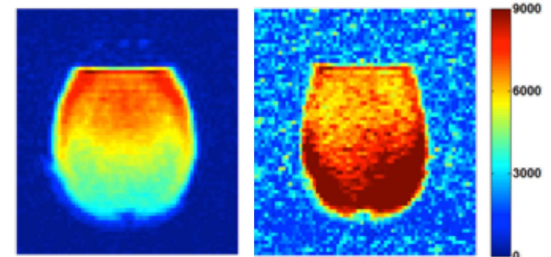


Figure 2: Equivalent slices in a head phantom acquired using the single channel spiral coil (A) and the 8-channel array (B) at 6.5 mT. Images are scaled by their maximum intensity.

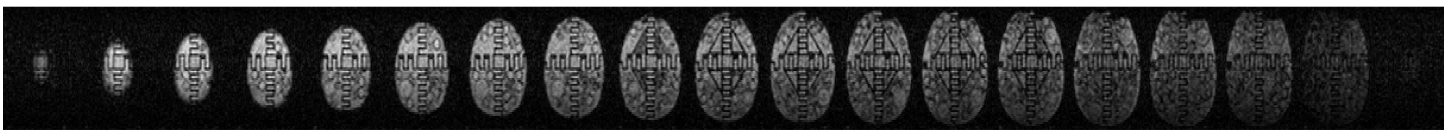


Figure 3: Axial view of a multi-compartment head-shaped phantom acquired with the Litz spiral volume coil at 6.5 mT in 10 minutes.

Discussion: A 30-turn single channel volume spiral coil designed for low field imaging significantly outperformed our 8-channel array coil. By minimizing losses in the coil, maximizing filling factor and eliminating coupling issues, we were able to obtain significantly higher SNR.

Conclusions: A high filling factor human-head Tx/Rx spiral volume imaging coil was successfully designed and constructed for 6.5 mT (276 kHz).

Financial Disclosure: This research was supported by the Department of Defense, Defense Medical Research and Development Program, Applied Research and Advanced Technology Development Award W81XWH-11-2-0076 (DM09094).

References: 1. LaPierre CD, et al. Proc. Intl. Soc. Mag. Reson. Med. 21 (2013) 2772

2. LaPierre CD, et al. Proc. Intl. Soc. Mag. Reson. Med. 22 (2014) 1325

3. Harpen MD. JJ Magn Res 1991;94(3):550–6.

4. Everett JE and Osemeikhian JE. J. Sci. Instrum. 1966;43(7):470.

6710

High Performance Probe for in vivo Overhauser MRI

David E J Waddington^{1,2}, Mathieu Sarraçanie^{1,3}, Najat Salameh^{1,3}, and Matthew S Rosen^{1,3}¹MGH/A.A. Martinos Center for Biomedical Imaging, Charlestown, MA, United States, ²ARC Centre of Excellence for Engineered Quantum Systems, School of Physics, University of Sydney, Sydney, NSW, Australia, ³Department of Physics, Harvard University, Cambridge, MA, United States

Purpose: Overhauser-enhanced MRI (OMRI) is an electron-proton double resonance imaging technique of much interest due to its ability to detect the concentration and distribution of free radicals. Tracking of exogenous free radicals with OMRI *in vivo* has enabled the development of oxymetry probes [1] and the imaging of redox reactions [2]. The large gyromagnetic ratio of electrons (28 GHz/T) demands that *in vivo* OMRI is performed at very low magnetic fields (~10 mT) in order to minimize RF heating and penetration depth issues. Operation at low magnetic field causes a drastic reduction in NMR sensitivity despite the signal enhancement that comes from the Overhauser effect, and emphasizes the need for high S/N probes. OMRI probe design is still relatively unexplored, despite its importance, and presents challenges unique to the frequencies of operation ($f_H = 276$ kHz and $f_e = 140.8$ MHz in our experiments at 6.5 mT). Here, we report the development of a high performance OMRI probe built to image free radical probes of the blood brain barrier following ischemic stroke in a rat model [3].

Methods: Our OMRI probe, consisting of an NMR solenoid inside a modified Alderman-Grant Resonator (Figure 1), was designed for use with a custom built, very low-field MRI scanner operating at 6.5 mT ($f_H = 276$ kHz) [4]. Images were acquired using a recently developed, fast, high-resolution b-SSFP based OMRI methodology [5]. NMR probe design in the low-field regime is fundamentally different to that at conventional MRI fields as thermal noise due to the intrinsic resistance of the pickup coil dominates over sample noise. This leads to a compromise where S/N improvements come at the expense of imaging bandwidth $S/N \sim \sqrt{Q} \sim 1/\sqrt{BW}$. An 85 turn solenoid was wound, using low AC resistance 5/39/42 litz wire, on a 3D printed polycarbonate former. This high filling factor coil has a bandwidth of 3 kHz.

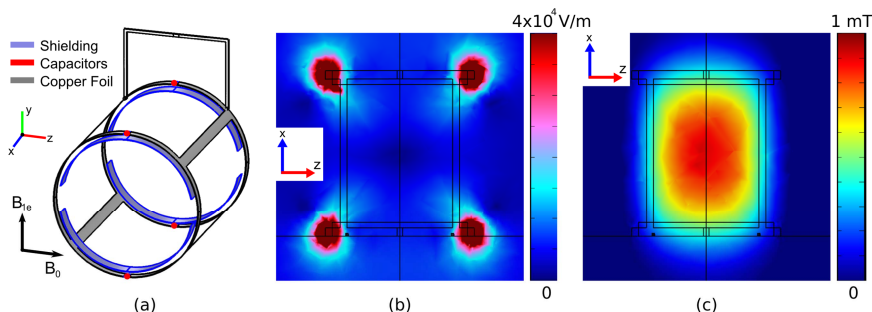


Figure 2: COMSOL Multiphysics simulations (a) Our modified Alderman-Grant Resonator. (b) Plot of $|E|$ showing that the electric field is strongly suppressed inside the resonator. (c) B_{1e} shows high homogeneity in the imaging volume – less than 10% variation across the imaging region.

TEMPOL (4-hydroxy-TEMPO) a stable radical, is detected by OMRI with high sensitivity, and because of its small size may facilitate imaging blood brain barrier leakage in cases of oxidative stress [3]. Simulations were validated in 2mM TEMPOL solutions (not shown) using simple spectroscopic measurements as well as fast imaging strategies [5]. The ESR resonator was tuned to 141 MHz, the lowest frequency of the TEMPOL triplet state at 6.5 mT, to minimize RF heating during ESR irradiation.

Results: Previously we reported the development of an OMRI probe for a rat head model utilizing an NMR solenoid and ESR surface coil [3]. Testing of our new OMRI probe shows that it has 3x the S/N of the probe reported in [3] and rectifies problems with B_{1e} homogeneity, yielding homogeneous enhancement of ~6.7 in 2mM TEMPOL when 10 W of RF power is applied. *In vivo* OMRI signal enhancement is clearly visible in the rat brain after TEMPOL injection, as shown in Figure 3. As the Overhauser-enhanced signal has a phase opposite to that of the thermal signal, the phase image in Figure 3 provides sensitive contrast in regions of low TEMPOL concentration.

Discussion and Conclusion: We have implemented a high performance probe for high temporal and spatial resolution OMRI in a rat brain. The S/N of this probe may be further improved, whilst maintaining imaging bandwidth, by using an active feedback circuit [7]. Higher S/N could also be realized through supercooling of the NMR solenoid or by using a free radical with a longer T_{1e} such as triphenylmethyl [1]. This probe may allow the *in vivo* detection of rapid redox changes in pathologic tissues, specifically in the context of brain trauma or stroke.

References: [1] K. Golman *et al.*, J. Mag. Res. Im., 12, 929-938 (2000). [2] Utsumi *et al.*, PNAS, 103, 1463-1468 (2006). [3] M. Rosen *et al.*, ISMRM, 6461 (2014). [4] Tsai *et al.*, J. Mag. Res., 193, 274-285 (2008). [5] M. Sarraçanie *et al.*, Magn Res. Med., 71, 735-745 (2014). [6] Mispelter *et al.*, 'NMR Probeheads: For Biophysical and Biomedical Experiments', Imperial College (2006). [7] Baudin *et al.*, J. of Phys. Conf. Series, 294, 012009 (2011).

Acknowledgements: This research was supported by DOD DMRDP Award W81XWH-11-2-0076 (DM09094). DW was supported by ANSTO and the Australian-American Fulbright Commission. NS was supported by the Swiss National Science Foundation (P3000P2_147768).

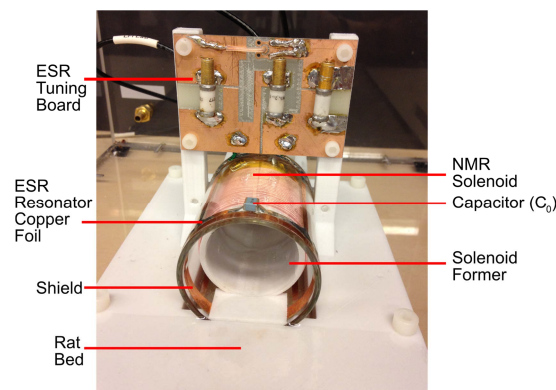


Figure 1: NMR/ESR rat head probe for operation at 6.5 mT. The ESR resonator is tuned to 140.8 MHz. The litz wire NMR solenoid coil (276 kHz) resonator board is not shown.

A modified Alderman-Grant ESR resonator was built using copper foil on Pyrex tubing. All metal placed in close proximity to the NMR solenoid strongly couples, reducing the NMR sensitivity. We therefore minimized amount of copper in the ESR resonator. Windows were removed from the panels on the sides of an Alderman-Grant resonator, a region of low current flow [6], in an attempt to reduce coupling whilst maintaining B_1 homogeneity. Shielding at the ends of the resonator prevents high electric fields at the capacitors penetrating the imaging volume, important because $P_{RF-absorbed} \sim E^2$. Slits in the shielding prevent the formation of closed loops that couple to the solenoid. Figure 2 demonstrates the high B_1 homogeneity and strong E suppression in our ESR resonator.

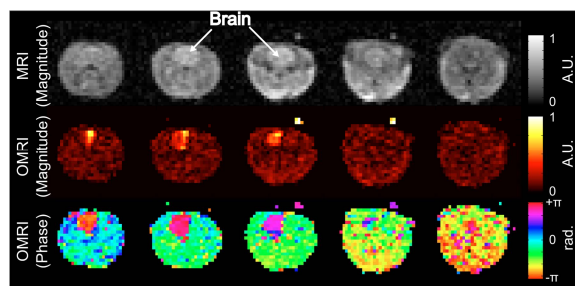


Figure 3: OMRI images acquired from a rat at 6.5 mT following injection of 1mL of 150 mM TEMPOL. Five slices from an 11 slice data set shown. OMRI (NA=1) imaging time was 9 seconds. Anatomical MRI (NA=30) was acquired in the OMRI scanner with ESR power disabled. All images, voxel size: 1.1 x 1.6 x 8 mm³, Matrix: 128 x 35 x 11

Dynamic *in vivo* free radical imaging with Overhauser-enhanced MRI

Mathieu Sarraçanie^{1,2}, Fanny Herisson³, Najat Salameh^{1,2}, David E J Waddington^{1,4}, Cenk Ayata³, and Matthew S Rosen^{1,2}

¹MGH/A.A. Martinos Center for Biomedical Imaging, Charlestown, MA, United States, ²Department of Physics, Harvard University, Cambridge, MA, United States, ³Neurovascular Research Lab, Department of Radiology, Massachusetts General Hospital, Charlestown, United States, ⁴ARC Center for Engineered Quantum Systems, School of Physics, University of Sydney, Sydney, NSW, Australia

PURPOSE: Free-radical-sensitive Overhauser-enhanced MRI (OMRI) is a promising technique for imaging the distribution and dynamics of free radicals, and a recently developed fast high-resolution OMRI methodology (1) offers new perspectives for the imaging of free radicals in living organisms. This method has been used to probe BBB breakdown following ischemic stroke in rats in conjunction with an injected stable free radical (2). Here we explore if OMRI can be used to acquire free radical images with sufficient spatial and temporal resolution to probe oxidative stress status in the brain. We present time-resolved *in vivo* measurements following a single injection of TEMPOL. TEMPOL (4-hydroxy-TEMPO), a small molecule with a stable unpaired electron spin, is detected by OMRI with very high sensitivity. According to the literature, TEMPOL does not cross the BBB in a normal physiological state but does pass into brain parenchyma under pathological circumstances associated with oxidative stress and disease (3). As TEMPOL reduction has been used to non-invasively monitor tissue redox status in animal models (4), we hypothesize that time-resolved OMRI may be a tool to elucidating the redox status of brain tissue in neurologic diseases in which oxidative stress plays a significant role such as reperfusion injury (5), head trauma (6), Alzheimer's dementia (7) and multiple sclerosis (8).

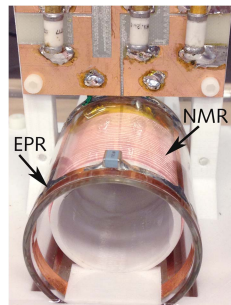


Figure 1: Probe for OMRI imaging at 6.5 mT: NMR: 276 kHz, ESR: 141 MHz.

METHODS: A custom built, low-field MRI scanner equipped with a biplanar 6.5 mT electromagnet and biplanar gradients was used in these experiments (9). 3D OMRI was performed using an optimized sequence based around b-SSFP as described in (1). *In vivo* experiments were performed using a modified Alderman-Grant ESR coil outside of a high sensitivity solenoid NMR coil wound from 5/39/42 Litz wire that fits the rat head (Figure 1). Under isoflurane anesthesia, the right carotid bifurcation of a male Sprague Dawley rat was dissected and the pterygopalatine artery ligated. Retrograde cannulation (Micro-Renathane MRE40, Braintree Scientific) of the right carotid bifurcation was performed through the external carotid artery. The catheter, filled with saline 0.9% with heparin 50U/ml, was then tunneled to the back of the animal and connected to the injection system. Oxygen saturation, temperature, and cardiac and respiratory rates were continuously monitored.

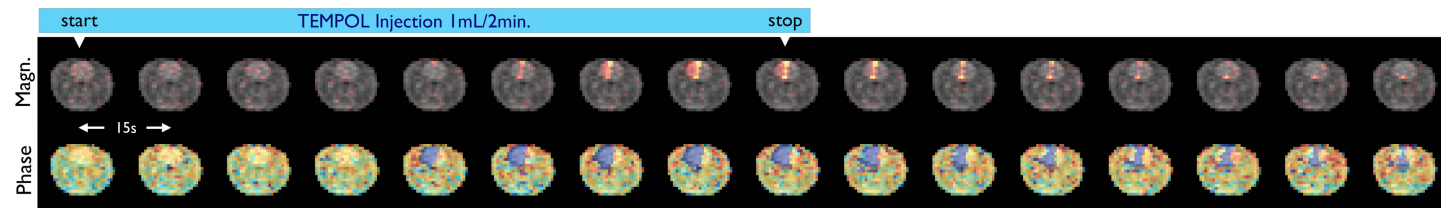


Figure 2: Dynamics of one slice from 3D OMRI dataset acquired from a rat at 6.5 mT: OMRI (color) magnitude and phase images (NA=1) are superimposed on anatomical MRI (grey), acquired in the OMRI scanner with DNP pulses disabled (NA=30). Anatomical imaging time was ~5 min. All images, voxel size 1.1×1.6×8 mm³, TE/TR=25/50 ms, Matrix 128×35×11. TEMPOL (1.4 µl/gbw) was injected into the right ICA over 2 minutes.

Following acquisition of two reference scans (one with EPR off and one with EPR on), 1 ml of 150 mM TEMPOL was injected over 2 min with an infusion pump (GenieTouch Kent Scientific). OMRI imaging began at the same time as the infusion, and continued for 105 seconds after the injection was complete. A full 11 slice OMRI acquisition was acquired every 9 seconds, followed by a 6 second delay. This was repeated 16 times. Total imaging time was 240 s.

RESULTS: The internal carotid artery is responsible of the vascularization of its ipsilateral hemisphere via its terminal branches. The Circle of Willis enables some cross vascularization of one hemisphere from the contralateral side. Therefore, one would expect the cerebral distribution of a compound injected directly into the ICA to reflect the ipsilateral hemisphere and to a lesser degree the contralateral hemisphere. This is consistent with our dynamic *in vivo* OMRI results shown in Figure 2 and Figure 3, where marked DNP enhancement is seen in the hemisphere ipsilateral to the TEMPOL injection. As the Overhauser-enhanced signal has phase opposite to that of the thermal signal, the phase of the OMRI image in Figure 2 provides very sensitive contrast even in cases where the radical concentration is very low and the Overhauser enhancement may be small.

DISCUSSION & CONCLUSION: We have imaged the free radical TEMPOL with time-resolved OMRI methods *in vivo*. The use of fast bSSFP-OMRI in conjunction with an exogenously administered free radical molecule to probe redox status is a novel approach. As a method, temporally resolved OMRI may be used to study redox status of brain tissue made permeable to TEMPOL from oxidative stress. We note here that the long clearance times seen in some regions of the brain in Figure 2 may indicate TEMPOL in the brain parenchyma.

REFERENCES: (1) Sarraçanie M et al. MRM 2014;71(2):735–45 ; (2) Rosen M S et al, Proc. ISMRM 2014 (22) 6461 ; (3) Behringer W et al. J Cereb Blood Flow Metab. 2002 22(1):105–17 ; (4) Hyodo F et al. J Pharm Pharmacol.2008 60(8):1049–60 ; (5) Chan PH. Stroke. 1996 27(6):1124–9 ; (6) Awasthi D, et al. Surg. Neuro. 1997 Jun;47(6):575–81 ; (7) Praticò D, et al Am. J. Med. 2000;109(7):577–85 ; (8) Fischer MT, et al Brain. Oxford Univ Press; 2012;135(3):886–99 ; (9) Tsai LL et al. JMR, 2008 93(2):274–85.

ACKNOWLEDGMENTS: This work supported by the Department of Defense, Defense Medical Research and Development Program, Applied Research and Advanced Technology Development Award W81XWH-11-2-0076 (DM09094).

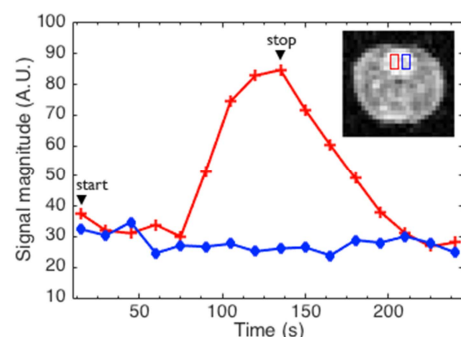


Figure 3: Mean OMRI magnitude from two brain ROIs: ipsilateral (red) and contralateral (blue) to the TEMPOL injection over the 240 s OMRI acquisition.

Clarissa Zimmerman Cooley^{1,2}, Jason P. Stockmann^{1,3}, Brandon D. Armstrong^{1,3}, Mathieu Sarraclanie^{1,3},
 Matthew S. Rosen^{1,3}, Lawrence L. Wald^{1,4}

¹A. A. Martinos Center for Biomedical Imaging, Dept. of Radiology, Massachusetts General Hospital, Charlestown, MA, USA, ²Dept. of Electrical Engineering and Computer Science, Massachusetts Institute of Technology, Cambridge, MA, USA, ³Dept. of Physics, Harvard University, Cambridge, MA, USA, ⁴Harvard-MIT Division of Health Sciences Technology, Cambridge, MA, USA

As the premiere modality for brain imaging, MRI could find wider applicability if lightweight, portable systems were available for siting in unconventional locations such as ICUs, physician offices, ambulances, emergency rooms, sports facilities, or rural healthcare sites.

In this work, a small rotating permanent magnet array with an inhomogeneous field is used to create a portable 2D MRI scanner. The field distribution is used for image encoding instead of gradient coils. The elimination of the gradient power amplifier allows the scanner to be run from a standard power outlet. The previously described 45 kg (36cm dia. 35.6cm length) Halbach cylinder magnet^{1,2} uses 20 rungs of NdFeB magnets (Fig. 1a) to create a 77.3mT transverse field (3.29MHz proton freq.) with 32 KHz variation across the center slice's 16cm diameter FOV (Fig. 1b). As the magnet is physically rotated around the object using a stepper motor, a RARE type spin echo sequence records the generalized projections onto the nonlinear field pattern. Each spin echo is acquired with a 256 point readout and a 20 KHz bandwidth. The individual echos are averaged to improve SNR.

The approximately quadrupolar spatial encoding magnetic field (SEM) is non-bijective which causes image aliasing, but can be disambiguated using parallel imaging as described by Schultz et al.³ We use an 8-channel receive array (Fig. 2a) with 8 cm circular loops for this purpose. The coil sensitivity maps (Fig. 2b) were modeled using the Biot-Savart law and are different for each magnet rotation angle. The coil sensitivity maps and field maps at each rotation angle are used to form the encoding matrix of the system. The images are then reconstructed with the Algebraic Reconstruction Technique^{2,4}.

Figure 3 shows experimental images of a "MIT/MGH" phantom (CuSO₄-doped water, 1.7cm thick, 13cm dia.) acquired with 7 coils of the Rx array, 32 averages of a 6 spin-echo train (TR = 550 ms, echo-spacing = 8ms) and 91 2° magnet rotations. Data was also acquired from a single field probe at each rotation to track field drift (due to temperature) and used to improve the reconstruction (Fig. 3b). The lengthy acquisition time of 66 minutes results from serially acquiring from the 8 coils into a single channel on the console and would be reduced to 7.3 minutes with true parallel acquisition. Figure 3c shows a 1cm thick lemon slice imaged using 5 surface coils to acquire a 128 echo train at 181 1° rotations (TR = 4500ms, echo spacing = 8ms). The total acquisition time was 93 minutes (15.5 minutes w/ parallel Rx). The nonlinear encoding field results in non-uniform image resolution. Blurring in the center (Fig. 3c) is due to the flat nature of the encoding field near the center of the FOV.

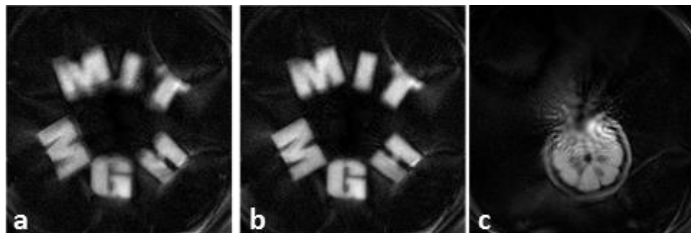


Figure 3: Experimental 16 cm FOV images. (a,b) 1.5cm thick phantom. (a) Temperature drift not corrected, (b) temperature drift corrected. (c) 1 cm thick lemon slice.

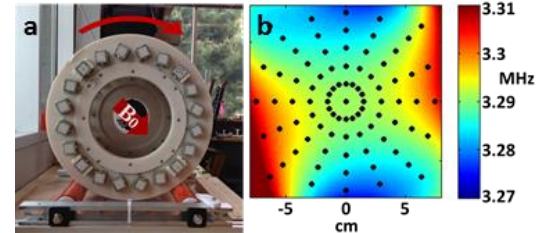


Figure 1: (a) magnet on high friction rollers, (b) field map formed as a polynomial fit to the measured field probe points (black dots).

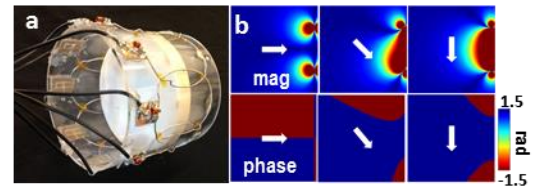


Figure 2: (a) 8-channel RX array coil with disk phantom. (b) Calculated B_1 in the center plane of a surface coil located at the right side of the FOV. The arrows show four representative orientations of B_0 .

Using an inhomogeneous rotating magnet for spatial encoding in lieu of gradient coils, we have constructed and demonstrated a lightweight scanner for 2D MR imaging with minimal power requirements. The addition of 3rd axis encoding is an obvious requirement for medical applications. A promising possibility for encoding the 3rd dimension (along the axis of rotation) is Transmit Array Spatial Encoding (TRASE)^{6,7}. With the future implementation of true parallel imaging and 3D encoding, this scanner has the potential to enable a truly portable, low-cost brain imaging device.

REFERENCES: (1) Zimmerman C, ISMRM 2012. (2) Cooley CZ, ISMRM 2013. (3) Schultz G, MRM 2010. (4) Gordon R, J Theor Biol 1970. (5) Stockmann JP, MRM 2013. (6) Sharp JC, MRM 2010. (7) Sharp JC, NMR Biomed 2013.

ACKNOWLEDGMENTS: The authors thank M Lev, C Lapierre, M Christensen, E Siskind, B Guerin, and S Cauley. Support by DoD/USAMRRA W81XWH-11-2-0076 (DM09094) and NIH P41EB015896.

Spatial resolution in rotating Spatial Encoding Magnetic field MRI (rSEM-MRI)

Clarissa Zimmerman Cooley^{1,2}, Jason P. Stockmann^{1,3}, Brandon D. Armstrong^{1,3}, Mathieu Sarraconie^{1,3}, Matthew S. Rosen^{1,3}, and Lawrence L. Wald^{1,4}

¹A. A. Martinos Center for Biomedical Imaging, Dept. of Radiology, Massachusetts General Hospital, Charlestown, MA, United States, ²Dept. of Electrical Engineering and Computer Science, Massachusetts Institute of Technology, Cambridge, MA, United States, ³Dept. of Physics, Harvard University, Cambridge, MA, United States, ⁴Harvard-MIT Division of Health Sciences and Technology, Cambridge, MA, United States

TARGET AUDIENCE: MR system engineers and those requiring portable MRI systems.

PURPOSE: As the premiere modality for brain imaging, MRI could find wider applicability if lightweight, portable systems were available for siting in unconventional locations. However, realization of such lightweight, low power systems will require non-standard spatial encoding approaches such as rotating non-linear Spatial Encoding Magnetic fields (rSEMs). In this work we examine the spatial variations in image resolution of different SEMs for rotating scanners. We compare modeled spatial resolutions to acquired images encoded by a rotating SEM from a lightweight rotating Halbach magnet.

METHODS: A small rotating permanent magnet Halbach array with an inhomogeneous field has been used to create a portable 2D MRI scanner^{1,2}. The field distribution, which is predominately quadrupolar (~ 320 Hz/cm²), is used for image encoding instead of gradient coils. As the magnet is physically rotated around the object using a stepper motor, a RARE type spin echo sequence records the generalized projections onto the SEM. If sufficient multi-polar terms are present in the SEM, as is the case for the Halbach field, then parallel imaging is required to disambiguate the encoding³. We use a stationary 8 channel Rx array containing 8 cm overlapping loops whose sensitivity profiles vary with magnet rotation (as B_0 is rotated relative to the coils).

Data was acquired with the rotating Halbach scanner, and simulated for multiple rotating SEMs and simulation objects. These SEMs include the measured field of the Halbach magnet with and without an additional linear shim field (1.2mT/m), and a pure linear SEM with the same magnetic field range of the Halbach SEM (6 mT/m). In order to evaluate spatial resolution, a line of point sources spaced 5mm apart along the radius of the 16cm circular FOV were simulated. A 2D Gaussian low-pass filter was used to smooth the point sources to 0.5mm FWHM. In addition, images of single point sources were simulated to evaluate the varying FWHM of point spread functions (PSFs) along the radius.

Assuming a 20 KHz sampling BW, 256 point spin echoes were simulated for each coil and each magnet rotation (181 angles spaced 1° apart). The phase accumulation with time in each voxel is calculated using the magnetic field map, then multiplied by the complex coil sensitivity map and the magnitude of the simulated object, and summed to form the net signal.

Data is reconstructed using the encoding matrix which contains the phase information estimated from the encoding field, as well as the effect of the coil sensitivities. This general encoding model is solved iteratively using the Algebraic Reconstruction Technique^{2,4}.

RESULTS: 2D and 1D images of a line of Gaussian points simulated from 3 rotating SEMs are shown in Figure 1a-b. Figure 1c shows variation in FWHM of simulated point spread functions along the radius. A uniform Rx coil was assumed for Fig. 1 simulations (the aliased portion is cropped). Simulated brain images using the 8 channel receive array, and the Halbach SEM or Halbach+linear SEM are shown in Figure 2

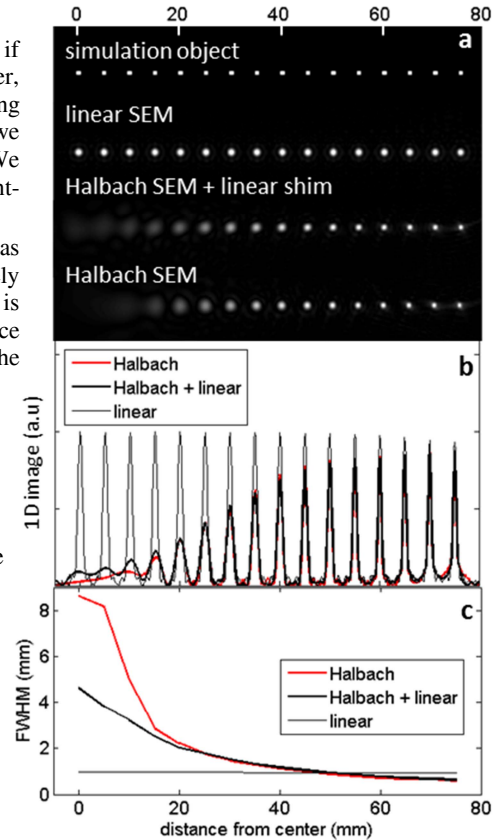


Figure 1: Simulated 2D (a) and 1D (b) images of a line of points starting at center of FOV using multiple rotating SEMs. (c) FWHM of the PSF along the radius. (x-axis common to fig. a,b, and c)

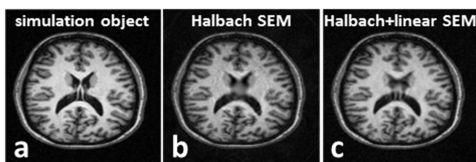


Figure 2: Simulations. (a) T1-weighted brain reference. (b) Simulated using Halbach SEM. (c) Simulated with Halbach SEM + linear field.

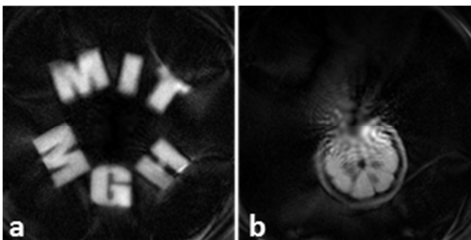


Figure 3: Experimental 16 cm FOV images. (a) 1.5cm thick phantom filled with CuSO4 doped water. (b) 1 cm thick lemon slice.

(noise levels matched to experimental data). Figure 3 shows experimental images using the Halbach SEM of a “MIT/MGH” phantom (CuSO₄-doped water, 1.7cm thick, 13cm dia.) acquired with 7 coils of the Rx array, 32 averages of a 6 spin echo train (TR = 550 ms, echo spacing = 8ms) and 91 2° magnet rotations. Figure 4b shows a 1cm thick lemon slice imaged with 5 coils, a 128 echo train (TR = 4500ms, echo spacing = 8ms), and 181 1° magnet rotations.

DISCUSSION & CONCLUSION: As expected, the resolution resulting from the rotating linear SEM is nearly uniform (Fig 1). Multi-polar SEMs have a steep gradient near the periphery and a shallow gradient near the center. This translates to the resulting resolution in images acquired with rSEMs with multi-polar components – higher resolution near the periphery and an “encoding hole” in the center (Fig 1, 2b, 3b). When a sufficient linear term is added to the SEM, the shallow encoding field region does not coincide with the axis of rotation. In this case, the “encoding hole” moves around the object resulting in less severe blurring (Fig 1, 2c). The simulations in Figure 2 show the theoretical resolution of the Halbach rSEM scanner when systematic errors are eliminated. These errors (effects seen in the experimental images, Fig. 3) likely result from field map or coil sensitivity profile inaccuracies propagating through the iterative reconstruction⁶.

REFERENCES: (1) Zimmerman C, ISMRM 2012. (2) Cooley CZ, ISMRM 2013. (3) Schultz G, MRM 2010. (4) Gordon R, Journal of theoretical biology 1970. (6) Stockmann JP, MRM 2013.

ACKNOWLEDGMENTS: The authors thank C Lapierre, M Christensen, E Siskind, B Guerin, and S Cauley. Support by DoD/USAMRRA W81XWH-11-2-0076 (DM09094) and NIH P41EB015896.

Conference Abstracts presented in 2014
An Optimized 8-Channel Helmet Array for Head Imaging at 6.5 mT

Cristen D. LaPierre^{1,2}, Mathieu Sarraclanie^{1,2}, Lawrence L. Wald^{1,3,4}, Matthew S. Rosen^{1,2,3}

¹A. A. Martinos Center for Biomedical Imaging, Department of Radiology, Massachusetts General Hospital, Charlestown, MA, ²Department of Physics, Harvard University, Cambridge, MA, ³Harvard Medical School, Boston, MA, ⁴Harvard-MIT Division of Health Sciences and Technology, Cambridge, MA

In many traumatic brain injury situations, time-critical diagnostic imaging is needed to properly triage and begin treatment. However, in some scenarios access to conventional MRI scanners is limited, owing in part to their siting requirements. A very low-field imager could enable a potentially transportable and rapidly deployable human imaging system free from many of the system requirements of high-field scanners. We previously demonstrated an eight-channel array [1] for our 6.5 mT electromagnet based scanner [2] capable of imaging objects up to 15.6 cm in diameter and implemented SENSE. The present work demonstrates parallel imaging *in vivo* in the human head with an optimized 8-channel array.

A tight fitting helmet was designed and 3D printed in-house (Fig. 1). Eight 30-turn receive-only coils (24 AWG, 4x12 cm and 4x14 cm loops) were tiled symmetrically about the sagittal plane. All coils were tuned to 276.0 kHz and were matched to at least -27 dB and geometrically decoupled from their nearest neighbors by at least -30 dB. Decoupling from next-nearest neighbors was at least -6 dB. A 30 cm diameter solenoid was used for transmit. Passive decoupling between transmit and receive was achieved using crossed diodes in series with transmit, and in parallel with receive.

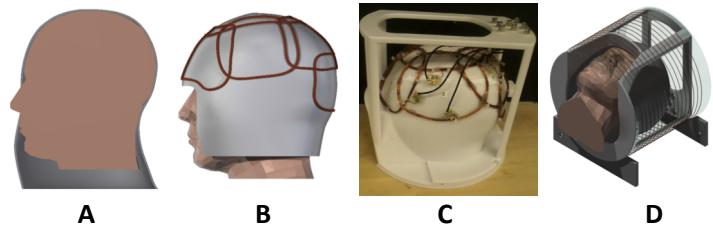


Figure 1: An 8Ch array designed as a tight-fitting helmet (gray) to an anatomically-correct CAD model of the human head (A), tiling of 8 receive-only coils (B) and construction on a 3D printed helmet. D) final assembly modeled in the 30 cm transmit coil.

Axial (Fig. 2.A) and sagittal (Fig. 2.B) images were acquired using a 3D b-SSFP sequence with 50% incoherent undersampling of k-space at 6.5 mT (276 kHz). Imaging parameters were: TR/TE = 33.2/21.6 ms, acquisition matrix = (64×64×9), voxel size = (3×3×6) mm³, number of averages (NA) = 200, and flip angle = 70°. The readout duration was 7.04 ms with a 9091 Hz bandwidth. The total acquisition time was 30 min. Both figures reveal recognizable anatomic features in the head including the skull, cortical structures (gyri/sulci) and the corpus callosum.

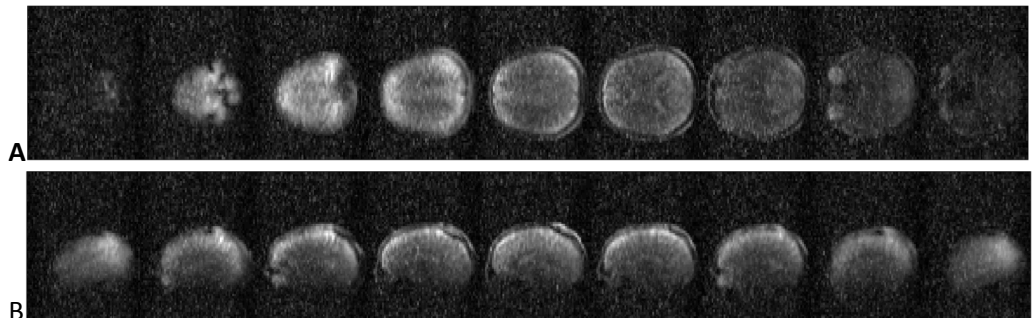


Figure 2: 3D b-SSFP performed *in vivo* in a human head in A. axial and B. sagittal orientation using the optimized 8-channel helmet array at 6.5 mT (276 kHz ¹H frequency). Magnitude images are shown. Voxel size was (3.3×4×17) mm³. Total acquisition time was 30 min.

We have demonstrated that an optimized 8-channel helmet array combined with fast acquisition techniques and undersampling strategies enables 3D imaging at very low field *in vivo*. With (3.3×4×17) mm³ total voxel size, we obtain 2 times greater spatial resolution than very recently published work using a SQUID detector in an ultra-low field MRI system with a 80 mT prepolarization field [3]. In addition, our 3D dataset (9 slices) was acquired more than seven times faster than the single slice 2D brain dataset of the SQUID-detected work. Future work will focus on improved coil decoupling schemes in this very-low-field regime as well as additional image acceleration techniques such as SENSE.

Acknowledgements: This work supported by the Department of Defense, Defense Medical Research and Development Program, Applied Research and Advanced Technology Development Award W81XWH-11-2-0076 (DM09094).

References: 1. LaPierre, M Sarraclanie, LL Wald, MS Rosen. *Proc. Intl. Soc. Mag. Reson. Med.* 21 (2013) 2772., 2. LL Tsai, RW Mair, MS Rosen, S Patz, RL Walsworth. An open-access, very-low-field MRI system for posture-dependent ³He human lung imaging. *J Magn Reson.* 193(2): 274-85 (2008)., 3. B Inglis, K Buckenmaier, P SanGiorgio, AF Pedersen, MA Nichols, J Clarke. MRI of the human brain at 130 microtesla. *PNAS* (Nov. 2013). doi: 10.1073/pnas.1319334110.

Overhauser-enhanced MRI with SENSE Acceleration in the Johnson Noise Dominated RegimeCristen D. LaPierre^{1,2}, Mathieu Sarraclanie^{1,2}, Brandon Armstrong^{1,2}, Jonathan R. Polimeni^{1,3}, Matthew S. Rosen^{1,2,3}¹A.A. Martinos Center for Biomedical Imaging, Department of Radiology, Massachusetts General Hospital, Charlestown, MA, ²Department of Physics, Harvard University, Cambridge, MA, ³Harvard Medical School, Boston, MA

MRI at low magnetic fields is time consuming owing to small Boltzmann polarization and consequently low signal. Enhancement techniques such as Dynamic Nuclear Polarization (DNP), and image acceleration techniques like SENSitivity Encoding (SENSE) are compelling tools to obtain high-quality images in reasonable times. The present work combines DNP with eight-channel parallel imaging at 6.5 mT.

Previously we constructed an 8-channel receive array¹ at 276 kHz for our 6.5 mT electromagnet-based scanner² and demonstrated SENSE reconstruction. This setup is now equipped to perform b-SSFP based Overhauser-MRI (OMRI)³. The 8-channel receive array nests inside a 14 cm diameter 140 MHz ESR saddle coil, which is placed inside a 30 cm diameter solenoid for NMR transmit at 276 kHz. An OMRI image of a 13 cm diameter structured phantom was acquired both with- and without SENSE acceleration (reduction factor $R=2$). Coil sensitivity profiles were acquired with the saddle coil in position but without DNP. A 3D balanced Steady State Free Precession (b-SSFP) sequence with full Cartesian acquisition of k -space was acquired with FOV=304×170×60 mm³, acquisition matrix=130×128×3, TE/TR=25.2/50.4 ms, number of acquisitions (NA)=35 except for (b) where NA=140.

Figure 1 shows the structured phantom (a) and images obtained without DNP or SENSE (b), with DNP but not SENSE (c) and using DNP and SENSE (d). The unenhanced image was acquired in 25.5 min. The DNP-only image was acquired in 11.5 min, and adding SENSE acceleration ($R=2$) reduced this time to 5.5 minutes at 6.5 mT.

Figure 2 shows the noise covariance matrix (a) and the correlation coefficient matrix (b) for the 8-channel array. The 8 channels are fairly well decoupled from each other. Channels 6 and 7 show increased mutual coupling—perhaps due to coupling via the EPR saddle coil.

With DNP alone, the SNR efficiency (SNR_{eff}) increased 23.4 fold while there was a 1.8 fold reduction in acquisition time. Combining DNP and SENSE, the SNR_{eff} decreased 22% and acquisition time decreased 4.6 fold. SNR_{eff} is max SNR in the sample normalized by the square root of NA.

These results represent the first use of DNP hyperpolarization combined with SENSE acceleration attained at 6.5 mT and represent important steps towards accelerating hyperpolarized imaging at low field. Future work will improve SENSE reconstruction as well as compare it to incoherent random undersampling strategies.

Acknowledgements: This work supported by the Department of Defense, Defense Medical Research and Development Program, Applied Research and Advanced Technology Development Award W81XWH-11-2-0076 (DM09094).

References: 1. CD LaPierre, M Sarraclanie, LL Wald, MS Rosen. *Proc. Intl. Soc. Mag. Reson. Med.* 21 (2013) 2772. 2. LL Tsai, RW Mair, MS Rosen, S Patz, RL Walsworth. An open-access, very-low-field MRI system for posture-dependent ³He human lung imaging. *J Magn Reson.* 193(2): 274-85 (2008) 3. M Sarraclanie, BD Armstrong, J Stockmann, MS Rosen. High speed 3D overhauser-enhanced MRI using combined b-SSFP and compressed sensing. *Magn Reson Med.* doi: 10.1002/mrm.24705

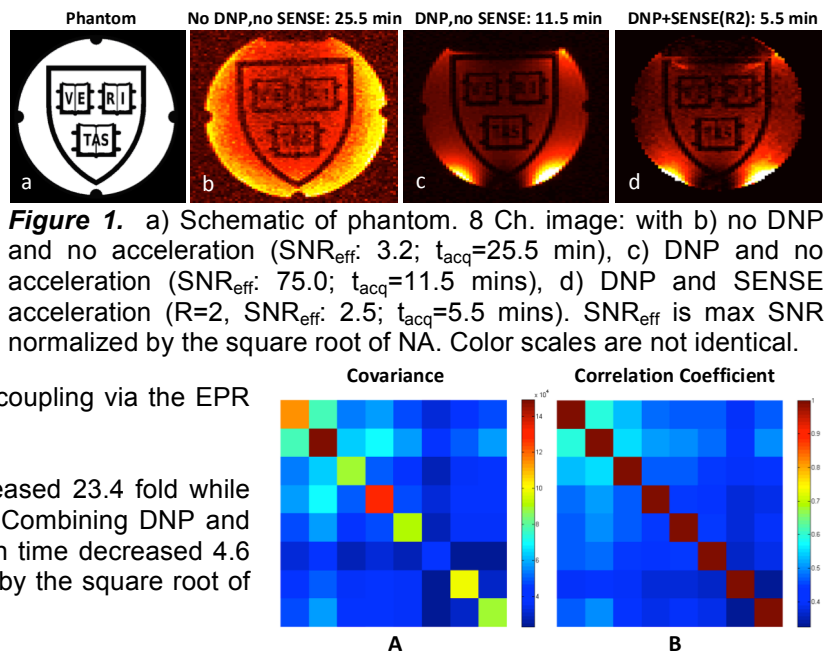


Figure 1. a) Schematic of phantom. 8 Ch. image: with b) no DNP and no acceleration (SNR_{eff} : 3.2; t_{acq} =25.5 min), c) DNP and no acceleration (SNR_{eff} : 75.0; t_{acq} =11.5 mins), d) DNP and SENSE acceleration ($R=2$, SNR_{eff} : 2.5; t_{acq} =5.5 mins). SNR_{eff} is max SNR normalized by the square root of NA. Color scales are not identical.

Mathieu Sarraclanie^{1,2}, Brandon D. Armstrong^{1,2} and Matthew S. Rosen^{1,2,3}

¹A. A. Martinos Center for Biomedical Imaging, 149 13th St., Suite 2301, Boston, MA. 02129, ²Department of Physics, Harvard University, 17 Oxford St. Cambridge, MA. 02138, ³Harvard Medical School, 25 Shattuck St, Boston, MA. 02115

High-field MRI instruments offer limited utility in field deployable and portable contexts. Our effort focuses on the critical challenges that must be solved to enable deployment of transportable MRI systems. In recent work [1], we demonstrated high performance MRI at low magnetic field by making use of high-efficiency steady state free precession techniques (b-SSFP) [2] and undersampling for compressed sensing MRI. Earlier in 2013, a new imaging technique termed “magnetic resonance fingerprinting” (MRF) was proposed [3]. Unlike all other MRI sequence strategies, MR Fingerprinting allows the simultaneous quantification of multiple properties of a material or tissue in a single acquisition. In the present work, we show the first implementation of MR Fingerprinting at very low magnetic field in a multi-compartment phantom.

MRF at low magnetic field creates a rapid dynamic series of low signal to noise ratio (SNR) images where the magnitude of each voxel of each image changes at every time step. The TR and flip angle of each image in the time series is varied pseudo-randomly [5]. No steady state is reached, and image voxels with different relaxation times evolve differently, thereby generating unique magnetization trajectories. The time evolution of each voxel is simulated offline using the Bloch equations with the TR and flip angle patterns used for the imaging sequence over a wide range of tissue parameters, and a database (dictionary) of trajectories is generated. The measured voxel trajectory is compared to the dictionary and the best match is chosen, identically providing the T_1 , T_2 , and off-resonance frequency value of that voxel. Lack of SNR at low magnetic field required redesigning our sequence to lower undersampling rates and bigger flip angle range. The resulting sequence is a 200 time points, 50% undersampled, slice-selective 20 spirals sequence. After an inversion pulse, flip angle ranges between 30 and 107°, TR varies between 46.1 ms and 52.7 ms. The dictionary was made of 2,751,975 signal time courses, each with 200 time points. MR total acquisition time was 13 min. The sequence was set with voxel size: $3 \times 3 \times 10 \text{ mm}^3$, FOV: $144 \times 144 \times 10 \text{ mm}^3$, number of average (NA):6. The low field MRI scanner was previously described [6].

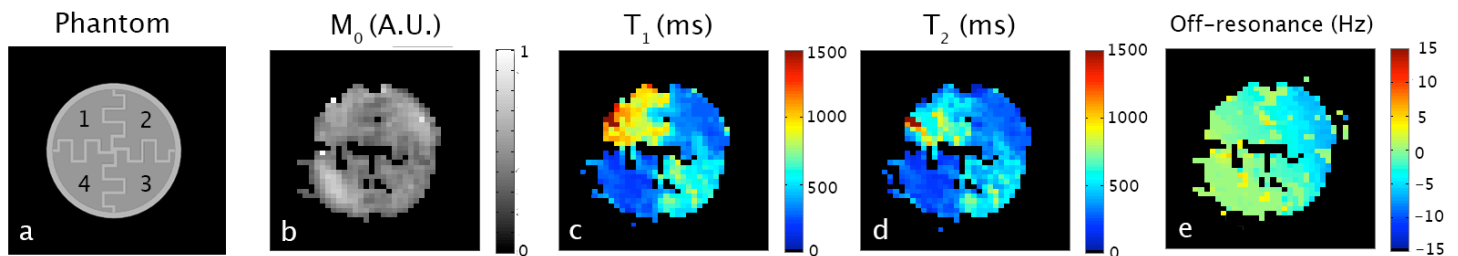


Figure 1: Slice selective MRF results obtained at 6.5 mT. The four-compartment liquid filled structured phantom shown schematically in (a). The compartments vary in relaxation properties. Each compartment had T_1 and T_2 measured in separate reference experiments (Inversion recovery & T2 CPMG respectively). 1: $T_1=1046$ ms, $T_2=700$ ms, 2: $T_1=425$ ms, $T_2=418$ ms, 3: $T_1=600$ ms, $T_2=591$ ms, 4: $T_1=340$ ms, $T_2=286$ ms. **b-e** show M_0 , T_1 , T_2 , and off-resonance frequency, respectively.

Each image generated in the reconstructed fingerprinting set (Figure 1 b–e) reveals different information. The spin density (M_0) map of Figure 1.a is equivalent to traditional b-SSFP, and no visible difference between compartments is seen. However, Figure 1. c–d reveals that compartments 1–4 have very different T_1 and T_2 relaxation properties. The MRF images show good agreement with the reference measurements. Additionally, a map of the magnetic field homogeneity of the LFI scanner is also generated during the MRF sequence (Figure 1.e).

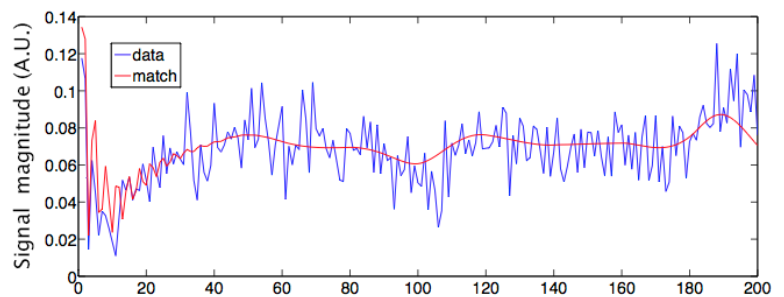


Figure 2: The magnetization trajectory of a single typical voxel over the 200 image fingerprinting sequence is shown (blue: data, red: best match from dictionary). All the parameters of the voxel (M_0 , T_1 , T_2 , and off-resonance frequency) are determined once the trajectory match is

We have demonstrated MR Fingerprinting at low magnetic field, which results in simultaneous measurement of 4 quantitative parameters, and thus provides 4 different image contrasts in a single acquisition (proton density, T_1 , T_2 and off-resonance) in less than 15 minutes. This technique is of particular relevance at low magnetic field where SNR and contrast are tied to long acquisition times. The combination of MRF with low field MRI scanners has great potential to revolutionize future transportable MRI systems.

References: [1] Sarraclanie M *et al.* ISMRM 2013 #5322; [2] Scheffler K *et al.* Eur Radiol 2003 13:2409-18; [3] Ma D *et al.* Nature 2013 495:187-193; [4] Perlin K *et al.* Comput Graphics 1985 19:287–296; [6] Tsai LL *et al.* JMR 2008; 193:174-85.

Acknowledgement: This research was supported by the Department of Defense, Defense Medical Research and Development Program, Applied Research and Advanced Technology Development Award W81XWH-11-2-0076 (DM09094).

Overhauser-enhanced MRI as a Non-invasive Probe of BBB Breakdown and Redox State in Stroke

Matthew S Rosen^{1,2,3}, Mathieu Sarraclanie^{1,2}, Brandon D. Armstrong^{1,2}, Fanny Herisson⁴, Najat Salameh^{1,2,5}, Cenk Ayata⁴

¹A. A. Martinos Center for Biomedical Imaging, Dept. of Radiology, Massachusetts General Hospital, Charlestown, MA, USA, ²Dept. of Physics, Harvard University, Cambridge, MA, USA, ³Harvard Medical School, Boston, MA, USA, ⁴Neurovascular Research Lab, Dept. of Radiology, Massachusetts General Hospital, Charlestown, MA, USA, ⁵Institut de Physique des Systèmes Biologiques, EPFL, Lausanne, Switzerland.

Acute reperfusion therapies have changed ischemic stroke care, but treatments are limited because of a short therapeutic window owing to the risk of reperfusion injury and hemorrhage. Detection of early and mild BBB disruption is an unmet need in acute stroke diagnosis [1] and although contrast from relaxation-based MRI contrast agents such as Gd-DTPA is correlated with hemorrhagic transformation of an infarct, it is not sensitive enough to probe more mild BBB disruption [2]. Overhauser-enhanced MRI (OMRI) is a promising technique for imaging free radicals, and a recently developed fast high-resolution OMRI methodology [3] offers new perspectives for the imaging of free radicals in living organisms. We describe here a method to probe hyperacute BBB breakdown following ischemic stroke using OMRI in conjunction with an injected stable free radical.

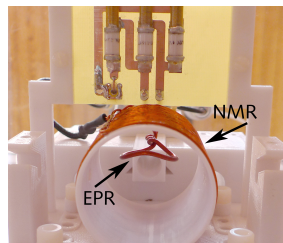


Figure 1: Probe for OMRI rat imaging at 6.5 mT: NMR@: 276 kHz, ESR@141 MHz.

TEMPOL (4-hydroxy-TEMPO) is detected by OMRI with very high sensitivity. In a normal physiological state, TEMPOL does not cross the BBB [4]. Because of its small size (172 Da) however, it may be able to cross the BBB under pathological circumstances associated with early BBB opening (e.g. ischemia), and act as an OMRI-detectable tracer. The use of TEMPOL as a small, exogenous OMRI agent would allow monitoring BBB disruption in stroke at the hyperacute stage, potentially much earlier than the traditional relaxation-based MRI contrast agents that rely on the leakage of larger molecules (such as Gd-DTPA) across the BBB.

A custom built, low-field 6.5 mT MRI scanner was used in these experiments [5]. 3D OMRI was performed using an optimized sequence based around b-SSFP as described in [3]. Sensitivity of b-SSFP-based OMRI to free radical concentration was performed using the NMR/ESR coil setup of [3] using vials containing TEMPOL in concentrations from 50 mM–2 mM, and a control containing only water. A rat model of cerebral ischemia/reperfusion was used to test the ability of our technique to detect injected TEMPOL free radicals crossing the BBB *in vivo*. *In vivo* experiments were performed using

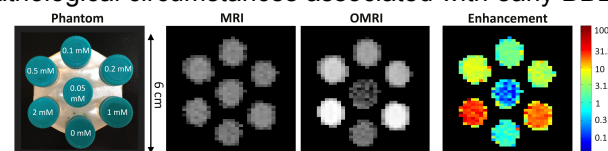


Figure 2: (left) Photo of TEMPOL concentration phantom All seven vials have very similar MRI magnitudes. OMRI demonstrates marked image-based free radical sensitivity.

with a single loop ESR coil inside a solenoid NMR coil (Figure 1). Under anesthesia, MCAO occlusion was performed in a 3 month old Wistar rat by insertion of filament via external carotid artery. Following 75 min MCAO and 60 min reperfusion, 3.6 μ l/gbw of 300 μ M TEMPOL was injected into the carotid artery after which the animal was sacrificed and OMRI imaging begun. The sensitivity of b-SSFP-based OMRI to free radical concentration is shown in Figure 2. The OMRI scan demonstrates marked image-based free radical sensitivity. The OMRI enhancement image is computed from the ratio of OMRI to MRI magnitude. *In vivo* OMRI signal enhancement in the frontal lobe and eye ipsilateral to the ischemic site is clearly visible in the OMRI images (Figure 3) following reperfusion. The phase of the OMRI image in Figure 3 provides sensitive contrast even in cases where the radical concentration is very low and the Overhauser enhancement may be small.

We have imaged TEMPOL at low concentrations with OMRI methods *in vitro*, and crossing the BBB following ischemia/reperfusion *in vivo*. The use of OMRI in conjunction with the stable free radical TEMPOL as an exogenously administered probe in hyperacute stroke is a new and novel approach, and this study suggests that TEMPOL may be a suitable probe for observing early BBB breakdown following reperfusion in rodent I/R models. Additionally, as TEMPOL reduction has been used as a functional probe to study redox status in tissue [6], we hypothesize that temporally resolved OMRI may be used to indicate the redox status of ischemic tissue.

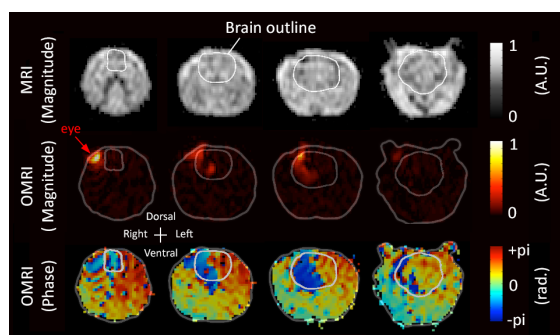


Figure 3: OMRI magnitude and phase images acquired from a rat at 6.5 mT following 75 min right MCAO and 60 min reperfusion. Four coronal slices from 10 slice data set shown. OMRI (NA=10) imaging time was 195 seconds. Low-resolution anatomical MRI (NA=80) was acquired in the OMRI scanner at 6.5 mT with DNP pulses disabled. MRI imaging time was 17 min. All images, voxel size: 1.1 x 1.6 x 8 mm³, TE/TR: 18/36 ms, Matrix: 128 x 35 x 10

References: (1) Pillai DR, *et al.* J Cereb Blood Flow Metab., 2009 Aug 5;29(11):1846–55 ; (2) Knight RA *et al.* J Cereb Blood Flow Metab. 2009; 29(5):1048–58 ; (3) Sarraclanie M *et al.* MRM 2013 DOI: 10.1002/mrm.24705 ; (4) Behringer W *et al.* J Cereb Blood Flow Metab. 2002 22(1):105–17 ; (5) Tsai LL *et al.* JMR, 2008 93(2):274–85 ; (6) Hyodo F *et al.* J Pharm Pharmacol.2008 60(8):1049–60.

Acknowledgements: This work supported by the Department of Defense, Defense Medical Research and Development Program, Applied Research and Advanced Technology Development Award W81XWH-11-2-0076 (DM09094).

High Speed 3D b-SSFP at 6.5 mTMathieu Sarraçanie^{1,2}, Brandon D. Armstrong^{1,2}, and Matthew S. Rosen^{1,2}¹Department of Physics, Harvard University, Cambridge, MA, United States, ²MGH/Martinos Center for Biomedical Imaging, Boston, MA, United States

Target audience: MR physicists and clinicians interested in performing fast 3D imaging at very-low magnetic field and on the design of high-performance purpose-built MRI systems.

Purpose

Without major innovation, high-field MRI instruments offer limited utility in field deployable and portable contexts. Our effort focuses on the high-risk and critical challenges that must be solved to enable deployment of transportable dedicated MRI systems. This includes the development of robust low-field scanner hardware methodologies, the development of state of the art high-speed imaging strategies and work on advanced adaptive reconstruction methods including navigators and sparse sampling. With the goal of demonstrating a proof-of-principle of a suite of techniques and technologies to advise future development of a field-deployable device with high diagnostic impact, the present work reports on the development of fast 3D imaging at very-low magnetic field (6.5 mT) using the intrinsic ¹H NMR signal and balanced steady state free precession (b-SSFP).

Methods

A very stable magnetic field is a critical element of the experiment as off-resonance effects can distort the image and cause severe banding artifacts [2]. A custom built, low-field MRI scanner with a bi-planar 6.5 mT electromagnet (B_0) and bi-planar gradients was used for all experiments and was previously described [1]. The system was upgraded and optimized for ¹H imaging resulting in improved B_0 stability, higher gradient slew rates, and lower overall noise. This effort included the use of an improved power supply (System 854T, Danfysik, Taastrup, Denmark) for the electromagnet with ± 1 ppm stability over 20 minutes and ± 2 ppm stability over 2 hours, and the addition of high-current shielded cables throughout the system. The scanner operates inside a double-screened enclosure (ETS-Lindgren, St. Louis, MO, USA) with a RF noise attenuation factor of 100 dB from 100 kHz to 1 GHz. The 3D imaging experiment was performed with Cartesian acquisition of k-space using b-SSFP. The sequence was set with TR/TE = 42/21 ms, acquisition matrix = 128×41×11, voxel size = 2.7×2.5×9 mm³, number of averages (NA) = 40. The readout duration was 7.04 ms with 9091 Hz bandwidth and total acquisition time was 12.6 min for fully sampled k-space.

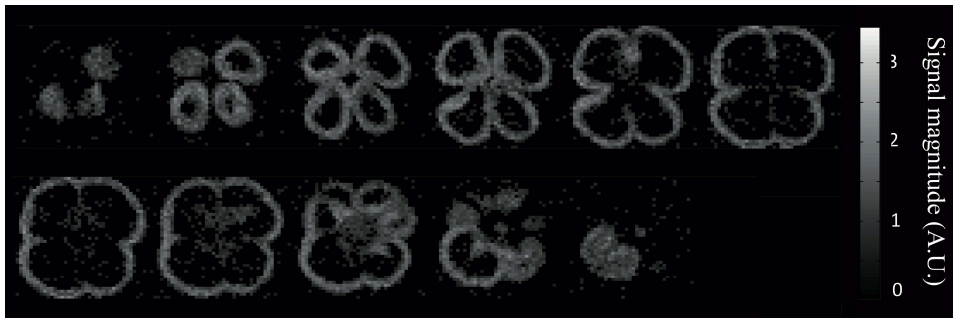


Figure 1: 11 slices of the imaged bell pepper at 6.5 mT with 2.7×2.5×9 mm³ resolution in 12.6 min.

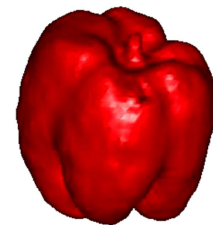


Figure 2: 3D rendered image of the bell pepper reconstructed from the acquired MRI dataset.

Results

Figure 1 shows the 11 slices of a bell pepper acquired using 3D b-SSFP with 2.7×2.5×9 mm³ resolution. Figure 2 shows a 3D rendered image of the reconstructed object.

Conclusion

3D imaging across a 10 cm diameter bell pepper with 2.7×2.5×9 mm³ voxel size was achieved within 13 min at 6.5 mT. This result is the first implementation of b-SSFP at very low magnetic field. The presented work overcomes the main limitations of working at low field, which typically results in poor SNR and prohibitively long acquisition times, by using a custom built optimized scanner with stable magnetic field B_0 and low overall noise that allows implementation of b-SSFP imaging. The use of undersampling strategies and compressed sensing reconstruction algorithms could further reduce the imaging time. We have recently shown that an undersampling rate of 70 % gives unperceivable reconstruction errors when compared with fully sampled data sets [3]. Thus, we expect the total acquisition time for the presented image to reach ~6 min and ~3 min with 50% and 70% undersampling respectively. The optimized bi-planar electromagnet combined with fast 3D imaging strategies and sparse sampling has potential to reach clinical standards for patient imaging and open new perspectives for a generation of low-cost, high-performance, and purpose-built imagers practical for operation in hospitals, battlefield medical facilities, or forward triage centers.

References: [1] Tsai LL *et al.* JMR 2008; 193: 174-85 ; [2] Scheffler K *et al.* Eur Radiol 2003;13:2409-18; [3] Sarraçanie M *et al.* MRM 2012; submitted.

Acknowledgement: This research was supported by the Department of Defense, Defense Medical Research and Development Program, Applied Research and Advanced Technology Development Award W81XWH-11-2-0076 (DM09094).

Parallel Imaging and Acceleration in the Johnson Noise Dominated Regime

Cristen D. LaPierre^{1,2}, Mathieu Sarraoane^{1,2}, Lawrence L. Wald^{1,3}, and Matthew S. Rosen^{1,2}

¹Department of Radiology, Mass General Hospital, A.A. Martinos Center for Biomedical Imaging, Charlestown, MA, United States, ²Department of Physics, Harvard University, Cambridge, MA, United States, ³Harvard-MIT Division of Health Sciences and Technology, Cambridge, MA, United States

Target Audience: Those interested in portable MRI, low field imaging, SENSE acceleration, and inductive coil and array construction at low magnetic fields.

Purpose: Low field imaging offers a potentially transportable and rapidly deployable human imaging system. Current research for low field human imaging is limited and generally uses superconducting quantum interference device (SQUID) sensors¹. At conventional magnetic field strengths body noise dominates, resulting in strongly correlated noise on each receive coil in the parallel array. At low field, uncorrelated Johnson noise dominates, providing a benefit to parallel imaging and accelerated imaging using SENSitivity Encoding (SENSE). The aim of this study was twofold. First, construct an eight-coil receive only array for 276 kHz. Second, acquire accelerated images using SENSE.

Methods: NMR parallel imaging at low frequency is a new regime; optimal parameters for inductive receive coils are unknown from the literature. Three design parameters were identified: diameter, wire gauge and number of turns. Parameters were selected using a fractional factorial design at the factor levels indicated in Table 1. Only circular coils were tested.

Once optimal parameters were determined an 8 channel receive-only 276 kHz ring array was constructed. Imaging of 13.1 cm diameter phantoms filled with 0.04% Gadolinium doped saline (0.9% NaCl) was performed in a previously described² custom built very-low field MRI scanner with a 6.5 mT biplanar electromagnet and biplanar gradients and eight receive channels. A 3D balanced Steady State Free Precession (b-SSFP) sequence with full Cartesian acquisition of k-space was applied over five 20 mm thick slices, with FOV=225×160×100 mm³, acquisition matrix=64×64×5, TE/TR=12/23 ms, number of averages (NA)=150. Image reconstruction was performed with a sum-of-squares method³.

1D SENSE reconstruction (reduction factor R=2) was simulated on the middle slice of the fully sampled image using in-house code previously developed in our lab. The noise covariance matrix and coil sensitivity maps were estimated from the data.

Finally, the corresponding experiment (R=2) was performed from a structured phantom. Noise data were acquired using a b-SSFP sequence with RF transmission disabled (sequence time = 704s). Sensitivity maps were estimated from the fully sampled data set acquired previously using third-order polynomial smoothing. Aliased images were unfolded using a modified version of the simulation code.

Gauge (AWG)	14 cm		Number of Turns					
	8 cm		Number of Turns					
			3	10	20	30	50	100
20			+	+	+		+	
24				+		+		+
28							+	+

Table 1. Fractional factorial design for determining optimal coil design. Parameters tested were number of turns, size of wire and diameter of coil.



Figure 1. 8 channel receive only 6.5 mT parallel imaging array.

Results: Optimal coil design parameters were identified as 8 cm diameter, 24 gage and 30 turns. An 8 channel receive only array with an inner diameter of 15.6 cm was built (Figure 1). Geometric decoupling between

neighbors was -38 dB or less for nearest neighbors and -11dB or less for next nearest neighbors. Figure 2 shows the design of the structured phantom (2a), as well as the reconstructed image of the structured phantom (2b) and a homogeneous phantom (2c) acquired with the 8 channel array. Figure 3 shows the noise covariance matrix (3a) and the correlation coefficient matrix (3b) of the array. Figure 4 shows the results of simulated (left) and actual (right)

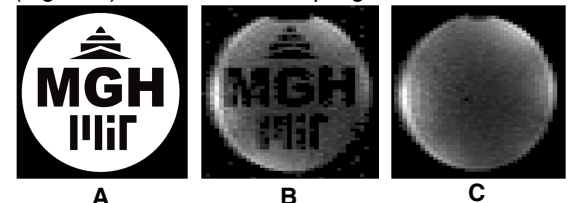


Figure 2. Phantom pattern (A), reconstruction of structured phantom (NA=150, B) and reconstruction of homogeneous phantom (NA=200, C). Images are masked to the phantom.

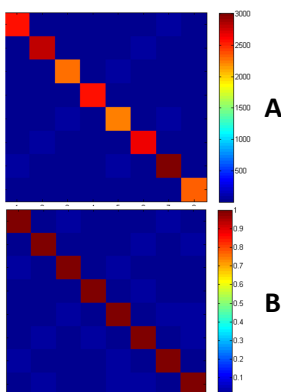


Figure 4. Noise covariance (A) and correlation coefficient (B) matrices.

SENSE reconstructed images.

Discussion: Due to low thermal signal, low field imaging requires signal averaging, increasing scan time. With the eight channel array, SENSE acceleration can be implemented, reducing scan time by at least a factor of 2. The negligible noise correlation between channels benefits this approach.

Conclusions: These results represent the first parallel and SENSE reduction images attained in the Johnson noise dominated regime. Development of parallel imaging and SENSE acceleration are important steps toward human imaging at very-low field. Future work will optimize the sequence to further improve image quality. Additional array designs will be tested and SENSE combined with random undersampling strategies will be investigated.

Acknowledgements: The authors would like to thank Jonathan Polimeni for his guidance on parallel imaging and Fa-Hsuan Lin for making available his SENSE reconstruction code.

Financial Disclosure: This research was supported by the Department of Defense, Defense Medical Research and

Development Program, Applied Research and Advanced Technology Development Award W81XWH-11-2-0076 (DM09094).

References: 1. Zotev VS, et al. JMR. Jun 2008;192(2):197-208

2. Tsai LL, et al. JMR. Aug 2008;193(2): 274-85

3. Roemer PB, et al. MRM. Nov 1990;16(2):192-225

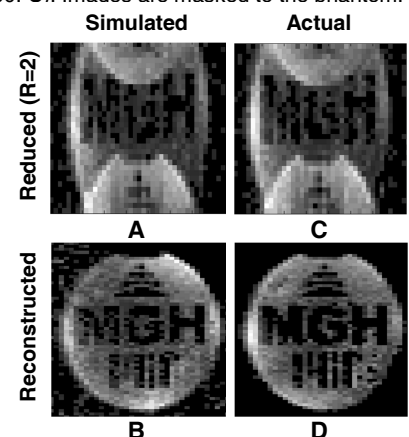


Figure 3. Simulated (A,B) and actual (C,D) results for SENSE reconstruction. Images are masked to the phantom.

Clarissa Zimmerman Cooley^{1,2}, Jason P Stockmann^{2,3}, Brandon D Armstrong^{2,3}, Matthew S Rosen^{2,3}, and Lawrence L Wald^{2,4}

¹Electrical Engineering, Massachusetts Institute of Technology, Cambridge, MA, United States, ²Athinoula A. Martinos Center for Biomedical Imaging, Department of Radiology, Massachusetts General Hospital, Charlestown, MA, United States, ³Department of Physics, Harvard University, Cambridge, MA, United States, ⁴Department of Radiology, Massachusetts General Hospital, Harvard Medical School, Boston, MA, United States

PURPOSE: We constructed and tested a portable permanent magnet based brain MRI scanner suitable for operation in an ambulance, battle field, sports arena, or at the patient's bedside. Our goal is to allow emergency medical teams to assess brain hemorrhage from surgical complications, traumatic brain injury or stroke to accelerate care to those requiring it. The system eliminates the need for gradient coils thru a novel encoding method which rotates the B_0 field inhomogeneity pattern of the lightweight permanent magnet creating generalized projections similar to O-Space¹ or PatLoc² encoding. We show experimental 2D, proof-of concept images, and discuss generalization to 3D.

METHODS: A 45 kg (36cm dia. 36cm length) Halbach cylinder magnet was built with NdFeB magnets (Fig. 1a)^{3,4}. The center field is 77 mT (3.285 MHz) with about 1 mT (43 kHz) field variation in the center slice FOV of 16 cm. The magnet's encoding field has a roughly hyperbolic multipolar shape (Fig. 1b) that is physically rotated around the phantom during data collection. Because the encoding field cannot be switched, a spin echo sequence is used for radiofrequency refocusing of the spins, forming a projection of the phantom at each rotation. The field maps are measured and used as prior knowledge to construct the encoding matrix. Data is collected on a TecMag Apollo spectrometer with a 250 W Tomco RF amplifier and the image is reconstructed using the iterative algebraic reconstruction technique (ART)⁵.

Accurate field maps at each rotation are critical to image reconstruction. A single row of 8 solenoidal field-probes each holding a 1-mm water-filled capillary doped with copper sulfate ($T_1=100$ ms) are used to collect field information as the magnet is rotated. The field measurements are fit using polynomial basis functions (Fig 1b). The lack of magnet shielding exposes our encoding field to external fields, the most significant being the earth's field which adds vectorially to the encoding field. This is explicitly corrected for when calculating the encoding matrix. Other external fields and magnet field drift ($\sim 1/2G/^\circ C$)⁶ are measured using an MR field probe fixed to the magnet and also incorporated into the reconstruction.

For proof of concept, imaging phantoms were made using two 1" balls of doped water (Fig. 3a and 3e). In one experiment high SNR was achieved by directly winding the TR coil around the balls of water. In another experiment we used a volume Tx coil and an array of 4x 6.5cm dia. loop coils for Rx. In both case short, high power excitation pulses (125 W for a 40 μ s refocusing pulse) were necessary to cover the bandwidth of the encoding field.

RESULTS: Fig. 2 shows an example set of rotated field maps and the corresponding projections from the phantom. Fig. 3b is the reconstructed image of the same phantom using the Rx single coil. The data consisted of 128-average spin echoes with TR/TE = 200ms/9.4ms and 40 kHz readout bandwidth. Eighty projection angles were used. Fig. 3c shows the same reconstructed phantom imaged using 4 surface coils, 24 projections angles, 256 averages, and TR/TE = 200ms/20.4ms. Fig. 3d shows a simulated reconstruction with the same parameters as Fig. 3c. Fig. 3f and 3g show the experimental and simulated single coil image from the phantom in Fig. 3e (w/ 128 averages of 35 projection angles). Unlike the first phantom, there is a ball in the center of the encoding field.

DISCUSSION: Blurring throughout the image is greatly improved by the external field and temperature drift corrections, but some obvious artifacts remain. In Fig. 2b, the balls are located in the top half of the phantom, but we clearly see aliasing in the reconstructed images. This is expected because of the non-bijectionality of the encoding field¹. The problem is resolved in Fig. 2c-d, in which the coil sensitivities from a 4 channel coil array are used to remove the ambiguity between frequency-matched isocontours in different quadrants. Blurring in the center is seen in Fig. 3f-g. Similar to Patloc imaging, the resolution of the images is lowest in the center because of the low field variation in that area. We propose shifting the encoding field off-center from the rotation axis (using shims) to address this, similar to O-Space imaging².

CONCLUSION: These initial images and simulations are a 2D proof of concept for imaging in a rotating inhomogeneous field without additional gradient coils. Reconstruction would be simpler if the magnet was RF shielded and if the temperature was painstakingly regulated.

However, this would limit portability of the system, and we have shown that these inconveniences can be mitigated by careful field calibration before imaging and field drift monitoring during imaging. Future work will include the use of Transmit Array Spatial Encoding (TRASE)⁷ for slice localization in the longitudinal direction to enable 3D imaging.

REFERENCES: (1) Schultz G, IEEE Trans Med Imag 2011. (2) Stockmann, MRM 2010. (3) Zimmerman C ISMRM 2012. (4) Halbach K, Nucl Instr Meth 1980. (5) Herman G, Comp. Biol. Med. 1976. (6) Campbell P, Permanent Magnet Materials & their Application, 1994. (7) Sharp J, MRM 2010. **ACKNOWLEDGMENTS:** The authors thank C Lapierre, M Saracanie, J Blau, and E Siskind for their help. Support by DoD/USAMRRA W81XWH-11-2-0076 (DM09094).

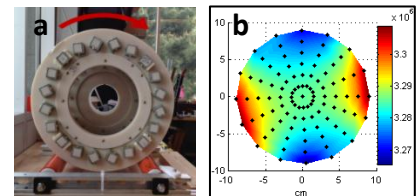


Figure 1: (a) magnet on high friction rollers, (b) interpolated field map in Hz, black dots are the field probe positions

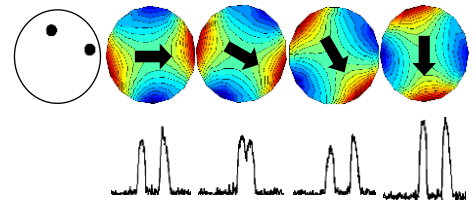


Figure 2: Six representative encoding field rotations and experimental projections of phantom on left. (1 coil, 128 averages, SNR ~ 30). Arrow is B_0 direction.

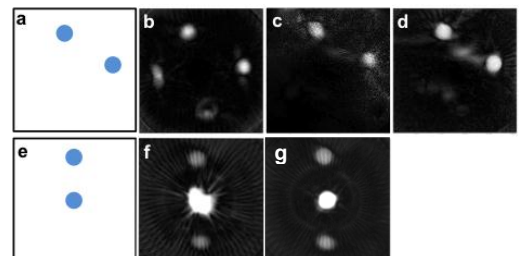


Figure 3: (a) ground truth phantom 1, (b) 80 projections of phantom 1 using one solenoid receive coil (c) 24 projections of phantom 1 using 4 receive coils, (d) simulated version of Fig. 3c, (e) ground truth phantom 2, (f) 35 projections of phantom 2 using one coil, (g) simulated version of Fig. 3f. Field of view is 16 cm in all images.

Flexible spatial encoding strategies using rotating multipolar fields for unconventional MRI applications

J. P. Stockmann^{1,2}, C. Z. Cooley³, M. S. Rosen^{1,2}, L. L. Wald¹¹Massachusetts General Hospital, Charlestown, MA²Department of Physics, Harvard University, Cambridge, MA³Department of Electrical Engineering, Massachusetts Institute of Technology, Cambridge, MA

PURPOSE: Our goal is to perform flexible MR imaging with rotating nonlinear spatial encoding magnetic (SEM) fields, removing constraints on hardware design, and reducing the cost, complexity, and weight of imaging systems. By shifting the burden away from hardware performance and toward computer power in the form of generalized reconstruction algorithms, we open the door to unconventional MR imaging systems for applications where spatially-varying resolution can be tolerated. Several encoding strategies using quadratic and nonlinear SEMs have recently been proposed as a way to accelerate parallel imaging and reduce peripheral nerve stimulation during field switching [1-3]. Common to all higher-order encoding methods is the problem of aliasing due to redundant frequency contours (causing a non-bijective mapping), which can be resolved using additional spatial encoding from local RF receive coils. Another issue is the flatness of higher-order SEMs at the center of the FOV, where encoding can only be achieved through the addition of linear SEMs. The present work builds on these approaches by assessing the encoding of a rotating SEM (wrt the object), with and without parallel imaging and a spatial offset between the axis of rotation and the axis of field symmetry, breaking the symmetry of the SEM within the FOV.

METHODS: We simulate imaging performance with a nonlinear SEM comprised primarily of second-order spherical harmonics with some additional higher-order terms (Fig. 1). To break the symmetry of the field by shifting it off-center, we also simulate the SEM with the addition of a linear field component (2000 Hz/cm or 3000 Hz/cm). We further simulate the use of multi-channel RF receive coils to remove aliasing. Approximate RF coil sensitivities for an 8-channel loop array are calculated using the Biot-Savart law (Fig. 2). Field maps of the SEM at each rotation angle as well as the coil sensitivities are used to build the encoding matrix. A GRE transverse brain slice acquired on a 3T scanner is used to generate the simulated data. The simulated readout duration is 7 ms with a 36 kHz bandwidth (Nyquist sampled). Reconstruction is performed using the algebraic reconstruction technique (ART) [4], which cycles through the encoding matrix one row at a time, back-projecting the data point corresponding to each row (Fig. 3). The algorithm iterates until convergence is achieved.

RESULTS: The spatially-varying resolution of the two SEMs can be visualized by looking at overlaid frequency isocontours of each SEM as it is rotated over the range of encoding angles (Fig. 4). Even with the non-ideal encoding fields used here, much of the detail in the object is retained in the reconstructions (Fig. 5). As expected, a linear offset SEM recovers resolution, though some detail is still lost at the center. Surface coils are effective in reducing aliasing artifacts and also in improving resolution, particularly when no field offset is used.

DISCUSSION: All SEMs can be approximated with linear combinations of spherical harmonics. The geometric similarity of a multipolar harmonic implies that unique projections of the object can be obtained using only a limited range of rotation angles [1]. For SEMs without a significant linear term, the range of rotation angles is $180^\circ/N$, where N is the order of the dominant SEM. For the multipolar SEM case considered here, the dominant components are the second-order harmonics XY and X^2-Y^2 , hence the SEM is rotated over 90° . However, when the multipolar symmetry of the field is broken by the addition of a linear term, unique projections of the object can be acquired over 360° , similar to O-Space imaging. The linear term shifts the symmetry point away from the rotation axis, improving image resolution near the center of the FOV, as shown in Fig. 5.

CONCLUSION: Flexible reconstruction methods relax the need for a homogenous B_0 field and linear gradient fields, as illustrated here using a single rotated multipolar SEM. This permits unconventional encoding strategies and MR imaging systems in applications that do not require isotropic resolution. Performance gains are achieved by breaking the symmetry of SEMs using multiple receive coils and/or a linear field offset. Future work will generalize the approach to three dimensions, possibly through curvilinear slice selection [5]. A total generalized variation prior [6] will also be used to help suppress streaking artifacts for highly undersampled data. **REFERENCES:** [1] Schultz G, TMI 2011. [2] Stockmann JP, MRM 2010. [3] Gallichan D, MRM 2011. [4] Kaczmarz S, Bull. Acad. Polon. Sci. Lett. A, 1937. [5] Weber, MRM 2012. [6] Knoll F, MRM 2012. **ACKNOWLEDGEMENTS:** Grant support DoD/USAMRRA W81XWH-11-2-0076 (DM09094).

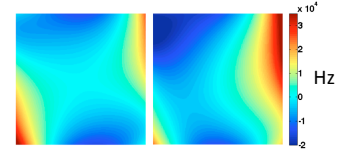


Fig. 1 Example SEM field dominated by second-order terms (left). In order to provide spatial encoding at the center of the FOV, the SEM is offset using a linear component (a 2000 Hz/cm offset is shown here).

Fig. 2 Encircling array of 8 RF receive coils used to remove aliasing caused by the non-bijectivity of the multipolar SEM.

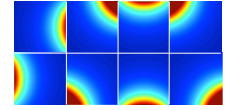


Fig. 3 ART backprojects the i_n^{th} row of encoding matrix E weighted so as to achieve consistency between data vector s and image m . The rate of convergence is controlled by λ .

$$\hat{m}^{(n+1)} = \hat{m}^{(n)} + \lambda \frac{s_{i_n} - \langle E_{i_n}, \hat{m}^{(n)} \rangle}{\|E_{i_n}\|^2} E_{i_n}^*$$

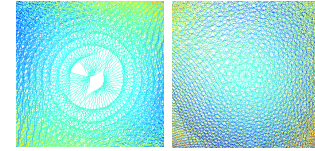


Fig. 4 Spatially-varying resolution illustrated qualitatively by the density of overlapping frequency isocontours from 16 rotations of the SEMs in Fig. 1. Isocontours are plotted with 1 kHz separation. The symmetric SEM (left) rotates over 90° while the offset SEM rotates over 360° and provides smaller voxel sizes in the center.

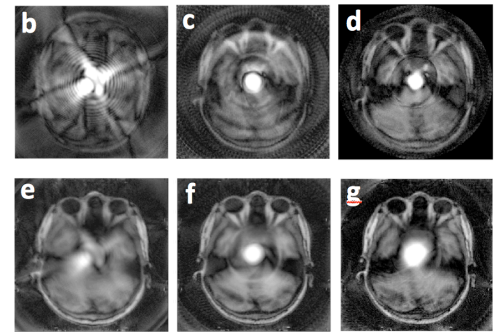


Fig. 5 Simulated 256×256 reconstructions of reference brain image (a) encoded using 128 projections by SEMs with no offset (a), 2000 Hz/cm offset (b), and 3000 Hz/cm (c) with no coil encoding. The offset removes most of the aliasing associated with the symmetry of the multipolar SEM and also recovers some resolution near the center. The addition of 8 receive coils for each case (e-g) improves resolution and removes aliasing, though resolution remains better near the periphery. FOV is 28 cm.

High Speed 3D Overhauser-Enhanced MRI using combined b-SSFP and Compressed SensingBrandon Dean Armstrong^{1,2}, Mathieu Sarraclanie^{1,2}, Jason Stockmann^{1,2}, and Matthew Rosen^{1,2}¹Physics, Harvard University, Cambridge, MA, United States, ²Martinos Center for Biomedical Imaging, Boston, MA, United States**Target Audience:** Free radical imaging, hyper-polarization, MR method development and hardware**Purpose**

Free radical imaging has been used to investigate physiological processes such as pO₂ mapping and to monitor the distribution and metabolism of free radicals in organs under oxidative stress. We present a new pulse sequence for rapid 3D imaging of free radicals using Overhauser-enhanced MRI (OMRI). In contrast to other OMRI methods that use a time consuming pre-polarization Overhauser irradiation step, the sequence presented here embeds the EPR pulses into the phase encode step of a balanced steady state free precession sequence (b-SSFP), greatly reducing the acquisition time. A further increase in temporal resolution is gained by undersampling of k-space and using compressed sensing reconstruction. This new OMRI sequence enables both improved spatial and temporal resolution of free radical distribution than other techniques.

Methods

Experiments were performed in a custom built, 6.5 mT, bi-planar electromagnet with bi-planar gradients. A 7 cm OD, 13 cm long Alderman-Grant coil was used to saturate the 140.8 MHz electron spin resonance of the nitroxide radical 4-hydroxy-TEMPO. The EPR coil was placed inside a 10 cm OD, 16 cm long solenoid coil for ¹H NMR excitation and detection. The EPR irradiation pulses were embedded into the phase encode and rewind steps of a fully balanced SSFP sequence as shown in Figure 1. 3D printed polycarbonate pieces 5.4 cm in diameter were used as a phantom (Figure 2a) with 2.5 mM TEMPO solution in water. Pieces were designed to evaluate the ability to resolve small feature in 3 dimensions. Image parameters were: matrix = 256x64x32, voxel size = 1x1x3.5mm, TR/TE = 54/27 ms, $\alpha = 90^\circ$, 70% undersampling rate, acquisition time = 65 s.

Results

Figure 2a) shows two segments of our phantom with the corresponding images in Figure 2b). The under-sampled data accurately reproduces the object, including the 1 mm diameter holes and 1 mm spacer. To confirm that this new sequence with imbedded EPR pulses is still a steady-state sequence, the sequence was run with only the read gradient while the echo amplitude was measured. After an initial buildup of polarization due to T₁, the signal reaches a steady-state amplitude that is ~ 30X larger than without embedded EPR pulses.

Conclusion

Embedding electron spin saturation into the phase encode step allows the use of a traditional b-SSFP sequence with no additional timings added. This is the first source of acceleration compared to traditional OMRI sequences that have a pre-polarization step of order T₁ before acquiring several lines of k-space. Further, for the phantom imaged here, only 30% of k-space is necessary to faithfully reproduce the image, reducing the acquisition time by a factor of 3. This technique will improve our ability to monitor physiological processes involving free radicals as the distribution of radicals can be tracked with greater spatial and temporal resolution.

Acknowledgement: Funded by DoD, Defense Medical Research and Development Program, Applied and Advanced Technology Development Award W81XWH-11-2-0076 (DM09094).

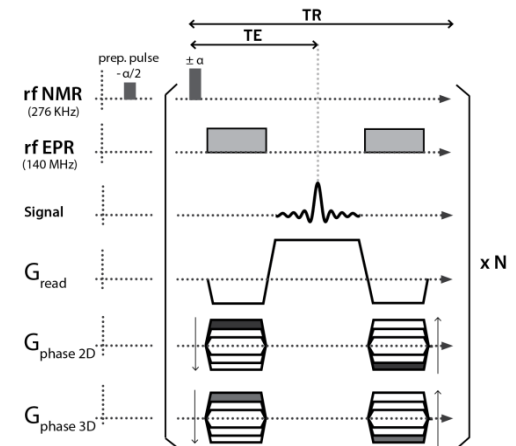


Figure 1. The 3D b-SSFP sequence with embedded EPR pulses.

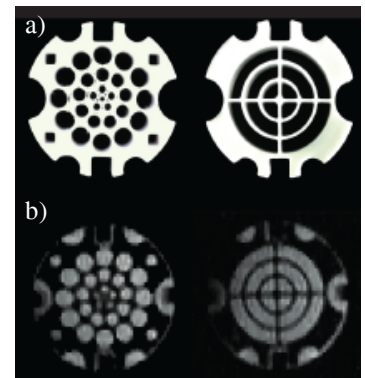


Figure 2. 2 slices from an OMRI image at 6.5 mT with 1x1x3.5 mm resolution over a 200 cm³ sample in 65 s. Phantom is 5.4 cm in diameter.

High Speed 3D Overhauser-Enhanced MRI Using Combined b-SSFP and Compressed Sensing

Mathieu Sarraclanie,^{1,2} Brandon D. Armstrong,^{1,2} Jason Stockmann,^{1,2} and Matthew S. Rosen^{1,2,3*}

Purpose: Overhauser-enhanced MRI is a promising technique for imaging the distribution and dynamics of free radicals. A key challenge for Overhauser-enhanced MRI is attaining high spatial and temporal resolution while simultaneously limiting resonator and sample heating due to the long, high power radio-frequency pulses needed to saturate the electron resonance.

Methods: The approach presented here embeds EPR pulses within a balanced steady state free precession sequence. Unlike other Overhauser-enhanced MRI methods, no separate Overhauser prepolarization step is required. This steady-state approach also eliminates the problem of time-varying Overhauser-enhanced signal and provides constant polarization in the sample during the acquisition. A further increase in temporal resolution was achieved by incorporating undersampled k-space strategies and compressed sensing reconstruction.

Results: We demonstrate $1 \times 2 \times 3.5 \text{ mm}^3$ resolution at 6.5 mT across a $54 \times 54 \times 110 \text{ mm}^3$ sample in 33 s while sampling 30% of k-space.

Conclusion: The work presented here overcomes the main limitations of Overhauser enhanced MRI as previously described in the literature, drastically improving speed and resolution, and enabling new opportunities for the measurement of free radicals in living organisms, and for the study of dynamic processes such as metabolism and flow. *Magn Reson Med* 71:735–745, 2014. © 2013 Wiley Periodicals, Inc.

Key words: 3D Overhauser MRI; free radicals; EPR; b-SSFP; compressed sensing

Imaging of free radicals has been used to investigate a number of important physiological processes such as the mapping of pO_2 (1–3), free radical distribution and metabolism (4–7), molecular imaging (8), and to monitor changes in local viscosity (9,10). Magnetic resonance

imaging (MRI) is a powerful and noninvasive tool that provides excellent anatomical detail. However, MRI is sensitive to nuclear spins (typically ^1H of water) and cannot alone reveal spatial information about the distribution of free radical species. EPR imaging (11–17) reveals the spatial distribution of unpaired electron spins, but requires a separate reference MRI to determine where the free radicals are located within the sample. While EPR imaging is a sensitive technique, images have poor resolution due to broad EPR lines, and are usually time-inefficient due to the usual CW acquisition strategy. Overhauser-enhanced MRI (18–23; OMRI, also known as proton-electron double resonance imaging) exploits the dipolar coupling between the unpaired electron of the free radical and the ^1H nuclei of water to increase nuclear magnetization via dynamic nuclear polarization (DNP) and subsequently images the enhanced nuclear spin polarization with MRI. OMRI provides an excellent way to image free radical species as narrow NMR line widths enable imaging using reasonable-strength encoding gradients. OMRI also benefits from the ability to use traditional MRI sequences, though specialized hardware is needed to drive the electron spin resonance, and the sequences must be modified to allow for EPR saturation pulses.

A difficulty of OMRI is the need for high power radio-frequency (RF) to saturate the electron spins. Additionally, as EPR frequencies are two orders of magnitude higher than ^1H frequencies, a high frequency resonator is required, and this leads to high specific absorption rate (SAR) and limited penetration depth. For these reasons, OMRI is usually performed at a low- to intermediate magnetic field (5,22,24) or in a field-cycled setup (4,25). A typical field-cycled OMRI experiment begins at very low magnetic field ($\sim 5 \text{ mT}$) where EPR irradiation is applied for approximately the nuclear T_1 of the sample at the irradiation magnetic field. The magnetic field is then quickly ramped up to the imaging field and a line or plane of k-space data is acquired. The magnetic field is then ramped down for EPR irradiation and repolarization because the DNP signal decays with the ^1H nuclear T_1 . Field-cycled OMRI helps to overcome both the hardware and penetration depth challenges by reducing the EPR frequency, but these experiments are much slower and more complex than traditional MRI due to the need to refresh the DNP-enhanced signal many times over the acquisition time.

We present here a new method for 3D OMRI based on b-SSFP at a constant field of 6.5 mT that provides up to 7-fold acceleration compared to the fastest OMRI sequence reported in the literature (24). We further

¹Department of Physics, Harvard University, Cambridge, Massachusetts, USA.

²Department of Radiology, A.A. Martinos Center for Biomedical Imaging, Massachusetts General Hospital, Boston, Massachusetts, USA.

³Department of Radiology, Harvard Medical School, Boston, Massachusetts, USA.

Grant sponsor: Department of Defense, Defense Medical Research and Development Program, Applied Research and Advanced Technology Development Award; Grant number: W81XWH-11-2-0076 (DM09094).

*Correspondence to: Matthew S. Rosen, Ph.D., Low Field MRI and Hyperpolarized Media Laboratory, A. A. Martinos Center for Biomedical Imaging, 149 13th Street, Suite 2301, Charlestown, MA 02129, USA.

E-mail: mrosen@cfa.harvard.edu

Received 30 October 2012; revised 11 January 2013; accepted 7 February 2013.

DOI 10.1002/mrm.24705

Published online 8 March 2013 in Wiley Online Library (wileyonlinelibrary.com).

© 2013 Wiley Periodicals, Inc.

maintain the high acquisition efficiency of b-SSFP by applying the Overhauser saturation pulses during the phase encode step, eliminating the time-consuming pre-irradiation step done in all previously reported OMRI. Additionally, we add undersampling strategies and compressed sensing (CS) techniques to increase the temporal resolution while also reducing the total number of EPR RF pulses. We obtain $1 \times 2 \times 3.5 \text{ mm}^3$ resolution on a $54 \times 54 \times 110 \text{ mm}^3$ sample in 33 s. We show that a steady-state signal is still achieved with this new OMRI b-SSFP sequence, and that simulations with no free parameters agree very well with the experimental results.

METHODS

OMRI Setup

A custom built, low-field MRI scanner with a biplanar 6.5 mT electromagnet (B_0) and biplanar gradients was used for all experiments and was previously described (26) (Fig. 1a). The system was upgraded and optimized for ^1H imaging for this work resulting in improved B_0 stability, higher gradient slew rates, and lower overall noise. This effort included the use of an improved power supply (System 854T, Danfysik, Taastrup, Denmark) for the electromagnet with ± 1 ppm stability over 20 min and ± 2 ppm stability over 8 h, and the addition of high-current shielded cables throughout the system. The

scanner operates inside a double-screened enclosure (ETS-Lindgren, St. Louis, MO) with a RF noise attenuation factor of 100 dB from 100 kHz to 1 GHz.

The transfer of electron spin polarization to dipolar or scalar coupled nuclear spins via the Overhauser effect requires high power irradiation of the electron spin resonance (27,28). A 7 cm OD, 13 cm long Alderman-Grant coil (29,30; Fig. 1b) with guard rings to reduce sample heating was used to saturate the electron spin resonance of the nitroxide radical 4-hydroxy TEMPO (Sigma-Aldrich, St. Louis, MO). The electron spin resonance is split into three transitions by the hyperfine coupling of the spin 1 ^{14}N nucleus (at 6.5 mT, there still exist other transitions described by the Breit-Rabi equations but their transition probabilities are small and ignored here; 31). As SAR scales with ω^2 (32–36) the EPR coil was tuned to the low energy transition of 140.8 MHz to minimize SAR. The EPR coil was placed inside a 10 cm OD, 16 cm long solenoid coil used for NMR excitation and detection at 276 kHz (Fig. 1c). The coils were oriented such that their B_1 fields were perpendicular to each other and to B_0 . Placing the NMR coil outside the ESR coil sacrifices NMR filling factor to gain larger B_1 for electron spin saturation as our DNP signal enhancement (defined as $\langle I_z \rangle / I_0$ where I_0 is the thermal equilibrium NMR signal and $\langle I_z \rangle$ is the DNP signal) is limited by the available RF power.

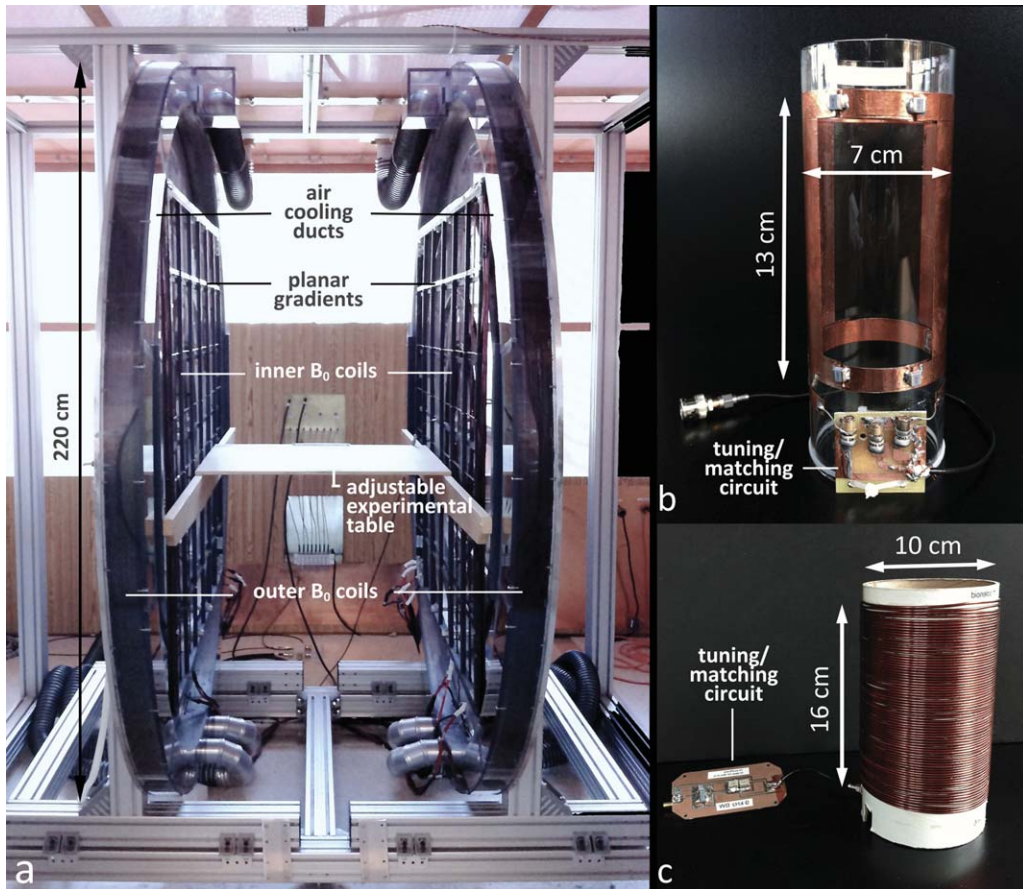


FIG. 1. OMRI setup. Photographs of (a) the custom built 6.5 mT MR scanner with bi-planar electromagnet and gradient set inside the shielded room, (b) the EPR (141 MHz), and (c) NMR (276 kHz) coils used for the OMRI experiments.

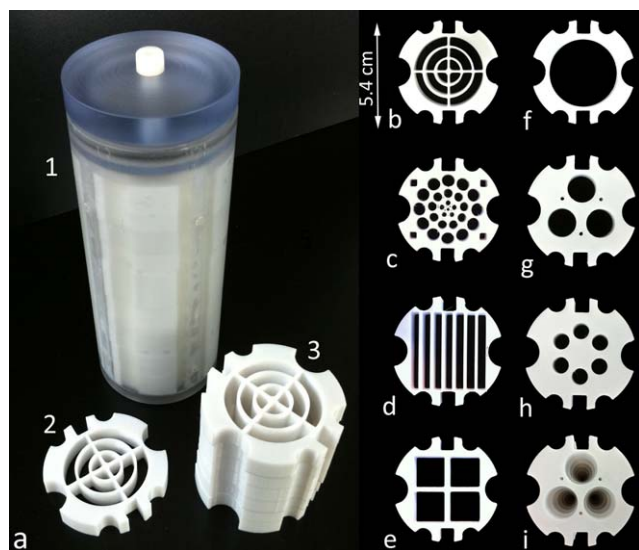


FIG. 2. Photograph of (a1) the assembled OMRI phantom, (a2) a 10 mm thick internal piece, and (a3) a stack of internal pieces. Shown in (b-h) are individual pieces of the phantom in configuration 1 (f-h) and configuration 2 (b-e). A top view of the stacked pieces for the phantom in configuration 1 as described in the text is shown in (i). [Color figure can be viewed in the online issue, which is available at wileyonlinelibrary.com.]

A Redstone NMR console (Tecmag, Houston, TX) was used for data acquisition and controlled the gradients and RF channels. The console has two transmit channels allowing for both NMR and EPR irradiation. A 100 W, CW amplifier (BT00100-DeltaB-CW) was used for EPR saturation and a 500 W pulsed amplifier (BT00500-AlphaS) was used for NMR (from both Tomco Technologies, Stepney, Australia).

Phantom Design

A configurable imaging phantom was built for these experiments. Various pieces designed to demonstrate resolution in three dimensions and test the ability to resolve sharp edges in under-sampled k-space were 3D printed in polycarbonate on a Fortus 360 mc (StrataSys, Eden Prairie, MN). The 3D printed pieces were stacked inside a 5.5 cm ID, 13 cm long machined polycarbonate cylinder. The advantage of this phantom is the flexibility to design and 3D print any desired structure for a particular experiment. The cylinder was then filled with 250 mL of 2.5 mM 4-hydroxy TEMPO solution in water, and a leak-tight polycarbonate cap inserted. The assembled phantom and individual pieces are shown in Figure 2. Imaging experiments were performed in two different phantom stacking configurations. The first stacked geometry consists of two interlocking sets of a trio of step-wise-smooth cones and was used to evaluate the 3D character of the sequence and the minimum structure sizes that can be resolved for round-shaped objects (Fig. 2f-i). The second configuration used more complex structures with finer details to assess the sequence performance, ability to resolve small in-plane structures, and the results of undersampling on sharp edges (Fig. 2b-e). Fiber optic temperature probes (Luxtron,

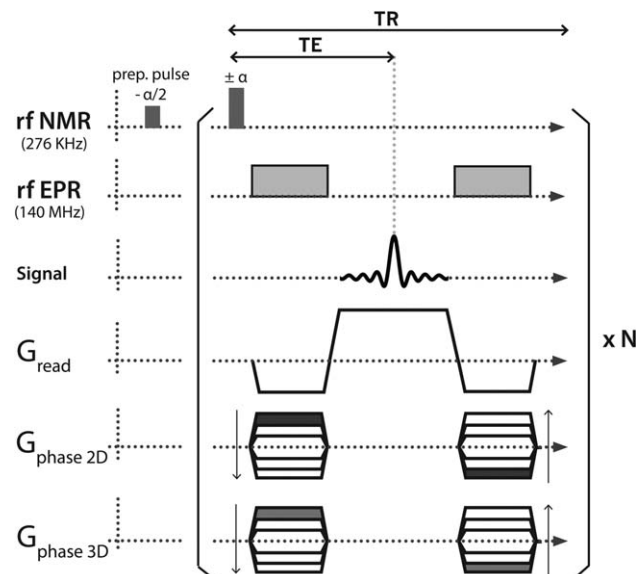


FIG. 3. Diagram of the 3D b-SSFP sequence with embedded EPR pulses (rf EPR). N is the total number of TRs in the sequence.

LumaSense Technologies, Santa Clara, CA) were placed inside the phantom and near a ring capacitor on the EPR coil during tests of the imaging sequence to monitor sample and coil temperatures.

3D Balanced SSFP with DNP

The pulse sequence used is shown in Figure 3. It is important to note that there is no separate EPR saturation step unlike all OMRI sequences reported in the literature. The sequence is a b-SSFP sequence with the addition of EPR (Overhauser) irradiation during the balanced phase encode gradients. The b-SSFP excitation train consists of an initial $-\alpha/2$ preparation pulse immediately followed by a train of alternating $\pm\alpha$ excitation pulses as previously described by Sheffler and Lehnardt (37). The $\pm\alpha$ pulses are separated by TR and the time interval between the $-\alpha/2$ preparation pulse and the first α pulse was set to 2 μ s. The main benefit of using a preparation pulse is that it prevents large fluctuations of the pre-steady state signal that would produce image artifacts and thus could not be used for signal acquisition (37). In b-SSFP, the optimal flip angle α is given by $\cos(\alpha) = \frac{T_1/T_2 - 1}{T_1/T_2 + 1}$ (37). T_1 and T_2 in our phantom were measured to be 545 ms and 488 ms, respectively, which leads to an optimal flip angle of $\alpha \sim 90^\circ$.

Bloch simulations were performed for a sequence without phase gradients (i.e., at the center of k-space), both with- and without EPR irradiation to model the buildup and time course of transverse magnetization as well as the signal enhancement provided by DNP. The simulations were run in MATLAB (MathWorks, Natick, MA) using code written in-house. Input parameters to the simulations were the measured T_1 and T_2 relaxation times, the measured enhancement provided by DNP with a 1.5 s EPR pulse ($\sim 3 \times {}^1\text{H } T_1$) in a 1D spectroscopy experiment (-44.5 fold enhancement), $\text{TR}/\text{TE} = 54/27$ ms and $\alpha = 90^\circ$. This negative enhancement results from

Overhauser DNP pumping into the opposite spin nuclear ground state compared with the Boltzmann case. This sign is important for the simulations. OMRI experiments with these parameters, a total bandwidth $BW = 9091$ Hz, and a 71 Hz bandwidth per pixel, were run and compared with the simulations.

The 3D imaging experiment was performed initially with full Cartesian acquisition of k-space. The sequence was set with $TR/TE = 54/27$ ms, a $256 \times 64 \times 112$ mm³ field of view, and acquisition matrix of $128 \times 64 \times 32$, resulting in a $2 \times 1 \times 3.5$ mm³ voxel size. The balanced phase gradient durations were both set to 20 ms to reach the desired in-plane spatial resolution when the gradient amplifiers were at maximum power. The readout duration was 14 ms with 9091 Hz bandwidth and total acquisition time was 114 s for fully sampled k-space. Critical to the success of these experiments is a very stable magnetic field as off-resonance effects can distort the image and cause severe banding artifacts (37).

It should be noted that the application of EPR saturation pulses while the gradients are on is only possible because our maximum gradient strength is low, 0.1 gauss cm⁻¹, giving a spread in electron resonance frequencies across the 5.5 cm sample (in-plane dimension) of ~ 1.54 MHz. The loaded Q of the EPR coil was determined using a vector network analyzer and an untuned pick up coil to measure the transmission response of the EPR coil (S21). The measured Q of 62 corresponds to a bandwidth of ~ 2.3 MHz, thus the spread in electron spin frequencies during the phase encode step is well covered.

Compressed Sensing

Most images are sparse in the sense that they can be accurately represented with fewer coefficients than one would assume given their spectral bandwidth (38). CS is a framework for exploiting sparsity to reconstruct high-fidelity MR images from undersampled k-space datasets that do not fulfill the Nyquist sampling theorem. In CS image reconstruction, image sparsity is enforced by truncating the small coefficients of an object's representation in a sparse basis, typically chosen to be a wavelet transform domain. During image reconstruction, the data are transformed from k-space (the sensing basis) into the wavelet basis via a sparsifying transform, ψ , taken for this work to be the Dirichlet wavelet transform.

CS uses norms to modify the objective function that is optimized during image reconstruction. To understand the role of norms in the objective function, it is helpful to recall standard Fourier reconstruction. For a discrete image m , Fourier operator F , and k-space dataset y , the L_2 -norm, $\|Fm - y\|_2 = (\sum_i |(Fm)_i - y_i|^2)^{1/2}$, is implicitly used to find an image whose Fourier transform differs as little as possible from the k-space data in the Euclidean sense. For fully sampled data, the least squares solution is provided by the Fourier transform. In the case of underdetermined matrix problems (as when the k-space data is undersampled), the L_2 -norm may be additionally used to constrain image reconstruction so as to reduce the noise (an approach known as Tikhonov regularization). However, when the L_2 -norm is used in this way, it functions as a low-pass filter, penalizing noise at the

expense of introducing bias. It does not promote image sparsity. By contrast, the L_1 -norm, defined as $\|x\|_1 = \sum_i |x_i|$ for an arbitrary function x , has a tendency to preserve edges and large coefficients, e.g., for neighboring voxels $\{0,3,0\}$ the L_2 -norm will tend to penalize the difference toward $\{1,1,1\}$, while the L_1 -norm of both cases is the same, preserving the edge.

The ability of the L_1 -norm to preserve large coefficients makes it an appealing choice for enforcing sparsity in images (39,40). In the CS framework, the L_1 -norm is applied to the wavelet transform of the image, where it naturally selects the large coefficients representing image features while reducing the small coefficients corresponding to noise and incoherent artifacts. For additional denoising and artifact suppression, a finite difference norm (a discrete implementation of the Total Variation, or TV , norm) is applied in the image domain (41). This norm has been shown to preserve object edges while eliminating noise.

As shown in (42), the resulting image reconstruction problem is expressed as a balance between the L_1 -norm constraints and the L_2 -norm data consistency constraint:

$$\min [\|F_u m - y\|_2 + \alpha \|\psi m\|_1 + \beta TV(m)]$$

where F_u is the undersampled Fourier transform operator, y is the undersampled k-space data, and coefficients α and β weight the relative contributions of each norm to the final image. A variety of algorithms are available for minimizing this nonlinear objective function (42). Specific details about our implementation of CS for OMRI b-SSFP are given below.

Undersampled OMRI b-SSFP

The use of CS in MRI relies on the possibility to acquire a priori compressed information and be able to reconstruct the original image as if the latter was fully sampled (42). In the context of data acquisition, this motivates the use of undersampling. CS has been found to work best when k-space is randomly undersampled to produce incoherent artifacts rather than the familiar wrap-around ghosts due to field-of-view contraction when k-space lines are skipped in a regular coherent pattern as is done in conventional parallel imaging (43). For the images presented here, a choice was made to acquire random lines of k-space in the phase-encode directions (k_y, k_z) following a gaussian probability density function. The readout direction was fully sampled. The standard deviations of the sampling pattern as a fraction of the field-of-view along y and z , σ_y , and σ_z , respectively, were adjusted manually to preserve adequate high-frequency information for each undersampling rate. We investigated four undersampling fractions, 50, 70, 80, and 90%. The undersampling patterns are shown in Figure 4. On the acquisition side, this resulted in programming different phase encode tables for each undersampled sequence. The total acquisition time for each undersampling rate is shown in Table 1. To perform image reconstruction according to the L_1 -norm and the data consistency constraints, the Sparse MRI code (<http://www.eecs.berkeley.edu/~mlustig/Software.html>) was used. This code solves the optimization problem using a

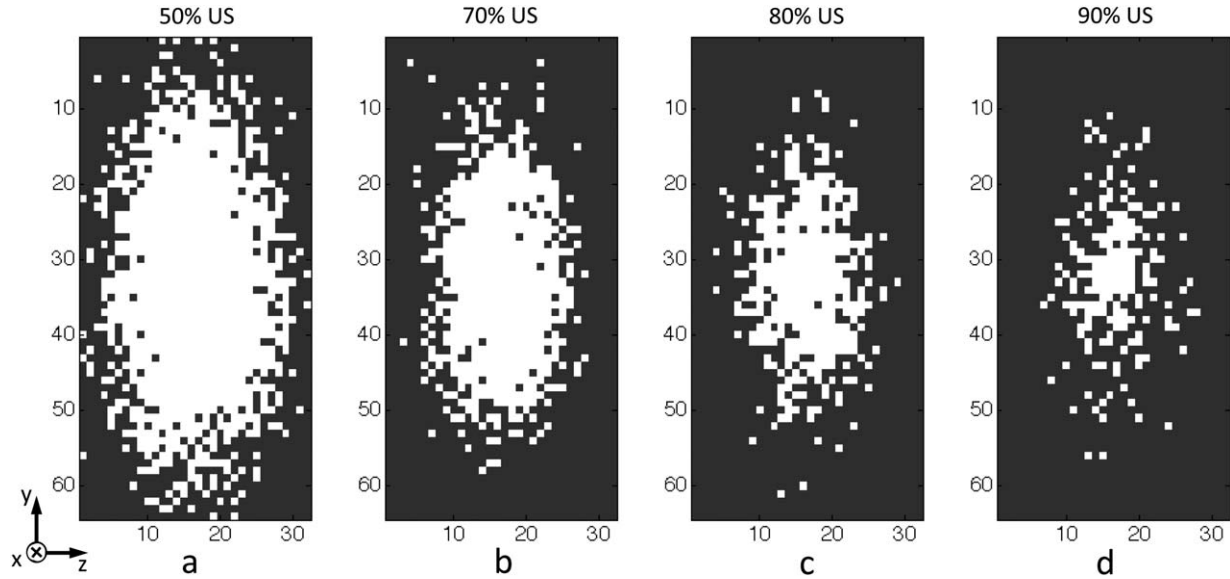


FIG. 4. Undersampling (US) patterns used for (a) 50% undersampling, (b) 70% undersampling, (c) 80% undersampling, and (d) 90% undersampling. For an undersampling rate of 50%, 995 of 2048 lines were acquired. For 70% undersampling, 585 of 2048 lines were acquired. For 80% and 90% undersampling, 383 and 185 of 2048 lines were acquired, respectively.

nonlinear conjugate gradient method along with backtracking line-search as described in (42). The parameters for the wavelet and image domain norms were tuned manually to produce low-noise images with preserved object features. The missing values in the acquired k-space data were made identically zero. To separate out the data into slices, a Fourier transform was performed along the readout direction (*x*). Each sagittal slice of k-space data (*y*–*z* plane) was then reconstructed by the Sparse MRI algorithm. After all slices were reconstructed, the resulting 3D block of image domain data was then displayed as transverse (*x*–*y*) slices. The computation time for a laptop equipped with a 2.3 GHz quad-core processor was 4.5 min, permitting CS image reconstruction immediately following k-space acquisition.

Table 1

Comparison of Acquisition Time, Maximum SNR, and Mean Absolute Error (MAE) as a Function of the Undersampling Fraction for the Two Different Phantom Configurations with the Maximum Applied RF Power of 62 W at the EPR Coil

	Acq. time (s)	Maximum SNR		MAE
		No CS	CS	
<i>Configuration 1</i>				
Fully sampled	114	23	40.6	
50% Undersampling	56	35.8	75.8	0.073 ± 0.006
70% Undersampling	33	44.6	95	0.072 ± 0.008
80% Undersampling	21	64.3	160	0.112 ± 0.011
90% Undersampling	10	69.8	148	0.149 ± 0.014
<i>Configuration 2</i>				
Fully sampled	114	24.6	42.6	
50% Undersampling	56	30.47	49.7	0.049 ± 0.005
70% Undersampling	33	42	78.3	0.059 ± 0.010
80% Undersampling	21	49.9	94.7	0.100 ± 0.013
90% Undersampling	10	58.1	88.3	0.114 ± 0.014

RESULTS

Steady-State Signal with Embedded EPR Pulses

To understand the approach of transverse magnetization to steady state with embedded EPR pulses in the sequence, Bloch simulations were performed without the phase encode gradients and compared with acquired data. The results are shown in Figure 5. The data was normalized such that the maximum measured signal and the maximum simulated signal were both set to 1. The experimental data with DNP (\square) begins at thermal equilibrium, but rapidly builds up to 30 times that of the non-DNP data (\circ). This build up corresponds to the T_1 relaxation time of the sample (545 ms). The signal reaches $\sim 90\%$ of its steady state value after 24 echoes, or 1.3 s, and the simulation is in good agreement with the data (dashed line; not a fit).

Fully Sampled Versus Undersampled

Images of the two different phantom configurations are shown in Figures 6 and 7 after CS reconstruction. Images reconstructed from fully sampled k-space and from 50, 70, 80, and 90% undersampling are shown. Figure 6a,b shows the top and center structures of the interlocking cones (configuration 1). Figure 6c displays 3D rendered images of the segmented cones for each undersampling fraction. Figure 7a–e shows the different segments of the phantom in configuration 2. For both phantom configurations, 50 and 70% undersampling reproduces the fully sampled images well. Even small structures such as 2 mm diameter holes (Fig. 6a), 1 and 1.5 mm solid separators and 2.5 mm holes (marked by white arrows in Fig. 7b–d) are well resolved at 70% undersampling. For 80 and 90% undersampling, most of the structures are still visible although substantial blurring and ghosting artifacts begin to appear. Figure 7a,e correspond to the top and bottom slice of the phantom and show lower signal

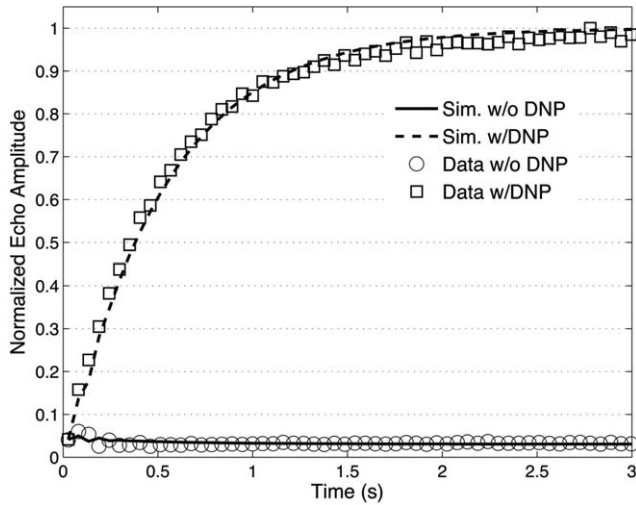


FIG. 5. Simulation and measurement of the approach to steady-state with- and without DNP. Plotted are the echo amplitudes acquired during the pulse sequence in Figure 3 with only the read gradient active. The DNP signal is nearly 30 times larger than the signal without DNP after reaching steady-state. Solid curves plotted are not a fit to the data but an exact simulation with no free parameters as described in the text.

magnitude due to the B_1 profile of the EPR coil. The maximum SNR was calculated from maximal signal amplitudes divided by two times the standard deviation of a user defined noise region before and after CS reconstruction and is shown in Table 1. The increase in SNR with undersampling rate is due to the undersampling

pattern acting as an apodization filter that removes high spatial frequencies from k-space. However, all images show an increase in SNR after CS reconstruction. The SNR enhancement using CS increases with the initial SNR of the image and ranges from about 1.5 to 2.5.

To quantify the errors that occur in the undersampled images, the mean absolute error (MAE) was calculated for each image (Table 1). The MAE was calculated by first thresholding the images such that only points that were five times greater than the noise (σ_n) were kept. The undersampled image was then subtracted from the fully sampled image and all non-zero values counted as an error. As seen in Table 1, the MAEs for the 50 and 70% undersampling rates are small and comparable while those for 80 and 90% increase significantly. The MAE for each of the 32 phase encode gradients along z for configuration 1 is shown in Figure 8 for all undersampling rates. There is little difference across the entire sample between 50 and 70%, again showing that the image is well reproduced with only 30% of the k-space data. Losses in SNR due to the B_1 profile of the EPR coil on slices 1–5 and 25–32 result in increased MAE values for all undersampling rates.

SAR Considerations

A problem limiting the use of OMRI is that the high power RF pulses necessary for DNP lead to high SAR. Two methods were used to estimate SAR. A fiber optic temperature probe was placed inside the sample and the fully sampled k-space sequence was run several times, waiting several minutes in between runs to allow the

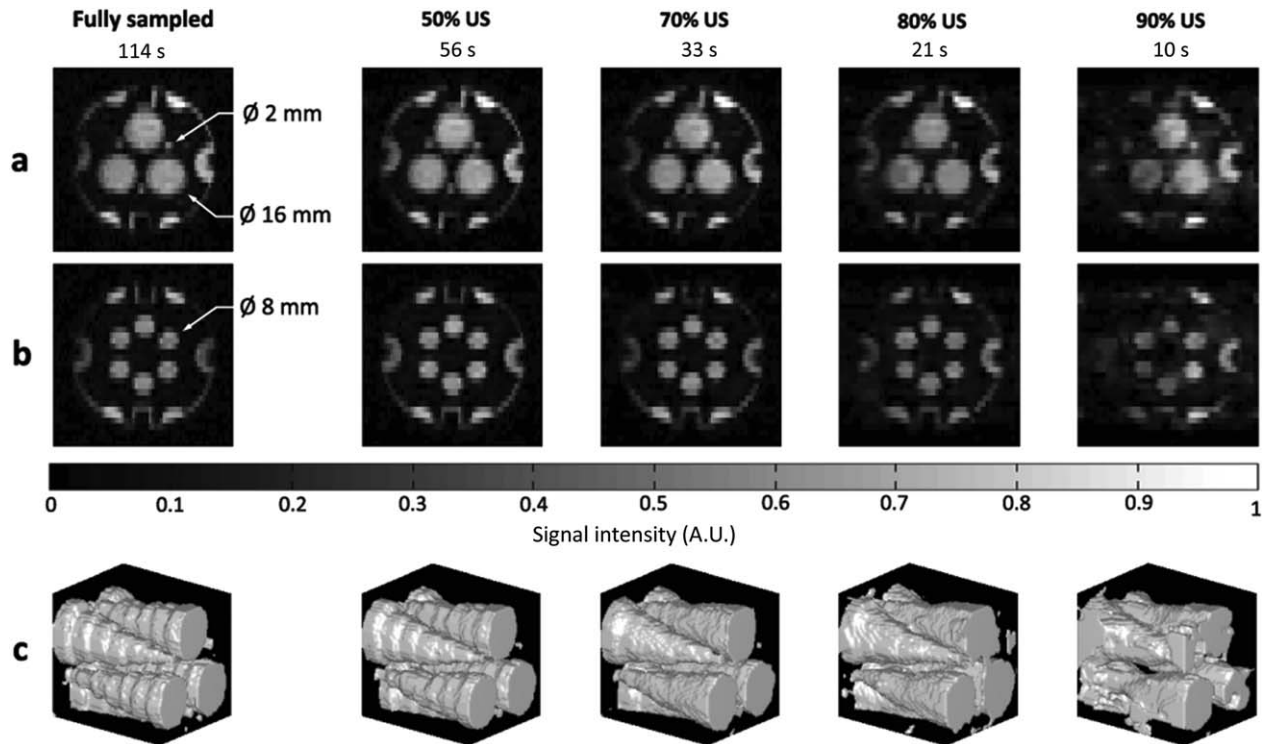


FIG. 6. Fully and undersampled (US) images of the phantom in configuration 1 after CS reconstruction as a function of undersampling fraction. a: Representative slices: Top (a) and center (b) of the full 32 slice dataset. Acquisition matrix: $128 \times 64 \times 32$, voxel size: $2 \times 1 \times 3.5 \text{ mm}^3$. c: 3D rendered images of the interlocked cone structure obtained from the fully and undersampled datasets.

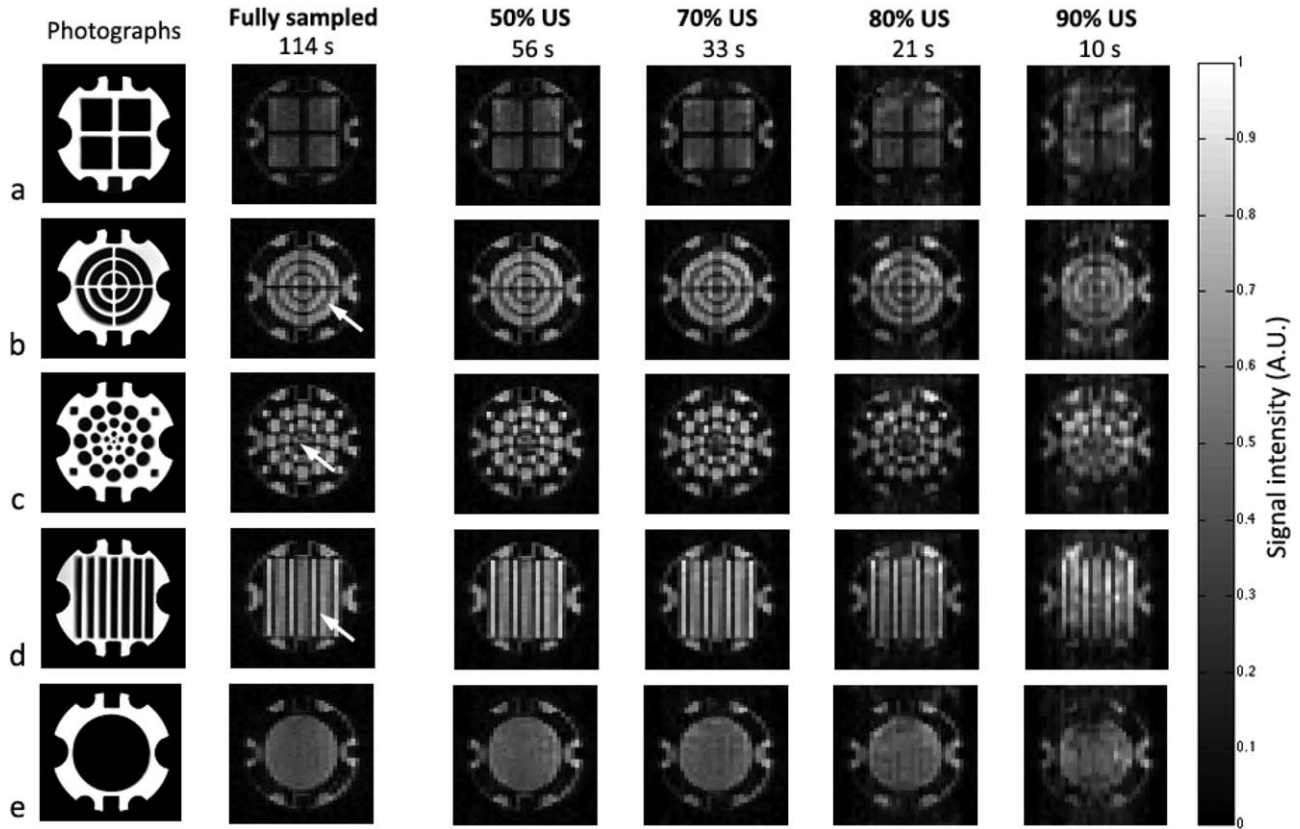


FIG. 7. Fully and undersampled (US) images of five representative slices after CS reconstruction. The full 32-slice data set was acquired with the phantom in configuration 2 as described in the text. MR images are shown alongside photographs of the corresponding phantom piece. Acquisition matrix: $128 \times 64 \times 32$, voxel size: $2 \times 1 \times 3.5 \text{ mm}^3$. White arrows indicate 1 and 1.5 mm solid separators, (b) and (d), respectively, and 2.5 mm diameter structures (c).

EPR coil to cool. The maximum measured temperature increase was 0.4°C . No temperature increase was measured for any of the undersampled sequences. Estimating

$\text{SAR} \sim cT/\Delta t$ (44) where c is the specific heat, ΔT is the temperature change and Δt is the time of the sequence gives $\text{SAR} = 15 \text{ W kg}^{-1}$. We expect this to represent a lower limit as heat may have dissipated during the sequence. As a second method, the power dissipated in the sample was estimated using (45):

$$P_{\text{sample}} = P_{\text{coil}}(1 - Q_{\text{loaded}}/Q_{\text{unloaded}})$$

The forward power was measured using a directional coupler (Model 3020A, Narda Microwave, Hauppauge, NY) and power meter (V3500A, Agilent Technologies, Santa Clara, CA), and the maximum forward power to the coil was $\sim 62 \text{ W}$. The loaded Q was measured to be 52 while the unloaded Q was 62. Thus the power to the sample during an EPR pulse is $\sim 10 \text{ W}$. The EPR irradiation is on for 73% of TR and the sample mass is 0.25 kg , therefore $\text{SAR} = 29 \text{ W kg}^{-1}$.

The 50% undersampled images in Figures 6 and 7 have high SNR and accurately represent the phantom. Therefore, we reduced the forward power to the coil by factors of 2, 4, 8, and 16 to investigate how much the SAR could be reduced (thusly reducing the Overhauser enhancement) while maintaining high image quality. The results are shown in Figure 9 and Table 2. Image quality is well maintained for 31 and 15.5 W forward power corresponding to an estimated SAR of ~ 14.5 and 7.25 W kg^{-1} , respectively.

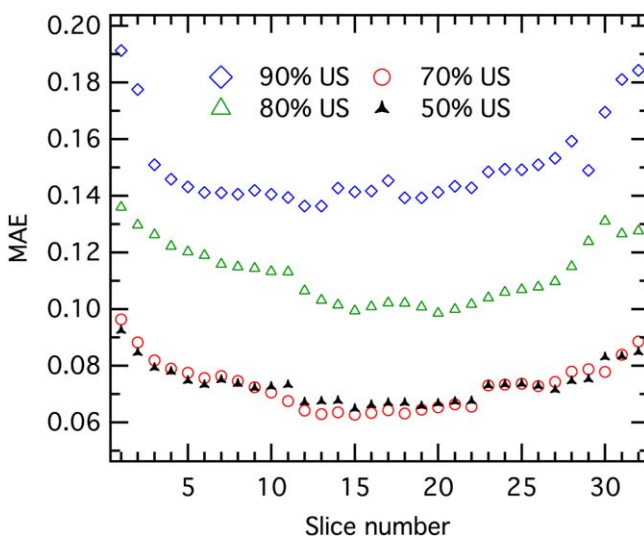


FIG. 8. MAE computed each slice number for each undersampling fraction with the phantom in configuration 1: 50% US (black), 70% US (red), 80% US (green), and 90% US (blue). [Color figure can be viewed in the online issue, which is available at wileyonlinelibrary.com.]

DISCUSSION

The 3D Overhauser-enhanced b-SSFP sequence presented here in combination with CS and undersampling techniques allows us to attain $1 \times 2 \times 3.5 \text{ mm}^3$ voxel size in our phantom in 33 s (70% undersampling in Figs. 6 and 7) at 6.5 mT. The resulting CS reconstructed image is nearly identical to the original fully sampled image and has ~ 2 times higher SNR. This was achieved by inserting the EPR saturation pulses within TR during the prephase/rephase gradients, thus removing the time consuming prepolarization step as in other OMRI sequences. As shown in our experiments and simulations (Fig. 5), a large steady-state signal is quickly reached with 90% of the maximum signal reached in < 1.5 s, and constant polarization in the sample is maintained during the remainder of the acquisition. This eliminates the need to correct acquisitions for T_1 decay and to rectify undesirable phase shifts that can occur when using prepolarization techniques (25,46). The maximum signal with b-SSFP at thermal equilibrium is given by $M_{ss} = \frac{1}{2} M_0 \sqrt{T_2/T_1} = 0.47 M_0$ (37). Overhauser saturation pulses during the phase gradient increases M_{ss} by ~ 30 for the sample used here, thus allowing high SNR images comparable to those obtained with conventional OMRI techniques. The simulations provide a reliable tool to optimize the phase encode gradient durations depending on T_1 and T_2 .

The application of EPR saturation pulses during the balanced phase encode gradient events is our first major source of acceleration. This allows us to acquire images twice as fast as spin echo OMRI sequences recently published in the literature (24) with nearly seven times higher spatial resolution ($1 \times 2 \times 3.5 \text{ mm}^3$ vs. $1.25 \times 1.25 \times 30 \text{ mm}^3$). This is possible by covering the spread in electron spin frequencies in the phantom when the maximum 0.1 gauss cm^{-1} phase encode gradient was turned on. This sets an upper limit on the Q factor of the EPR coil, or alternatively, the maximum gradient strength that can be used for these experiments. While the maximum steady-state DNP enhancements would benefit from a higher Q coil, the goal of maintaining nearly constant signal enhancement across the sample during imaging would suffer. However, when the EPR irradiation occurs as separate step before imaging as in other OMRI sequences, the DNP signal is also not constant across the image due to the decay of polarization, so a compromise of higher gradient strength for uneven DNP polarization may be acceptable.

Partial sampling of k-space (and subsequent reconstruction via CS) is our second major acceleration factor. In the case of 70% undersampling, this result in additional 3.5 fold acceleration while keeping the voxel size unchanged, thus resulting in seven times faster acquisition compared with recently published work (24). By undersampling in each phase encode direction according to a gaussian probability density function, the center of k-space is emphasized, preserving image contrast without completely sacrificing the high frequency information at the edge of k-space. However, the choice of the lines sampled in k-space was empirically determined and only a few undersampling patterns were empirically

tested for a given undersampling rate. The degrees of freedom in the generation of undersampling patterns is large (choice of lines sampled, $\sigma_{y,z}$) and a large number of combinations could have been tested with the opportunity to give even better results. However, for the $\sigma_{y,z}$'s used here, the 50% and 70% undersampling rates accurately reproduced the image for different random samplings of k-space. In addition, this work focuses on Cartesian sampling, but alternative sampling trajectories (spiral and radial) have been shown to offer more flexibility in the design of 3D incoherent sampling sequences that are particularly well for the use of CS techniques (47–50).

CS performs natural denoising, bringing an improvement in SNR. Incoherent artifacts resulting from subsampled k-space are efficiently suppressed using L_1 -norm constraints in the image and wavelet domains as previously detailed in the literature (42). However, more than 70% undersampling could not provide satisfying reconstruction in spite of high SNR. The incorporation of prior knowledge (51–53) in the image reconstruction process could overcome this limitation by partially recovering irretrievable loss of information caused by heavy undersampling and further increase our temporal resolution. In addition, it is important to note that the 4.5 min computation time required for the CS reconstruction does not significantly penalize the time saved from undersampling.

The gain in temporal resolution obtained here for 70% undersampling, around 1 s per acquired slice, provides new insight for investigating cases where high temporal resolution is needed, such as monitoring the concentration change, oxidation, and metabolism of free radicals that correlate directly with organ functions and tissue health. In addition, shorter durations for the read and phase encode gradients could have been implemented to give significantly shorter acquisition times but at the cost of a decreased spatial resolution. Likewise, doubling the gradient strength in read and both phase encode directions would allow us to reach 2^3 times higher spatial resolution for a fixed acquisition time.

Considering the SAR resulting from the sequence, the amount of power sent to the EPR coil was decreased by a factor of 4 while still keeping the SNR > 25 . Even if a compromise has to be found between the desired spatial resolution of the image and sample heating due to the high power RF, the total amount of RF power sent to the sample during imaging is considerably reduced by the use of undersampling strategies. No temperature rise was measured in the sample for the 50 to 90% undersampling fractions with the maximum EPR power used in this study. With the maximum available EPR power, we acquired images with an in-plane resolution of $1 \times 1 \text{ mm}^2$ as shown in Figure 10 with 70% undersampling (while maintaining the 3.5 mm slice thickness). Total acquisition time was 65 s. This image displays excellent in-plane resolution with very little blurring of the 1 mm features and high SNR.

The images presented here were acquired with a sufficiently long TR to obtain the desired in-plane resolution while keeping the gradient strength low enough for

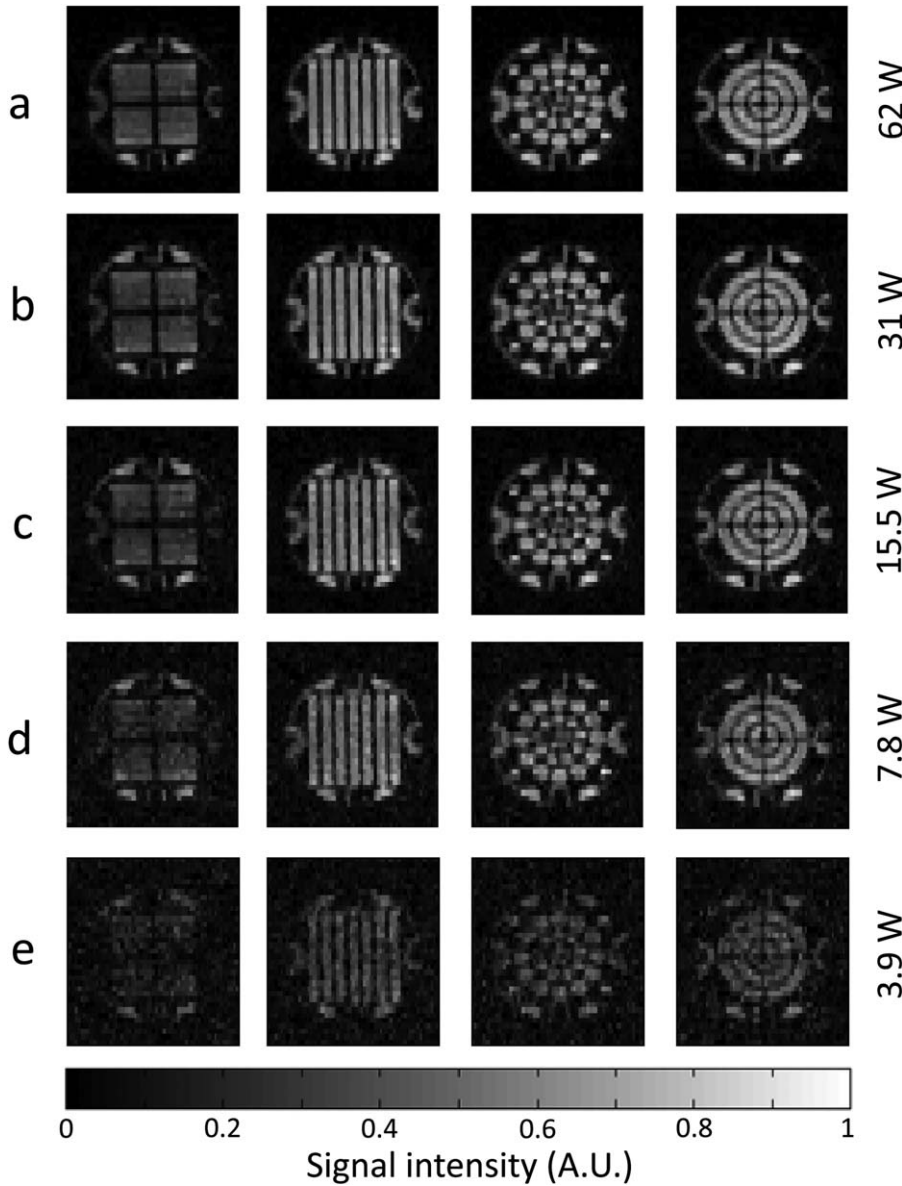


FIG. 9. Images taken with the phantom in configuration 2 and 50% under-sampling as a function of Overhauser drive power: (a) 62 W, (b) 31 W, (c) 15.5 W, (d) 7.8 W, and (e) 3.9 W EPR power. Acquisition matrix: $128 \times 64 \times 32$, voxel size: $2 \times 1 \times 3.5 \text{ mm}^3$, and TR/TE: 54/27 ms. Total acquisition time per image was 56 s.

efficient EPR saturation during phase encoding. We note that the phantom used here has significantly longer T_2 and T_1 relaxation times than would be expected for in vivo applications. Bloch simulations were run to estimate how the current sequence would perform with relaxation times 10 times shorter than the phantom used here. Keeping all simulation parameters as in Figure 5, but decreasing T_1 to 55 ms and T_2 to 49 ms resulted in

Table 2
The Maximum SNR as a Function of Power at the EPR Coil with and without CS for the Phantom in Configuration 2

Power to EPR coil (W)	Max. SNR	
	No CS	CS
62	36	75
31	29.3	48
15.5	21	26.4
7.8	15.2	18.2
3.9	11.4	16.2

<15% reduction in signal intensity (compared with the dashed line in Figure 5). While relaxation times comparable to TR tend to reduce signal, this is partially offset by a faster approach to steady state. More likely to hamper the effectiveness of OMRI in vivo, however, is a decrease in the maximum DNP signal enhancement due to extra ^1H nuclear spin relaxation pathways that compete with relaxation caused by dipolar coupling to the electron spin (27). To observe this effect, simulations were run with the short T_1 and T_2 times above while decreasing the maximum DNP signal enhancement to -10 and -5 . This reduced the steady state signal intensity by 80 and 90%, respectively, compared with the dashed line in Figure 5. Although the signal is much smaller, it is still a factor of 7 and 3.5 times larger than the thermal equilibrium signal with the same parameters, and therefore still provides very useful contrast. In the case of injected free radical detection, this decrease in signal can be partially overcome by increasing the free radical concentration. For example, injection of 0.6 mL

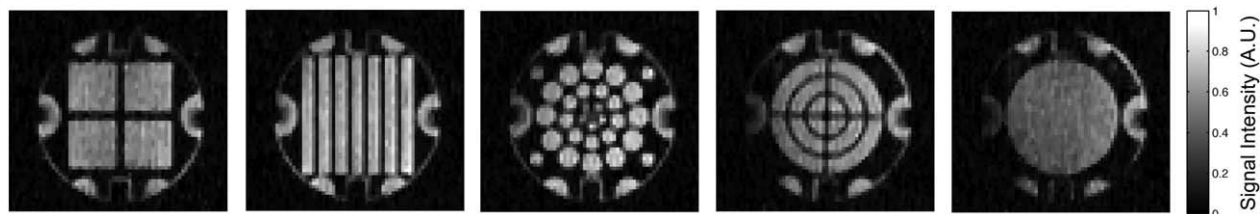


FIG. 10. High-resolution CS reconstructed images taken in the phantom in configuration 2 (five slices are shown) with 70% undersampling. Acquisition matrix: $256 \times 64 \times 32$, voxel size: $1 \times 1 \times 3.5 \text{ mm}^3$, and TR/TE: 54/27 ms. Total acquisition time was 65 s.

of 100 mM nitroxide radical in mice has been reported in recent work (24). Assuming 60–80 mL of blood per kg of bodyweight (54), the dilution factor is between 3 and 4 for a 30 g mouse, resulting in a nominal 29 mM free radical concentration, more than 10 times higher than the 2.5 mM used in the work presented here.

CONCLUSION

We have demonstrated a new strategy for fast high-resolution 3D Overhauser MRI using b-SSFP in a phantom containing 2.5 mM 4-hydroxy TEMPO solution at 6.5 mT. The embedding of EPR excitation pulses directly into the b-SSFP sequence eliminates the prepolarization step used in other OMRI sequences, reducing the acquisition time and obviating the need for long, high power RF EPR pulses. The use of undersampling strategies and CS reconstruction algorithms further reduces imaging time. We have shown that an undersampling rate of 70% gives unperceivable reconstruction errors when compared with the fully sampled data sets, allowing the acquisition of 32 slices in our phantom volume within 33 s. This work overcomes the main limitations of Overhauser enhanced MRI as previously described in the literature, drastically improving speed and resolution, and enabling new opportunities for the measurement of free radicals in living organisms, and for the study of dynamic processes such as metabolism and flow.

ACKNOWLEDGMENTS

The authors thank Ronald Walsworth and Stephen DeVience for assistance with relocating and upgrading the low-field scanner, Jennifer McNab and Thomas Witzel for valuable discussions on implementing b-SSFP sequences at 6.5 mT, and David Donoho and Michael Lustig for sharing the package wavelet toolbox (Wavelab) online with the scientific community.

REFERENCES

- Ardenkjaer-Larsen JH, Laursen I, Leunbach I, Ehnholm G, Wistrand LG, Petersson JS, Golman K. EPR and DNP properties of certain novel single electron contrast agents intended for oximetric imaging. *J Magn Reson* 1998;133:1–12.
- James PE, Madhani M, Roebuck W, Jackson SK, Swartz HM. Endotoxin-induced liver hypoxia: defective oxygen delivery versus oxygen consumption. *Nitric Oxide* 2002;6:18–28.
- Ahn KH, Scott G, Stang P, Conolly S, Hristov D. Multiparametric imaging of tumor oxygenation, redox status, and anatomical structure using overhauser-enhanced MRI–prepolarized MRI system. *Magn Reson Med* 2011;65:1416–1422.
- Lurie DJ, Davies GR, Foster MA, Hutchison JMS. Field-cycled PEDRI imaging of free radicals with detection at 450 mT. *Magn Reson Imaging* 2005;23:175–181.
- Massot P, Parzy E, Pourtau L, Mellet P, Madelin G, Marque S, Franconi J-M, Thiaudiere E. In vivo high-resolution 3D Overhauser-enhanced MRI in mice at 0.2 T. *Contrast Media Mol Imaging* 2012;7:45–50.
- Kosem N, Naganuma T, Ichikawa K, Phumala Morales N, Yasukawa K, Hyodo F, Yamada K-I, Utsumi H. Whole-body kinetic image of a redox probe in mice using Overhauser-enhanced MRI. *Free Radic Biol Med* 2012;53:328–386.
- Caia GL, Efimova OV, Velayutham M, El-Mahdy MA, Abdelghany TM, Kesselring E, Petryakov S, Sun Z, Samouilov A, Zweier JL. Organ specific mapping of in vivo redox state in control and cigarette smoke-exposed mice using EPR/NMR co-imaging. *J Magn Reson* 2012;216:21–27.
- Mellet P, Massot P, Madelin G, Marque SRA, Harte E, Franconi J-M, Thiaudiere E. New concepts in molecular imaging: non-invasive MRI spotting of proteolysis using an overhauser effect switch. *PLoS One* 2009;4:e5244.
- Halpern HJ, Chandramouli GV, Barth ED, Yu C, Peric M, Grdina DJ, Teicher BA. Diminished aqueous microviscosity of tumors in murine models measured with in vivo radiofrequency electron paramagnetic resonance. *Cancer Res* 1999;59:5836–5841.
- Barros W, Engelsberg M. Enhanced Overhauser contrast in proton-electron double-resonance imaging of the formation of an alginate hydrogel. *J Magn Reson* 2007;184:101–107.
- Eaton GR, Eaton SS, Ohno K. EPR imaging and in vivo EPR. Boca Raton: CRC Press; 1991.
- Kuppusamy P, Chzhan M, Zweier J. Principles of imaging. In: Berliner LJ, editor. *Biological magnetic resonance*, Vol. 18. In vivo EPR (ESR): theory and applications. New York: Kluwer Academic/Plenum Publishers; 2003. p 99–152.
- Halpern HJ, Yu C, Peric M, Barth ED, Karczmar GS, River JN, Grdina DJ, Teicher BA. Measurement of differences in pO₂ in response to perfluorocarbon/carbogen in F5a and NFSa murine fibrosarcomas with low-frequency electron paramagnetic resonance oximetry. *Radiat Res* 1996;145:610–618.
- Halpern HJ, Yu C, Peric M, Barth E, Grdina DJ, Teicher BA. Oxymetry deep in tissues with low-frequency electron paramagnetic resonance. *Proc Natl Acad Sci USA* 1994;91:13047–13051.
- Subramanian S, Yamada K-I, Irie A, Murugesan R, Cook JA, Devashayam N, Van Dam GM, Mitchell JB, Krishna MC. Noninvasive in vivo oximetric imaging by radiofrequency FT EPR. *Magn Reson Med* 2002;47:1001–1008.
- Velayutham M, Li H, Kuppusamy P, Zweier JL. Mapping ischemic risk region and necrosis in the isolated heart using EPR imaging. *Magn Reson Med* 2003;49:1181–1187.
- He G, Samouilov A, Kuppusamy P, Zweier JL. In vivo imaging of free radicals: applications from mouse to man. *Mol Cell Biochem* 2002;234/235:359–367.
- Lurie DJ, Bussell DM, Bell LH, Mallard JR. Proton-electron double magnetic resonance imaging of free radical solutions. *J Magn Reson* 1988;76:366–370.
- Golman K, Petersson JS, Ardenkjaer-Larsen JH, Leunbach I, Wistrand LG, Ehnholm G, Liu K. Dynamic in vivo oxymetry using overhauser enhanced MR imaging. *J Magn Reson Imaging* 2000;12:929–938.
- Krishna MC, English S, Yamada K, et al. Overhauser enhanced magnetic resonator imaging for tumor oximetry: coregistration of tumor anatomy and tissue oxygen concentration. *Proc Natl Acad Sci USA* 2002;99:2216–2221.

21. Utsumi H, Yamada K-I, Ichikawa K, Sakai K, Kinoshita Y, Matsumoto S, Nagai M. Simultaneous molecular imaging of redox reactions monitored by Overhauser-enhanced MRI with ^{14}N - and ^{15}N -labeled nitroxyl radicals. *Proc Natl Acad Sci USA* 2006;103:1463–1468.
22. Li H, He G, Deng Y, Kuppusamy P, Zweier JL. In vivo proton electron double resonance imaging of the distribution and clearance of nitroxide radicals in mice. *Magn Reson Med* 2006;55:669–675.
23. Benial AM, Ichikawa K, Murugesan R, Yamada K, Utsumi H. Dynamic nuclear polarization properties of nitroxyl radicals used in Overhauser-enhanced MRI for simultaneous molecular imaging. *J Magn Reson* 2006;182:273–282.
24. Sun Z, Li H, Petryakov S, Samouilov A, Zweier JL. In vivo proton electron double resonance imaging of mice with fast spin echo pulse sequence. *J Magn Reson Imaging* 2012;35:471–475.
25. Youngdeed W, Lurie DJ, Foster MA. Rapid imaging of free radicals in vivo using hybrid FISP field-cycled PEDRI. *Phys Med Biol* 2002;47:1091–1100.
26. Tsai LL, Mair RW, Rosen MS, Patz S, Walsworth RL. An open-access, very-low-field MRI system for posture-dependent ^3He human lung imaging. *J Magn Reson* 2008;193:274–285.
27. Hausser KH, Stehlik D. Dynamic nuclear polarization in liquids. *Adv Magn Reson* 1968;3:79–139.
28. Muller-Warmuth W, Meise-Gresch K. Molecular motions and interactions as studied by dynamic nuclear polarization (DNP) in free radical solutions. *Adv Magn Reson* 1983;11:1–45.
29. Alderman DW, Grant DM. An efficient decoupler coil design which reduces heating in conductive samples in superconducting spectrometers. *J Magn Reson* 1979;36:447–451.
30. Lurie DJ, Li H, Petryakov S, Zweier JL. Development of a PEDRI free-radical imager using a 0.38 T clinical MRI system. *Magn Reson Med* 2002;47:181–186.
31. Rabi II, Zacharias JR, Millman S, Kusch P. A new method of measuring nuclear magnetic moment. *Phys Rev* 1938;53:318.
32. Bottomley PA, Andrew ER. RF magnetic field penetration, phase shift and power dissipation in biological tissue: implications for NMR imaging. *Phys Med Biol* 1978;23:630–643.
33. Jin J. Electromagnetic analysis and design in magnetic resonance imaging. Boca Raton, FL: CRC Press; 1998.
34. Collins CM, Li S, Smith MB. SAR and B1 field distributions in a heterogeneous human head model within a birdcage coil. Specific energy absorption rate. *Magn Reson Med* 1998;40:847–856.
35. Collins CMC, Smith MBM. Calculations of B(1) distribution, SNR, and SAR for a surface coil adjacent to an anatomically-accurate human body model. *Magn Reson Med* 2001;45:692–699.
36. Collins CM, Wang Z. Calculation of radiofrequency electromagnetic fields and their effects in MRI of human subjects. *Magn Reson Med* 2011;65:1470–1482.
37. Scheffler K, Lehnhardt S. Principles and applications of balanced SSFP techniques. *Eur Radiol* 2003;13:2409–2418.
38. Candes EJ, Romberg J, Tao T. Robust uncertainty principles: exact signal reconstruction from highly incomplete frequency information. *IEEE Trans Inform Theory* 2006;52:489–509.
39. Donoho DL. Compressed sensing. *IEEE Trans Inform Theory* 2006;52:1289–1306.
40. Candes EJ, Wakin MB. An introduction to compressive sampling. *IEEE Signal Process Mag* 2008;25:21–30.
41. Rudin LI, Osher S, Fatemi E. Nonlinear total variation based noise removal algorithms. *Phys D: Nonlinear Phenom* 1992;60:259–268.
42. Lustig M, Donoho D, Pauly JM. Sparse MRI: the application of compressed sensing for rapid MR imaging. *Magn Reson Med* 2007;58:1182–1195.
43. Pruessmann KP, Weiger M, Scheidegger MB, Boesiger P. SENSE: sensitivity encoding for fast MRI. *Magn Reson Med* 1999;42:952–962.
44. Oh S, Webb AG, Neuberger T, Park B, Collins CM. Experimental and numerical assessment of MRI-induced temperature change and SAR distributions in phantoms and in vivo. *Magn Reson Med* 2010;63:218–223.
45. Matsumoto S, Yamada K, Hirata H, Yasukawa K, Hyodo F, Ichikawa K, Utsumi H. Advantageous application of a surface coil to EPR irradiation in overhauser-enhanced MRI. *Magn Reson Med* 2007;57:806–811.
46. Puwanich P, Lurie DJ, Foster MA. Rapid imaging of free radicals in vivo using field cycled PEDRI. *Phys Med Biol* 1999;44:2867–2877.
47. Lustig M, Lee J, Donoho D, Pauly J. Faster imaging with randomly perturbed, undersampled spirals and L1 reconstruction. In *Proceedings of the 13th Annual Meeting of ISMRM*, Miami Beach, Florida, USA, 2005. p. 155.
48. Santos JM, Cunningham CH, Lustig M, Hargreaves BA, Hu BS, Nishimura DG, Pauly JM. Single breath-hold whole-heart MRA using variable-density spirals at 3T. *Magn Reson Med* 2006;55:371–379.
49. Ye JC, Tak S, Han Y, Park HW. Projection reconstruction MR imaging using FOCUSS. *Magn Reson Med* 2007;57:764–775.
50. Block KT, Uecker M, Frahm J. Undersampled radial MRI with multiple coils. Iterative image reconstruction using a total variation constraint. *Magn Reson Med* 2007;57:1086–1098.
51. Mistretta CA, Wieben O, Velikina J, Block W, Perry J, Wu Y, Johnson K, Wu Y. Highly constrained backprojection for time-resolved MRI. *Magn Reson Med* 2005;55:30–40.
52. Chen G-H, Tang J, Leng S. Prior image constrained compressed sensing (PICCS): a method to accurately reconstruct dynamic CT images from highly undersampled projection data sets. *Med Phys* 2008;35:660–663.
53. Lauzier PT, Tang J, Chen G-H. Prior image constrained compressed sensing: implementation and performance evaluation. *Med Phys* 2012;39:66–80.
54. Sluiter W, Oomens LWM, Brand A, Van Furth R. Determination of blood volume in the mouse with ^{51}Cr -labelled erythrocytes. *J Immunol Methods* 1984;73:221–225.

Two-Dimensional Imaging in a Lightweight Portable MRI Scanner without Gradient Coils

Clarissa Zimmerman Cooley,^{1,2*} Jason P. Stockmann,^{1,3} Brandon D. Armstrong,^{1,3} Mathieu Sarraclanie,^{1,3} Michael H. Lev,^{4,5} Matthew S. Rosen,^{1,3,5} and Lawrence L. Wald^{1,5,6}

Purpose: As the premiere modality for brain imaging, MRI could find wider applicability if lightweight, portable systems were available for siting in unconventional locations such as intensive care units, physician offices, surgical suites, ambulances, emergency rooms, sports facilities, or rural healthcare sites.

Methods: We construct and validate a truly portable (<100 kg) and silent proof-of-concept MRI scanner which replaces conventional gradient encoding with a rotating lightweight cryogen-free, low-field magnet. When rotated about the object, the inhomogeneous field pattern is used as a rotating spatial encoding magnetic field (rSEM) to create generalized projections which encode the iteratively reconstructed two-dimensional (2D) image. Multiple receive channels are used to disambiguate the nonbijective encoding field.

Results: The system is validated with experimental images of 2D test phantoms. Similar to other nonlinear field encoding schemes, the spatial resolution is position dependent with blurring in the center, but is shown to be likely sufficient for many medical applications.

Conclusion: The presented MRI scanner demonstrates the potential for portability by simultaneously relaxing the magnet homogeneity criteria and eliminating the gradient coil. This new architecture and encoding scheme shows convincing proof of concept images that are expected to be further improved with refinement of the calibration and methodology. **Magn Reson Med 000:000–000, 2014. © 2014 Wiley Periodicals, Inc.**

Key words: portable MRI; low-field MRI; nonlinear SEMs; Halbach magnet; parallel imaging

INTRODUCTION

Specialized, portable MRI systems have the potential to make MR neuroimaging possible at sites where it is currently unavailable and enable immediate, “point-of-care” detection and diagnosis of acute intracranial pathology which can be critical in patient management. For example, the characterization of acute posttraumatic space occupying brain hemorrhage is a time-sensitive emergency for which simple clinical assessment and even urgent computed tomography scanning may be insufficient. While conventional MR scanners are capable of making this diagnosis, they are not available in remote locations. In Intensive Care Units scanners are generally nearby, but are difficult to use because of the dangers associated with transporting critical care patients. A portable bed-side scanner could offer major benefits in such situations. Portable, low-cost scanners are compelling for applications where power, siting, and cost constraints prohibit conventional scanners. Examples include clinics in rural or underdeveloped areas, military field hospitals, sports arenas, and ambulances. Finally, analogous to the current use of ultra-sound, a low-cost and easy-to-implement scanner could find uses in neurology, neurosurgery, or neuro-oncology examination rooms for routine disease monitoring (e.g., monitoring ventricle size after stent placement). The development of a portable scanner relies on the co-design of a new image encoding methods and simplified hardware. This approach is detailed in the present work.

Traditional Fourier MR imaging methods rely on homogeneous static polarizing fields (B_0) and high strength linear spatial encoding magnetic fields (SEMs) produced by magnetic gradient coils. Conventional scanners use high cost superconducting wire, liquid cryogen cooling systems, and high power supplies and electronics. These aspects make it difficult to simply scale-down conventional MRI scanners to portable, low cost devices. Recently in Kose and Haishi (1) and Kimura et al (2), high resolution imaging has been achieved with tabletop and small bore permanent magnet systems with long acquisition times (1), including a mobile MRI system developed for outdoor imaging of small tree branches (2), but these scanners lack a bore size suitable for brain imaging and the long acquisition times are not conducive to imaging in triage settings. Other approaches that scale-down the size of conventional systems for intra-operative MRI show promise (3). However, while these systems are relatively easy to retrofit in operating room, they are not truly portable.

¹A.A. Martinos Center for Biomedical Imaging, Department of Radiology, Massachusetts General Hospital, Charlestown, Massachusetts, USA.

²Department of Electrical Engineering and Computer Science, Massachusetts Institute of Technology, Cambridge, Massachusetts, USA.

³Department of Physics, Harvard University, Cambridge, Massachusetts, USA.

⁴Department of Radiology, Massachusetts General Hospital, Boston, Massachusetts, USA.

⁵Harvard Medical School, Boston, Massachusetts, USA.

⁶Harvard-MIT Division of Health Sciences Technology, Cambridge, Massachusetts, USA.

Grant sponsor: The Department of Defense, Defense Medical Research and Development Program, Applied Research and Advanced Technology Development Award; Grant number: W81XWH-11-2-0076 (DM09094); Grant sponsor: NIH; Grant numbers: P41EB015896, T32DC00038; Grant sponsor: NIH Blueprint for Neuroscience Research; Grant number: T90DA022759/R90DA023427.

*Correspondence to: Clarissa Zimmerman Cooley, M.Eng., 149 13th Street, Room 2301, Charlestown, MA 02129. E-mail: clzimmer@mit.edu

Additional Supporting Information may be found in the online version of this article.

Received 16 September 2013; revised 2 December 2013; accepted 5 January 2014

DOI 10.1002/mrm.25147

Published online 00 Month 2014 in Wiley Online Library (wileyonlinelibrary.com).

© 2014 Wiley Periodicals, Inc.

In the present work, we use a novel image encoding method based on rotating spatial encoding magnetic fields (rSEMs) to create a portable scanner. We replace the B_0 magnet and linear gradient coils with a rotating permanent magnet featuring an inhomogeneous field pattern used for spatial encoding. In this scheme, the inhomogeneity in the B_0 field serves as a spatial encoding magnetic field (SEM), and is requirement for image encoding not a nuisance. Loosening the homogeneity constraint of some conventional magnet designs leads to a reduction in the minimum required magnet material, and allows for more sparse/lightweight designs (45 kg in our prototype). Additionally, the rotation of the magnet's inhomogeneous field pattern replaces the function of heavy switchable gradient coils with significant power requirements.

Several NMR devices for niche applications have explored relaxing the magnet homogeneity constraint, as well as reducing the reliance on traditional Fourier image encoding. The oil well-logging industry was the first to explore the idea of mobile NMR using "external sample" or "inside-out" NMR tools for measuring fluid in rock formations down-hole (4). This work was initially done with electromagnets or in the earth's field, but the advent of rare-earth magnets with high energy products such as SmCo and NdFeB (5), has allowed more effective borehole NMR tools to be developed (6). Some portable single-sided NMR devices (7,8) exploit inhomogeneous magnetic fields from permanent magnets for 1D spatial encoding. In these systems a rare-earth magnet array is placed against the object such that the field falls off roughly linearly with depth. Broadband excitation and spin-echo refocusing are used to obtain a one-dimensional (1D) depth profile of the water content in the object (9–11). Thus, these systems use the inhomogeneity of the small magnet to spatially encode the depth of the water; a principle that we will exploit in a more complete way.

Previously, Cho et al implemented a mechanically rotating DC gradient field in conjunction with a conventional MRI scanner with the motivation of silent imaging (12). In that case, the rotating electromagnet produced a linear gradient field so traditional projection reconstruction methods could be used. In the presently described portable scanner, the dominant SEM field term is quadrupolar, which requires specialized acquisition and reconstruction techniques. Spatial encoding with similar nonlinear fields created with electromagnets has recently drawn attention as a way to achieve focused high imaging resolutions, reduced peripheral nerve stimulation (13), and improved parallel imaging performance (14). In our scanner, the approximately quadrupolar SEM fields are physically rotated around the object along with the B_0 field, and stationary RF coils are used to acquire generalized projections of the object in spin-echo train form.

In this manuscript, we describe the design, construction, and testing of a portable 2D MRI scanner. We show that the encoding scheme we introduce can achieve a resolution of a few millimeters in phantom images. While full 3D encoding is not demonstrated, the system is compatible with RF encoding schemes, such as the transmit array spatial encoding (TRASE) method (15,16),

capable of adequately encoding the third dimension (along the axis of the cylindrical magnet). The magnet design and initial encoding attempts were previously reported in abstract form (17–19).

METHODS

Magnet and Field Mapping

The described rSEM encoding method is valid for arbitrary encoding field shapes, although the shape will affect the spatially variable resolution of the images. A sparse dipolar Halbach cylinder design similar to the "NMR Mandhala" (20,21) was chosen to produce the rotating B_0 field presented here. This arrangement of permanent magnets produces an approximately uniform field directed transverse to the axis of the cylinder (22). The major design criteria for our Halbach magnet were: (i) maximum average field for highest signal to noise ratio (SNR), (ii) sufficient field variation for spatial encoding while maintaining reasonable measurement and excitation bandwidths, (iii) minimum volume of permanent magnet material to keep cost and weight down, (iv) use of stock rare-earth magnet material shapes, and (v) minimum size to fit the head (to maximize B_0). Note, the design was not focused on the specific spatial encoding field shape, and the resulting pattern in the constructed magnet was accepted as the SEM for the presented scanner. The Halbach cylinder design consists of a 36-cm-diameter array of 20 rungs comprising N42 grade NdFeB magnets that are each $1 \times 1 \times 14''$ (magnetized through the 1'' thickness). Two additional Halbach rings made up of twenty 1'' NdFeB cubes are added to the ends of the cylinder to reduce field fall-off caused by the relatively short length of cylinder. Figure 1 shows a 3D drawing of the magnet, the simulated field, and constructed magnet.

The predicted field pattern (Fig. 1a,b), as well as the forces between the magnet rungs were simulated using COMSOL Multiphysics (Stockholm, Sweden). This calculation estimated an internal force of 178 N, which is adequately handled by the fiberglass and ABS frame designed to hold the NdFeB magnet array. The magnet rungs consist of NdFeB magnets stacked inside square fiberglass tubes (McMaster-Carr, Elmhurst, IL, USA), which are fixed by five water jet cut 3/8" ABS rings (Fig. 1d). Each 14'' long magnet rung is comprised of four individual bar magnets (Applied Magnet, Plano, TX, USA) which were bonded together (three 4'' bars and a 2'' bar). The ABS/fiberglass frame was assembled before NdFeB magnet handling, and then the magnet rungs were populated one at a time. Because the four magnets comprising each rung repel each other as they are inserted, a magnet loading and pushing jig was necessary to force the magnets together while the magnet bonding adhesive cured (Loctite p/n 331 and 7387, Düsseldorf, Germany). The jig was a simple threaded rod mounted to the magnet assembly frame above the opening of the fiberglass tube.

The constructed magnet weighs 45 kg and has a 77.3 mT average field in the 16-cm field of view (FOV) center plane, corresponding to a 3.29 MHz proton Larmor frequency. The cylindrical magnet sits on aluminum rollers

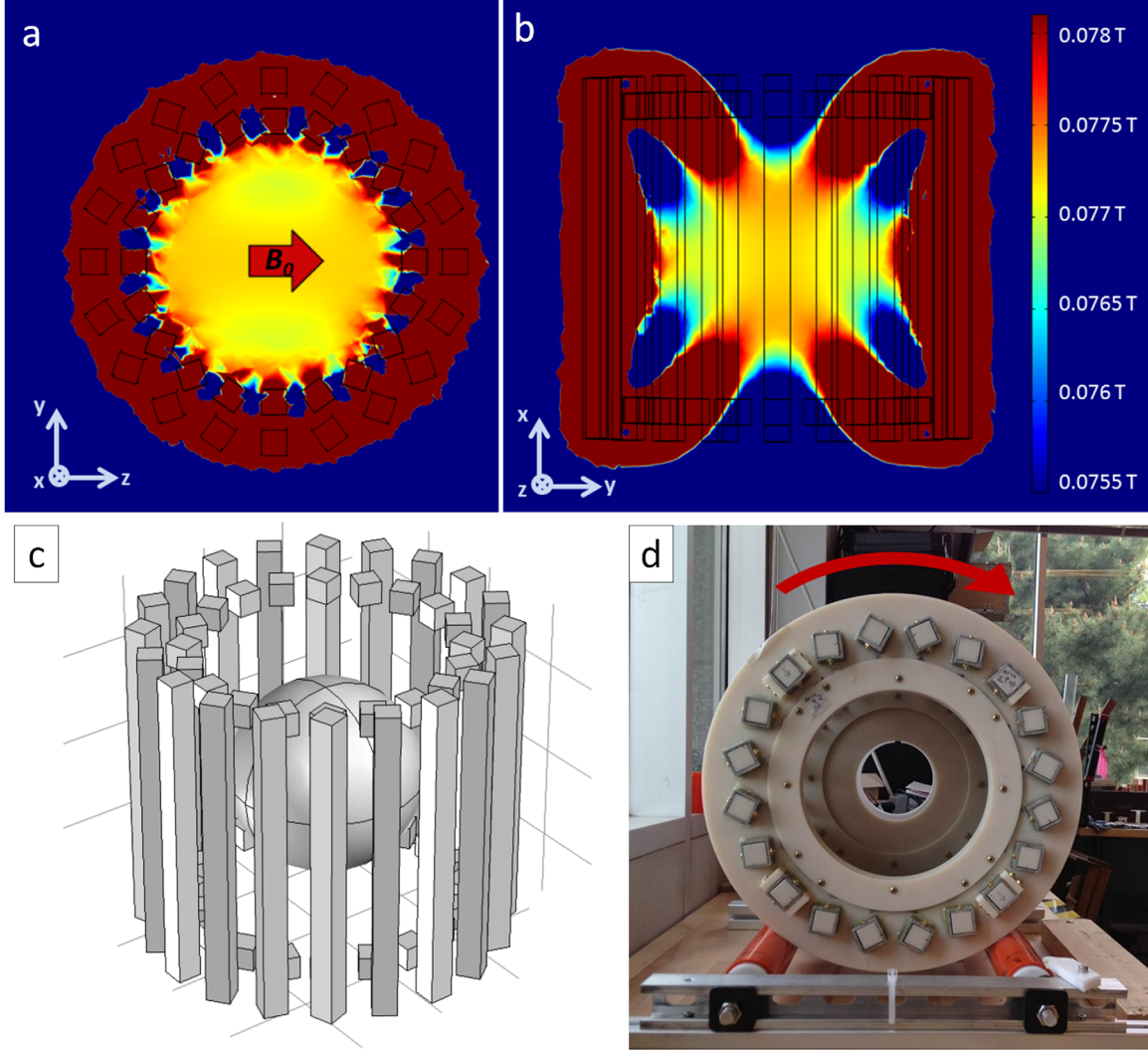


FIG. 1. The magnet array consists of twenty $1'' \times 1'' \times 14''$ NdFeB magnets oriented in the $k = 2$ Halbach mode. Additional Halbach rings made of $1'' \times 1'' \times 1''$ magnets were added at the ends to reduce field fall off along the cylindrical axis. **a,b**: Simulation of the magnetic field in two planes. The field is oriented transverse to the cylinder axis (z-direction). **c**: Schematic of NdFeB magnets composing array. The targeted spherical imaging region (18-cm diameter) is depicted at isocenter. **d**: End-view photo of the Halbach magnet mounted on high friction rollers. Magnet was constructed with ABS plastic and square fiberglass tubes containing the NdFeB magnets. Faraday cage not shown.

covered with a high friction urethane. The MRI console is used to drive a stepper motor (model 34Y106S-LW8, Anaheim Automation, Anaheim, CA, USA) that is attached to the aluminum axle of one of the rollers through a 5:1 gearbox (model GBPH-0901-NS-005, Anaheim Automation). Magnet rotation is incorporated into the pulse sequence so that it is controlled by the MRI console to a precision of one degree at a rate of 10 deg/s. Peripheral nerve stimulation is not a concern with this B_0 rotation rate. Even at $10\times$ the current rotation rate, the dB/dt from the rotating magnet is two orders of magnitude below the dB/dt generated by a modest clinical gradient system. The magnet assembly is enclosed in a copper mesh Faraday cage to reduce RF interference.

An initial 3D field map was obtained with a three-axis gaussmeter probe attached to a motorized stage. The measured field shape is roughly quadrupolar, similar to the fields used in the initial realization of multipolar Pat-

Loc (Parallel Imaging Technique using Localized Gradients) encoding (13), but with significant higher-order components as well. The measured field variation range in y - z (imaging plane), x - z , and x - y planes of a 16-cm sphere were $\Delta f_{yz} = 95$ kHz, $\Delta f_{xz} = 60$ kHz and $\Delta f_{xy} = 52$ kHz. Large Larmor frequency bandwidths make it difficult to design RF excitation and refocusing pulses that achieve the same flip angle and phase across all the spins. In addition, it is difficult to make transmit and receive coils uniformly sensitive over the entire bandwidth. Therefore, shimming was done to decrease field variation (no attempt was made to reshape the SEM). The field variation was shimmed down to $\Delta f_{yz} = 32$ kHz, $\Delta f_{xz} = 32.5$ kHz and $\Delta f_{xy} = 19$ kHz with the addition of small shim magnets ($0.5''$ diameter, $0.25''$ length cylindrical NdFeB magnets) which were attached to the fiberglass rungs. The three planes of the shimmed field map are shown in Figure 2.

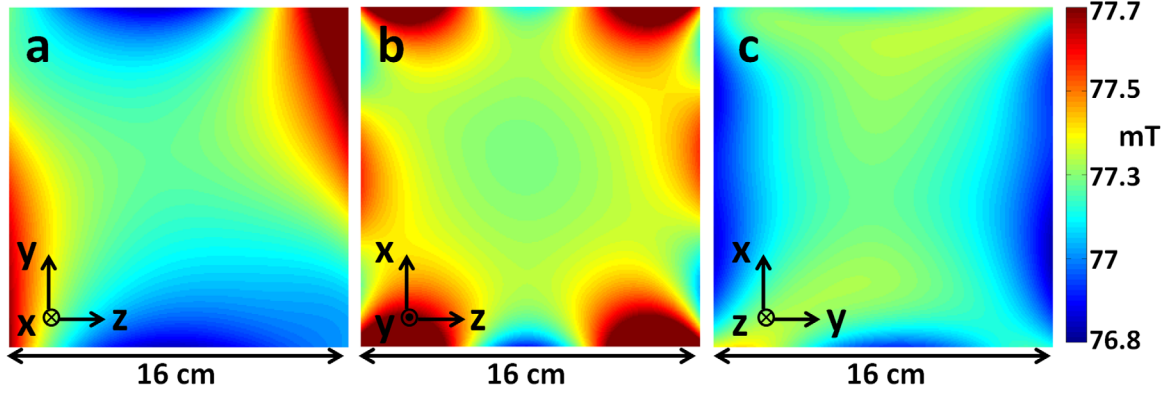


FIG. 2. Gaussmeter-measured field maps of the spatial encoding magnetic field (SEM) in the z - y (imaging plane), z - x , and y - x planes of shimmed the Halbach magnet. The B_0 field is oriented in the z direction.

An accurate field map is critical for image reconstruction, particularly when nonlinear encoding fields force the use of iterative matrix solvers rather than the Fourier transform (14). The field is perturbed by external fields (including the earth's magnetic field), and must be remapped when the magnet is relocated. To quickly acquire center-plane field maps, a linear array of seven field probes spaced 1.5 cm apart was constructed (Fig. 3a). The field probes are tuned 5-mm-long, 4-mm-diameter, 18-turn solenoids measuring signal from 1-mm capillaries of CuSO_4 -doped water (23). To acquire a field map the probes are held stationary while the magnet is rotated around them. Polynomial basis functions are then fit to the measured points and the field map (Fig. 3b) is synthesized. The polynomial coefficients up to 6th order of one magnet rotation angle are shown in Table 1. The net magnetic field from the NdFeB magnets is sensitive to temperature (on the order of 4 kHz/deg C for the Halbach magnet) as well as interactions with external fields, so an additional field probe is used to monitor field drift during data acquisition. This navigator probe is mounted to the Halbach array and rotates with the magnet. The measured field changes, ΔB_0 , are then accounted for in the image reconstruction.

Acquisition Method

To acquire data, the magnet is physically rotated around the sample in discrete steps. At each rotation step, generalized projections onto the nonlinear field are acquired (similar to those described in Schultz et al) (24). Exam-

ples of these projections are shown in Figure 4 for a simple two-sphere phantom. The field experienced by the spheres changes at each rotation due to the nonlinear SEM, providing new information in each projection.

The constructed Rx coil array (Fig. 5a) consists of eight 8-cm-diameter loops of wire encircling the FOV on the surface of a 14-cm-diameter cylinder. The inductances of the coils are roughly 230 nH, requiring capacitors on the order of 10 nF (Voltronics, Salisbury, MD) for tuning. Geometric decoupling and PIN diode detuning were implemented (25,26). The coils are tuned and matched to 50 Ohm impedance low noise preamplifiers (MITEQ P/N AU-1583, Hauppauge, NY, USA).

A Tecmag Apollo console with TNMR software (Houston, TX, USA) was used. The console has one transmit channel, three gradient channels, and one receive channel. Because the programmable gradient analog outputs are not needed for gradient coils, they are used for other purposes. For example, the G_z gradient output is used to control the stepper motor for magnet rotation. The fact that the console only has 1 receive channel means that true parallel imaging cannot be performed. Instead, the receive channel is switched between the coils in the array, acquiring data serially. The G_x gradient output along with a RelComm Technologies (Salisbury, MD, USA) relay and Arduino UNO board are used to switch between the receive coils. Although preamp decoupling has not been implemented yet, data is being acquired from one coil at a time, permitting the other receive coils to be detuned to prevent coupling.

Two scanner coordinate systems are defined because the object and RF coils remain stationary while B_0 is

Table 1
Polynomial Composition of Halbach Magnet SEM in Hz/cm^(m+n)a

$z^n y^m$	n=0	n=1	n=2	n=3	n=4	n=5	n=6
m=0	$z^0 y^0 : 3.3\text{e}6$	$z^1 y^0 : -89$	$z^2 y^0 : -274$	$z^3 y^0 : 1.9$	$z^4 y^0 : 1.1\text{e}-2$	$z^5 y^0 : 2.4\text{e}-2$	$z^6 y^0 : 9.2\text{e}-3$
m=1	$z^0 y^1 : -62$	$z^1 y^1 : 104$	$z^2 y^1 : -8.3$	$z^3 y^1 : -1.7$	$z^4 y^1 : -4.6\text{e}-2$	$z^5 y^1 : -1.8\text{e}-3$	
m=2	$z^0 y^2 : 164$	$z^1 y^2 : -13.3$	$z^2 y^2 : -0.53$	$z^3 y^2 : -0.12$	$z^4 y^2 : 0.11$		
m=3	$z^0 y^3 : 3.9$	$z^1 y^3 : 6.5$	$z^2 y^3 : 4.4\text{e}-2$	$z^3 y^3 : -2.3\text{e}-2$			
m=4	$z^0 y^4 : 0.95$	$z^1 y^4 : 0.21$	$z^2 y^4 : -1.9\text{e}-2$				
m=5	$z^0 y^5 : -3.9\text{e}-3$	$z^1 y^5 : -6.6\text{e}-2$					
m=6	$z^0 y^6 : 9.2\text{e}-3$						

^aThe calculated polynomial coefficients composing the z - y plane (2D imaging plane) of the Halbach spatial encoding field are shown. Measured points from the linear array of field probes (Fig. 3) were used for this sixth order polynomial fit.

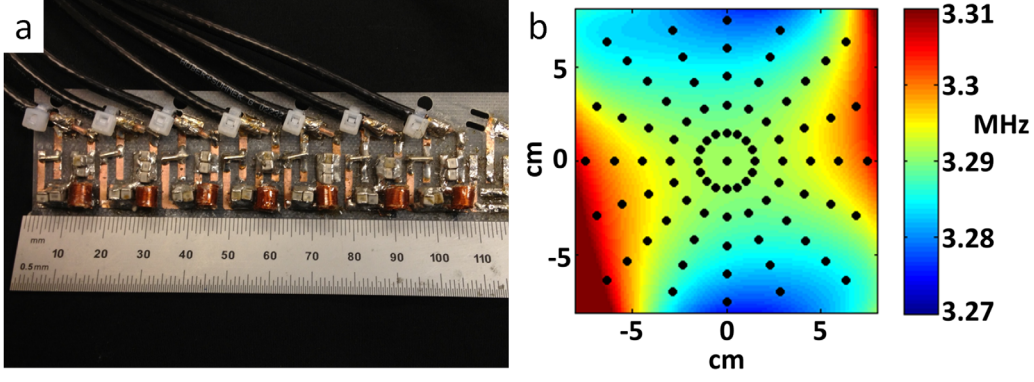


FIG. 3. **a**: Linear array of seven NMR field probes used for mapping the static magnetic field. The probes are held stationary, while the magnet is rotated around them and points on the 2D center plane are sampled. **b**: Measured field map for the center transverse slice through the magnet after fitting 6th order polynomials to the probe data. The black dots mark the location of the probe measurements. The field is plotted in MHz (proton Larmor frequency). This field distribution serves as the SEM information used in image reconstruction.

rotated. The rotating coordinate system of the magnet and the spins is defined as x', y', z' (examples shown in Fig. 6b), and the fixed coordinate system for the coils and objects is defined as x, y, z (shown in Figs. 1,2). Image reconstruction requires accurate knowledge of the coil sensitivity map, $C_{q,r}(x)$. Here the index q refers to the coil channel and r to the rotation position of the magnet. The coil sensitivity map is different for each rotation position because B_1^- is formed from a projection of the coil's B_1 field onto the $x'-y'$ plane (which rotates with the magnet). In conventional MRI, B_1^- is mapped by imaging a phantom with fully sampled encoding by the gradient waveforms. However, this approach is not possible with our encoding scheme because knowledge of $C_{q,r}(x)$ is necessary to form an image without aliasing.

Because of the difficulty of measuring B_1^- on our scanner, we use estimated B_1^- maps. Magnetostatic approximations are suitable at the 3.29 MHz Larmor frequency, so B_1 of the individual coils was modeled with Biot-Savart calculations. By symmetry, the x component of the circular surface coils' B_1 is zero in the center plane FOV. The x' component of B_0 is also nearly zero because of the geometry of the magnet. So the coil sensitivity calculation reduces to a two dimensional problem,

because only the B_1 component perpendicular to B_0 contributes to the sensitivity map.

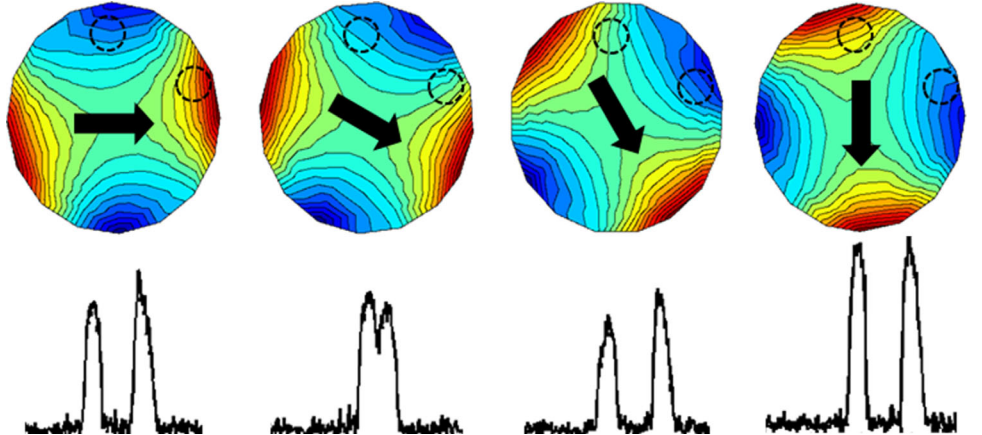
To calculate the coil sensitivity map for each rotation (r), the B_1 component parallel to B_{0r} (the B_0 vector for rotation r) is subtracted and we are left with the perpendicular component.

$$B_{1r}^\perp = B_1 - (B_1 \cdot B_{0r})B_{0r}. \quad [1]$$

The phase is equal to the angle, θ_r , between B_{1r}^\perp and B_{0r} , which will either be $+90^\circ$ or -90° due to the symmetry properties discussed above. The variation in a single coil's B_1^- as a function of B_0 angle is illustrated in Figure 6a,b, and the B_1^- magnitude for four coils and a single B_0 angle is shown in Figure 6c. When B_0 points along the normal to the coil, the sensitivity profile resembles a “donut” pattern with low sensitivity in the center of the FOV. Maximum signal sensitivity occurs when B_0 is oriented orthogonal to the normal vector of the coil loop.

Similar to single-sided imaging methods (7), echo formation requires the use of spin echo sequences in the presence of the inhomogeneous field. The T_2^* of the signal is short due to the static SEM and it is impossible to do the equivalent of gradient echo refocusing because the sign of the SEMs cannot be quickly switched. However,

FIG. 4. Schematic depiction of the generalized projections (bottom row) of an object onto the rotating SEM field. The object consists of two water-filled spheres depicted as dashed black lines which are superimposed on the Halbach magnet's SEM field at a few rotations (black arrow depicts B_0 orientation). The NMR spectrum was acquired with a single volume Rx coil.



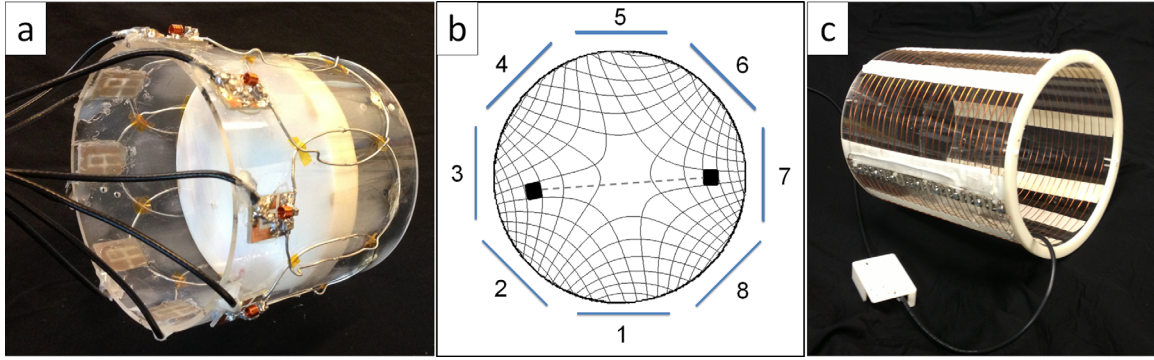


FIG. 5. **a:** Photo of the eight-channel receiver array coil with 3D printed disk-phantom at isocenter. The 14-cm-diameter array is made up of eight, 8-cm loops overlapped to reduce mutual inductance. **b:** Relative voxel size is illustrated as a function of radius from the center using two rotations of the magnet's SEM (field isocontour lines illustrated in figure). Symmetry of the isocontours causes aliasing of each voxel through the origin. Using the local sensitivity profiles of an encircling array of coils, the correct location of each signal source in the FOV can be resolved. (adapted from (28)) **(C)** Photo of the 25 turn, 20-cm diameter, 25-cm length solenoid transmit coil.

the encoding can be repeated and averaged to improve SNR in a spin-echo train, which does refocus the SEM. Unlike in high-field systems, the specific absorption rate (SAR) from the consecutive 180° pulses is negligible because of the low excitation frequency (3.29 MHz).

Unlike conventional MRI scanners, the B_0 field of the Halbach magnet is oriented radially instead of along the

bore of the magnet. This means that in order for B_1^+ to be orthogonal to B_0 at all rotations, it should be directed along the cylindrical axis of the Halbach magnet. This makes a solenoid more suitable than a birdcage coil for radiofrequency (RF) excitation. The constructed solenoid, shown in Figure 5c, has a 20-cm diameter and a 25-cm length. $N = 25$ turns of AWG 20 was chosen as a

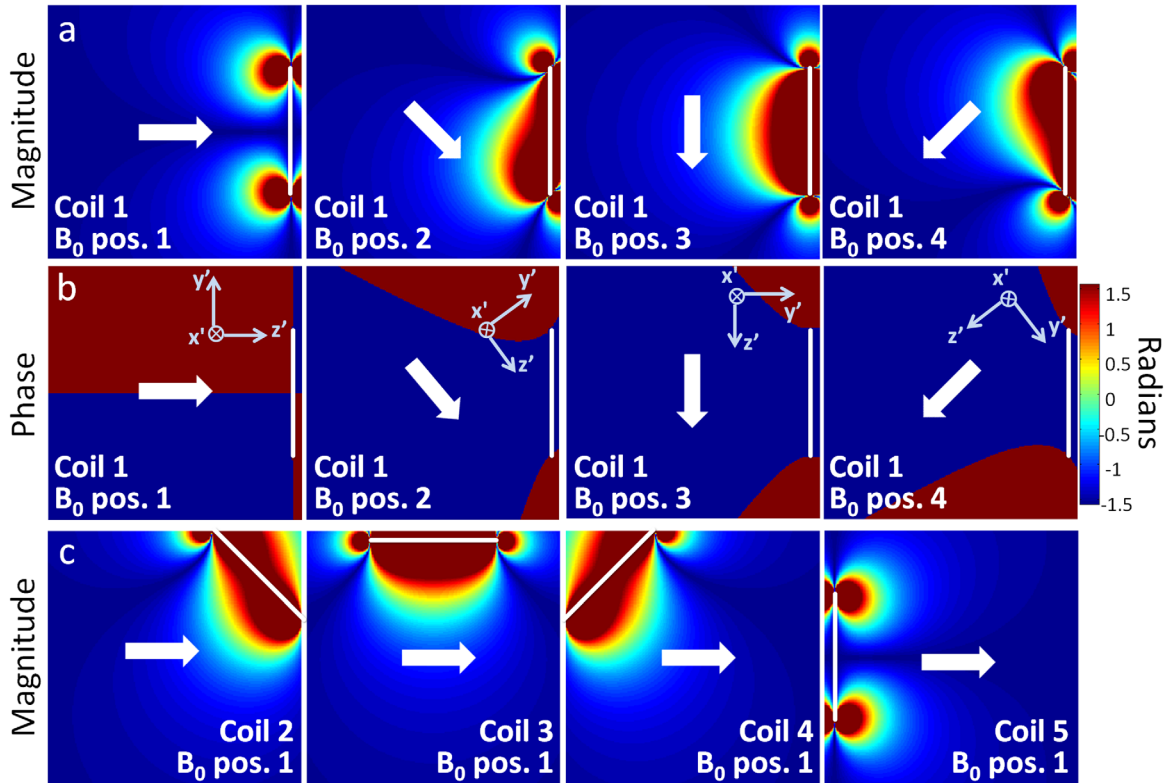


FIG. 6. Biot-Savart calculation of the sensitivity map of the Rx coil array. The white arrows show representative orientations of B_0 , which define the spin coordinate system orientation (x' , y' , z'). Image reconstruction requires accurate coil sensitivity profiles for each B_0 angle used in the experiment. **a,b:** B_1^- magnitude and phase for a single representative surface coil located at the right side of the FOV (position marked with white line). Because of the symmetry of the coils' at isocenter, the coils' x' component is approximately zero, and the process of taking the projection onto the $x'-y'$ plane (to solve for B_1^-) will produce a vector parallel or antiparallel to y' . Therefore, the B_1^- phase is always $+90^\circ$ or -90° in the depicted transverse isocenter plane. **c:** B_1^- magnitude of four different coils of the array (marked with white lines) for a single magnet rotation position.

reasonable value in the tradeoff between B_1^+ homogeneity and parasitic capacitance from closely spaced windings. The 70 μH Tx coil is tuned to 3.29 MHz with eight 230 pF series capacitors distributed along the length of the solenoid, which reduces the susceptibility to stray capacitance. Because the static SEM field is “always on”, the transmit coil must have a relatively low Q to excite a wide bandwidth of spins. The Q of the coil is approximately 60 corresponding to a 55 KHz bandwidth. A 1 KW power amplifier (Tomco, Stepney, SA, Australia) is used to produce short 600 W pulses for broadband excitation (25 μs for 90° pulses and 50 μs for 180° pulses).

PIN diode detuning is used in the transmit and receiver coils to prevent coil interaction (25). The tuning/matching circuits are constructed so that the transmit coil is tuned and the receive coils are detuned when the pin diodes are forward biased with console controlled DC voltage. The converse is true when the diodes are reverse biased (Tx coil detuned and Rx coils tuned).

Reconstruction Method

The Halbach magnet’s spatial encoding field is approximately quadrupolar and, therefore, produces a nonbijective mapping between object space and encoding space. This encoding ambiguity leads to aliasing in the image through the origin. As described by Hennig et al (13), parallel imaging with encircling receive coils can be used to disambiguate the nonbijective mapping. This is possible because the coil sensitivity profiles provide additional spatial encoding that localizes signal within each source quadrant of the FOV, eliminating aliasing. This idea is illustrated in Figure 5b. This specific implementation of the portable scanner closely resembles the case of PatLoc imaging with quadrupolar fields and a radial frequency-domain trajectory (28). However, the measured Halbach SEM is not purely quadrupolar, and the presence of arbitrary field components prevents the decomposition of the rotating SEM into linear combinations of two orthogonal encoding fields. For this reason, the direct back-projection reconstruction method described in Schultz et al (28) is not valid, and iterative matrix methods such as those described in Stockmann et al (29) are used.

The discretized signal acquired by a coil (q) at a given magnet rotation (r) at time n can be described as

$$s_{q,r}(n) = \sum_{\mathbf{x}} C_{q,r}(\mathbf{x}) e^{-i2\pi k(r,\mathbf{x},n)} m(\mathbf{x}) \quad [2]$$

where $m(\mathbf{x})$ is the magnetization of the object at location vector \mathbf{x} , $C_{q,r}(\mathbf{x})$ is the complex sensitivity of the coil at location \mathbf{x} , and $k(r, \mathbf{x}, n)$ is the evolved phase from the nonlinear gradient at rotation r , location \mathbf{x} , and time n . The exponential term and coil sensitivity term can be grouped together to form the encoding function $enc_{q,r}(\mathbf{x}, n)$.

$$s_{q,r}(n) = \sum_{\mathbf{x}} enc_{q,r}(\mathbf{x}, n) m(\mathbf{x}) \quad [3]$$

The matrix form of this signal equation for a single projection readout acquired with one RF coil is simply

$$S_{q,r} = E_{q,r} \mathbf{m}. \quad [4]$$

The acquired signal, $S_{q,r}$, is a vector made up of the sampled readout points (N_{smp}). The object that we are solving for, \mathbf{m} , is a vector made up of all the image voxels (N_{vox}). The encoding matrix, $E_{q,r}$, contains the evolved phase of each voxel in the FOV for each time point in the acquisition as well as the coil sensitivity multiplier. With linear gradient fields, E is made up of the sinusoidal Fourier basis set, which allows the image to be reconstructed using radial back-projection, k-space re-gridding, and other approaches. In the nonlinear SEM case, E is more complicated, but can be calculated from the measured field maps. Before the appropriately rotated field map is used to calculate the phase evolution, the field change captured by the navigator probe during the acquisition is added as a global offset.

A separate block of the encoding matrix, $E_{q,r}$ is calculated for the data acquired by each coil at each rotation. There will be a total of $R \times C$ blocks (where R is total number of rotation and C is the total number of coils), which are vertically concatenated to form the full encoding matrix, E . S is also made up of vertically concatenated subparts, $S_{q,r}$, which are the signals acquired from each coil at each rotation.

To reconstruct the image from the acquired data, the object, \mathbf{m} , can be found by inverting the matrix, E . However, the full encoding matrix size is $N_{\text{smp}} \times R \times C \times N_{\text{vox}}$. In the typical case of 256 readout points, 181 rotations, eight coils, and a 256×256 voxel reconstructed image, the full matrix size is $371K \times 65K$. Because it is not computationally feasible to invert this matrix, iterative methods such as the Conjugate Gradient method (30) and the Algebraic Reconstruction Technique (31,32) can be used to solve for the minimum norm least squares estimator of \mathbf{m} . The generality of this approach allows arbitrary field shapes and coil profiles as well as systematic errors such as temperature-dependent field drifts to be incorporated into the encoding matrix.

The reconstructed images and simulations shown here were done using the Algebraic Reconstruction Technique. The encoding matrix was calculated line by line during the reconstruction using the appropriately rotated and temperature drift-corrected field map and the calculated coil sensitivity profiles for the given B_0 direction. To demonstrate the importance of temperature drift compensation, a phantom image was also reconstructed with an uncorrected encoding matrix. The field of view of the images is 16 cm and the in-plane voxel size is 0.625 mm.

Phantom Imaging Methods

Images of a “MIT/MGH” phantom were acquired both with a single channel solenoid Rx coil and with seven coils of the Rx array. The 3D printed polycarbonate phantom is 1.7-cm thick with a 13-cm diameter, and is filled with CuSO_4 -doped water. Thirty-two averages of a six spin-echo train ($\text{TR} = 550$ ms, echo-spacing = 8ms) were acquired for 91 rotation angles over 180 degrees. Navigator field probe data was also acquired at each rotation. The coil array’s lengthy acquisition time of 66 min

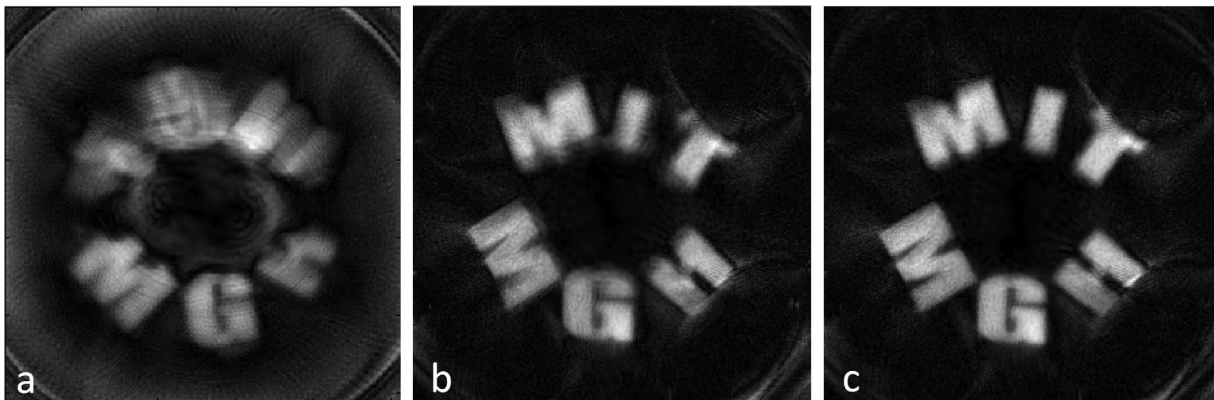


FIG. 7. Experimental 256×256 voxel, 16-cm FOV images of a 3D printed phantom with CuSO_4 doped water occupying the interior of the letters and polycarbonate plastic surrounding it. The phantom has a 13-cm diameter and is 1.7 cm thick. 91 magnet rotations spaced 2° apart were used, readout bandwidth/Npts = 40 KHz/256, TR = 550 ms, spin-echo train length = 6 or 16, with 8 ms echo-spacing. Echoes in the spin-echo train for a given rotation were averaged. **a:** Image acquired with solenoid Rx coil (32 averages of a 6 spin-echo train). **b:** Image acquired with seven coils of the Rx coil array (8 averages of a 16 spin-echo train). Temperature drift was not corrected for. **c:** Image from same data as (B), but with temperature drift correction implemented.

results from multiplexing a single console receiver and would be reduced to 7.3 min by acquiring data from all channels and the field probe in parallel.

A 1-cm-thick lemon slice was imaged using only the bottom five surface coils with $181 \times 1^\circ$ rotations. The total acquisition time was 93 minutes (15.5 min if surface coils and navigator probe were acquired in parallel). A single average of a 128 echo train at each rotation provided sufficient SNR. Each echo was recorded as 256 pts with a 40 KHz BW (TR = 4500 ms, echo spacing = 8 ms). For comparison, the lemon image was also reconstructed using only 91 rotations of 181 acquired rotations in addition to the full reconstruction.

Image Simulation Methods

The described acquisition method was simulated using the measured field map from the central slice of the Halbach magnet. Images were simulated using a high resolution T_1 brain image or a numerically generated checkerboard with 2.5-mm grid size as the “object.” The measured field map and calculated coil profiles of the eight coil array were used in the forward model to generate the simulated data. In one simulation, an artificial field map was used to simulate the addition of a linear field component to measured SEM. Complex noise was added to the simulations to match noise levels observed in comparable phantom projection. These simulations were done with the same sequence parameters of the lemon image: $181 \times 1^\circ$ magnet rotations, 256 pt readout, 40 KHz BW, echo spacing = 8 ms.

RESULTS

Experimental images of the 3D printed “MIT/MGH” phantom are shown in Figure 7. The image acquired with the solenoid coil used in transmit/receive mode is shown in Figure 7a. Only the “MGH” part of the phantom was filled at the time, so the top half of the image should ideally be empty. Instead the expected aliasing pattern is seen through the center onto frequency

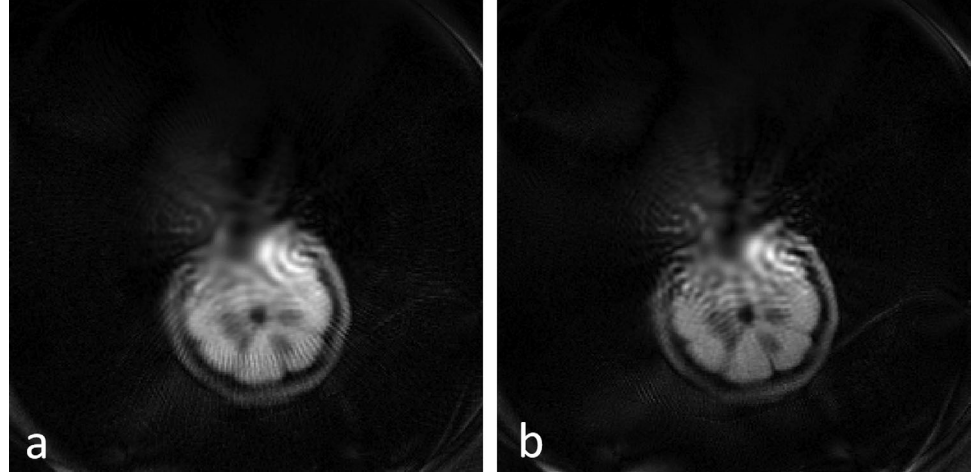
matched quadrants of the FOV. The aliased image is markedly more blurry than one would expect for a purely quadrupolar field, which maps all signals symmetrically about the center during reconstruction. This discrepancy likely arises due to the presence of first-order and higher-order field terms which perturb the symmetry of the dominant quadrupolar field.

The importance of monitoring and correcting for field drift due to temperature is emphasized by comparing Figure 7b and Figure 7c which show images with and without temperature drift correction. The drift correction is achieved by monitoring the frequency seen by the navigator field probe which rotates with the magnet. This probe’s frequency is ideally independent of the rotation angle during the acquisition, but varies due to two causes. First, small changes in room temperature translate to a global scaling of the Halbach array’s magnetization and thus the central B_0 . With no attempt to insulate or stabilize the magnet’s temperature, changes up to 0.4°C and 1.6 KHz were observed over an hour. The second cause for the fixed probe’s change in field as a function of rotation is due to the changing vector sum of the earth’s field and the Halbach field. This effect creates a peak-peak variation of 3.7 KHz for the magnet location and orientation. This effect must also be incorporated in the encoding matrix. Even though field drift correction is applied to Figure 7c, some of the letters are sharper than others; this is likely attributable to field map inaccuracies.

The 1-cm lemon slice images are seen in Figure 8. The use of five of eight coils of the receive array prevents aliasing in the image, but center blurring is more pronounced in these images than in the simulations (Fig. 9). Figure 8a was reconstructed using half of the rotations angles of Figure 8b, resulting in poorer image quality and streaking artifacts.

Figure 9 shows an encoding and reconstruction simulation using a typical high field T_1 -weighted brain MRI as the imaging object (Fig. 9a). Noise was added to the object model to simulate the lower SNR of the low field

FIG. 8. Experimental 256×256 voxel, 16-cm FOV image of a 1-cm thick slice of lemon placed off axis in the magnet. Five receiver coils of the array were used to acquire one average of a 128 spin-echo train, readout bandwidth/Npts = 40 KHz/256, TR = 4500 ms, echo-spacing = 8 ms. **a**: 91 magnet rotations spaced 2° apart were used **(b)** 181 magnet rotations spaced 1° apart were used.



scanner. Figure 9b shows a simulated image using the measured encoding field of Halbach magnet. There is no aliasing in the image because the calculated coil sensitivity profiles of the eight channel Rx array were used. However, there is blurring in the center which coincides with the shallow region of the nonlinear gradient field. The center blurring in Figure 9c is reduced because the image was simulated using an artificial field map that consists of our measured SEM plus an additional linear field of 500 Hz/cm. The simulation of the 2.5-mm grid numerical phantom (Fig. 9d) shows the ultimate resolution possible with the existing experimental protocol in the absence of systematic errors. Outstanding resolution at the periphery gradually gives way to a blurry central region.

DISCUSSION

As expected, the nonbijective mapping of the Halbach magnet's SEM results in aliasing. Fortunately, as

described in Hennig et al (13) the aliasing is resolved by the addition of a multichannel receive array with differing spatial profiles and an appropriate geometry. Because the Halbach encoding is dominated by the quadrupolar "PatLoc" SEM, the system's spatially varying voxel size changes approximately as c/ρ within the FOV, where ρ is the radius and the constant c depends on the strength of the SEM and the length of the readout (27). This means that our Halbach magnet encoding field results in higher resolution at the periphery due to the uniform nature of the SEM near the center of the FOV. This center blurring is seen in both the experimental images in Figure 8 and the simulations in Figure 9.

While we did not attempt to control the precise spherical harmonic distribution in the magnet design, future work will likely benefit from shimming the magnet to obtain a more desirable SEM. For example, if a sufficient linear term were added, the uniform encoding field region would not lie on-axis with the rotation. In this case,

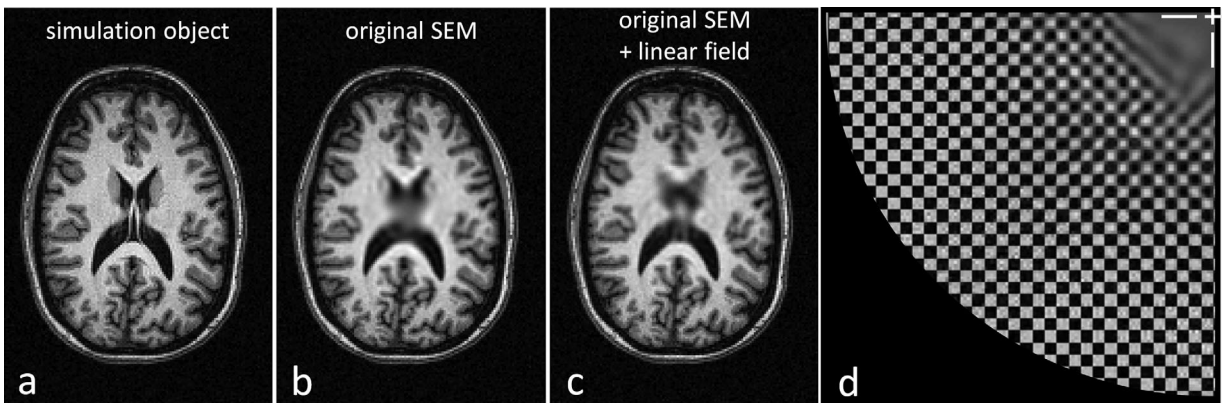


FIG. 9. Simulated images using the calculated sensitivity profiles of the eight coil Rx array to generate the forward model for 181 1° rotations of the encoding field, 6.4 ms, 256 point readouts. The data seen by the Halbach scanner was simulated by processing this "object" through the forward model and adding noise to make it consistent with the SNR of the time-domain signals measured in a water phantom. The model data was then reconstructed using the Algebraic Reconstruction Technique in a 16-cm FOV. **a**: Reference high resolution 3T T_1 weighted brain image used as the model object. Note: the SEMs were scaled to the brain FOV. **b**: Simulated reconstruction using the measured SEM to generate the forward model. **c**: Simulated reconstruction using the measured SEM with the additional artificial linear field component (500 Hz/cm). **d**: Simulated reconstruction of a 2.5-mm grid numerical phantom. Only one quadrant of the FOV is shown, the center of the FOV is marked with white cross-hairs in the upper right.

which is simulated in Figure 9c, the “blind-spot” would move around the object allowing some rotations to contribute to encoding of any given pixel, as previously explored in “O-space imaging” (14). Pursuing this strategy even further would result in a SEM containing only a linear term. In this case, the encoding becomes very similar to a radial imaging scheme with conventional gradients, and to the strategy proposed by Cho et al. who used a rotating gradient coil in a conventional magnet (12). With accurate field mapping instrumentation and shimming software, we suspect that the magnet could be shimmed to a more desirable SEM. Although a linear SEM would eliminate the encoding hole and allow a more straightforward reconstruction method, there are advantages to second-order SEMs, including the coincidence of the high spatial resolution area and high coil sensitivity area near the edge of the FOV.

The lemon images of Figure 8 show that when 91 projection rotations are used instead of 181, a radial streaking artifact is visible. The streaking artifacts are consistent with those arising in conventional undersampled radial trajectories played by linear SEMs as well as undersampled radial trajectories played by PatLoc SEMs (27). It has been shown that the use of total variation and total generalized variation priors during reconstruction suppresses streaking artifacts in undersampled conventional radial (33) and PatLoc radial (34) acquisitions. Similar techniques may be pursued in future work to suppress streaking in images obtained with fewer projection rotations of our scanner.

The simulations in Figure 9 show the theoretical resolution of the scanner when systematic errors are eliminated. These errors are most likely a result of field map and coil sensitivity profile inaccuracies, which are critical to the iterative reconstruction (14). The current coil sensitivity profiles facilitate proof-of-concept reconstructions, but their fidelity is suspect because they were calculated rather than measured. In these calculations the magnetostatic Biot Savart approximation was used with no external structures present. While wavelength effects in the body are not expected at this frequency, the close proximity of the conducting magnets and other coils might perturb the experimental fields. Additionally, a 2D field map is currently used to reconstruct thin samples (1 to 1.5 cm thick), but field variation does exist in the x direction (along the axis of the Halbach cylinder) within the sample thickness. This causes through-plane dephasing and must be incorporated into the encoding matrix based on a 3D field map.

Field map errors arise from temperature drifts which are significant on the time scale of the imaging and mapping acquisitions. We have shown that any uncorrected temperature drift causes substantial blurring in the image (Fig. 7b). Temperature drift is a pervasive problem in permanent magnet MRI and has been addressed in several ways. In the current experimental protocol the frequency at a fixed point is measured at every rotation and the drift is built into the encoding matrix as a global offset to the field maps. This method reduces blurring considerably (Fig. 7c), but other options have been proposed for permanent magnet NMR and MRI that may offer

higher encoding matrix accuracy. For example, Kose and Haishi (1) describe the implementation of a NMR lock method plus thermal insulation. Additionally, a new Halbach design was recently reported which uses two types of magnet materials with different temperature coefficients to substantially reduce the effect of temperature changes on the B_0 field (35). When compared with an uncompensated SmCo magnet, this reduced their temperature coefficient 100-fold, bringing the field drift down to 10 ppm for a 3°C temperature change. However this method has the disadvantage of producing a lower field and requiring more magnet material than the traditional design.

For time-efficient acquisitions, true parallel imaging will be needed. To accomplish this goal, a multichannel receiver console is required, as well as the implementation of preamp decoupling. This is advantageous for practical diagnostic reasons and will also alleviate the field drift problem by shortening acquisition times. In addition to multiple channels, future prototypes must be made larger to accommodate the human head. Although the head can be fit into the presented magnet, its 36-cm diameter does not leave sufficient room for the transmit and receive arrays as well as the structural supports for the magnetic material. Construction of a larger diameter magnet with the same basic design will result in a reduced B_0 field, although this could be mitigated by adding more magnet material and/or higher grade material. The current B_0 field of 77.3 mT is estimated to decrease to 62 mT if the diameter is increased to 40 cm. However if 24 N45 NdFeB magnet rungs are used instead of 20 N42 rungs, a field of 80 mT is theoretically achievable. The standard landmark for brain imaging (between the eyebrows) is 18 cm above the shoulders. The presented Halbach magnet was designed using the maximum cylinder length that allows the brain to be centered in the magnet (2×18 cm). Future magnet designs will likely adhere to this constraint because increasing the length of the magnet requires increasing the bore size to fit shoulders, which would result in a considerably weaker B_0 .

In the described experiments the B_0 field rotates relative to the receiver coils (coils are stationary), which causes the shape of the coil profiles to change with each acquisition angle. However this arrangement is not a requirement for rotating SEM imaging, and in theory the receiver coils could rotate with the magnet. In this case, the coil sensitivity profiles are simply rotated for each acquisition angle, but the shapes of profiles do not change. Data acquisition with rotating coils and stationary coils was simulated. However, there was not a significant difference in performance in either the visual appearance of the reconstructed images or the RMSE (root mean squared error). For data simulated with 91 magnet rotations there was a 0.2% RMSE improvement when using the rotating coil profiles, and for data simulated with 23 magnet rotations (undersampled) there was a 3.6% RMSE improvement. This suggests that rotating the coil array may improve performance when data is undersampled. The 23 rotation simulated images are included in the supplemental material. The rotating receive coil case is similar to the RRFC (Rotating RF

Coils) method described in Trakic et al and Li et al (36,37), where continuously rotating surface coils are used in a conventional magnet for parallel imaging.

The goal of the current work was to provide a proof-of-principle that the basic 2D encoding scheme can be performed, which was demonstrated with 2D imaging of thin samples. However, the addition of third axis encoding is an obvious requirement for medical applications. A promising possibility for encoding the third dimension (along the axis of rotation) is TRASE (15,16). TRASE uses custom-designed RF coils to generate uniform amplitude but linear B_1^+ phase variation along the encoding axis. Spatial encoding is achieved using at least two Tx coils with different phase gradients (typically differing by their sign). Spin-echo trains are used in which the linear phase variation is changed by 180 degrees in between successive refocusing pulses. As the sign of the refocusing pulse is flipped over the course of the echo train, k-space is traversed one echo at a time. The resolution depends on the number of echoes used and the slope of the transmitted B_1 phase ramp across the FOV (16). The approach is synergistic with the echo trains used in the presented encoding scheme for purposes of signal averaging. Furthermore, at low field, TRASE spin-echo trains do not suffer from the SAR limits that may impact the method's performance at high field.

CONCLUSIONS

Using an inhomogeneous magnet for spatial encoding in lieu of gradient coils, we have constructed and demonstrated a lightweight scanner for 2D MR imaging with minimal power requirements. The 2D proof-of-concept images from this nearly head-sized imager show the ability of this encoding scheme to produce sufficient spatial resolution and sensitivity for the detection and characterization of many common neurological disorders such as hydrocephalus and traumatic space-occupying hemorrhages. Future work in perfecting the calibration methods is likely to bring experimental image quality closer to the theoretical limit, but the resolution of the current system is sufficient for identifying gross pathologies. With the future implementation of true parallel imaging and 3D encoding, this scanner has the potential to enable a truly portable, low-cost brain imaging device.

ACKNOWLEDGMENTS

The authors thank Matthew Christensen and Cris LaPierre for their 3D modeling and design work, Bastien Guerin for advice on calculating coil sensitivities, and Stephen Cauley for help with reconstruction methods. This research was carried out at the Athinoula A. Martinos Center for Biomedical Imaging at the Massachusetts General Hospital, using resources provided by the Center for Functional Neuroimaging Technologies. This project was supported by a training grant from the NIH Blueprint for Neuroscience Research. Its contents are solely the responsibility of the authors and do not necessarily represent the official views of the NIH.

REFERENCES

1. Kose K, Haishi T. High resolution NMR imaging using a high field yokeless permanent magnet. *Magn Reson Med Sci* 2011;10:159–167.
2. Kimura T, Geya Y, Terada Y, Kose K, Haishi T, Gemma H, Sekozawa Y. Development of a mobile magnetic resonance imaging system for outdoor tree measurements. *Rev Sci Instrum* 2011;82:053704.
3. Gerlach R, du Mesnil de Rochemont R, Gasser T, Marquardt G, Reusch J, Imoehl L, Seifert V. Feasibility of Polestar N20, an ultra-low-field intraoperative magnetic resonance imaging system in resection control of pituitary macroadenomas: lessons learned from the first 40 cases. *Neurosurgery* 2008;63:272–284; discussion 284–285.
4. Jackson JA, Burnett LJ, Harmon JF. Remote (inside-out) NMR. III. Detection of nuclear magnetic resonance in a remotely produced region of homogeneous magnetic field. *J Magn Reson* 1980;41:411–421.
5. Sagawa M, Fujimura S, Togawa N, Yamamoto H, Matsuura Y. New material for permanent magnets on a base of Nd and Fe (invited). *J Appl Phys* 1984;55:2083–2087.
6. Kleinberg R, Sezginer A, Griffin D, Fukuhara M. Novel NMR apparatus for investigating an external sample. *J Magn Reson* 1992;97:466–485.
7. Casanova F, Perlo J, Blümich B. Single-sided NMR. New York: Springer; 2011.
8. Eidmann RS. The NMR MOUSE, a mobile universal surface explorer. *J Magn Reson Series A* 1996;122:104–109.
9. Todica M, Fecete R, Blümich B. Selective NMR excitation in strongly inhomogeneous magnetic fields. *J Magn Reson* 2003;164:220–227.
10. Perlo J, Casanova F, Blümich B. 3D imaging with a single-sided sensor: an open tomograph. *J Magn Reson* 2004;166:228–235.
11. Landeghem MV, Danieli E, Perlo J, Blümich B, Casanova F. Low-gradient single-sided NMR sensor for one-shot profiling of human skin. *J Magn Reson* 2012;215:74–84.
12. Cho ZH, Chung ST, Chung JY, Park SH, Kim JS, Moon CH, Hong IK. A new silent magnetic resonance imaging using a rotating DC gradient. *Magn Reson Med* 1998;39:317–321.
13. Hennig J, Welz AM, Schultz G, Korvink J, Liu Z, Speck O, Zaitsev M. Parallel imaging in non-bijective, curvilinear magnetic field gradients: a concept study. *Magn Reson Mater Phys* 2008;21:5–14.
14. Stockmann JP, Galiana G, Tam L, Juchem C, Nixon TW, Constable RT. In vivo O-Space imaging with a dedicated 12 cm Z2 insert coil on a human 3T scanner using phase map calibration. *Magn Reson Med* 2013;69:444–455.
15. Sharp JC, King SB. MRI using radiofrequency magnetic field phase gradients. *Magn Reson Med* 2010;63:151–161.
16. Sharp JC, King SB, Deng Q, Volotovskyy V, Tomanek B. High-resolution MRI encoding using radiofrequency phase gradients. *NMR Biomed* 2013;26:1602–1607.
17. Zimmerman C, Blau J, Rosen MS, Wald LL. Design and construction of a Halbach array magnet for portable brain MRI. In Proceedings of the 20th Annual Meeting of ISMRM, Melbourne, Australia, 2012. Abstract 2575.
18. Cooley CZ, Stockmann JP, Armstrong BD, Rosen MS, Wald LL. A lightweight, portable MRI brain scanner based on a rotating Halbach magnet. In Proceedings of the 21st Annual Meeting of ISMRM, Salt Lake City, Utah, USA, 2013. Abstract 137.
19. Stockmann JP, Cooley CZ, Rosen MS, Wald LL. Flexible spatial encoding strategies using rotating multipolar fields for unconventional MRI applications. In Proceedings of the 21st Annual Meeting of ISMRM, Salt Lake City, Utah, USA, 2013. Abstract 2664.
20. Raich H, Blümli P. Design and construction of a dipolar Halbach array with a homogeneous field from identical bar magnets: NMR Mandhala. *Concepts Magn Reson Part B Magn Reson Eng* 2004;23B:16–25.
21. Wroblewski P, Szyszko J, Smolik WT. Mandhala magnet for ultra low-field MRI. In 2011 IEEE International Conference on Imaging Systems and Techniques (IST), 2011. pp. 248–252.
22. Halbach K. Design of permanent multipole magnets with oriented rare earth cobalt material. *Nucl Instrum Methods* 1980;169:1–10.
23. De Zanche N, Barmet C, Nordmeyer-Massner JA, Pruessmann KP. NMR probes for measuring magnetic fields and field dynamics in MR systems. *Magn Reson Med* 2008;60:176–186.

24. Schultz G, Gallichan D, Reiser M, Hennig J, Zaitsev M. MR image reconstruction from generalized projections. *Magn Reson Med* 2013. doi: 10.1002/mrm.24928.
25. Edelstein W, Hardy C, Mueller O. Electronic decoupling of surface-coil receivers for NMR imaging and spectroscopy. *J Magn Reson* (1969). 1986;67:156–161.
26. Roemer PB, Edelstein WA, Hayes CE, Souza SP, Mueller OM. The NMR phased array. *Magn Reson Med* 1990;16:192–225.
27. Schultz G, Ullmann P, Lehr H, Welz AM, Hennig J, Zaitsev M. Reconstruction of MRI data encoded with arbitrarily shaped, curvilinear, nonbijective magnetic fields. *Magn Reson Med* 2010;64:1390–1403.
28. Schultz G, Weber H, Gallichan D, Witschey WRT, Welz AM, Coccosco CA, Hennig J, Zaitsev M. Radial imaging with multipolar magnetic encoding fields. *IEEE Trans Med Imaging* 2011;30:2134–2145.
29. Stockmann JP, Ciris PA, Galiana G, Tam L, Constable RT. O-space imaging: highly efficient parallel imaging using second-order nonlinear fields as encoding gradients with no phase encoding. *Magn Reson Med* 2010;64:447–456.
30. Hestenes M, Stiefel E. Methods of conjugate gradients for solving linear systems. *J Res Natl Bur Stand* 1952;49:409–436.
31. Kaczmarz S. Angenäherte Auflösung von Systemen linearer Gleichungen. *Bull Int Acad Pol Sci let Cl Med*. 1937;35:355–357.
32. Gordon R, Bender R, Herman GT. Algebraic reconstruction techniques (ART) for three-dimensional electron microscopy and x-ray photography. *J Theor Biol* 1970;29:471–481.
33. Block KT, Uecker M, Frahm J. Undersampled radial MRI with multiple coils. Iterative image reconstruction using a total variation constraint. *Magn Reson Med* 2007;57:1086–1098.
34. Knoll F, Schultz G, Bredies K, Gallichan D, Zaitsev M, Hennig J, Stollberger R. Reconstruction of undersampled radial PatLoc imaging using total generalized variation. *Magn Reson Med* 2013;70:40–52.
35. Danielli E, Perlo J, Blümich B, Casanova F. Highly stable and finely tuned magnetic fields generated by permanent magnet assemblies. *Phys Rev Lett* 2013;110:180801.
36. Trakic A, Weber E, Li BK, Wang H, Liu F, Engstrom C, Crozier S. Electromechanical design and construction of a rotating radio-frequency coil system for applications in magnetic resonance. *IEEE Trans Biomed Eng* 2012;59:1068–1075.
37. Li M, Jin J, Trakic A, Liu F, Weber E, Li Y, Crozier S. High acceleration with a rotating radiofrequency coil array (RRFCA) in parallel magnetic resonance imaging (MRI). In 2012 Annual International Conference of the IEEE Engineering in Medicine and Biology Society (EMBC), 2012. p 1098–1101.

SCIENTIFIC REPORTS

OPEN

Low-Cost High-Performance MRI

Mathieu Sarraclanie^{1,2}, Cristen D. LaPierre^{1,2}, Najat Salameh^{1,2,3}, David E. J. Waddington^{1,2,4}, Thomas Witzel¹ & Matthew S. Rosen^{1,2,5}

Received: 05 May 2015

Accepted: 18 September 2015

Published: 15 October 2015

Magnetic Resonance Imaging (MRI) is unparalleled in its ability to visualize anatomical structure and function non-invasively with high spatial and temporal resolution. Yet to overcome the low sensitivity inherent in inductive detection of weakly polarized nuclear spins, the vast majority of clinical MRI scanners employ superconducting magnets producing very high magnetic fields. Commonly found at 1.5–3 tesla (T), these powerful magnets are massive and have very strict infrastructure demands that preclude operation in many environments. MRI scanners are costly to purchase, site, and maintain, with the purchase price approaching \$1 M per tesla (T) of magnetic field. We present here a remarkably simple, non-cryogenic approach to high-performance human MRI at ultra-low magnetic field, whereby modern under-sampling strategies are combined with fully-refocused dynamic spin control using steady-state free precession techniques. At 6.5 mT (more than 450 times lower than clinical MRI scanners) we demonstrate $(2.5 \times 3.5 \times 8.5)$ mm³ imaging resolution in the living human brain using a simple, open-geometry electromagnet, with 3D image acquisition over the entire brain in 6 minutes. We contend that these practical ultra-low magnetic field implementations of MRI (<10 mT) will complement traditional MRI, providing clinically relevant images and setting new standards for affordable (<\$50,000) and robust portable devices.

Magnetic Resonance Imaging (MRI) is a powerful, non-invasive technique for revealing the internal structure and function of the human body with a rich range of biological contrasts. Despite considerable improvements in imaging quality and speed, the underlying technology remains remarkably unchanged compared to the first generation scanners that emerged on the market 30 years ago. The fact that very strong magnetic fields are needed to overcome the intrinsic lack of sensitivity of NMR-based methods continues to dominate scanner construction, and drives both pricing and scanner siting requirements. MRI scanners are built around massive superconducting magnets with a nominal cost of \$1 M per tesla of magnetic field. With 1.5 tesla (T) and 3 T scanners in common use, and increasing demand for 7 T, the extreme cost of these devices limits the number of scanners on site and requires hospitals to carefully prioritize patients. Additionally, these massive scanners are strictly confined to the MRI suite within a hospital thus precluding mobile operation in many environments including surgical intervention, triage and primary care suites.

Undeniably, one of the next revolutions in health care will center on cost-effectiveness. Thus the prospect of low-cost (<\$50,000) but high-performance MRI systems to complement traditional MRI scanners is compelling. A promising solution is MRI at very low magnetic field where scalable electro-magnets become practical. Operation at low magnetic field enables imaging in environments where high magnetic fields would be contraindicated (such as in the presence of nearby ferrous materials), and raises the potential for scanners to be built at significantly reduced total cost, and with open geometry designs that ease patient handling and positioning.

The unique role that very low magnetic field MRI scanners can play in neurocritical care was recognized 30 years ago in the pioneering work of Sepponen, *et al.*¹, who explored the clinical validity of brain MRI acquired in a 20 mT scanner located in a hospital emergency department. These early images

¹MGH/A.A. Martinos Center for Biomedical Imaging, 149 13th St, Suite 2301, Charlestown MA 02129, USA.

²Department of Physics, Harvard University, 17 Oxford St, Cambridge, MA 02138, USA. ³Institute of Physics of Biological Systems, Ecole Polytechnique Fédérale de Lausanne, CH-1015 Lausanne, Switzerland. ⁴School of Physics, University of Sydney, Physics Rd, Sydney NSW 2006, Australia. ⁵Harvard Medical School, 25 Shattuck St, Boston, MA 02115, USA. Correspondence and requests for materials should be addressed to M.S.R. (email: mrosen@cfa.harvard.edu)

were acquired at the lowest field strength reported in clinical MRI at that time, and although limited to a single 15 mm slice, were obtained with good contrast in a reasonable four minute acquisition.

In an effort to improve the performance of very low field MRI systems, Macovski and Conolly introduced the concept of pre-polarized MRI (also known as PMRI) in 1993², which employs a strong, inhomogeneous pulsed magnet field to generate increased nuclear polarization, and a second much weaker homogeneous magnetic field for signal detection. This PMRI strategy has been the acquisition strategy for nearly all very low field MRI systems since its introduction. In 2006, PMRI in human subjects with metal implants was reported *in vivo* in human wrists³, where a 0.4 T field was used for pre-polarization, and a 54 mT field used for signal detection.

The ultra-low field (ULF) MRI regime is defined⁴ when the magnetic field used for signal detection is below 10 mT. In 2007, PMRI was demonstrated with detection in the ULF regime, orders of magnitude lower than reported in Venook *et al.*³, using arrays of very sensitive superconducting quantum interference devices (SQUIDs)⁵ as magnetometers to measure the spatially encoded nuclear spin precession⁶. Pre-polarized cryogenic SQUID-detected ULF MRI has been demonstrated in the human brain as well as in the human hand and wrist by several groups^{7–15}. Results from late 2013 demonstrate *in vivo* 2D images of the human brain (pre-polarized to 80 mT) with (2.5×1.9) mm² in-plane resolution over a (10×10) cm² region of interest and a 100 mm thick slice, acquired in ~26 minutes¹⁶. Very recent results from the Los Alamos ULF effort demonstrate 3D images of the human brain (pre-polarized to 100 mT) with $(2.1 \times 2.4 \times 15)$ mm³ resolution (5 slices) in 67 minutes¹⁵.

Although SQUIDs are the most technically mature of the non-inductive magnetometers used at ULF, several alternative detection technologies have been explored. Optical measurement of nitrogen-vacancy (NV) color centers in diamond^{17–19} form the basis of robust solid-state magnetometers with unmatched magnetic field sensitivity at nanoscale resolutions. As of yet, however, NV-diamond magnetometers do not provide obvious benefits for human scale MRI. Atomic magnetometers (AM) have also been applied to pre-polarized NMR²⁰ and MRI^{21,22}, and improvements in these devices have resulted in a magnetic field sensitivity approaching SQUID performance²³ without the need for cryogenics. The first attempt at imaging the living human brain with an atomic magnetometer was reported in 2013²⁴. In this work, nuclear spins are pre-polarized at 80 mT and detection is performed at 4 mT. Despite the ultra-high sensitivity and dynamic range of the AM magnetometer, the setup as described provides limited 3D coverage and significant improvement in resolution and SNR (Signal-to-Noise Ratio) is needed in order to clearly discern anatomical features, which will inevitably increase the acquisition time.

Independent of which detection technology is used, all pre-polarized ULF MRI suffers from intrinsically long acquisition times, most of which is incompressible, that result from the time needed to generate nuclear polarization. In the present work, we demonstrate fast and efficient brain ULF MRI at 6.5 mT with no pre-polarization nor cryogenics, combining under-sampling strategies with a high performance fully refocused steady-state-based acquisition in a simple, inexpensive system. With a novel inductive single channel detector, we report the fastest 3D MRI of the living human brain in the ULF regime compared to the state-of-the-art as reported in the literature^{11,12,15,16,24}.

Results

Ultra-low field acquisition strategy. High performance imaging at ultra-low magnetic field focuses on significantly reducing acquisition time using fast imaging techniques. Here, fast imaging was enabled using 3D balanced steady state free precession sequences (b-SSFP)²⁵. Originally described by Carr in 1958 as a technique for improving the signal-to-noise ratio (SNR) in NMR experiments²⁶, b-SSFP was implemented as an efficient acquisition strategy for MRI in 1986 by Oppelt *et al.*²⁷, and extensively investigated in the early 2000s^{25,28–32}. Unlike traditional gradient- and spin-echo techniques, b-SSFP sequences dynamically refocus spin magnetization following measurement, eliminating the extra delays typically used for T_2 decay and T_1 recovery. This considerably reduces acquisition times and provides the highest SNR per unit time of all imaging sequences^{25,27}. These sequences are very sensitive to the amount of spin dephasing that occurs between consecutive RF pulses (the pulse repetition time, TR), and typical banding artifacts are expected to appear within a range of $\pm 1/(2 \cdot TR)$ Hz that result from inhomogeneity in the static magnetic field²⁵. This sets a strict requirement on the absolute field homogeneity over the field-of-view (FOV), which for operation at 3 T is typically at the sub-PPM level.

In the millitesla regime, however, the fractional homogeneity requirement is three orders of magnitude lower, significantly easing the engineering burden for low-field magnet design. With a current TR = 22.5 ms, our b-SSFP sequence is completely immune to banding artifacts for up to 160 ppm inhomogeneity at 6.5 mT. Furthermore, magnetic susceptibility differences are significantly reduced at ULF, preventing off-resonance b-SSFP artifacts. As a result, provided reasonable magnetic field homogeneity, b-SSFP at very low magnetic field alleviates the necessity of ultra-short TRs and provides good image quality over a large FOV without the need for sophisticated ultrafast gradient power amplifiers. Our 6.5 mT MRI scanner³³ (Fig. 1) was upgraded for improved B_0 stability³⁴, and was used for all the low-field b-SSFP experiments described here.

RF Coil design. The design of inductive detection coils for use in ULF MRI presents a different set of challenges to those present in conventional high-field MRI. In particular, issues of coil resistance and

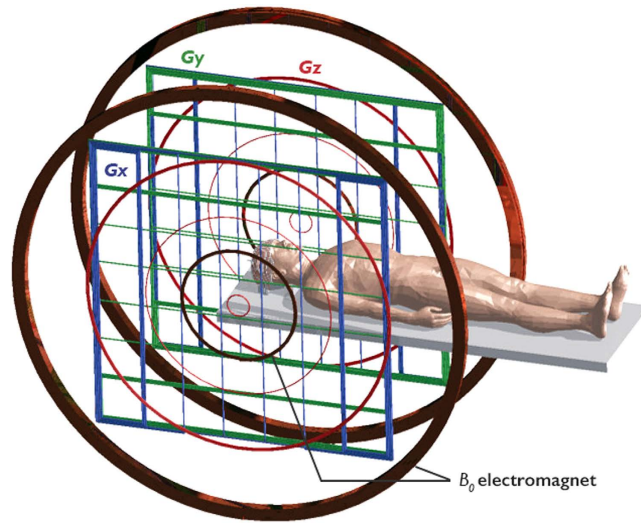


Figure 1. Ultra-low field MRI system. Custom built biplanar 6.5 mT electromagnet with biplanar gradients (Gx, Gy, and Gz). The diameter of the outermost B_0 coil is 220 cm. The subject lays supine in the scanner and a custom built single channel transmit/receive spiral head coil wound with litz wire for operation at 276 kHz is placed to cradle the head.

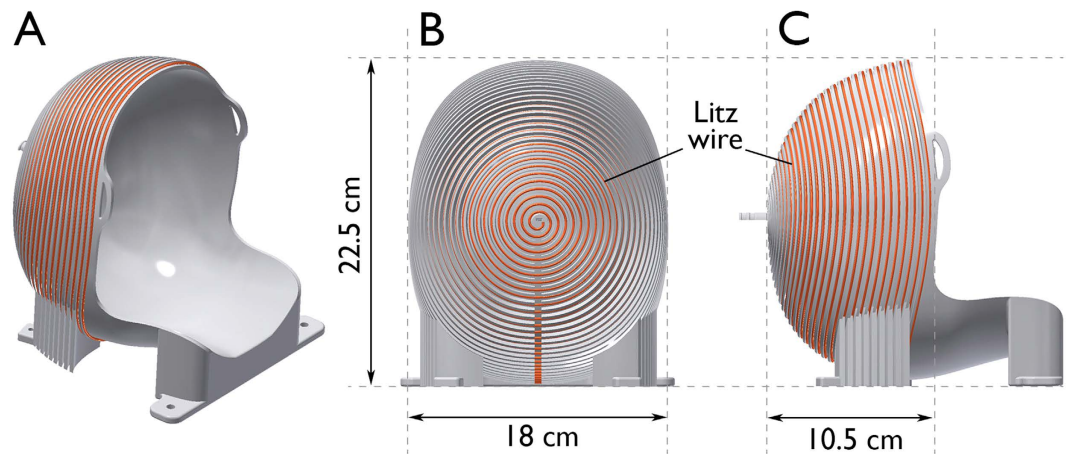


Figure 2. 3D renderings of the single channel form-fitting head coil. (A) isometric, (B) back, and (C) side views are shown. The final design was 3D printed on a Fortus 360 mc printer (Stratasys, Eden Prairie, MN, USA) in polycarbonate using fused deposition modeling technology. The 30-turn spiral was wound with Type 1 40/38 Litz wire, parallel resonated to 276 kHz, and capacitively matched to 50 ohms.

probe bandwidth manifest differently. In conventional MRI, the dominant source of noise is the presence of small currents in the lossy sample (the so-called “body noise” regime) to which a characteristic sample resistance R_s is attributed. Both the sample and the coil contribute to Johnson noise but in practice R_s is much larger than the coil resistance R_c (i.e. $R_s \gg R_c$), and thus R_c can be neglected in SNR calculations. However, at low field, R_s becomes much smaller and R_c becomes the dominant noise contribution (i.e., the so-called Johnson noise dominated regime). To minimize the coil resistance in a simple design, larger diameter wire or stranded litz wire can be used, but one needs to consider the impact this has on coil bandwidth. Given the maximum imaging gradient strength of ~ 1 mT/m attainable in our 6.5 mT electromagnet Low Field Imager (LFI), a 20 cm (head-sized) FOV will span a frequency encode bandwidth of ~ 10 kHz. This sets the minimum bandwidth needed for the detection circuit so as to not significantly convolve the coil response function with the object being imaged. At our Larmor frequency of 276 kHz, this corresponds to a maximum coil Q of ~ 30 . A single channel inductive coil for operation at 276 kHz (Fig. 2) was designed and built using 3D printing fused deposition modeling technology and multi-strand litz wire³⁵. A 30-turn 3D Archimedean spiral with an aligned turn-to-turn distance of 5.6 mm guided wire placement, thus ensuring that \vec{B}_1 produced by the spiral pattern is everywhere orthogonal to the main magnetic field \vec{B}_0 . The hemispheric spiral design results in a very homogeneous magnetic field^{36,37}

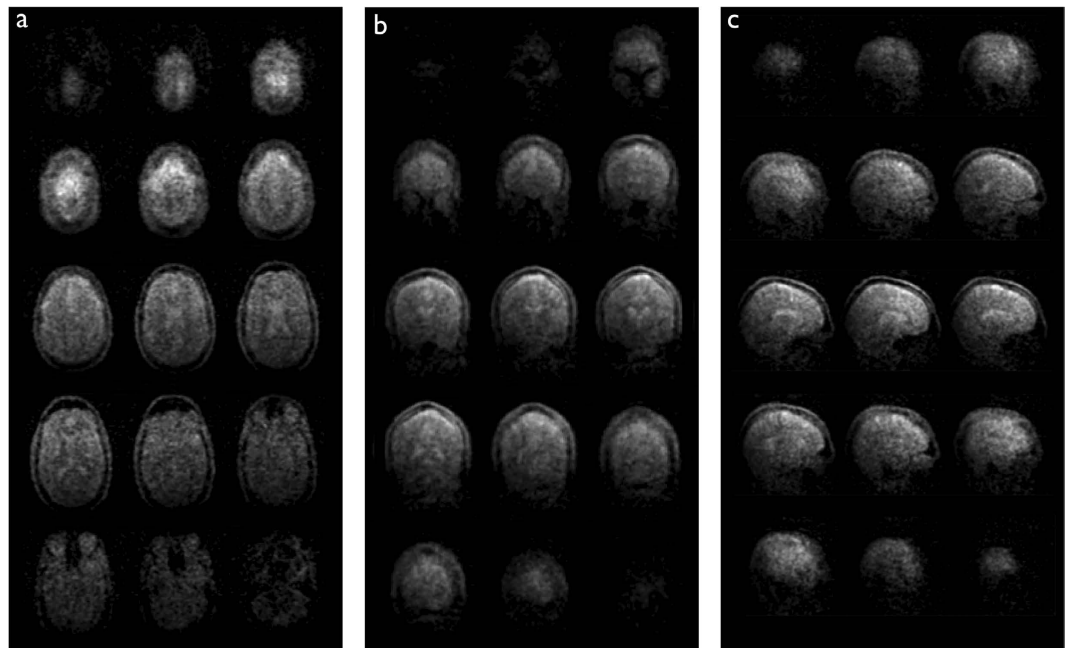


Figure 3. 3D images of the living brain acquired in 6 minutes at 6.5 mT in (a) axial, (b) coronal, and (c) sagittal orientation. The corresponding maximum SNRs are a. 15, b. 21, and c. 16. Acquisition matrix: $64 \times 75 \times 15$, voxel size: a. $(2.5 \times 3.5 \times 8.5) \text{ mm}^3$, b. $(2.5 \times 3.5 \times 11.5) \text{ mm}^3$, and c. $(2.5 \times 3.5 \times 14.4) \text{ mm}^3$.

over the volume of interest, making it suitable for both RF transmit and receive. The number of turns in the coil was chosen to obtain the inductance needed to achieve the desired Q . Litz wire was preferred in this low frequency application due to its lower AC resistance compared to solid copper wire of the same physical size.

Image reconstruction and processing. MRI images are reconstructed from frequency- and phase-encoded information in the k -space formalism^{38,39}. Previously, we described our use of under-sampling strategies to accelerate low-field imaging³⁴. We make use of this here by randomly sampling 50% of k -space using a variable density Gaussian pattern. The variable density Gaussian sampling pattern emphasizes sampling in the center of k -space, where most of the information is located, and randomly skips lines near the edges. The resulting images do not exhibit coherent artifacts, such as typical wrap-around ghosts due to FOV contraction. Missing values in the acquired k -space were set to zero. The standard deviation of the sampling pattern as a fraction of the FOV was optimized to preserve adequate high-frequency information. Once reconstructed, the images were apodized and processed using Perona and Malik anisotropic diffusion filtering^{40,41} (ADF). ADF is a powerful denoising filter that convolves images of interest with adaptive Gaussian kernels. The Perona and Malik approach works as an iterative multi-scale smoothing and edge detection process that removes noise but prevents image blurring by adjusting filter sharpness as a function of signal intensity gradients.

In vivo brain MRI at 6.5 mT. Three-dimensional under-sampled images acquired at 6.5 mT in 6 minutes are shown in Fig. 3 for each of the three spatial orientations (axial, coronal, and sagittal). The maximum image SNR was computed from the ratio of maximum signal amplitude to the standard deviation over a user defined noise region; SNR of 15, 21, and 16 were measured in axial, coronal, and sagittal orientations respectively. With a maximum gradient strength of $\sim 1 \text{ mT} \cdot \text{m}^{-1}$ and maximal slew rate of $0.7 \text{ mT} \cdot \text{m}^{-1} \cdot \text{ms}^{-1}$, no artifacts from concomitant field effect are seen over the 20 cm field of view. The sinuses are easily recognizable in black on the images, as well as the skull. Surrounding the brain, we can identify the dura in bright grey on the coronal and sagittal images (Fig. 3b,c). In the brain, the two hemispheres and the cerebellum are distinct, and cortical tissue can be distinguished from white matter. Liquid compartments, here CSF, appear in bright grey and white. Images acquired in the axial orientation are compared to images acquired in the same subject at high magnetic field (3 T) using traditional T_1 , T_2 , and proton density (PD) weighted sequences (Fig. 4). In b-SSFP, contrast is related to the T_2/T_1 ratio of the imaged sample²⁵. At high field, liquids and tissue typically have rather different relaxation times but at 6.5 mT their ratio (T_2/T_1) is of order unity resulting in the distinct PD-weighted contrast of Fig. 4b. Most of the anatomic features seen at 3 T can be identified in the ultra-low-field scans. Figure 5 compares b-SSFP at 3 T to 0.0065 T.

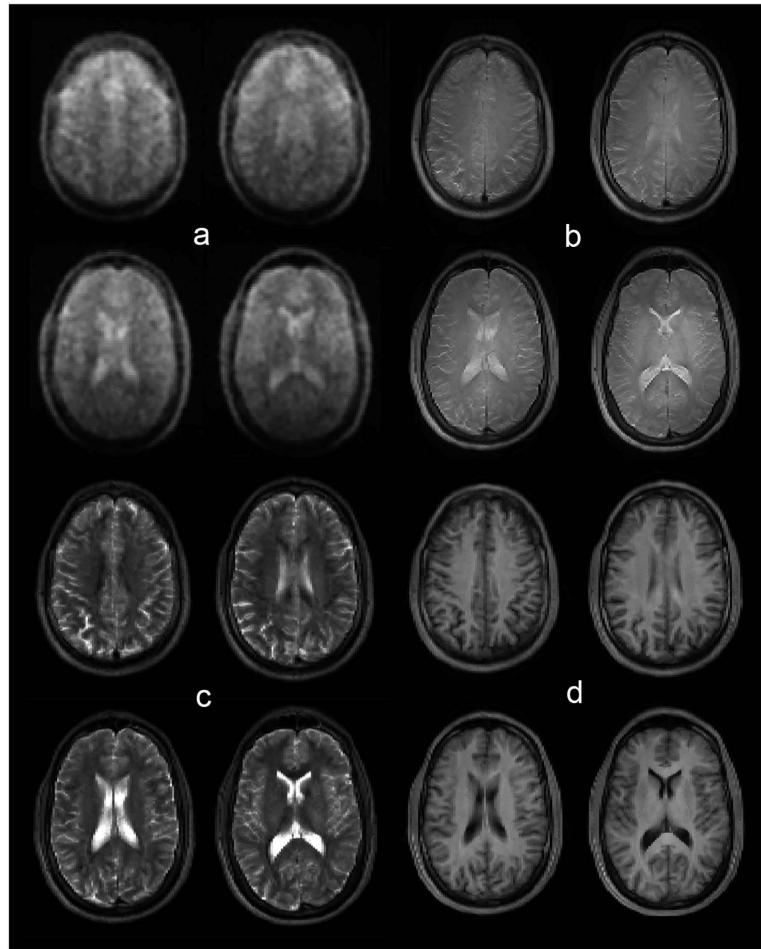


Figure 4. Comparison of single channel ULF MRI to 32-channel high magnetic field scans. (a) b-SSFP at 6.5 mT. **(b–d)**, PD, T_2 , and T_1 weighted contrast at 3 T, respectively. Most of the anatomic features seen at higher magnetic field can be identified on the ultra-low field scans. At low field, T_2 approaches T_1 , and the resulting image contrast in **(a)** is very similar to PD-weighting **(b)**.

The maximum SNR in the high field (HF) b-SSFP image is 317. In order to interpret the difference in SNR between the HF and the ULF scans, we scale the HF image SNR by a factor corresponding to the difference in the ULF spatial resolution ($2.5 \times 3.5 \times 8.5$ in the axial orientation), and by a second factor to account for signal averaging as done at ULF (Fig. 5b, NA = 160). The SNR in the downsampled HF scan is equivalent to $317 \times (2.5 \times 3.5 \times 8.5) \times \sqrt{160} \approx 300000$, which gives the ratio $\frac{SNR_{3T}}{SNR_{0.0065}} \approx 8300$ in the axial orientation. If we assume similar coil performance, and neglect the difference in magnetization at steady state for the two magnetic fields, the resulting 8300-fold difference in SNR agrees reasonably well with the simplified approximation that SNR increases with magnetic field to the 3/2 power⁴², here $460^{3/2} = 9866$. Strong banding artifacts appear at high field (Fig. 5a, yellow arrows), mainly due to magnetic susceptibility differences at the air-tissue interface. At 276 kHz, on the other hand, no imaging artifact is seen over a 20 cm FOV despite a $3 \times$ longer TR (Fig. 5b). Our results demonstrate excellent immunity to magnetic field inhomogeneity of the order of ± 22 Hz, i.e., 160 ppm at 6.5 mT.

Discussion

The work presented here demonstrates the shortest acquisition times and highest SNR per unit time in ULF MRI to date owing to our use of modern sparse sampling strategies and a fully refocused sequence in an optimized electromagnet scanner. These images were acquired without pre-polarization techniques, at a fixed magnetic field and with a simple single channel inductive detector. With an eye towards optimization, we note that for a given spatial resolution, the minimum TR—and consequently the total scan time—is limited by the maximum attainable time-integrated gradient strength. The maximum gradient strength in the LFI is currently $\sim 1 \text{ mT} \cdot \text{m}^{-1}$, resulting in a minimum TR of ~ 23 ms. Weak gradients especially impact phase encoding in balanced sequences like b-SSFP, as every phase-encode pulse is paired with an opposite polarity rewinding pulse. An increase in gradient strength would allow shorter

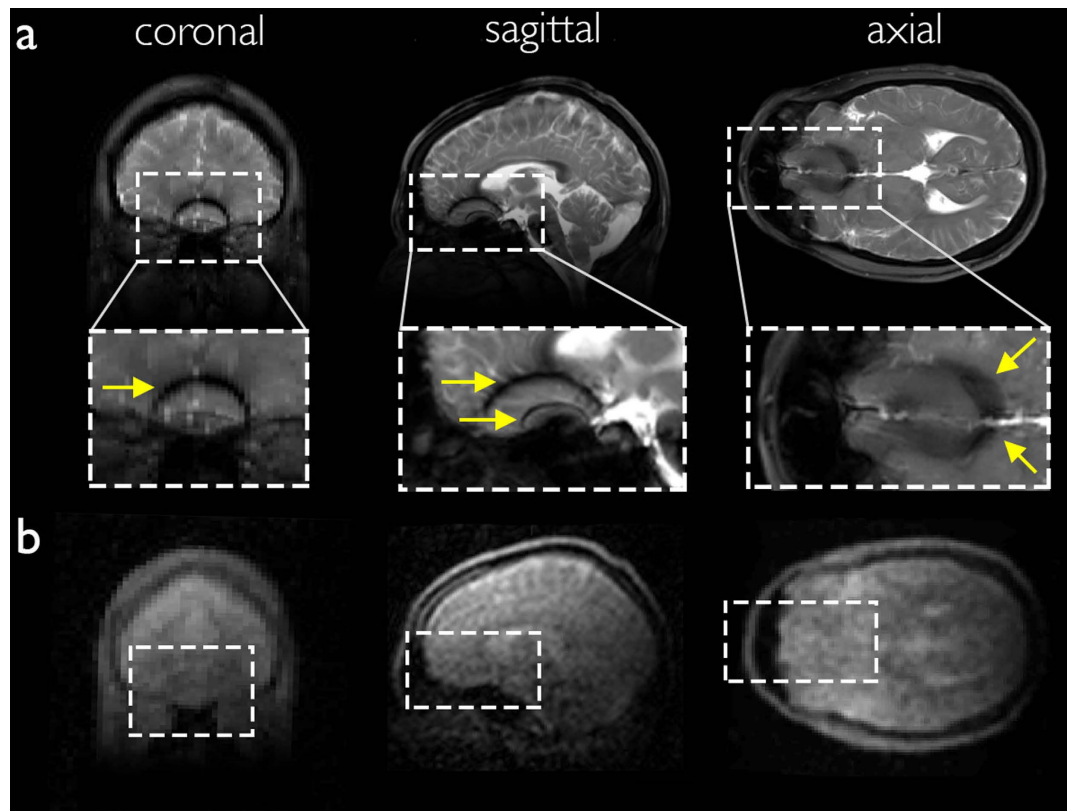


Figure 5. Comparison of b-SFP images at (a) 3T and (b) 6.5 mT. Strong banding artifacts appear at high magnetic field (yellow arrows) in all orientations (coronal, sagittal, and axial) whereas no artifact is seen in the images acquired at ultra-low field.

phase encode pulses, thus decreasing total imaging time while maintaining SNR, provided that image distortion from non-linear magnetic fields that accompany the desired encoding gradient (the so called “concomitant field” artifacts⁴³) can be mitigated. At 6.5 mT, an increase in gradient strength in the range of $2\text{--}5\times$, combined with efficient strategies to eliminate concomitant field artifacts^{44–46}, can reasonably be envisioned. Additionally, improvements in the electronic noise floor can go a long way to improving scanner sensitivity. In our system, the scanner noise floor is dominated by poor filtering of the high current lines from the gradient power amplifiers into the RF shielded enclosure of the LFI. More effective filtering of electronic noise coming from our gradient power amplifiers would reduce our system noise floor by a measured factor of 3, thus decreasing the total acquisition time by another factor of $3^2 = 9$. As SNR increases with magnetic field to the $3/2$ power⁴², a simple doubling of magnetic field would result in a sequence about 8 times faster with similar SNR. In the case of human brain imaging, images with similar resolution and SNR as presented here could be then acquired in less than 3 seconds in such an optimized scanner.

A key challenge in obtaining clinically relevant MRI images at ULF is the ability to acquire T_1 and/or T_2 relaxation-weighted images, and thereby provide contrast to different types of tissue. Typically, magnetization prepared gradient-echo, and spin-echo sequences are used to obtain relaxation-weighted images, but these types of imaging experiments become prohibitively time consuming at ultra-low magnetic fields where signal averaging and recovery of the longitudinal magnetization are required. We have investigated a new strategy to provide contrast based on b-SFP called “magnetic resonance fingerprinting” (MRF)⁴⁷, and have successfully started its implementation at 6.5 mT.⁴⁸

Finally, theoretical frameworks exist that allow image reconstruction of highly undersampled datasets with multiple channel acquisition^{49–56}. Acquisition schemes combining high undersampling rates with parallel imaging techniques such as SENSE⁵⁷ or GRAPPA⁵⁸ could reduce the total acquisition time even further, to less than a second. Recent work from Murphy *et al.*⁵⁹ successfully mitigates the computational expense by exploiting massively parallelized computing.

We contend that ULF MRI scanners operating at this expected level of performance could complement traditional MRI by relieving hospital congestion and shortening triage delays. Outside of the radiology suite, mobile ULF scanners might be deployable during military conflicts or during sport events and enable the acquisition of immediate after-trauma knowledge, typically in the case of traumatic brain

injuries. Finally, ULF MRI technology may allow resource-poor environments access to MRI systems, without the strict siting requirements and high costs of conventional scanners.

Methods

Consent and IRB. Informed consent was obtained from each healthy human volunteer prior to the experiment in accordance with the Human Research Committee of the Massachusetts General Hospital (MGH). All MRI imaging was performed in accordance with approved guidelines and regulations, using experimental protocols that were approved by the MGH Human Research Committee.

Ultra-low field MRI. All ULF MR images were acquired at 6.5 mT in a healthy human volunteer with the 30-turn single channel well-fitting spiral head coil described above (Fig. 2). The subject was placed supine, head first into the electromagnet. The b-SSFP 3D sequence with under-sampling rate of 50%, acquisition matrix of $64 \times 75 \times 15$, at a spatial resolution of $(2.5 \times 3.5 \times 8.5) \text{ mm}^3$, $(2.5 \times 3.5 \times 14.4) \text{ mm}^3$, and $(2.5 \times 3.5 \times 11.5) \text{ mm}^3$, was used in axial, sagittal and coronal orientations, respectively. $\text{TR} = 22.5 \text{ ms}$, $\text{TE} = 11 \text{ ms}$. Total acquisition time was 6 minutes for images with number of averages (NA) = 30 (Fig. 3), and 32 minutes with NA = 160 (Figs 4 and 5). All acquired data were processed using anisotropic diffusion filtering and interpolated in Fourier domain in two dimensions to a 96×96 matrix.

High field MRI. Reference high magnetic field images of the head were acquired in the same subject at 3 T on a standard whole-body scanner (Skyra, Siemens Healthcare) using a 32-channel head receiver coil with the subject in a supine position. All high field sequences were acquired with an acceleration factor of 2. Proton density, T_2 , and T_1 weighted sequences were acquired with matrix = $256 \times 256 \times 176$ at a spatial resolution of $(1 \times 1 \times 1) \text{ mm}^3$, with total acquisition times of 10 minutes, 5 minutes and 6 minutes respectively. A b-SSFP sequence was acquired with matrix = $256 \times 256 \times 192$ at a spatial resolution of $(1 \times 1 \times 1) \text{ mm}^3$, and NA = 1. The total acquisition time was ~3 minutes.

References

- Sepponen, R. E., Sipponen, J. T. & Sivula, A. Low Field (0.02 T) Nuclear Magnetic Resonance Imaging of the Brain. *Journal of Computer Assisted Tomography* **9**, 237 (1985).
- Macovski, A. & Conolly, S. Novel approaches to low-cost MRI. *Magnetic Resonance in Medicine* **30**, 221–230 (1993).
- Venook, R. D. *et al.* Prepolarized magnetic resonance imaging around metal orthopedic implants. *Magnetic Resonance in Medicine* **56**, 177–186 (2006).
- Robert Kraus, J., Espy, M., Magnelind, P. & Volegov, P. *Ultra-Low Field Nuclear Magnetic Resonance*. (Oxford University Press, 2014). doi: 10.1093/med/9780199796434.001.0001/med-9780199796434.
- Clarke, J. & Braginski, A. I. *The SQUID Handbook: Fundamentals and Technology of SQUIDS and SQUID Systems, Volume I*. (Wiley-VCH Verlag GmbH & Co. KGaA, 2004).
- Clarke, J., Hatridge, M. & Mölle, M. SQUID-Detected Magnetic Resonance Imaging in Microtesla Fields. *Annu. Rev. Biomed. Eng.* **9**, 389–413 (2007).
- Zotev, V. S. *et al.* Parallel MRI at microtesla fields. *Journal of Magnetic Resonance* **192**, 197–208 (2008).
- Zotev, V. S. *et al.* Microtesla MRI of the human brain combined with MEG. *Journal of Magnetic Resonance* **194**, 115–120 (2008).
- Zotev, V. S. *et al.* SQUID-based microtesla MRI for *in vivo* relaxometry of the human brain. *Applied Superconductivity, IEEE Transactions on* **19**, 823–826 (2009).
- Savukov, I. *et al.* Non-cryogenic anatomical imaging in ultra-low field regime: Hand MRI demonstration. *Journal of Magnetic Resonance* **211**, 101–108 (2011).
- Magnelind, P. E. *et al.* Co-Registration of Interleaved MEG and ULF MRI Using a 7 Channel Low-Tc SQUID System. *Applied Superconductivity, IEEE Transactions on* **21**, 456–460 (2011).
- Vesonen, P. T. *et al.* Hybrid ultra-low-field MRI and magnetoencephalography system based on a commercial whole-head neuromagnetometer. *Magnetic Resonance in Medicine* **69**, 1795–1804 (2012).
- Espy, M., Matlashov, A. & Volegov, P. SQUID-detected ultra-low field MRI. *Journal of Magnetic Resonance* **228**, 1–15 (2013).
- Savukov, I., Karaulanov, T., Wurden, C. J. V. & Schultz, L. Non-cryogenic ultra-low field MRI of wrist-forearm area. *Journal of Magnetic Resonance* **233**, 103–106 (2013).
- Espy, M. A. *et al.* Progress Toward a Deployable SQUID-Based Ultra-Low Field MRI System for Anatomical Imaging. *Applied Superconductivity, IEEE Transactions on* **25**, 1–5 (2015).
- Inglis, B. *et al.* MRI of the human brain at 130 microtesla. *Proceedings of the National Academy of Sciences of the United States of America* **110**, 19194–19201 (2013).
- Maze, J. R. *et al.* Nanoscale magnetic sensing with an individual electronic spin in diamond. *Nature* **455**, 644–647 (2008).
- Taylor, J. M. *et al.* High-sensitivity diamond magnetometer with nanoscale resolution. *Nat Phys* **4**, 810–816 (2008).
- Devience, S. J. *et al.* Nanoscale NMR spectroscopy and imaging of multiple nuclear species. *Nat Nano* **10**, 129–134 (2015).
- Savukov, I. M. & Romalis, M. V. NMR detection with an atomic magnetometer. *Phys. Rev. Lett.* **94**, 123001 (2005).
- Xu, S., Rochester, S. M., Yashchuk, V. V., Donaldson, M. H. & Budker, D. Construction and applications of an atomic magnetic gradiometer based on nonlinear magneto-optical rotation. *Review of Scientific Instruments* **77**, 083106 (2006).
- Xu, S. *et al.* Magnetic resonance imaging with an optical atomic magnetometer. *Proceedings of the National Academy of Sciences* **103**, 12668–12671 (2006).
- Kominis, I. K., Kornack, T. W., Allred, J. C. & Romalis, M. V. A subfemtotesla multichannel atomic magnetometer. *Nature* **422**, 596–599 (2003).
- Savukov, I. & Karaulanov, T. Magnetic-resonance imaging of the human brain with an atomic magnetometer. *Applied Physics Letters* **103**, 043703 (2013).
- Scheffler, K. & Lehnhardt, S. Principles and applications of balanced SSFP techniques. *European Radiology* **13**, 2409–2418 (2003).
- Carr, H. Steady-State Free Precession in Nuclear Magnetic Resonance. *Physical Review* **112**, 1693–1701 (1958).
- Oppelt, A. *et al.* FISP—a new fast MRI sequence. *Electromedica* **54**, 15–18 (1986).
- Plein, S. *et al.* Steady-state free precession magnetic resonance imaging of the heart: Comparison with segmented k-space gradient-echo imaging. *Journal of Magnetic Resonance Imaging* **14**, 230–236 (2001).

29. Scheffler, K., Heid, O. & Hennig, J. Magnetization preparation during the steady state: Fat-saturated 3D TrueFISP. *Magnetic Resonance in Medicine* **45**, 1075–1080 (2001).
30. Deshpande, V. S. *et al.* 3D magnetization-prepared true-FISP: A new technique for imaging coronary arteries. *Magnetic Resonance in Medicine* **46**, 494–502 (2001).
31. Miller, K. L. *et al.* Functional brain imaging using a blood oxygenation sensitive steady state. *Magnetic Resonance in Medicine* **50**, 675–683 (2003).
32. Schmitt, P. *et al.* Inversion recovery TrueFISP: Quantification of T1, T2, and spin density. *Magnetic Resonance in Medicine* **51**, 661–667 (2004).
33. Tsai, L. L., Mair, R. W., Rosen, M. S., Patz, S. & Walsworth, R. L. An open-access, very-low-field MRI system for posture-dependent ^3He human lung imaging. *Journal of Magnetic Resonance* **193**, 274–285 (2008).
34. Sarraçanie, M., Armstrong, B. D., Stockmann, J. & Rosen, M. S. High speed 3D overhauser-enhanced MRI using combined b-SSFP and compressed sensing. *Magnetic Resonance in Medicine* **71**, 735–745 (2014).
35. LaPierre, C. D., Sarraçanie, M., Waddington, D. E. J. & Rosen, M. S. A single channel spiral volume coil for *in vivo* imaging of the whole human brain at 6.5mT, Presented at the International Society of Magnetic Resonance in Medicine, 5902, Toronto (2015).
36. Harpen, M. D. The spherical birdcage resonator. *Journal of Magnetic Resonance* (1969) **94**, 550–556 (1991).
37. Everett, J. E. & Osemeikhian, J. E. Spherical coils for uniform magnetic fields. *J. Sci. Instrum.* **43**, 470 (1966).
38. Ljunggren, S. A simple graphical representation of fourier-based imaging methods. *Journal of Magnetic Resonance* (1969) **54**, 338–343 (1983).
39. Twieg, D. B. The k-trajectory formulation of the NMR imaging process with applications in analysis and synthesis of imaging methods. *Med Phys* **10**, 610–621 (1983).
40. Perona, P. & Malik, J. Scale-space and edge detection using anisotropic diffusion. *IEEE Trans. Pattern Anal. Machine Intell.* **12**, 629–639 (1990).
41. Weickert, J. In *Lecture Notes in Computer Science* (eds Haar Romeny, ter, B., Florack, L., Koenderink, J. & Viergever, M.) **1252**, 1–28–28 (Springer Berlin Heidelberg, 1997).
42. Hoult, D. I. & Richards, R. E. The signal-to-noise ratio of the nuclear magnetic resonance experiment. *Journal of Magnetic Resonance* **24**, 71–85 (1976).
43. Sica, C. T. & Meyer, C. H. Concomitant gradient field effects in balanced steady-state free precession. *Magnetic Resonance in Medicine* **57**, 721–730 (2007).
44. Myers, W. R., Mößle, M. & Clarke, J. Correction of concomitant gradient artifacts in experimental microtesla MRI. *Journal of Magnetic Resonance* **177**, 274–284 (2005).
45. Volegov, P. L., Mosher, J. C., Espy, M. A. & Kraus, R. H., Jr. On concomitant gradients in low-field MRI. *Journal of Magnetic Resonance* **175**, 103–113 (2005).
46. Nieminen, J. O. & Ilmoniemi, R. J. Solving the problem of concomitant gradients in ultra-low-field MRI. *Journal of Magnetic Resonance* **207**, 213–219 (2010).
47. Ma, D. *et al.* Magnetic resonance fingerprinting. *Nature* **495**, 187–192 (2013).
48. Sarraçanie, M., Cohen, O. & Rosen, M. S. 3D Balanced-EPI Magnetic Resonance Fingerprinting at 6.5 mT, Presented at the International Society of Magnetic Resonance in Medicine, 6266, Toronto (2015).
49. Block, K. T., Uecker, M. & Frahm, J. Undersampled radial MRI with multiple coils. Iterative image reconstruction using a total variation constraint. *Magnetic Resonance in Medicine* **57**, 1086–1098 (2007).
50. Liang, D., Liu, B., Wang, J. & Ying, L. Accelerating SENSE using compressed sensing. *Magnetic Resonance in Medicine* **62**, 1574–1584 (2009).
51. Otazo, R., Kim, D., Axel, L. & Sodickson, D. K. Combination of compressed sensing and parallel imaging for highly accelerated first-pass cardiac perfusion MRI. *Magnetic Resonance in Medicine* **64**, 767–776 (2010).
52. Trzasko, J. D. *et al.* Sparse-CAPR: Highly accelerated 4D CE-MRA with parallel imaging and nonconvex compressive sensing. *Magnetic Resonance in Medicine* **66**, 1019–1032 (2011).
53. Ying, L. & Sheng, J. Joint image reconstruction and sensitivity estimation in SENSE (JSENSE). *Magnetic Resonance in Medicine* **57**, 1196–1202 (2007).
54. Knoll, F., Clason, C., Bredies, K., Uecker, M. & Stollberger, R. Parallel imaging with nonlinear reconstruction using variational penalties. *Magnetic Resonance in Medicine* **67**, 34–41 (2012).
55. Huang, F. *et al.* A rapid and robust numerical algorithm for sensitivity encoding with sparsity constraints: Self-feeding sparse SENSE. *Magnetic Resonance in Medicine* **64**, 1078–1088 (2010).
56. Lustig, M. & Pauly, J. M. SPIRiT: Iterative self-consistent parallel imaging reconstruction from arbitrary k-space. *Magnetic Resonance in Medicine* **64**, 457–471 (2010).
57. Pruessmann, K. P., Weiger, M., Scheidegger, M. B. & Boesiger, P. SENSE: sensitivity encoding for fast MRI. *Magnetic Resonance in Medicine* **42**, 952–962 (1999).
58. Griswold, M. A. *et al.* Generalized autocalibrating partially parallel acquisitions (GRAPPA). *Magnetic Resonance in Medicine* **47**, 1202–1210 (2002).
59. Murphy, M. *et al.* Fast L1-SPIRiT Compressed Sensing Parallel Imaging MRI: Scalable Parallel Implementation and Clinically Feasible Runtime. *Medical Imaging, IEEE Transactions on* **31**, 1250–1262 (2012).

Acknowledgements

This work was supported by the U.S. Army Medical Research and Materiel Command (USAMRMC), Defense Medical Research and Development Program (DMRDP) award W81XWH-11-2-0076 (DM09094). N.S. was supported by the Swiss National Science Foundation (P300P2_147768). D.E.J.W. was supported by ANSTO and the Australian-American Fulbright Commission. This research was carried out at the Athinoula A. Martinos Center for Biomedical Imaging at the Massachusetts General Hospital, using resources provided by the Center for Functional Neuroimaging Technologies, P41EB015896, a P41 Biotechnology Resource Grant supported by the National Institute of Biomedical Imaging and Bioengineering (NIBIB), National Institutes of Health. The authors thank Bruce Rosen and Ronald Walsworth for their comments on this manuscript.

Author Contributions

M.S., C.D.L., N.S., D.E.J.W., T.W. and M.S.R. all contributed significantly to the work presented in this manuscript.

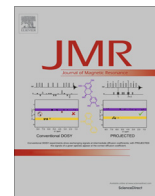
Additional Information

Competing financial interests: The authors declare no competing financial interests.

How to cite this article: Saracanie, M. *et al.* Low-Cost High-Performance MRI. *Sci. Rep.* **5**, 15177; doi: 10.1038/srep15177 (2015).



This work is licensed under a Creative Commons Attribution 4.0 International License. The images or other third party material in this article are included in the article's Creative Commons license, unless indicated otherwise in the credit line; if the material is not included under the Creative Commons license, users will need to obtain permission from the license holder to reproduce the material. To view a copy of this license, visit <http://creativecommons.org/licenses/by/4.0/>



Transmit Array Spatial Encoding (TRASE) using broadband WURST pulses for RF spatial encoding in inhomogeneous B_0 fields

Jason P. Stockmann^{a,*}, Clarissa Z. Cooley^a, Bastien Guerin^{a,c}, Matthew S. Rosen^{a,b,c}, Lawrence L. Wald^{a,c}

^aA.A. Martinos Center for Biomedical Imaging, Massachusetts General Hospital, Charlestown, MA 02129, United States

^bDepartment of Physics, Harvard University, Cambridge, MA 02141, United States

^cHarvard Medical School, Boston, MA, United States

ARTICLE INFO

Article history:

Received 14 January 2016

Revised 17 March 2016

Accepted 7 April 2016

Available online 8 April 2016

Keywords:

Transmit Array Spatial Encoding

Swept RF pulses

Low field imaging

Portable MRI

Quadratic phase modulation

ABSTRACT

Transmit Array Spatial Encoding (TRASE) is a promising new MR encoding method that uses transmit RF (B_1^+) phase gradients over the field-of-view to perform Fourier spatial encoding. Acquisitions use a spin echo train in which the transmit coil phase ramp is modulated to jump from one k -space point to the next. This work extends the capability of TRASE by using swept radiofrequency (RF) pulses and a quadratic phase removal method to enable TRASE where it is arguably most needed: portable imaging systems with inhomogeneous B_0 fields. The approach is particularly well-suited for portable MR scanners where (a) inhomogeneous B_0 fields are a byproduct of lightweight magnet design, (b) heavy, high power-consumption gradient coil systems are a limitation to siting the system in non-conventional locations and (c) synergy with the use of spin echo trains is required to overcome intra-voxel dephasing (short T_2^*) in the inhomogeneous field. TRASE does not use a modulation of the B_0 field to encode, but it does suffer from secondary effects of the inhomogeneous field. Severe artifacts arise in TRASE images due to off-resonance effects when the RF pulse does not cover the full bandwidth of spin resonances in the imaging FOV. Thus, for highly inhomogeneous B_0 fields, the peak RF power needed for high-bandwidth refocusing hard pulses becomes very expensive, in addition to requiring RF coils that can withstand thousands of volts. In this work, we use swept WURST RF pulse echo trains to achieve TRASE imaging in a highly inhomogeneous magnetic field ($\Delta B_0/B_0 \sim 0.33\%$ over the sample). By accurately exciting and refocusing the full bandwidth of spins, the WURST pulses eliminate artifacts caused by the limited bandwidth of the hard pulses used in previous realizations of TRASE imaging. We introduce a correction scheme to remove the unwanted quadratic phase modulation caused by the swept pulses. Also, a phase alternation scheme is employed to mitigate artifacts caused by mixture of the even and odd-echo coherence pathways due to defects in the refocusing pulse. In this paper, we describe this needed methodology and demonstrate the ability of TRASE to Fourier encode in an inhomogeneous field ($\Delta B_0/B_0 \sim 1\%$ over the full FOV).

© 2016 Elsevier Inc. All rights reserved.

1. Introduction

A growing body of research explores the use of lightweight, low-field, portable magnetic resonance relaxometers and imaging systems for medical applications and materials analysis. Single sided scanners [1] such as the NMR-MOUSE [2] use portable permanent magnets for profiling and relaxometry. The NMR-MOUSE magnet's rapid field decay over the sensitive region is used to create 1D profiles of samples such as human skin [3].

* Corresponding author at: Athinoula A. Martinos Center for Biomedical Imaging, Massachusetts General Hospital, 149 Thirteenth Street, Suite 2301, Charlestown, MA 02129, United States.

E-mail address: jaystock@nmr.mgh.harvard.edu (J.P. Stockmann).

The NMR-MOUSE's capability has been extended to 2D [4] and 3D imaging [5], however the device can only image thin samples and is not applicable to brain imaging. Other approaches based on single-sided and "inside-out" magnets have been used for rock porosity analysis in oil well prospecting [6] and for assessing properties of soil and food [1]. Adding Fourier encoding to these systems in directions other than the readout (projection) direction is made difficult by the extremely inhomogeneous field.

A major difference between portable NMR systems and conventional MRI scanners is that, in the former, the main B_0 field is usually inhomogeneous. This concession can dramatically reduce the complexity of the device, thus minimizing weight, cost, and power requirements and enhancing portability. But this inhomogeneity introduces two significant obstacles to performing Fourier imaging

with conventional B_0 gradient encoding. First, the bandwidth of spins in the sample may become too broad to be excited by typical RF pulses (e.g. hard pulses) at safe RF power levels. Second, to perform traditional Fourier readout spatial encoding (and/or slice selection), the applied linear B_0 gradients must dominate the variations in the background B_0 field. Phase encoding in a spin echo sequence has been demonstrated in highly inhomogeneous fields [7], but 2D and 3D encoding with pure phase encoding are time-consuming since only one k -space point is acquired per echo, and moreover the need for gradient coils and power amplifiers can limit portability.

Nonetheless, light-weight, inhomogeneous MR scanners based on arrays of permanent magnets have been proposed as portable devices for human imaging. In one such approach [8], the background B_0 field variation is used as a “built-in” gradient field for acquiring generalized spin echo projections of the sample that can be reconstructed using iterative matrix solvers. This system still requires a method of encoding along the axis of rotation and the B_0 inhomogeneity (short T_2^*) requires the use of spin echo acquisitions.

Methods for creating long spin echo trains in highly inhomogeneous fields have been demonstrated using frequency-swept pulses that excite and refocus all spins over the sample with dramatically lower peak power levels compared to hard pulses [9,10]. In Ref. [9], frequency-swept pulses were played in a CPMG spin echo train to acquire echoes from a sample with a 120 kHz linewidth in an inhomogeneous B_0 field. Compared with hard pulses, the frequency-swept pulses provided a 3-fold or greater signal enhancement and corresponding increase in the spectral width of the acquired data (Fourier transform of the echoes).

Frequency-swept RF pulses have also been used as key components of spatial encoding schemes that provide improved robustness to B_0 inhomogeneity, including *MRI by steering resonance through space* (STEREO) [11] and *spatiotemporally-encoded MRI* (SPEN) [12–16]. Both methods use swept RF pulses to excite and/or refocus different Larmor frequency isochromats at different times. The focal point of the resulting quadratic phase profile is then steered across the object during readout using linear encoding gradients. While these methods show significant promise, they still rely on slewed linear B_0 gradient systems whose coils must overcome the B_0 inhomogeneities and whose power amplifiers and cooling systems are an encumbrance to remote siting and portability. Further, while they are being pursued for use in inhomogeneous fields, this class of methods has only been experimentally demonstrated with modest inhomogeneities (i.e. ~ 100 s of Hz) [11,12].

The Bloch–Siegert shift imparted by off-resonant RF pulses has been recently exploited for frequency [17] and phase [18] encoding using pure transmit RF field (B_1^+) spatial encoding. In this approach, an RF coil with a spatially varying B_1^+ amplitude along the encoding direction is used (typically a linear profile). When an off-resonant RF pulse is played on such a coil after spin excitation by a uniform B_1^+ coil, the spin phase becomes a function of position and can be used for spatial encoding. While early results in relatively homogeneous B_0 fields show promise, the utility of the method for highly inhomogeneous fields is limited by the trade-off between Bloch–Siegert encoding efficiency and off-resonance performance.

In the present work, we show that *Transmit Array Spatial Encoding* (TRASE) [19], a recently-introduced B_1^+ spatial encoding method, can be adapted for imaging in highly inhomogeneous B_0 fields without the use of external imaging gradients. TRASE uses B_1^+ phase gradients produced by tailored RF transmit coils to impart a progressively increasing spatial phase modulation to each echo in a spin echo train. The center point of each echo is a sample in k -space with the echo-train traversing a line in k -space (for 1D TRASE) analogous to conventional phase encoding with linear B_0 gradients. TRASE can be performed along any dimension for 1D, 2D, or 3D imaging using appropriate coils for generating B_1^+ phase gradients along each

desired encoding direction. This allows image formation without using conventional B_0 imaging gradients. High-resolution 2D TRASE images acquired in a 0.2 Tesla homogeneous field display comparable image quality to conventional B_0 gradient encoded images [20].

The TRASE method is best-suited for low field imaging where specific absorption rates (SAR) are lower, allowing long spin echo trains without significant RF heating. Adding to its versatility, TRASE is compatible with the use of parallel RF receive arrays [21] and parallel imaging approaches [22,23] for accelerated imaging using undersampled k -space data. Moreover, even though TRASE is a type of phase encoding, un-encoded signal outside the FOV does not alias into the image as a wrapping artifact, but instead manifests as line artifacts in the corner of the image [24]. Finally, since TRASE switches only RF gradient fields, it has the benefit of being silent.

TRASE is particularly appealing for portable MR systems since it only uses the transmit RF system for spatial encoding. This reduces or eliminates the need for high power gradient amplifiers as well as heavy, noisy gradient coils and their associated water cooling. The result is a dramatically simplified imaging system. As an independent encoding mechanism, TRASE can be used in highly inhomogeneous B_0 fields without requiring that the B_1^+ phase gradient dominate the variation in B_0 . This stands in contrast to other methods that have been proposed for portable MRI systems, such as STEREO [11], which still rely on a B_0 gradient system for spatial encoding.

Although TRASE appears well-suited for portable imagers and their spatially inhomogeneous fields, the excitation and refocusing pulses must cover the bandwidth of the spins in the imaging volume. If the full spin bandwidth is not covered, then off-resonance effects degrade performance by introducing flip angle and phase errors to spin isochromats outside the pulse bandwidth. Bloch simulations show that significant TRASE artifacts arise for refocusing pulse flip angles of less than 150° [25]. A recent paper states that for echo trains of hard pulses with duration t_p , “good” TRASE performance is achieved for sample bandwidths on the order of $0.1/t_p$ and “fair” performance was noted for bandwidths on the order of $0.2/t_p$ [20]. The authors suggest that TRASE could benefit from composite refocusing pulses, but do not explore the topic experimentally.

For proof-of-concept 1D imaging, we target a bandwidth of 30 kHz in a highly inhomogeneous human head-sized permanent magnet ($\Delta B_0/B_0 \sim 1\%$) [7]. For this field inhomogeneity, the use of hard pulses would require impractical peak power. For example, to achieve “fair” TRASE performance a refocusing pulse length of $\sim 6 \mu\text{s}$ would be required. This corresponds to an 83 kHz (1.9 mT) peak field, about 2 orders of magnitude higher than the field achievable using the body RF coil of conventional clinical scanners.

In this work, we demonstrate a method for overcoming off-resonance artifacts in TRASE imaging by replacing hard pulses with WURST frequency-swept pulses in the spin echo train [8]. The swept pulses minimize flip angle and phase errors resulting from the range of B_0 fields across the FOV. However, the WURST pulses introduce a quadratic phase across the excitation bandwidth. To mitigate the effect of this phase in TRASE imaging, we introduce a simple phase correction method to remove the quadratic phase modulation imparted by the swept pulses to even-numbered echoes in the train. This renders the entire echo train compatible with TRASE spatial encoding. We show experimental 1D TRASE images of two water phantoms in a field with a peak inhomogeneity range of 30 kHz. Some results were previously presented in abstract form [26].

2. Theory

In this section, we briefly review the use of RF pulses with linear frequency sweeps (quadratic phase sweeps) on the signal phase in

a spin echo train. We then discuss a simple correction method for removing the unwanted quadratic phase modulation from even-numbered echoes in the train, restoring a conventional echo shape and making the entire spin echo train usable for TRASE imaging.

As described by Kunz [27], when frequency-swept excitation and refocusing pulses are applied in the presence of a static inhomogeneous B_0 field, they impart a frequency-dependent phase to the spins. Assuming a symmetric frequency sweep around the Larmor frequency, the relevant phase of the spin isochromats following the $\pi/2$ excitation pulse is:

$$\phi_{\text{exc}}(f) = \pi f^2 / R_{\text{exc}} \quad (1)$$

and the phase imparted by the π refocusing pulse is:

$$\phi_{\text{ref}}(f) = 2\pi f^2 / R_{\text{ref}}, \quad (2)$$

where f is the frequency offset from the Larmor frequency and R is the RF pulse frequency sweep rate. Because the refocusing pulse inverts the phase profile imparted by the excitation pulse, the overall phase after an excitation pulse followed by a single refocusing pulse is:

$$\phi(f) = -\pi f^2 / R_{\text{exc}} + 2\pi f^2 / R_{\text{ref}}. \quad (3)$$

The quadratic phase imparted by the pulse pair vanishes if the sweep rates are set to $R_{\text{ref}} = 2R_{\text{exc}}$. For simple linear frequency sweeps, this condition is typically met by setting the duration of the refocusing pulse to be half the duration of the excitation pulse.

In swept pulse spin echo trains, this sweep rate condition ($R_{\text{ref}} = 2R_{\text{exc}}$) cancels quadratic phase in odd-numbered echoes, leaving these echoes with only conventional B_0 -based phase modulations. However, the quadratic phase modulation remains on even-numbered echoes. Here, the frequency-domain signal is multiplied by the quadratic phase profile (ϕ_{ref}) applied by the last, uncanceled refocusing pulse [28]. Likewise, the time-domain signal is convolved by the time-domain quadratic phase function [28]. Since the shape of the quadratic phase function is preserved under the Fourier transform, the time domain function is also a quadratic phase “chirp” kernel proportional to $\exp(i2\pi\beta t^2)$, where coefficient β depends on the sweep rate of the refocusing pulse.

Time-domain convolution of the echo with this kernel leads to smearing of the signal across the readout window, such that the shape of the time-domain signal comes to approximate the histogram of spin frequencies in the inhomogeneous B_0 field (i.e., a projection of the sample if the inhomogeneity originated from a gradient field). This effect is due to each Larmor frequency isochromat refocusing at a different point in time. Spin echoes acquired in this manner have been called “spectral echoes” [9] because of their resemblance to the frequency spectrum of the sample. The width of the spectral echo in the time domain depends on the bandwidth of the spins over the sample and the sweep rate of the RF pulse. The faster the pulse is swept, the narrower the time delay between excitation and refocusing of the isochromats, and the shorter the duration of the resulting spectral echo. Spatial quadratic phase profiles applied by RF pulses and/or nonlinear B_0 fields have been proposed in the past to perform slice selection [29], “phase scrambling” for dynamic range compression during signal reception [30], and reduced FOV imaging [31–33]. While spectral echoes are useful for some applications, they cannot be directly used with TRASE imaging.

Assuming the acquisition window is wide enough to capture the full “bandwidth” of the spectral echo, then convolution of the conventional echo with the chirp kernel is an information-preserving transform. To restore a conventional echo shape, the quadratic phase modulation can be removed in one of two ways: (a) convolution by the complex conjugate of the chirp kernel in the time domain, or (b) division by the quadratic phase profile in

the frequency domain [32]. The second operation is equivalent to subtracting out the phase difference between the Fourier transforms of two successive echoes in the train, which removes the phase imparted by the frequency-swept pulse while retaining the phase contributed by the intended encoding schemes.

Spectral echoes that have been transformed into conventional echoes can be used for TRASE imaging. However, the success of the quadratic phase removal depends on the echo train consisting of interleaved conventional (odd) and spectral (even) echoes with no mixture of the two. In ordinary spin echo trains that satisfy the CPMG conditions [34], defects in the refocusing pulse lead to multiple spin echo and stimulated echo pathways, which all refocus at the same time and constructively interfere to form a conventional echo shape. Unfortunately, in frequency-swept echo trains, defects in the refocusing pulse flip angle can lead to “mixing” of the conventional and spectral echoes. This complicates the quadratic phase removal and leads to image artifacts with TRASE. However, this problem can be largely avoided through careful choice of a pulse phase alternation scheme for each group of four successive echoes, as described in Section 3.

To implement quadratic phase removal in the frequency domain, the signal acquired in the n th readout, denoted w_n , is first Fourier transformed to yield $W_n = \mathcal{F}\{w_n\} = a_n e^{i\phi_n}$, where \mathcal{F} is the Fourier transform operator. The phase correction is then computed as the difference in Fourier domain phase of the first two echoes in the train: $(\phi_2 - \phi_1)$. This phase difference corresponds to the extra phase modulation applied by the second swept refocusing pulse. This term is subtracted in the Fourier domain from the phase of all even-numbered echoes in the train and the result is inverse Fourier transformed to generate the set of phase-corrected echoes, denoted \hat{w}_n . A phase factor of π is additionally applied to remove the effects of the pulse phase-alternation scheme. The correction applied to echoes in each group of four is thus described as follows:

$$\hat{w}_n = \begin{cases} w_n, & n = 1, 5, 9, \dots \\ \mathcal{F}^{-1} \{a_n e^{i(\phi_n - (\phi_2 - \phi_1))}\}, & n = 2, 6, 10, \dots \\ w_n e^{i\pi}, & n = 3, 7, 11, \dots \\ \mathcal{F}^{-1} \{a_n e^{i(\phi_n - (\phi_2 - \phi_1))}\} e^{i\pi}, & n = 4, 8, 12, \dots \end{cases} \quad (4)$$

For noisy data, it may be advantageous to fit the phase difference $(\phi_2 - \phi_1)$ to a second-order polynomial (weighted by the magnitude of the spectrum at each point) in order to limit noise propagation.

The phase correction term can also be calculated directly based on the sweep rate of the refocusing pulses: $e^{-i(\phi_2 - \phi_1)} = e^{-i2\pi f^2 / R_{\text{ref}}}$. The Fourier transform of the echo is multiplied by this phase correction factor and then inverse Fourier transformed to obtain the corrected echo. Equivalently, the time-domain echo can be convolved with the chirp kernel that is the Fourier transform of the phase correction:

$$\mathcal{F}^{-1} \{e^{-i2\pi f^2 / R_{\text{ref}}}\} = \sqrt{\frac{R_{\text{ref}}}{2}} e^{i\pi/4} e^{-i\pi R_{\text{ref}} t^2 / 2} \quad (5)$$

When implementing the convolution numerically, it is necessary to divide by the number of elements in the echo signal multiplied by the number of elements in the chirp kernel. In either domain, care must be taken in computing the phase correction analytically, since it does not account for timing errors in the pulse sequence (which translate the quadratic phase profile relative to the echo time origin) or other defects.

3. Methods

WURST pulses are a close approximation to the simplest frequency swept pulse: a rectangular amplitude envelope with linear frequency sweep. The WURST pulse deviates from this basic swept

pulse by softening the rising and falling edge with an amplitude taper and therefore reduces ringing in the off-resonance spin response. Hyperbolic secant swept pulses [35], an alternative pulse shape option, give sharper frequency band transitions than WURST pulses; this provides advantages for applications such as slice selection. Moreover, hyperbolic secant pulses can be paired in a way that cancels the quadratic phase modulation in the first echo [10]. However, hyperbolic secant pulses are not as efficient as WURST pulses for very wide bandwidths (as proposed here), and therefore tend to be longer. Since TRASE imaging relies on long echo trains, it is important to use the shortest refocusing pulses possible to minimize image artifacts caused by T_2 -decay. For signals acquired in the presence of strong gradients, if the echo spacing becomes too long, TRASE imaging performance may also be limited by the diffusion weighting [1]. For these reasons, the choice of WURST pulses for TRASE imaging in an inhomogeneous field is motivated by the need to optimize pulse efficiency; the sharpness of the band edge transitions of the spin isochromats is not important in this application.

A WURST pulse pair is used to demonstrate the properties of frequency-swept spin echo trains in a highly inhomogeneous field using a large bottle phantom (following the experiments in Ref. [8]). The refocusing pulse design (Fig. 1) uses a WURST-40 amplitude envelope [36] and a linear frequency sweep of $R = 50$ kHz over pulse duration $\tau_{ref} = 3$ ms to adequately cover the 30 kHz bandwidth (Fig. 2). The excitation has the same envelope and sweep width but with twice the pulse duration to satisfy the previously described sweep rate condition for quadratic phase cancellation. The peak pulse amplitudes are $\gamma B_{1,exc}/2\pi = 780$ Hz and $\gamma B_{1,ref}/2\pi = 3.12$ kHz. In addition, a second pulse pair is designed with an $R = 25$ kHz sweep width and half the pulse duration for efficient 1D TRASE imaging of smaller, structured phantoms with narrower spin frequency histograms. The reduced sweep width enables shorter pulse lengths and reduced echo spacing, limiting blurring from T_2 -decay. This is advantageous for high-resolution TRASE imaging, where long echo trains are necessary.

Fig. 2 shows Bloch simulations of the 50 kHz sweep width WURST excitation and refocusing pulse pair along with the shortest hard pulse pair achievable with the same hardware. The Bloch simulations use 2×2 rotation matrices specified by Cayley–Klein

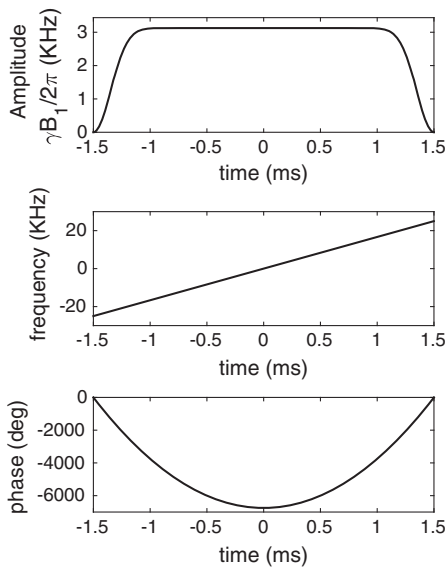


Fig. 1. Profile of WURST-40 refocusing pulse design. Sweep width is 50 kHz, pulse duration is 3 ms, peak $\gamma B_1/2\pi$ is 3.12 kHz, and amplitude taper coefficient is 40. The excitation pulse uses the same profile but with duration 6 ms and $\gamma B_1/2\pi = 780$ Hz.

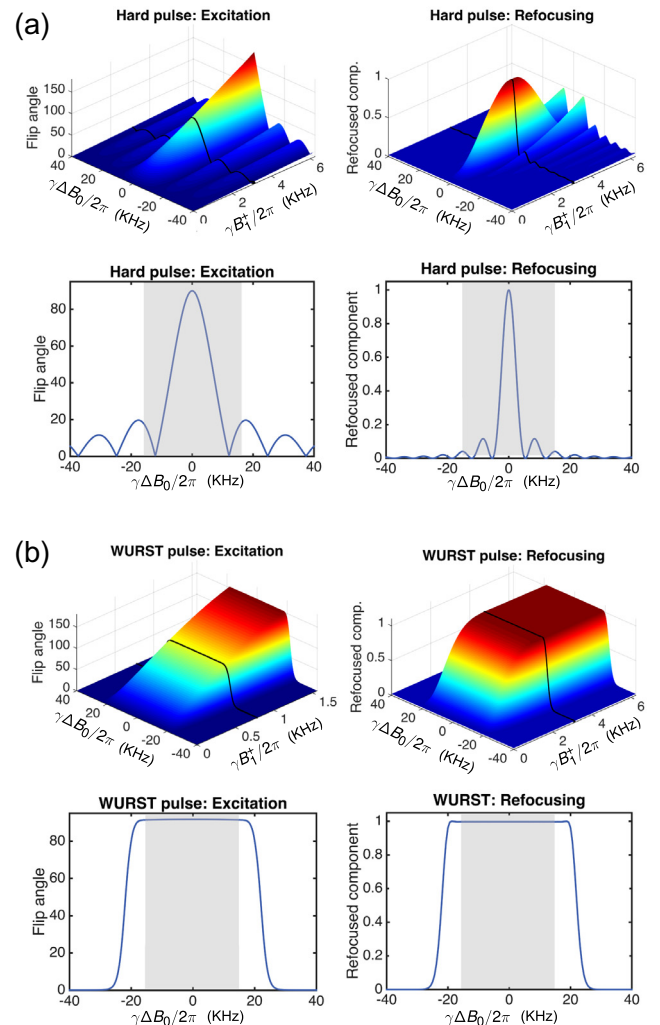


Fig. 2. Simulated flip angle and refocused component as a function of off-resonance (ΔB_0) and transmit RF amplitude deviation (ΔB_1^*) for hard pulses and 50 kHz WURST pulses. The 1D plots correspond to the black lines on the 2D plots at the nominal B_1^* values used in experiments. The target B_0 bandwidth of 30 kHz is indicated with gray shading in the 1D profile plots. (a) Hard pulse pair (80 μ s and 160 μ s, the shortest achievable pulse lengths with the available amplifier and coil hardware). Hard pulse performance degrades rapidly with both B_0 and B_1^* variation, motivating the use of swept WURST pulses. (b) The WURST pulse pair (described in Fig. 1) covers the desired excitation bandwidth. The WURST refocusing pulse amplitude is chosen to lie in the adiabatic regime ($|B_1^*| > dB_1/dt$). Refocusing pulse errors can create multiple coherence pathways in the echo train and “mixing” of conventional and spectral echoes (see Fig. 4). As a precaution against this effect, the refocusing pulse phase is alternated in the echo train to prevent a mixture of conventional and “spectral” echoes.

parameters to represent the action of the RF pulse on magnetization at each time point and isochromat [37]. The simulation time step is chosen so that no spin isochromat undergoes a rotation of more than 15° during the interval. Each pulse is simulated over an 80 kHz bandwidth for a range of B_1^* amplitudes. The accuracy of refocusing pulses is evaluated using the refocused component [38]. A refocused component amplitude of unity for a particular isochromat means that the transverse spins are flipped symmetrically about the intended refocusing axis and are independent of B_0 inhomogeneity.

The simulations show that while a hard excitation pulse achieves a 90° flip angle only at the center of the spin bandwidth, the WURST pulse achieves a nearly-uniform 90° flip angle over the entire 30 kHz bandwidth (indicated in gray). The difference in the

refocused component between hard pulses and WURST pulses is even more pronounced. In addition to covering the entire target bandwidth, the WURST refocusing pulse is also more robust to B_1^+ amplitude deviations in the adiabatic regime, where $|B_1^+| > dB_1/dt$. The refocused component is therefore relatively insensitive to flip angle errors within the adiabatic regime, reducing the likelihood of artifacts in TRASE images.

All experiments are performed in an inhomogeneous Halbach cylinder permanent magnet previously described in Ref. [8]. The average B_0 field strength and center frequency of the magnet are 77 mT and 3.29 MHz, respectively. The imaging field-of-view (FOV) is a 16 cm diameter sphere. The B_0 field vector is oriented along the Halbach cylinder's diameter (z-direction), and TRASE encoding is performed along the cylinder axis (x-direction). Data are acquired with a single-channel Tecmag Apollo console (Houston, Texas, USA). The 1D TRASE images in Figs. 9 and 10 are acquired using a custom-built TRASE array of two transmit coils. The frequency histogram and spin echo train data from the large bottle phantom in Figs. 3 and 8 are acquired using a solenoid coil whose region of homogeneous B_1^+ amplitude is larger than that of the TRASE coil array.

The B_0 field map over the three cardinal planes is shown in Fig. 3 along with a calculated histogram (dashed-line) of spin frequencies over the volume of a bottle phantom (9 cm diameter, 14 cm length) inside the magnet. More than 35 kHz of field variation exists over the spherical imaging volume, providing $\Delta B_0/B_0 \sim 1\%$. The ground-truth histogram shown in Fig. 3 is calculated from a set of axial B_0 field maps acquired at 1 cm intervals along x using a Hall-effect probe mounted to a computer-controlled positioning arm. Overlaid

on the calculated histogram are experimental histograms (projections) of the bottle phantom obtained by Fourier transforming spin echo readouts obtained using both the hard and the 50 kHz sweep WURST pulse pairs. The WURST pulse histogram corresponds well to the calculated histogram, and the area under the curve is 70% greater than the area of the hard pulse histogram, demonstrating much better coverage of the isochromats within the bottle phantom.

Fig. 4 shows the effect of phase alternation on the echo train, comparing no alternation and a scheme with a 90° difference between successive refocusing pulses (used in Ref. [9]). In the first pulse sequence, with no phase alternation (Fig. 4a), effects from experimental imperfections (i.e. refocusing pulse flip angle errors) accumulate and create stimulated echoes and other coherences later in the echo train. This causes a mixture of conventional and spectral echoes, which complicates the quadratic phase correction method described above. To mitigate this problem, the phase alternation scheme [9,39] shown in the second pulse sequence (Fig. 4b) is used to create two separate coherence pathways, effectively separating the conventional and spectral echoes along the entire echo train. The full pulse phase scheme including cycling over multiple TRs [9] is described in the Fig. 4 caption.

In Fig. 5, a Bloch simulation illustrates the proposed quadratic phase correction method for restoring spectral echoes to conventional echoes when the previously described 50 kHz sweep WURST pulses are used. Echoes from a numerical phantom with two features are simulated in a linear B_0 gradient field traversing a 40 kHz bandwidth over the field of view (~ 30 kHz over the phantom). The shape of the spectral echo resembles a projection of the phantom in the linear gradient; this correspondence is easier to see

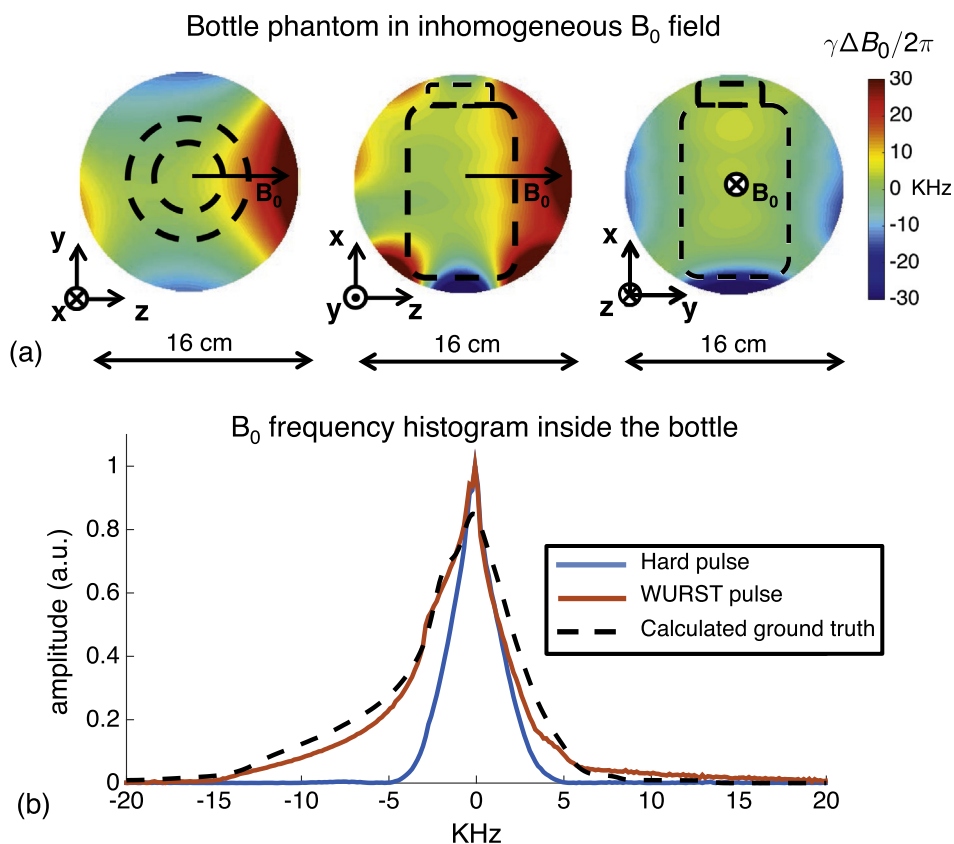


Fig. 3. Measured B_0 variation with respect to a 9 cm dia., 14 cm long bottle phantom (shown in outline). The $\Delta B_0/B_0$ over the bottle is about 1%. A solenoid volume coil is used for excitation and signal reception. (a) B_0 maps in the 3 orthogonal planes. (b) Frequency histogram of signal inside the bottle (obtained from Fourier transforms of spin echoes) after a hard-pulse pair (80 μ s and 160 μ s) or a WURST pulse pair (6 ms and 3 ms, sweep width = 50 kHz). For comparison, the dotted black curve shows the calculated ground truth histogram, which is expected if all of the spins inside the bottle were perfectly excited and refocused. When WURST pulses are used for excitation and refocusing, the area of the projection is increased by 70% as compared with hard pulses. The WURST projections also better agree with the simulated ground truth projection.

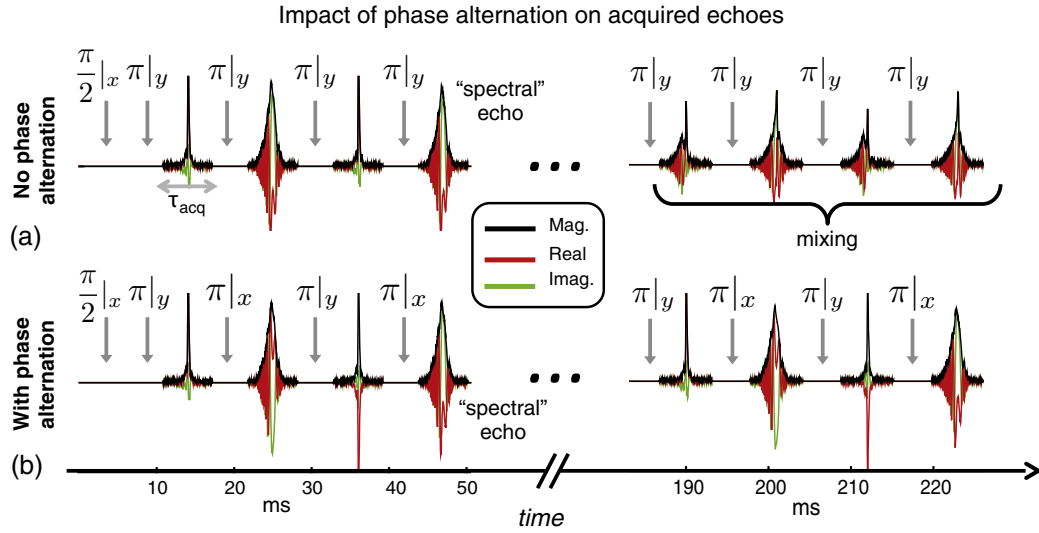


Fig. 4. Spin echo train acquired from bottle phantom in the inhomogeneous B_0 field using WURST swept pulses. Since $R_{ref} = 2R_{exc}$, the quadratic phase modulation is removed from the first echo. Because the same R_{ref} is used on all refocusing pulses, the quadratic phase is also removed from subsequent odd-numbered echoes. However, even-numbered echoes retain a quadratic phase. This creates “spectral echoes” in which different isochromats refocus at different times depending on where they occur in the frequency sweep. This causes the echo shape to resemble a projection of the object. (a) Without phase alternation all RF refocusing pulses use the same phase (noted in the subscripts). Errors in the refocusing pulse flip angle lead to mixing of the conventional and spectral echoes in later echoes. This renders the data difficult to use with TRASE. (b) With the chosen phase alternation scheme, the refocusing pulse phase alternates between 0° and 90° . This forms two coherence pathways and maintains better separation between the spectral and conventional echoes. To limit spin history effects between TRs, the phase of the excitation pulse, refocusing pulse pairs, and receiver is varied every four TRs as follows: $\phi_{exc} = [0, 180, 90, 270]$, $\phi_{ref1} = [90, 90, 0, 0]$, $\phi_{ref2} = [0, 0, 90, 90]$, $\phi_{acq} = [90, 270, 180, 0]$.

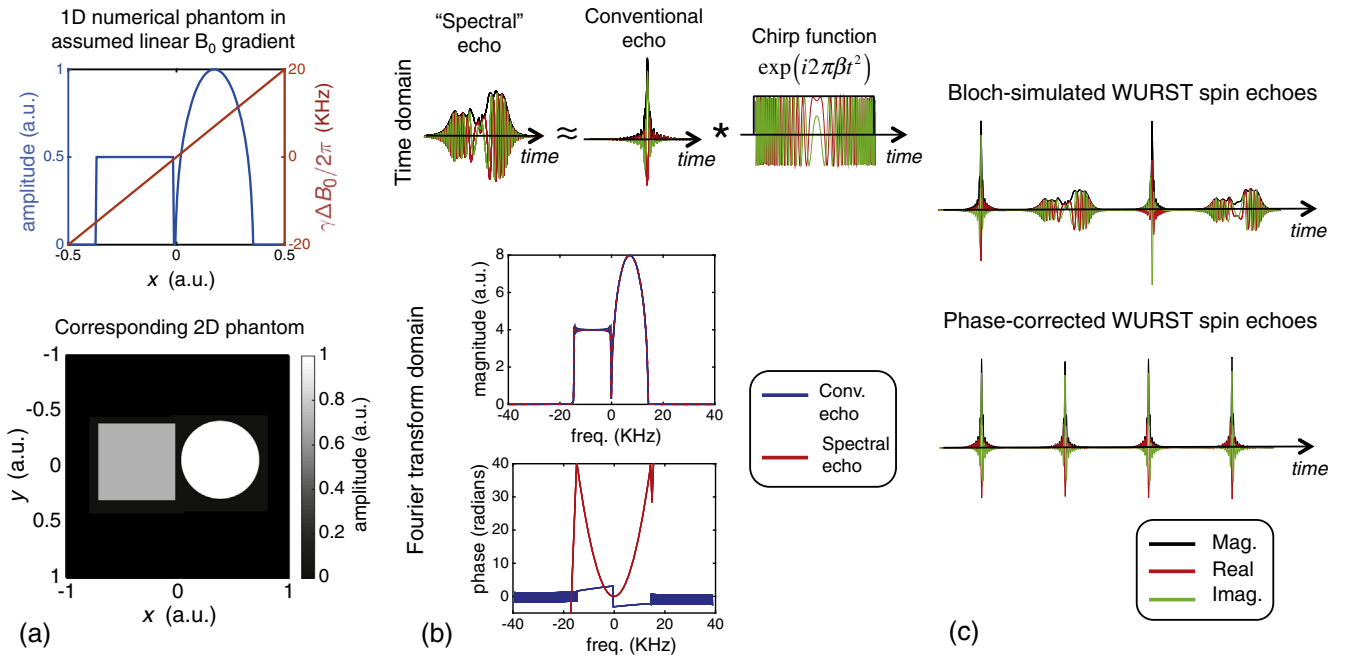


Fig. 5. 1D Bloch simulation and method of restoring the spectral echoes from the smearing caused by the quadratic phase. (a) Numerical phantom and its 1D projection. A linear variation in ΔB_0 field was assumed. (b) Echoes simulated using the 1D phantom. The spectral echo is represented as a convolution of a conventional echo with a temporal chirp function. Real and imaginary components and magnitudes are shown. In the Fourier transform domain, the magnitude spectrum of the two echo types look almost identical. However, the phase of the conventional echo is relatively flat while the spectral echo has a quadratic phase profile. (c) The conventional echo shape is restored by subtracting the difference between the phase profiles of the two echo types in the Fourier transform domain, and then transforming back to the time. A π phase shift is also applied to the third and fourth echoes to compensate for the effects of the RF pulse phase alternation scheme (see Fig. 4). After the phase correction, all echoes in the train have a conventional echo shape. As long as the readout window is long enough to contain the entire spectral echo, the transform is information-preserving. *Simulated parameters:* $\tau_{exc} = 6$ ms, $R_{exc} = 50$ kHz/6 ms, peak $\gamma B_{1,exc}/2\pi = 780$ Hz, $\tau_{ref} = 3$ ms, $R_{ref} = 50$ kHz/3 ms, peak $\gamma B_{1,ref}/2\pi = 3.12$ kHz, echo spacing = 10 ms, TR = 2.5 s, readout duration = 6.4 ms.

for the simulated linear gradient than for the experimental inhomogeneous B_0 field.

As discussed previously, the time domain spectral echo can be described as a convolution of the conventional echo with a

temporal chirp function whose scaling parameter, β , depends on the sweep rate of the WURST pulse (Fig. 5b top). In the Fourier transform domain, the two echo types have essentially the same magnitude (some Gibbs ringing is seen due to the finite duration

of the spectral echo readout window) but the phases differ by a quadratic offset over the spin bandwidth (Fig. 5b bottom). To restore the spectral echoes to conventional echoes, the difference between the phase of the Fourier-transformed conventional and spectral echoes is subtracted out, and the signals are inverse Fourier transformed back to the time domain (Fig. 5c). The equivalent operation can be performed in the time domain by convolving the spectral echo with an appropriately scaled, conjugated version of the quadratic phase chirp function (Eq. (5)).

The procedure for performing 1D TRASE phase encoding with two B_1^+ phase gradients is illustrated in Fig. 6, but is more fully described in Refs. [19,20]. While TRASE can in general be performed using any two distinct B_1^+ phase profiles, we assume two equal and opposite phase ramps in this work described by slopes $+2\pi k_1$ and $-2\pi k_1$. These phase ramps are designed to reach a maximum phase dispersion of $\pi/8$ at the edge of the FOV of the image, and determine the TRASE k -space origins: $+k_1$ and $-k_1$. The first echo in the WURST spin echo train is refocused with the positive

B_1^+ phase slope, and has applied phase-weighting $+k_1$. When the sign of phase gradient is flipped for the second refocusing pulse, the phase of the acquired echo is reflected across the $-k_1$ origin. The third pulse has positive phase gradient and in turn reflects the k -space trajectory across the $+k_1$ origin. Each successive pulse thereby has the effect of adding $\Delta k = 4k_1$ to the trajectory. Because the spacing between points is equal to $4k_1$, the result is that $\text{FOV} = 1/\Delta k = 1/4k_1$. The value $4k_1$ is analogous to the gradient moment of a phase encoding step, $\gamma G_0 \Delta t$, which is the k -space distance traversed by a conventional B_0 gradient with amplitude G_0 and pulse duration Δt , where γ is the gyromagnetic ratio.

In order to perform the quadratic phase correction in the experimental implementation of TRASE with WURST pulses, the sign of the TRASE phase slope is not flipped until the third refocusing pulse in the echo train (not shown in Fig. 6). Therefore the first two echoes have no TRASE phase encoding and any phase differences between the two echoes are attributable to the quadratic phase profile imparted by the WURST refocusing pulse. As such, the phase difference between the Fourier transforms of the two echoes is used for quadratic phase removal, restoring all spectral echoes in the train to conventional echoes.

At the echo refocusing time, TE, phase terms from the inhomogeneous B_0 field are completely refocused by the spin echo, leaving only modulation caused by the TRASE phase encoding along with T_2 decay and a very small diffusion weighting. To form a 1D projection of the object using TRASE, a k -space vector is assembled by re-ordering the mid-points of each phase-corrected echo in the train (Fig. 6b). The 1D image is then formed by taking the Fourier transform of the TRASE k -space vector.

Equivalently, the on-resonance component can be obtained by integrating the Fourier transform of each echo in the train. The resulting points are then and re-ordered to form TRASE k -space. While this is mathematically equivalent to taking the mid-point of the echo under ideal circumstances, it has the advantage of being less sensitive to timing errors in the pulse sequence.

To realize a TRASE gradient B_1^+ field, a two-channel transmit array was designed that consists of two nested cylindrical coils (Fig. 7) [40]. In the spirit of the TRASE coil in Ref. [41], we combine a “cosine” B_1^+ amplitude coil in spatial quadrature with a “sine” B_1^+ amplitude coil to generate a linear phase ramp between $-\pi/8$ and $\pi/8$ across the FOV. Coil 1 is a short 4-turn birdcage coil (12 rungs, 18 cm diam., 22 cm length) that produces a B_1^+ field pointed along y with a cosine shape variation along x , $B_{1y}^+ = |B_{1xy}^+| \cos(2\pi k_1 x)$. The use of multiple turns in the birdcage coil, previously described in Ref. [42], increases the B_1^+ efficiency of the coil, reducing the RF power requirements. Coil 2 is a 10-turn Maxwell coil (22 cm diam., 18 cm length). The Maxwell coil produces a B_1^+ field pointed along x with a sine shape variation along x , $B_{1x}^+ = |B_{1xy}^+| \sin(2\pi k_1 x)$. The coils are tuned to the Larmor frequency (3.29 MHz) and decoupled with a toroidal transformer ($S_{21} = -15$ dB isolation).

Fig. 7 shows the ideal relative magnitude of B_{1x} and B_{1y} from the two coils over the 20 cm encoded field-of-view. When the two coils are driven to produce an equal $|B_{1xy}^+|$ amplitude and their fields vary according to the same spatial frequency, k_1 , they produce the desired B_1^+ field, $B_1^+(x) = |B_{1xy}^+| e^{i2\pi k_1 x}$ (uniform magnitude and linear phase). To control the sign of the B_1^+ phase gradient, a 180° phase shifter is added in the Maxwell coil RF path. Pulses with the 180° phase shift produce a negative phase gradient, $B_1^+(x) = |B_{1xy}^+| e^{-i2\pi k_1 x}$, which allows for a sign change on every other refocusing pulse in TRASE echo trains. The birdcage coil is used for signal reception since it has a more uniform B_1^+ amplitude than the Maxwell coil over the phantom VOI. The B_1^+ magnitude and phase of each coil are separately mapped using a small field probe on a

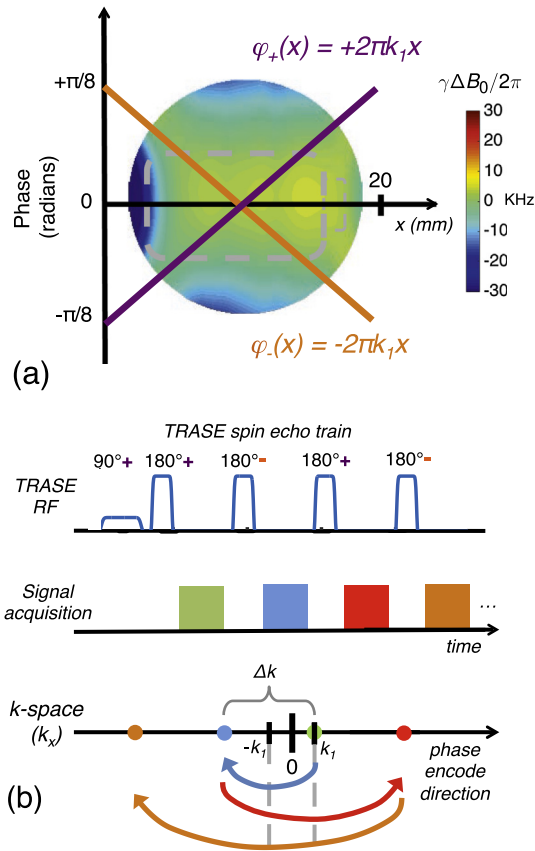


Fig. 6. TRASE k -space encoding using opposite sign, spatially linear B_1^+ phase ramps, which alternate between even and odd numbered spin echoes. (a) The two switchable B_1^+ phase slopes applied by a specialized transmit coil array over the FOV. (b) k -space is traversed by alternating the sign of the phase ramp between successive echoes in a spin echo train. For a conventional coil with no phase ramp the spin-echo reflection point is at $k = 0$. For the TRASE coil with a phase ramp described by $\varphi_+(x) = +2\pi k_1 x$, the reflection point is $+k_1$. If the pulse is played with a second phase ramp described by $\varphi_-(x) = -2\pi k_1 x$, the reflection point is $-k_1$. The signal of the first echo records the $k = +k_1$ because the excitation imparts a phase of $+k_1$ and the refocusing pulse reflects this around the origin for this phase ramp ($+k_1$) leaving it at k_1 . The second refocusing pulse (a “−” pulse), reflects the signal around its origin ($-k_1$) as shown by the blue arrow, leaving the signal at $k = -3k_1$. The third refocusing pulse is a “+” pulse and thus reflects about $+k_1$ leaving the signal at $k = +5k_1$. Defining $\Delta k = 4k_1$ allows us to interpret the resultant sampling pattern as Cartesian sampling with a $\text{FOV} = 1/\Delta k$ and a spatial resolution of FOV/ETL where ETL is the echo train length. Figure adapted from Ref. [19].

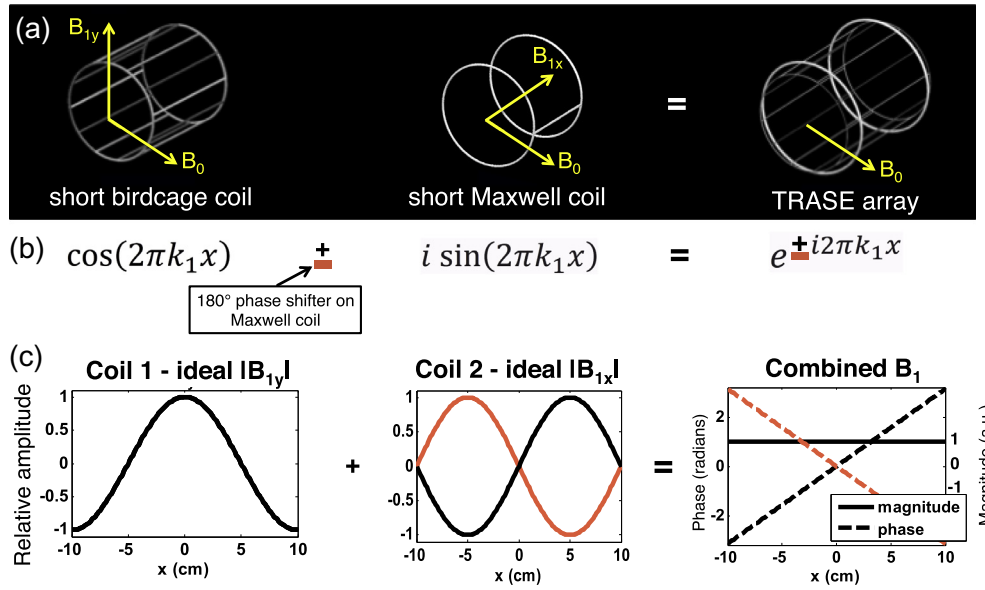


Fig. 7. Design of experimental TRASE transmit coil with uniform B_1^+ amplitude and linear phase along the encoding direction. The B_0 field is transverse to the axis of the cylindrical TRASE coil array. (a) The coil array is realized as a multi-turn birdcage coil with a nested Maxwell pair coil. (b) The coils are designed to approximate the cosine and sine terms of Euler's equation for a linear phase ramp. The sign of the phase ramp can be flipped by applying a 180 deg. phase shift to the Maxwell coil RF transmit path. (c) The birdcage coil generates a transverse field (B_{1y}) with cosine amplitude variation over the FOV (x direction), while the Maxwell coil generates a longitudinal field (B_{1z}) with approximately sine amplitude variation. Four turns of wire are used in each birdcage rung to provide increased B_1^+ field for minimizing the needed swept RF pulse duration. The coils are decoupled to $S_{12} = -15$ dB using a toroidal transformer to cancel the mutual inductance.

computer-controlled positioning arm to measure S_{21} between each coil and the probe. The two measurements are weighted proportional to the RF transmit voltage applied to each coil and combined to create a B_1 map for the TRASE array coil (see [Supplemental Fig. 1](#)). This map is used to determine the FOV suitable for TRASE imaging.

Because of the low Larmor frequency of 3.29 MHz and the wide pulse bandwidths of 25 kHz and 50 kHz ($\sim 1\%$ of the Larmor frequency), care must be taken to ensure that the coil is impedance matched across the entire bandwidth to avoid errors for off-resonant spins. A 10 ohm resistor is added to each of the two coils to decrease the quality factor (Q) and widen the impedance match of the coil so that RF energy is transmitted evenly across the entire pulse bandwidth.

The two TRASE coils are driven by two independent RF power amplifiers (Tomco, Stepney, Australia). To implement the B_{1x}^+ sign change, the small-signal RF input to one of the amplifiers is phase shifted using a PIN-diode actuated lumped-element 180° phase shifter. This approach eliminates the need for a high-power phase shifter and unequal power divider, as used for TRASE imaging in Ref. [41]. A length of coaxial cable is added to one of the transmit paths to equalize the temporal RF phase at the inputs to the two TRASE coils (as measured on a network analyzer). A high-power directional coupler is used to measure the incident and reflected RF power in each of the two paths. The power balance between the two TRASE coils is adjusted by adding attenuators to the signal input to the Maxwell coil RF power amplifier until the desired TRASE B_1^+ phase slope is achieved across the FOV.

Experimental TRASE 1D images are acquired on two simple tap water phantoms. T_1 and T_2 of the tap water is measured with a Bruker Minispec mq20 relaxometer (Billerica, MA, USA) at 7.5 MHz to assess the impact of relaxation on the TRASE images.

TRASE spin echo image data are acquired using the WURST pulses as well as hard pulses for comparison. The two pulse phasing schemes described in Fig. 4 are also compared. The WURST pulse sweep width is set to 25 kHz. The single-shot echo train length (and number of TRASE k -space points) is 128. The excitation

pulse duration is 3 ms and the refocusing pulse duration is 1.5 ms. Peak RF power $\gamma B_1/2\pi$ is 650 Hz for excitation and 2.6 kHz for refocusing. The readout sampling bandwidth is set to 40 kHz and 96 samples are acquired. The width of the spectral echoes depends on the WURST refocusing pulse sweep rate. For the pulse used here, the 2.4 ms acquisition window is wide enough to capture all signals in the spectral echoes that refocus at different points in time. The acquisition window and WURST pulse duration set the minimum echo spacing at 7.6 ms, corresponding to an echo train length of 972.8 ms for 128 echoes. The TR is set to 2.5 s and 96 averages are acquired for a total acquisition time is 240 s. Unfortunately, a suitable linear B_0 gradient coil is unfeasible for projection imaging in the highly inhomogeneous low field scanner. Consequently, we are not able to acquire a reference 1D image to use as ground truth (as in Refs. [19,20]).

The diffusion weighting in the CPMG echo train is estimated using the following equation [1],

$$\frac{1}{T_{diff}} = \frac{1}{12} \gamma^2 G_0^2 D t_{TE}^2 \quad (6)$$

where $\frac{1}{T_2} = \frac{1}{T_2} + \frac{1}{T_{diff}}$ and D is assumed to be $2.3e-5$ cm²/s for tap water [1]. While this equation only describes the diffusion weighting of the CPMG component, and coherences such as stimulated echoes have a different (and potentially larger) diffusion weighting, we take this to be a reasonable approximation for our CPMG experiment, since care has been taken to minimize the signal contribution of unwanted coherences. To estimate the “worst-case” maximum possible diffusion weighting, we consider spins at the edge of the region-of-interest at a radius of approximately 8 cm from the magnet isocenter, where the local B_0 field variation is approximately 5000 Hz/cm. We also calculate the average diffusion weighting over the full FOV. Finally, TRASE image reconstruction is simulated on a 1D numerical phantom with and without blurring due to relaxation and diffusion.

4. Results

The T_1 and T_2 values for the tap water used in the imaging phantoms were measured to be 3400 ms and 2500 ms, respectively, at 7.5 MHz. Given the relative insensitivity of T_2 to field strength, this T_2 value is taken to be a reasonable approximation to T_2 at our experimental Larmor frequency of 3.3 MHz. For areas of objects extending to the edge of the 8 cm spherical FOV, Eq. (4) yields an effective relaxation constant of $T_2 = 1962$ ms, corresponding to only 7% extra signal attenuation at the end of the 972.8 ms echo train. Similarly, the average frequency gradient over the FOV is estimated to be 2500 Hz/cm, yielding an average $T_2 = 2338$ ms (only 2% extra attenuation at the end of the echo train). Since these values of T_2 are still considerably longer than the 972.8 ms echo train used to acquire the TRASE data, the impact of the diffusion weighting on the signal intensity is quite modest for our experimental parameters. Supplemental Fig. 2 shows that the combined effect of T_2 decay and the worst-case diffusion weighting causes only a minor blurring of the object (shown with the orange arrow).

Experimental validation of the quadratic phase correction method is shown in Fig. 8. The first four echoes of a WURST echo train acquired on a large bottle phantom are plotted. The spectral echoes (Fig. 8a) show the characteristic broadening caused by the refocusing of each isochromat at different time points, resembling a 1D projection of the bottle phantom in the inhomogeneous B_0 field. The projection shape roughly corresponds to the histogram of frequencies within the bottle shown in Fig. 3. When the spectral echoes are Fourier transformed and the quadratic phase is subtracted out, their time-domain shape is restored to that of a conventional echo (Fig. 8b), as previously shown in simulations in Fig. 5. The third and fourth echo (and multiples of those echoes later in the train) are further multiplied by $\exp(i\pi)$ to compensate for the $-\pi$ phase offset applied by the phase alternation of the refocusing pulses.

Measured B_1^+ amplitude and phase field maps for the TRASE array coil are plotted in Supplemental Fig. 1 for the three cardinal planes with 5% delta contours overlaid. The phase gradient varies between approximately $-\pi/8$ and $+\pi/8$ over a distance of 20 cm. This nominally determines the TRASE Δk step size and the corresponding encoding FOV of 20 cm. However, the B_1^+ amplitude drops off sharply toward the edge of the TRASE axis and also in the plane transverse to this axis. As discussed below, B_1^+ amplitude variation greater than $\sim 10\%$ can cause echo train defects and TRASE image

artifacts. So although the phase gradient is capable of encoding a FOV of 20 cm, the usable axial FOV is limited to ~ 13 cm due to the B_1^+ amplitude roll-off. In the y and z directions, B_1^+ is deemed sufficiently uniform over a roughly ± 2 cm region. Consequently, the phantoms used for TRASE imaging are restricted to the $4 \text{ cm} \times 4 \text{ cm} \times 13 \text{ cm}$ rectangular VOI overlaid on the plots in gray.

Fig. 9 shows 1D TRASE imaging performed on a phantom made up of three 2.54 cm dia. (1") tap water-filled spheres separated by a gap of 2.54 cm (12.7 cm total spatial extent). Fig. 9b shows experimental data in which spectral echoes have been converted to conventional echoes using the proposed phase correction method. The effect of TRASE phase encoding is easily seen in the shape of the echoes, which no longer all have the same shape and whose mid-points no longer follow a smooth T_2 -decay curve. TRASE k -space (Fig. 9c) is formed by rearranging the mid-points of each echo in the train. The k -space data is Fourier transformed to generate a 1D image (Fig. 9d) that clearly shows the position of the three balls within this FOV. The FOV estimated from the TRASE coil phase slope is 20 cm, however this FOV places the balls slightly too close together (closer to ~ 4 cm) along the x axis. We have therefore used the known position of the balls to infer the effective FOV to be 25 cm for the TRASE coil, and we have set the x axis in the plot accordingly. We note that this method is commonly used for calibration; B_0 gradient coil sensitivity is often measured using projections of an object of known size. Ignoring the minor effect of T_2 and diffusion, the nominal spatial resolution is the TRASE FOV (set by the slope of the coil phase gradient) divided by the echo train length: $\sim 25 \text{ cm}/128 = 0.2 \text{ cm}$.

While Fig. 9 shows results using the appropriate RF pulses, phase corrections, and phase alternation scheme, Fig. 10 demonstrates the importance of these choices. The TRASE data in Fig. 10 was acquired on the cylinder-and-sphere water phantom (Fig. 10a). For this phantom, the WURST echo train is shown before and after phase-correction (Fig. 10b). The corrected train is then overlaid with and without TRASE phase encoding enabled for the first eight echoes in the train, highlighting the spin dephasing caused by the TRASE phase gradient. The 1D image obtained from hard pulse data (Fig. 10c) shows severe off-resonance effects resulting in distorted shapes for the two objects in the FOV as well as a large “DC” artifact created by un-encoded spins (at the edge of the FOV). Severe artifacts also result when data is acquired using WURST pulses without phase alternation (Fig. 10d). In this case, the shape of the two objects is distorted and the DC artifact occurs

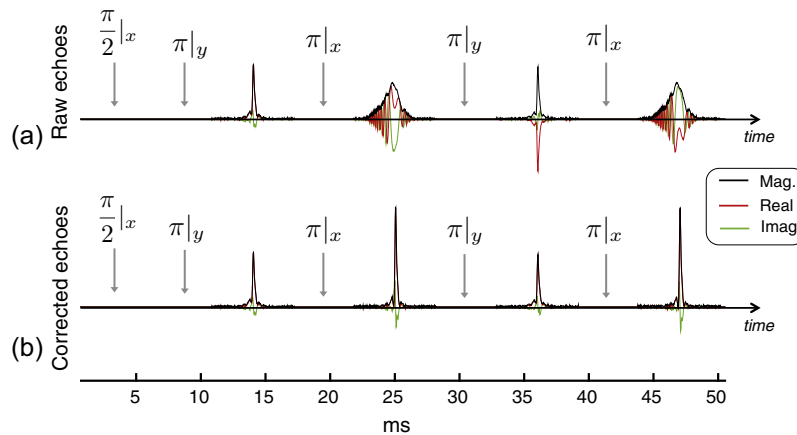


Fig. 8. Experimental demonstration of phase correction method to change spectral echoes to a conventional echo shape in the phantom with an inhomogeneous B_0 field. Data are acquired using the same 9 cm dia., 14 cm long bottle phantom as in Figs. 3 and 4. The spin echo train uses phase alternation (noted in subscript) on the refocusing pulses but no TRASE modulation applied. The difference in echo amplitude between even and odd echoes is attributed to B_1^+ field variations over the large volume of the sample within the TRASE coil. Sequence parameters: $\tau_{exc} = 6$ ms, $R_{exc} = 50$ kHz/6 ms, peak $\gamma B_{1,exc}/2\pi = 780$ Hz, $\tau_{ref} = 3$ ms, $R_{ref} = 50$ kHz/3 ms, peak $\gamma B_{1,ref}/2\pi = 3.12$ kHz, echo spacing = 10 ms, TR = 2.5 s, readout duration = 6.4 ms, sampling bandwidth = 40 kHz, number of averages = 8.

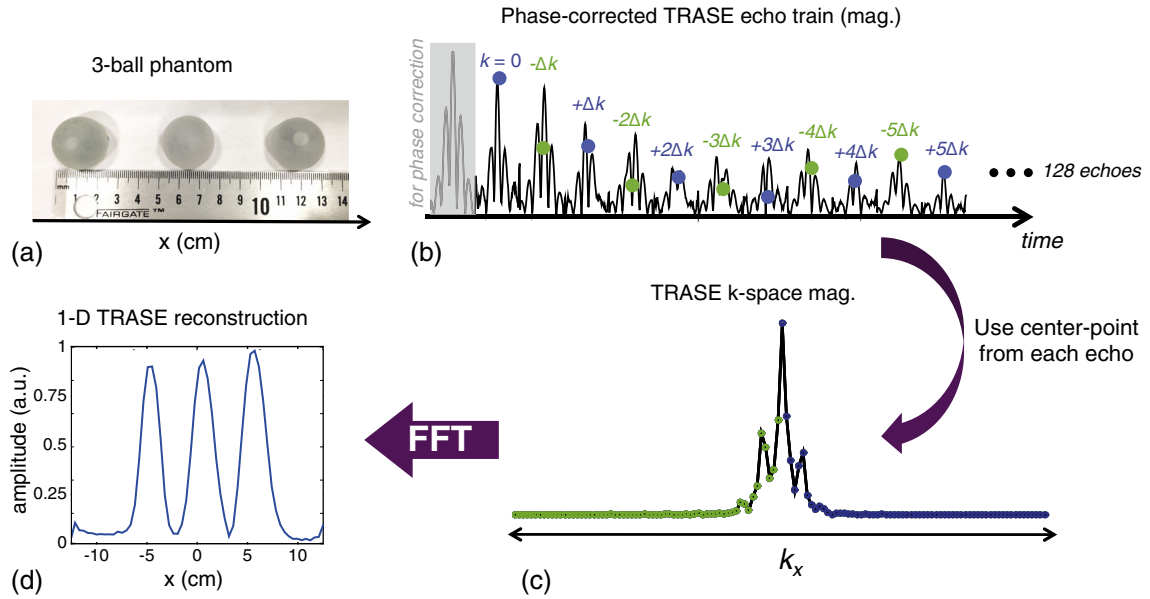


Fig. 9. Experimental 1D TRASE imaging performed using single-shot WURST spin echo train in an inhomogeneous field. (a) Three-ball tap water-filled phantom used in experiment. The balls are 2.54 cm in diameter (1") and the gap between them is also 2.54 cm. The full width of the phantom is 12.7 cm. (b) The first 12 echoes out of 128 echo train that have been corrected with the quadratic phase correction procedure. An extra echo at the beginning (gray shaded) of the train is acquired with no TRASE phase modulation and is used to perform the phase correction on the even-numbered echoes in the train. The mid-point of each 96-point echo is used as the TRASE k -space sample since the echo mid-point is modulated only by TRASE and not by the inhomogeneous B_0 field. (c) 1D k -space formed by re-ordering the mid-points of each echo. (d) The 1D image magnitude formed from the k -space data. The projections of the three balls are clearly visible in the 25 cm field-of-view 1D image. Sequence parameters: $\tau_{exc} = 3$ ms, $R_{exc} = 25$ kHz/3 ms, peak $\gamma B_{1,exc}/2\pi = 650$ Hz, $\tau_{ref} = 1.5$ ms, $R_{ref} = 25$ kHz/1.5 ms, peak $\gamma B_{1,ref}/2\pi = 2.6$ kHz, echo spacing = 7.6 ms, TR = 2.5 s, readout duration = 2.4 ms, echo train length = 128, echo train duration = 972.8 ms, sampling bandwidth = 40 kHz, number of averages = 96.

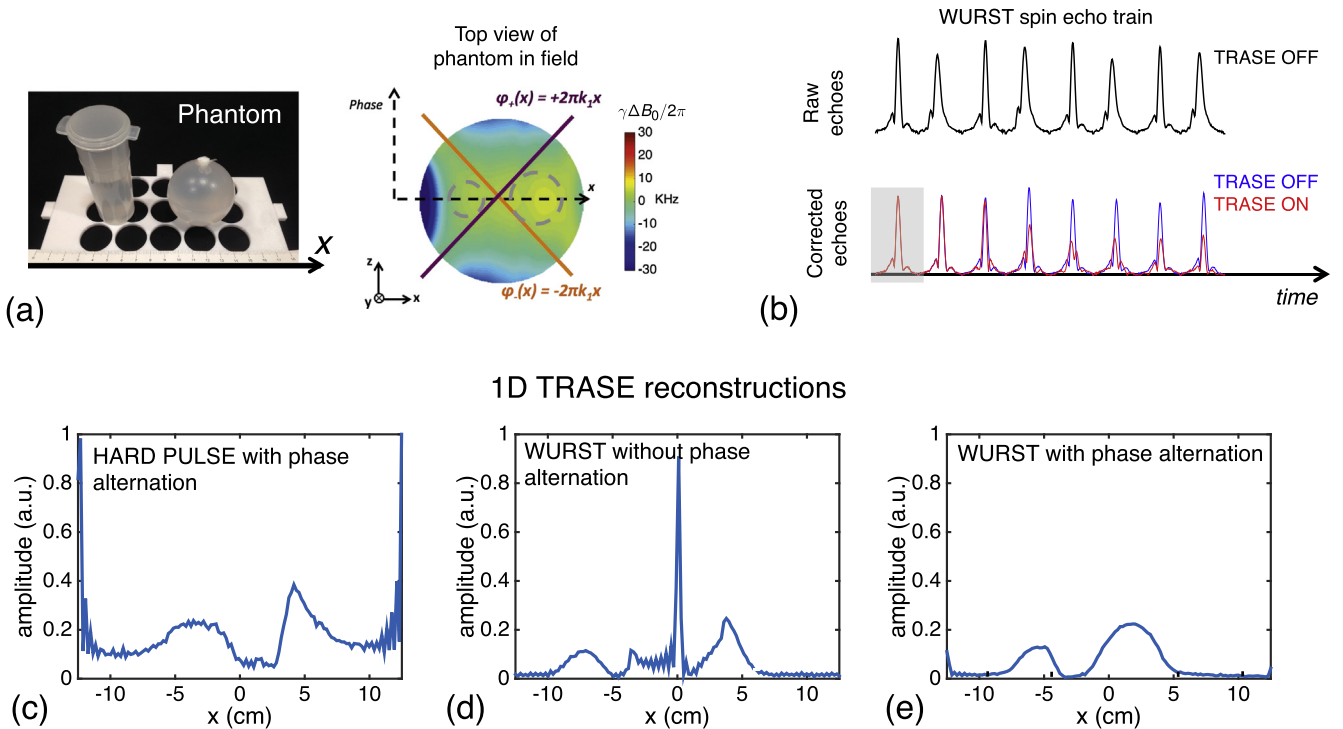


Fig. 10. Experimental comparison of WURST pulses, hard pulses, and the two different refocusing pulse phasing schemes for 1D imaging. (a) Tap-water phantom comprised of 3 cm wide cylinder and 5 cm diameter sphere. (b) Echo train without (raw) and with (corrected) quadratic phase removal. The effect of turning on the TRASE modulation is also shown. (c–e) 1D images reconstructed from the hard pulses and WURST pulse trains. The WURST reconstructions are shown with and without phase alternation of the RF pulses. (c) Hard pulse TRASE image. As expected, the projections formed using hard pulses with TRASE modulation are severely distorted due to flip angle and phase errors caused by the limited bandwidth of the hard pulses (80 μ s and 160 μ s for excitation and refocusing pulses). Hard pulse results without phase alternation (not shown) are even more distorted. (d) WURST image without phase alternation. Refocusing pulse defects can cause mixing of conventional and spectral echo types for echoes in the train (see Fig. 4), corrupting the reconstruction. (e) WURST image with phase alternation. The phase alternation mitigates coherence pathway problems, producing a higher fidelity TRASE image. WURST sequence parameters: $\tau_{exc} = 3$ ms, $R_{exc} = 25$ kHz/3 ms, peak $\gamma B_{1,exc}/2\pi = 650$ Hz, $\tau_{ref} = 1.5$ ms, $R_{ref} = 25$ kHz/1.5 ms, peak $\gamma B_{1,ref}/2\pi = 2.6$ kHz, echo spacing = 7.6 ms, TR = 2.5 s, readout duration = 2.4 ms, echo train length = 128, echo train duration = 972.8 ms, sampling bandwidth = 40 kHz, number of averages = 96. Ignoring the relatively minor T_2 and diffusion weightings, the effective spatial resolution is approximately $FOV/128 = 25/128 = 0.2$ cm.

in the center of the FOV rather than the edge. By contrast, when phase alternation is used with the WURST pulses (Fig. 10e), the projections show the expected correspondence to the shape and size of the phantoms as well as the distance between them. There is still a DC component artifact at the edge of the FOV, but it is greatly attenuated.

5. Discussion

Initial 1D image results demonstrate that TRASE can be adapted to perform spatial encoding in highly inhomogeneous B_0 fields. When hard pulses (used in previous realizations of TRASE) are replaced by WURST pulses and suitable phase alternation and phase correction are applied, 1D TRASE images acquired in the inhomogeneous field are markedly improved (Figs. 9 and 10). Our extension of the TRASE method thus substantially mitigates off-resonance effects on image quality, which the inventors of TRASE anticipated in Ref. [20] as a chief obstacle to widespread adoption of the method.

The phase correction method introduced here allows spectral echoes to be used for populating one half of k -space. For TRASE imaging, we implement the phase correction by taking the difference between the phase of the Fourier transform of the first two echoes in the train (and optionally fitting this difference to a polynomial). We note that while this approach has the advantage of being “auto-calibrating”, it may be unsuitable for data with poor SNR. In the latter case, the quadratic phase profile should be calculated analytically and applied to the Fourier transform of the spectral echoes (or equivalently, applied as a convolution in the time-domain).

Given that TRASE is synergistic with lightweight, low-field imaging systems, where it may not be practical to achieve a highly uniform B_0 field, our results represent a significant advance toward developing this application with TRASE. However, the results also show that there is room for further refinement of the TRASE-WURST acquisition and reconstruction. For example, a modest DC component still exists in the projections in Figs. 9 and 10 at the edge of the FOV, most likely arising from spin coherence pathways that are not properly excited and/or refocused in the echo train. Therefore, these spins are not properly encoded by the TRASE phase gradient. Additionally, in Fig. 8, the even and odd phase-corrected echoes show differences in amplitude that can arise from $|B_1^+|$ spatial variation over the sample. In TRASE data, this can create a bias offset between the positive and negative halves of the acquired TRASE k -space data, causing artifacts.

Bloch simulations show that the echo amplitude alternation in Fig. 8 can arise from B_1^+ variations over the large bottle phantom. Supplemental Fig. 3 displays echoes that are simulated using the same RF pulses and sequence parameters as the large bottle experiment in Fig. 8. For simplicity, a rectangular 1D phantom is used and a linear B_1^+ field with $\pm 10\%$ variation over the phantom is assumed. Simulations are compared for an inhomogeneous quadratic B_0 field with ~ 25 kHz variation over the phantom as well as for a uniform B_0 field. In the latter case, an artificial T_2^* weighting is added to permit echo formation for purposes of illustration. The B_1^+ amplitude variation creates echo amplitude differences consistent with those observed for the large bottle phantom in Fig. 8. Specifically, the phase-corrected spectral echoes show a higher peak amplitude than the conventional echoes. Altering the excitation flip angle does not reproduce the alternating echo amplitude effect. For the TRASE array coil used in this work, B_1^+ roll-off near the edge of the coil limits the usable FOV to ~ 13 cm. In practice, the coil's limited impedance match bandwidth may also contribute to the effective B_1^+ variation applied to spin isochromats in the sample.

Table 1

A summary of previously published T_1 and T_2 measurements at low magnetic field strengths for gray matter, white matter, and cerebrospinal fluid.

Tissue type	T_1 (ms)	B_0 (T)	Ref.	T_2 (ms)	B_0 (T)	Ref.
Gray matter	500	0.08	[43]	60	0.2	[44]
				55–74	0.5	[45]
White matter	250	0.08	[43]	42	0.2	[44]
				64	0.5	[45]
Cerebrospinal fluid	4360	0.15	[46]	1760	0.15	[46]

We note that the even/odd echo amplitude variation effect is a separate phenomenon from the “mixing” of conventional and spectral echoes that occurs when the refocusing pulse is not in the adiabatic regime. However, as illustrated in Fig. 4, the echo mixing effect is readily circumvented through the use of phase alternation to separate the coherence pathways of the conventional and spectral echoes.

A disadvantage of using WURST pulses instead of hard pulses is the longer pulse duration and corresponding increase in echo spacing, which increases attenuation of high frequency k -space points by T_2 -decay. For our proof-of-concept experiments, we used tap water phantoms with T_2 greater than the entire echo train duration, minimizing the impact of T_2 -decay and isolating to the extent possible the effect of TRASE phase modulation on the signal intensity and the TRASE image quality. In practice, for *in vivo* brain imaging, where T_2 is much shorter, there is a trade-off between the desired image resolution and the amount of available RF power (and hence the minimum pulse duration) [20]. For our experiments at a Larmor frequency of 3.3 MHz (0.078 T), we estimate T_1 and T_2 based on published measurements made between 0.08 T and 0.5 T, as summarized in Table 1.

Given these approximate T_2 values for brain tissue at low field, the 128-echo, 972.8 ms echo train used in this work would suffer heavy attenuation of high-frequency TRASE k -space points acquired late in the echo train, leading to severe blurring. However, as a mitigating circumstance, we note that the practical use of TRASE for brain slice encoding would not require 128 slices. Acquiring a more modest number of slices, such as 32, would yield a more tractable echo train length of 243 ms, greatly reducing the blurring.

In principle there are ways to overcome the limit imposed on resolution by T_2 , albeit at the cost of increased scan time. For example, as suggested in Refs. [19,47], if a new TRASE coil is designed with a doubled phase gradient slope, it can be used to acquire two separate echo trains (with reduced FOVs) that can be interleaved to encode the full FOV. The two separate echo trains would be acquired with an opposite order of the alternating coil phase gradients. While each of these echo trains will generate aliased images due to the reduced FOV (increased Δk), the interleaved dataset will encode the full FOV. This approach will be explored in future work and improvements in resolution will be assessed.

While simple swept WURST pulses are used in this proof-of-concept to demonstrate TRASE in an inhomogeneous B_0 field, there is a whole class of composite, shaped, adiabatic, and optimal control pulses that could be explored for enabling TRASE imaging of broadband samples [48]. To take one promising example, “symmetric phase-alternating” composite refocusing pulses with equal duration to a narrowband hard pulse have been shown to provide increased CPMG signal amplitudes from samples with wide bandwidths [49]. These refocusing pulses work most efficiently when their imperfections are compensated by an “axis-matched” excitation pulse [48].

The bandwidth of the TRASE transmit coil array imposes another constraint on the use of TRASE in highly inhomogeneous B_0 fields. While resistive Q -spoiling overcomes this limitation for

purposes of the present work, in general this solution may be impractical since it decreases the efficiency of the coil. A more elegant approach is to add a high- Q resonant circuit between the RF amplifier and the RF coil and inductively couple this circuit to the resonant coil. If the two resonant circuits are appropriately overcoupled, the bandwidth is increased with only a modest impact on coil efficiency across the band. The approach is used in Ref. [50] for widening receive coil bandwidth (by a factor of 5), but it is equally applicable to transmit coils. Another potential solution is to use untuned transmit coils and custom RF power amplifiers, an approach that has recently been explored for low field imaging [51].

Improved decoupling and orthogonality of the two TRASE coil's fields could also improve performance. In the echo train data acquired here, the amplitude of the even and odd-numbered RF pulses in the echo train had to be adjusted slightly (a few percent) to account for the effect of an undesired concomitant B_{1y}^+ field component generated by the Maxwell coil (collinear with the desired birdcage B_{1y}^+ field). The ratio of Maxwell to birdcage B_{1y}^+ in the center of the FOV is approximately 25%. If left uncompensated, this B_{1y}^+ field impacts the refocusing pulse accuracy and the resulting TRASE image quality. However, varying the refocusing pulse does not completely compensate the effects of the Maxwell B_{1y}^+ field because the field varies spatially over the VOI. In future work, we will strive for improved decoupling of the TRASE coils and better orthogonality between the field components generated by each coil (B_{1x}^+ and B_{1y}^+). As TRASE phase gradient coils are still a relatively recent innovation, there is a large space of potential designs to explore. We plan to explore different coil geometries and wire patterns – such as designs based on the target-field method [52] – in the hopes of minimizing concomitant fields and maximizing the FOV usable for TRASE imaging. However, as the present topic is the use of swept pulses to enable TRASE in an inhomogeneous B_0 field, we considered the Maxwell-birdcage coil sufficient for proof-of-concept broadband TRASE imaging in spite of its obvious flaws.

In this work, TRASE image reconstruction is performed using a simple Fourier transform. However, improved image fidelity could potentially be achieved by incorporating B_1^+ phase gradient nonlinearity [53], $|B_1^+|$ variations, and T_2 -decay into the forward model encoding matrix. Generalized image reconstruction then proceeds using an iterative matrix solver such as the conjugate gradients algorithm [54]. In addition to reducing image artifacts, the generalized reconstruction would allow TRASE encoding to be incorporated into flexible encoding schemes that also use B_0 gradient encoding with linear and/or nonlinear fields, a hybrid approach that our group has begun exploring for low field imaging [40]. Using a single encoding matrix to explicitly account for the actual B_1^+ and/or B_0 field profiles provides maximum freedom for designing acquisition schemes. This in turn has the potential to relax the requirements on hardware design for low field scanners.

6. Conclusion

Proof-of-concept 1D images show that TRASE phase encoding in a highly inhomogeneous B_0 field is possible with ordinary RF power levels and a simple spin echo pulse sequence using WURST swept RF pulses. TRASE imaging is successfully demonstrating on phantoms with spin bandwidths too wide to be accurately refocused by hard pulses ($\Delta B_0/B_0 \sim 0.3\%$). Using a correction method, we compensate for the quadratic phase modulation imparted by the swept WURST pulses, enabling the entire echo train to be used for TRASE. While WURST pulses are longer than hard pulses and lengthen the echo train, increasing blurring from T_2 -decay, this limitation can in principle be partially overcome by interleaving

multiple spin echo trains that each acquire different subsets of k -space. The swept pulse TRASE approach is generalizable to 2-D and 3-D encoding using RF transmit arrays with B_1^+ phase gradients along each encoding direction. TRASE provides pure B_1^+ encoding that is independent of the B_0 field and thus does not need to dominate B_0 field variation over the sample, as in conventional B_0 slice-select and readout gradient encoding. TRASE therefore provides an appealing option for MRI spatial encoding for portable low-field applications, where it reduces weight, cost, size, and power requirements on system design.

Acknowledgments

The authors thank Jonathan Sharp, Scott King, Michael Garwood, Robin de Graaf, Soumyajit Mandal, and Mathieu Sarracanie for illuminating discussions, and Lina Colucci for help with relaxation measurements. We also thank the anonymous reviewers of this work for their many helpful insights and suggestions. Support comes from NIH R01EB018976, K99 EB019482 and DoD/USAMRRA W81XWH-11-2-0076 (DM09094).

Appendix A. Supplementary material

Supplementary data associated with this article can be found, in the online version, at <http://dx.doi.org/10.1016/j.jmr.2016.04.005>.

References

- [1] F. Casanova, J. Perlo, *Single-Sided NMR*, Springer, Berlin Heidelberg, 2011, <http://dx.doi.org/10.1007/978-3-642-16307-4>.
- [2] B. Blümich, P. Blümmler, G. Eidmann, A. Guthausen, R. Haken, U. Schmitz, et al., The NMR-MOUSE: construction, excitation, and applications, *Magn. Reson. Imag.* 16 (1998) 479–484, [http://dx.doi.org/10.1016/S0730-725X\(98\)00069-1](http://dx.doi.org/10.1016/S0730-725X(98)00069-1).
- [3] M. Van Landeghem, E. Danieli, J. Perlo, B. Blümich, F. Casanova, Low-gradient single-sided NMR sensor for one-shot profiling of human skin, *J. Magn. Reson.* 215 (2012) 74–84, <http://dx.doi.org/10.1016/j.jmr.2011.12.010>.
- [4] F. Casanova, B. Blümich, Two-dimensional imaging with a single-sided NMR probe, *J. Magn. Reson.* 163 (2003) 38–45, [http://dx.doi.org/10.1016/S1090-7807\(03\)00123-X](http://dx.doi.org/10.1016/S1090-7807(03)00123-X).
- [5] J. Perlo, F. Casanova, B. Blümich, 3D imaging with a single-sided sensor: an open tomograph, *J. Magn. Reson.* 166 (2004) 228–235, <http://dx.doi.org/10.1016/j.jmr.2003.10.018>.
- [6] J. Mitchell, E.J. Fordham, Nuclear magnetic resonance core analysis at 0.3 T, *Rev. Sci. Instrum.* 85 (2014) 111502, <http://dx.doi.org/10.1063/1.4902093>.
- [7] P.J. Prado, B. Blümich, U. Schmitz, One-dimensional imaging with a palm-size probe, *J. Magn. Reson.* 144 (2) (2000) 200–206.
- [8] C.Z. Cooley, J.P. Stockmann, B.D. Armstrong, M. Sarracanie, M.H. Lev, M.S. Rosen, et al., Two-dimensional imaging in a lightweight portable MRI scanner without gradient coils, *Magn. Reson. Med.* 72 (2015) 872–883, <http://dx.doi.org/10.1002/mrm.25147>.
- [9] L.B. Casabianca, D. Mohr, S. Mandal, Y.-Q. Song, L. Frydman, Chirped CPMG for well-logging NMR applications, *J. Magn. Reson.* 242 (2014) 197–202, <http://dx.doi.org/10.1016/j.jmr.2014.02.025>.
- [10] J.-Y. Park, M. Garwood, Spin-echo MRI using $\pi/2$ and π hyperbolic secant pulses, *Magn. Reson. Med.* 61 (2009) 175–187, <http://dx.doi.org/10.1002/mrm.21822>.
- [11] A.L. Snyder, C. Corum, S. Moeller, N. Powell, M. Garwood, MRI by steering resonance through space, *Magn. Reson. Med.* 72 (2014) 49–58, <http://dx.doi.org/10.1016/j.micinf.2011.07.011.innate>.
- [12] N. Ben-Eliezer, M. Irani, L. Frydman, Super-resolved spatially encoded single-scan 2D MRI, *Magn. Reson. Med.* 63 (2010) 1594–1600, <http://dx.doi.org/10.1002/mrm.22377>.
- [13] N. Ben-Eliezer, Y. Shrot, L. Frydman, D.K. Sodickson, Parametric analysis of the spatial resolution and signal-to-noise ratio in super-resolved spatiotemporally encoded (SPEN) MRI, *Magn. Reson. Med.* 72 (2014) 418–429, <http://dx.doi.org/10.1002/mrm.24954>.
- [14] R. Schmidt, L. Frydman, New spatiotemporal approaches for fully refocused, multislice ultrafast 2D MRI, *Magn. Reson. Med.* 71 (2) (2014) 711–722, <http://dx.doi.org/10.1002/mrm.24714>.
- [15] Y. Shrot, L. Frydman, Spatially encoded NMR and the acquisition of 2D magnetic resonance images within a single scan, *J. Magn. Reson.* 172 (2005) 179–190, <http://dx.doi.org/10.1016/j.jmr.2004.09.024>.
- [16] A. Tal, B. Shapira, L. Frydman, A continuous phase-modulated approach to spatial encoding in ultrafast 2D NMR spectroscopy, *J. Magn. Reson.* 176 (2005) 107–114, <http://dx.doi.org/10.1016/j.jmr.2005.05.009>.
- [17] Z. Cao, E.Y. Chekmenev, W.A. Grissom, Frequency encoding by Bloch–Siegert shift, in: *Proc. 22nd Annu. Meet. Int. Soc. Magn. Res. Med.*, 2014, p. 4220.

- [18] R. Kartäusch, T. Driessle, T. Kampf, T.C. Basse-Lüsebrink, U.C. Hoelscher, P.M. Jakob, et al., Spatial phase encoding exploiting the Bloch–Siegert shift effect, *MAGMA* 27 (2014) 363–371, <http://dx.doi.org/10.1007/s10334-013-0417-0>.
- [19] J.C. Sharp, S.B. King, MRI using radiofrequency magnetic field phase gradients, *Magn. Reson. Med.* 63 (2010) 151–161, <http://dx.doi.org/10.1002/mrm.22188>.
- [20] J.C. Sharp, S.B. King, Q. Deng, V. Volotovskyy, B. Tomanek, High-resolution MRI encoding using radiofrequency phase gradients, *NMR Biomed.* 26 (2013) 1602–1607, <http://dx.doi.org/10.1002/nbm.3023>.
- [21] G.C. Wiggins, C. Triantafyllou, a. Potthast, A. Reykowski, M. Nittka, L.L. Wald, 32-channel 3 Tesla receive-only phased-array head coil with soccer-ball element geometry, *Magn. Reson. Med.* 56 (2006) 216–223, <http://dx.doi.org/10.1002/mrm.20925>.
- [22] K.P. Pruessmann, M. Weiger, M.B. Scheidegger, P. Boesiger, SENSE: sensitivity encoding for fast MRI, *Magn. Reson. Med.* 42 (1999) 952–962. <http://www.ncbi.nlm.nih.gov/pubmed/10542355>.
- [23] M.A. Griswold, P.M. Jakob, R.M. Heidemann, M. Nittka, V. Jellus, J. Wang, et al., Generalized autocalibrating partially parallel acquisitions (GRAPPA), *Magn. Reson. Med.* 47 (2002) 1202–1210, <http://dx.doi.org/10.1002/mrm.10171>.
- [24] J. Sharp, Q. Deng, V. Volotovskyy, R. Tyson, D. Yin, R. Bernhardt, et al., Imaging without gradients: first in vivo MR images using the TRASE RF imaging method, in: *Proc. 20th Annu. Meet. Int. Soc. Magn. Res. Med.*, 2012, p. 705.
- [25] J.C. Sharp, D. Yin, B. Tomanek, S.B. King, Point-spread-functions for RF imaging with TRASE: implications for phase gradient coil design and flip angle calibration 1, in: *Proc. 18th Annu. Meet. Int. Soc. Magn. Res. Med.*, 2010, p. 1469.
- [26] J.P. Stockmann, C.Z. Cooley, M. Sarraçanie, M.S. Rosen, L.L. Wald, Transmit Array Spatial Encoding (TRASE) with broadband WURST pulses for robust spatial encoding in inhomogeneous B₀, in: *Proc. 23rd Annu. Meet. Int. Soc. Magn. Res. Med.*, Toronto, 2015, p. 0917.
- [27] D. Kunz, Frequency-modulated radiofrequency pulses in spin-echo and stimulated-echo experiments, *Magn. Reson. Med.* 4 (1987) 129–136.
- [28] A. Tal, L. Frydman, Spatial encoding and the single-scan acquisition of high definition MR images in inhomogeneous fields, *J. Magn. Reson.* 182 (2006) 179–194, <http://dx.doi.org/10.1016/j.jmr.2006.06.022>.
- [29] J.G. Pipe, Spatial encoding and reconstruction in MRI with quadratic phase profiles, *Magn. Reson. Med.* 33 (1995) 24–33.
- [30] A. Maudsley, Dynamic range improvement in NMR imaging using phase scrambling, *J. Magn. Reson.* 72 (1988) 287–305.
- [31] W.R.T. Witschey, C.A. Cocosco, D. Gallichan, G. Schultz, H. Weber, A. Welz, et al., Localization by nonlinear phase preparation and k-space trajectory design, *Magn. Reson. Med.* 67 (2012) 1620–1632, <http://dx.doi.org/10.1002/mrm.23146>.
- [32] S. Ito, Y. Yamada, Alias-free image reconstruction using fresnel transform in the phase-scrambling fourier imaging, *Magn. Reson. Med.* 430 (2008) 422–430, <http://dx.doi.org/10.1002/mrm.21672>.
- [33] H. Weber, G. Schultz, D. Gallichan, J. Hennig, M. Zaitsev, Local field of view imaging for alias-free undersampling with nonlinear spatial encoding magnetic fields, *Magn. Reson. Med.* 1014 (2013) 1002–1014, <http://dx.doi.org/10.1002/mrm.24754>.
- [34] S. Meiboom, D. Gill, Modified spin-echo method for measuring nuclear relaxation times, *Rev. Sci. Instrum.* 29 (1958) 688, <http://dx.doi.org/10.1063/1.1716296>.
- [35] A. Tannús, M. Garwood, Adiabatic pulses, *NMR Biomed.* 10 (1997) 423–434. <http://www.ncbi.nlm.nih.gov/pubmed/9542739>.
- [36] L.A. O'Dell, The WURST kind of pulses in solid-state NMR, *Solid State Nucl. Magn. Reson.* 55–56 (2013) 28–41, <http://dx.doi.org/10.1016/j.ssnmr.2013.10.003>.
- [37] J. Pauly, P. Le Roux, D. Nishimura, A. Macovski, Parameter relations for the Shinnar-Le Roux selective excitation pulse design algorithm [NMR imaging], *IEEE Trans. Med. Imag.* 10 (1991) 53–65, <http://dx.doi.org/10.1109/42.75611>.
- [38] R.A. de Graaf, K. Nicolay, Adiabatic RF pulses: applications to in vivo NMR, *Concepts Magn. Reson.* 9 (1997) 247–268, [http://dx.doi.org/10.1002/\(SICI\)1099-0534\(1997\)9:4<247::AID-CMR4>3.0.CO;2-Z](http://dx.doi.org/10.1002/(SICI)1099-0534(1997)9:4<247::AID-CMR4>3.0.CO;2-Z).
- [39] A. Maudsley, Modified Carr–Purcell–Meiboom–Gill sequence for NMR Fourier imaging applications, *J. Magn. Reson.* 69 (1986) 488–491, [http://dx.doi.org/10.1016/0022-2364\(86\)90160-5](http://dx.doi.org/10.1016/0022-2364(86)90160-5).
- [40] C.Z. Cooley, J.P. Stockmann, M. Sarraçanie, M.S. Rosen, L.L. Wald, 3D Imaging in a portable MRI scanner using Rotating Spatial Encoding Magnetic Fields and Transmit Array Spatial Encoding, in: *Proc. 23rd Annu. Meet. Int. Soc. Magn. Res. Med.*, Toronto, 2015, p. 76.
- [41] Q. Deng, S.B. King, V. Volotovskyy, B. Tomanek, J.C. Sharp, B1 transmit phase gradient coil for single-axis TRASE RF encoding, *Magn. Reson. Imag.* 31 (2013) 891–899, <http://dx.doi.org/10.1016/j.mri.2013.03.017>.
- [42] T. Claassen-Vujcic, H.M. Borsboom, H.J.G. Gaykerna, T. Mehlkopf, Transverse low-field RF coils in MRI, *Magn. Reson. Med.* 36 (1996) 111–116.
- [43] H.W. Fischer, P.A. Rinck, Y. van Haverbeek, R.N. Muller, Nuclear relaxation of human brain gray and white matter: analysis of field dependence and implications for MRI, *Magn. Reson. Med.* 16 (1990) 317–334.
- [44] W.D. Rooney, G. Johnson, X. Li, E.R. Cohen, S.-G. Kim, K. Ugurbil, C.S. Springer, Magnetic field and tissue dependencies of human brain longitudinal 1H2O relaxation in vivo, *Magn. Reson. Med.* 57 (2007) 308–317.
- [45] G. Bartzokis, M. Aravagiri, W.H. Oldendorf, J. Mintz, S.R. Marder, Field dependent transverse relaxation rate increase may be a specific measure of tissue iron stores, *Magn. Reson. Med.* 29 (1993) 459–464.
- [46] A.L. Hopkins, H.N. Yeung, C.B. Bratton, Multiple field strength in vivo T₁ and T₂ for Cerebrospinal fluid protons, *Magn. Reson. Med.* 3 (1986) 303–311.
- [47] S.B. King, P. Latta, V. Volotovskyy, J.C. Sharp, B. Tomanek, Phase encoding without gradients using TRASE-FSE MRI, in: *Proc. 15th Annual Meet. Int. Soc. Mag. Reson. Med.*, 2007, p. 680.
- [48] S. Mandal, V.D.M. Koroleva, T.W. Borneman, Y.-Q. Song, M.D. Hürlimann, Axis-matching excitation pulses for CPMG-like sequences in inhomogeneous fields, *J. Magn. Reson.* 237 (2013) 1–10, <http://dx.doi.org/10.1016/j.jmr.2013.09.004>.
- [49] V.D.M. Koroleva, S. Mandal, Y.-Q. Song, M.D. Hürlimann, Broadband CPMG sequence with short composite refocusing pulses, *J. Magn. Reson.* 230 (2013) 64–75, <http://dx.doi.org/10.1016/j.jmr.2013.01.006>.
- [50] A. Raad, L. Darrasse, Optimization of NMR receiver bandwidth by inductive coupling, *Magn. Reson. Imag.* 10 (1992) 55–65, [http://dx.doi.org/10.1016/0730-725X\(92\)90373-8](http://dx.doi.org/10.1016/0730-725X(92)90373-8).
- [51] S. Mandal, S. Utsuzawa, D.G. Cory, M. Hürlimann, M. Poitzsch, Y.-Q. Song, An ultra-broadband low-frequency magnetic resonance system, *J. Magn. Reson.* 242 (2014) 113–125, <http://dx.doi.org/10.1016/j.jmr.2014.02.019>.
- [52] J. Bellec, S.B. King, C.-Y. Liu, C.P. Bidinosti, Target field based RF phase gradient transmit array for 3D TRASE MRI, in: *Int. Soc. Magn. Reson. Med.*, 2013, p. 138.
- [53] S. Salajeghe, P. Babyn, J.C. Sharp, G.E. Sarty, Non-linear TRASE, in: *Proc. 23rd Annu. Meet. Int. Soc. Magn. Res. Med.*, 2015, p. 2461.
- [54] M.R. Hestenes, E. Stiefel, Methods of conjugate gradients for solving linear systems 1, *J. Res. Natl. Bur. Stand.* 49 (1954) 409–436.